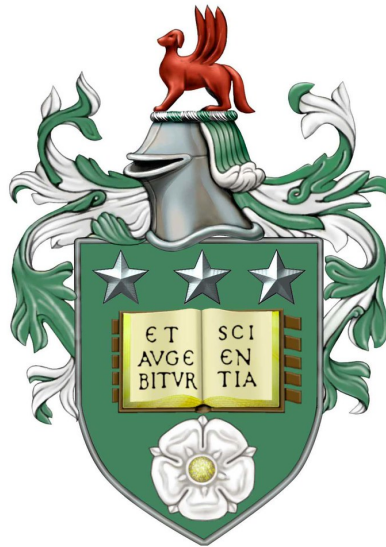


# Three-Dimensional Convection in Dry Salt Lakes

Matthew Robert Threadgold

Submitted in accordance with the requirements for the degree of

*Doctor of Philosophy*



University of Leeds

Department of Applied Mathematics

June 2024



## Intellectual Property Statement

The candidate confirms that the work submitted is his own, except where work which has formed part of jointly authored publications has been included. The contribution of the candidate and the other authors to this work has been explicitly indicated below. The candidate confirms that the appropriate credit has been given within the thesis where reference has been made to the work of others.

Section 4.6 is based on work from the jointly authored publication:

J. Lasser, J. M. Nield, M. Ernst, V. Karius, G. F. S. Wiggs, M. R. Threadgold, C. Beaume & L. Goehring. Salt Polygons and Porous Media Convection. *Physical Review X*, **13**, 011025 (2023)

The candidate performed numerical experiments and analysed the data from the three-dimensional simulations.

This copy has been supplied on the understanding that it is copyright material and that no quotation from the thesis may be published without proper acknowledgement.



## Acknowledgements

I would like to express my deepest gratitude to my supervisors, Cédric Beaume, Lucas Goehring and Steve Tobias, for their unwavering support, guidance and patience throughout my PhD. I would also like to thank Cédric for writing the code and for making extensive iterations to improve it at every possible opportunity.

This work was undertaken on ARC4, part of the High Performance Computing facilities at the University of Leeds UK and was supported by the Leeds-York-Hull Natural Environment Research Council (NERC) Doctoral Training Partnership (DTP) Panorama under grant NE/S007458/1.



## Abstract

Dry salt lakes are striking geological features, displaying patterns consisting of flat polygons bounded by raised ridges. They are found in semi-arid regions of the world, with the patterns typically being one to a few metres across, a characteristic of dry lakes that can be observed worldwide. The groundwater in the porous soil beneath dry lakes collects salts as it flows towards these terminal valleys, and despite the intense environment, the water table can often be found close to the surface. As the water evaporates, salt is left behind, forming a crust, allowing the ridges to grow and develop into an intricate network.

To balance the evaporation of water from the surface, a throughflow is present in the porous soil, which transports the dissolved salts to the surface. As the groundwater evaporates, heavier saltier water overlies lighter fresher water and the competition between the upward advection and the downward diffusion of salt gives rise to a natural steady state. This state may become unstable, resulting in buoyancy-driven convection within the porous soil beneath the lake. This results in spatial variation of the salt transport to the surface, which may aid the growth of the crust in some places and hinder it in others. This provides a possible explanation for the emergence of the surface pattern observed at dry lakes: the polygonal pattern is a surface expression of the subsurface fluid dynamics.

In this thesis, the linear instability resulting from the natural steady state is analysed, showing that an instability can only occur when the throughflow is sufficiently weaker than the opposing buoyancy effects. The convection resulting from this initial instability is investigated through numerical simulation. Patterns in the salinity transport to the surface are observed, providing evidence that this may be a significant contributor to the crust pattern observed at dry lakes. The net rate of salinity transport and the overall pattern scale are analysed as the lake conditions are changed, showing agreement with observations taken from the field.



# Contents

<b>1</b>	<b>Introduction</b>	<b>1</b>
1.1	Dry Lakes, Crusts and Patterns . . . . .	1
1.2	Importance . . . . .	4
1.3	Convection . . . . .	7
1.4	Overview . . . . .	10
<b>2</b>	<b>Theory</b>	<b>11</b>
2.1	Establishing the Governing Equations . . . . .	12
2.2	Dry Lake Equations . . . . .	14
2.3	Scalings . . . . .	18
2.4	Parameter Values . . . . .	20
2.5	Linear Stability . . . . .	21
2.6	Other Convection Systems . . . . .	24
<b>3</b>	<b>Numerics</b>	<b>29</b>
3.1	Linear Stability . . . . .	29
3.1.1	Linear Stability Validation . . . . .	31
3.2	Fully Nonlinear Dynamics . . . . .	32
3.3	Temporal discretisation . . . . .	35
3.3.1	Time Derivative . . . . .	35
3.3.2	Nonlinear Term . . . . .	36
3.3.3	Method of Solution . . . . .	37
3.4	Horizontal Discretisation . . . . .	38
3.4.1	Fourier Discretisation in One Dimension . . . . .	38
3.4.2	De-aliasing . . . . .	41
3.4.3	Fourier Discretisation in Two Dimensions . . . . .	43

## CONTENTS

---

3.5	Vertical Discretisation . . . . .	44
3.5.1	Spectral Elements . . . . .	50
3.5.2	Schur Decomposition . . . . .	55
3.6	Solving the Dry Lake Equations . . . . .	59
3.7	Validation . . . . .	62
3.7.1	Horizontal Directions . . . . .	62
3.7.2	Vertical Direction . . . . .	65
3.7.3	Time Step . . . . .	70
<b>4</b>	<b>Results</b>	<b>73</b>
4.1	Overview of Dynamics . . . . .	73
4.2	Linear Stability . . . . .	80
4.2.1	Linear Regime . . . . .	83
4.2.2	Alternative Perturbation . . . . .	86
4.3	Emergence of Polygons . . . . .	89
4.4	Late-Time Dynamics . . . . .	92
4.5	Parametric Study . . . . .	98
4.5.1	Dependence on the Lake Depth . . . . .	98
4.5.2	Dependence on the Rayleigh Number . . . . .	101
4.6	Comparison to Field Observations . . . . .	108
<b>5</b>	<b>Discussion</b>	<b>113</b>
5.1	Overview . . . . .	113
5.1.1	Comparisons . . . . .	114
5.2	Limitations . . . . .	115
5.2.1	Bottom Boundary Condition . . . . .	115
5.2.2	Dominant Wavenumber . . . . .	120
5.2.3	Crust Feedback . . . . .	122
5.3	Perspectives . . . . .	122
5.3.1	Evaporation Rate . . . . .	122
5.3.2	Patterns . . . . .	124
5.3.3	Heterogeneous Porous Media . . . . .	125
<b>A</b>	<b>One-Dimensional Crust Growth</b>	<b>127</b>
A.1	Introduction . . . . .	127
A.2	Model . . . . .	127

A.2.1	Steady State Solution . . . . .	131
A.2.2	Conservation Equations . . . . .	132
A.2.3	Solution . . . . .	133
A.3	Initial Value Problem . . . . .	134
A.3.1	Method of Solution . . . . .	136
A.3.2	Results . . . . .	138
A.4	A Sinking Crust . . . . .	139
A.4.1	Results . . . . .	141
A.5	Discussion . . . . .	143
	<b>References</b>	<b>143</b>



# List of Figures

1.1	Images of crust patterns observed at dry salt lakes. . . . .	2
1.2	Image from the film ‘Star Wars: The Last Jedi’ displaying a crust pattern at Salar de Uyuni. . . . .	2
1.3	Crust thickness and polygon wavelength from observations taken from Badwater Basin and Owens Lake. . . . .	4
2.1	Sketch of a dry lake illustrating the porous soil and incompressible fluid flow.	15
3.1	Relative error of the growth rate against the number of collocation points and the law to determine the number of collocation points as a function of the domain depth. . . . .	32
3.2	Example of a Fourier mesh for $\Gamma = 4$ and $M = 8$ . . . . .	38
3.3	Illustration of aliasing for the functions $\cos(2\pi x/\Gamma)$ and $\cos(18\pi x/\Gamma)$ for $\Gamma = 4$ and $M = 8$ . . . . .	39
3.4	Sketch of the wavenumber folding arising from a nonlinearity. . . . .	42
3.5	First four Legendre polynomials. . . . .	45
3.6	Example of a spectral element mesh using $N_e = 3$ and $N_z = 10$ for a domain with $h = 3$ . . . . .	51
3.7	Example of the threshold criterion used for the horizontal mesh validation.	64
3.8	Maximum number of mesh points required as a function of time for several values of the threshold energy. . . . .	64
3.9	Required horizontal mesh density as a function of $Ra$ . . . . .	65
3.10	Maximum and minimum vertical mesh densities as a function of the number of mesh points in the vertical direction. . . . .	66
3.11	Relative error in the average salinity and the number of mesh points per element as a function of the number of elements. . . . .	69
3.12	Vertical mesh density used as a function of $Ra$ for $h = 10$ . . . . .	70

LIST OF FIGURES

---

4.1	Snapshots of the salinity and the surface flux from a two-dimensional simulation at $t = 0.5$ , $t = 0.9$ and $t = 1.4$ with $Ra = 100$ , $h = 10$ and $\Gamma_x = 12\pi$ .	75
4.2	Snapshots of the salinity and the surface flux from a two-dimensional simulation at $t = 1.7$ , $t = 2.5$ and $t = 10$ with $Ra = 100$ , $h = 10$ and $\Gamma_x = 12\pi$ .	76
4.3	Streamlines at $t = 1.5$ from a two-dimensional simulation with $Ra = 100$ , $h = 10$ and $\Gamma_x = 12\pi$ .	77
4.4	Snapshot of the salinity and the surface flux from a three-dimensional simulation with $Ra = 100$ , $h = 10$ and $\Gamma_x = \Gamma_y = 24\pi$ .	78
4.5	Snapshots of the surface flux from a three-dimensional simulation with $Ra = 100$ , $h = 10$ and $\Gamma_x = \Gamma_y = 12\pi$ .	79
4.6	Growth rate as a function of the wavenumber $k$ and Rayleigh number $Ra$ for $h = 10$ .	81
4.7	Growth rates for various $Ra$ and $h = 10$ as a function of the wavenumber and the most unstable eigenfunctions.	81
4.8	Neutral stability curves, most destabilising eigenmode and most unstable eigenfunctions for $Ra = 100$ and various $h$ .	82
4.9	Relative error between the critical values of a finite depth lake and an infinitely deep lake.	83
4.10	Departure from the base state and average flux of salinity to the surface for $Ra = 100$ and $h = 10$ .	84
4.11	Normalised radial power spectrum of the salinity flux to the surface.	86
4.12	Exponential fit to the most unstable eigenfunction and decay rate as a function of $Ra$ .	87
4.13	Departure from the base state and average salinity flux to the surface comparing different vertical profiles for the initial condition.	88
4.14	Two-dimensional simulation demonstrating how the asymmetry of the boundary layer leads to the formation of salinity plumes.	90
4.15	Time evolution of the average salinity flux to the surface and out through the bottom of the domain.	90
4.16	Salinity flux to the surface during the growth and decay of the low-wavenumber modes following the linear instability.	91
4.17	Regions of the surface flux of size $6\pi \times 6\pi$ and horizontal velocity field for $Ra = 100$ , $h = 10$ and $\Gamma_x = \Gamma_y = 12\pi$ .	92

4.18	Representation of the depth of penetration of the salinity contour $S = 0.75$ for a region of size $6\pi \times 6\pi$ for $Ra = 100$ , $h = 10$ and $\Gamma_x = \Gamma_y = 12\pi$ . . . . .	93
4.19	Average wavenumber of the salinity as a function of depth at $t = 10$ and the evolution of the average wavenumber of the salinity at the midplane. . . . .	95
4.20	Salinity as a function of its time derivative at four selected points and the time evolution of the average surface flux and average wavenumber. . . . .	97
4.21	Average surface flux, average bottom flux and average total flux for simulations with varying $h$ and $Ra$ . . . . .	99
4.22	Surface flux departure times and maximum upwelling and downwelling speeds as functions of $(Ra - Ra_c)/Ra_c$ . . . . .	100
4.23	Average surface flux, average wavenumber and dominant wavenumber when plumes reach the bottom of the domain and when the disturbance has propagated back to the surface. . . . .	101
4.24	Surface flux for three-dimensional simulations with varying $h$ , $Ra = 100$ and $\Gamma_x = \Gamma_y = 12\pi$ . . . . .	102
4.25	Average surface flux and average flux through the bottom of the domain as functions of the rescaled time. . . . .	103
4.26	Average surface flux, average wavenumber and dominant wavenumber when plumes reach the bottom of the domain and when the disturbance has propagated back to the surface. . . . .	104
4.27	Fraction of positive flux as a function of the rescaled time and the flux fraction when plumes reach the bottom of the domain and when the disturbance has propagated back to the surface. . . . .	105
4.28	Surface flux for three-dimensional simulations with varying $Ra$ , $h = 10$ and $\Gamma_x = \Gamma_y = 12\pi$ . . . . .	106
4.29	Time-averaged surface flux for three-dimensional simulations with varying $Ra$ , $h = 10$ and $\Gamma_x = \Gamma_y = 12\pi$ . . . . .	107
4.30	Surface height maps, salinity profiles and exponential fits from data taken from observations. . . . .	108
4.31	Surface salinity flux and salinity fields at two different cross sections taken under the surface. . . . .	109
4.32	Field data and simulation data for average and dominant wavenumbers with varying $Ra$ . . . . .	110

LIST OF FIGURES

---

5.1 Salinity field from two-dimensional simulations with  $Ra = 500$ ,  $h = 10$  and  $\Gamma_x = 4\pi$  for the natural and uniform bottom boundary conditions. . . . . 116

5.2 Vertical salinity profiles from two-dimensional simulations with  $Ra = 500$ ,  $h = 10$  and  $\Gamma_x = 4\pi$  for the natural and uniform bottom boundary conditions. 117

5.3 Salinity flux out through the bottom of the domain for  $Ra = 100$ ,  $h = 10$  and  $\Gamma_x = \Gamma_y = 12\pi$  for the natural and uniform bottom boundary condition. 119

5.4 Dominant wavenumber for a two- and three-dimensional simulation with  $Ra = 100$ ,  $h = 10$  and  $\Gamma_x = \Gamma_y = 12\pi$ . . . . . 120

5.5 Surface flux and power spectrum for a two-dimensional simulation with  $Ra = 100$ ,  $h = 10$  and  $\Gamma_x = 12\pi$ . . . . . 121

5.6 Post-treated surface flux and power spectrum for a two-dimensional simulation with  $Ra = 100$ ,  $h = 10$  and  $\Gamma_x = 12\pi$ . . . . . 121

A.1 Sketch of the one-dimensional model with a crust. . . . . 128

A.2 Sketch of the initial lake–crust interface with an inconsistent salt flux. . . . . 129

A.3 Sketch of the one-dimensional model with a crust and brine layer. . . . . 130

A.4 Sketch of the local water conservation at the crust–air interface. . . . . 132

A.5 Sketch of the local salt conservation at the crust–brine interface. . . . . 133

A.6 Throughflow, crust thickness and brine thickness as functions of time from a one-dimensional simulation. . . . . 138

A.7 Sketch of the one-dimensional model with a sinking crust. . . . . 140

A.8 Throughflow, sink rate and crust thickness as functions of time from a one-dimensional simulation. . . . . 142

# List of Tables

2.1	Minimum and maximum values for data collected at Badwater Basin, Owens Lake and Sua Pan. . . . .	20
3.1	Time derivative scheme coefficients. . . . .	36
3.2	Nonlinear term scheme coefficients. . . . .	37
3.3	Matrices associated with the vertical discretisation that are computed at the start of a simulation. . . . .	58
5.1	Divergence observations of two-dimensional simulations for $Ra = 500$ , $h = 10$ and $\Gamma_x = 4\pi$ for the natural and uniform bottom boundary conditions and two different time steps. . . . .	118



# Chapter 1

## Introduction

### 1.1 Dry Lakes, Crusts and Patterns

Salt lakes are spectacular geological features, displaying breathtaking patterns on their surface. These lakes emerge in semi-arid regions of the world making them one of the most inhospitable environments on the planet. Salt lakes (also referred to as playa (Briere, 2000)) are found in terminal valleys, from which water mainly leaves by evaporation (Briere, 2000; Lowenstein & Hardie, 1985). Dry salt lakes form when the water evaporates at a rate faster than it can be replenished (Yechieli & Wood, 2002). However, elevated terrain surrounding these endorheic basins prevents direct precipitation on the valley floor (Hollett et al., 1991), and the majority of the inflow is from precipitation on the adjacent mountains, which can make its way to the basin by runoff (Briere, 2000).

When the average rate of evaporation exceeds that of precipitation, a flow of water through the soil must be present to balance the evaporative losses, and this groundwater flow also acts as a route for transporting salt. As water evaporates from the lake, the ground surface may become exposed to the atmosphere and, as salts precipitate, a superficial crust can grow on the surface (Eugster & Hardie, 1978) while fluid continues to flow in the soil beneath. As shown in Figure 1.1, the salt crust that develops under these conditions often displays an intricate network of polygons, typically one to a few metres across, a characteristic length scale that can be observed worldwide (Krinsley, 1970; Lasser et al., 2023; Nield et al., 2015). Huge amounts of tourists flock to these fascinating locations every year, especially Salar de Uyuni (Bolivia), which was used to film a scene in the movie ‘Star Wars: The Last Jedi’ (Star Wars: The Last Jedi, 2017), shown in Figure 1.2.

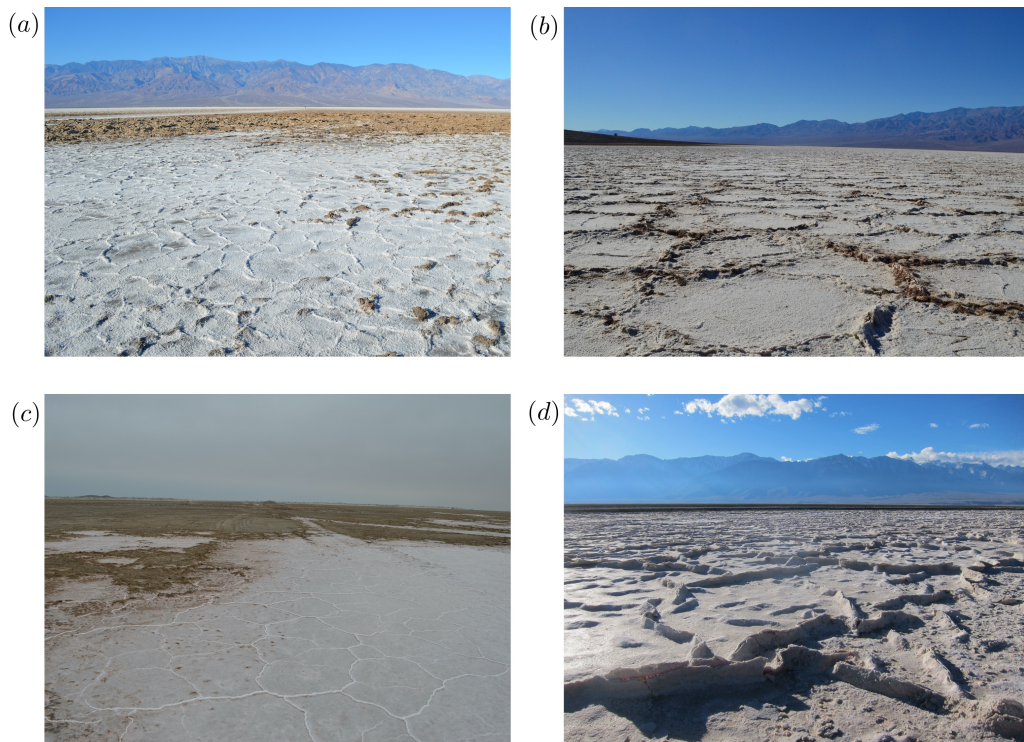


Figure 1.1: Images of crust patterns in dry salt lakes at (a), (b) Badwater Basin, California, (c) the Skeleton Coast, Namibia, and (d) Owens Lake, California. Images courtesy of Lucas Goehring.



Figure 1.2: Image from the film 'Star Wars: The Last Jedi' (Star Wars: The Last Jedi, 2017) displaying the surface pattern at Salar de Uyuni.

Crust patterns emerge on the surface of dry salt lakes all over the world and in vastly different environments. For example, in North America, Owens Lake is located at 1084 m above sea level and Badwater Basin is located at 86 m below sea level. On the other hand, the largest dry lake in the world, Salar de Uyuni, Bolivia (Sanchez-Lopez, 2021), is located at 3656 m above sea level. In Africa, there are violent precipitation events, yet dry lakes can still be found, for example, the Makgadikgadi Pans in Botswana (Eckardt et al., 2008; Nield et al., 2015), Chott el Djerid in Tunisia (Wadge et al., 1994) and the Skeleton Coast in Namibia. Dry lakes can also be found in Asia: the Dead Sea, located in Israel (Talbot et al., 1996), the Kavir Desert, lying in the Iranian Plateau (Krinsley, 1970) and Dalangtan Playa in China (Dang et al., 2018). Similar features can also form when groundwater collects near enough to the surface to evaporate over long periods, for example in the coastal sabkhas of Abu Dhabi (Sanford & Wood, 2001). Across these locations, the patterns that emerge in the surface crust are remarkably similar, with the size of the polygons being quite robust at one to a few metres across, independent of seemingly important external factors. For example, the crust composition varies greatly: some crusts are predominantly sodium chloride, such as those at Badwater Basin (Death Valley), while other sites including Owens Lake (California), are covered by crusts rich in hydrated sodium sulfate (Lasser et al., 2020). Flooding events (Bryant & Rainey, 2002) can also dissolve the crust pattern periodically, allowing the polygonal pattern to restart its growth which subsequently appears with a similar pattern wavelength (Nield et al., 2015).

The patterns observed in the salt crust have been attempted to be explained by the cracking of the crust (Dellwig, 1968; Tucker, 1981) or the buckling of the crust (Christiansen, 1963; Lokier, 2012). These studies attempt to explain the development of polygons in the salt crust due to the compressional stresses from salt precipitation, salt crystal growth and the increased summer temperatures. The stresses are thought to cause the salt crust to fracture in the observed polygonal pattern, with initial fractures starting at the weak points in the crust which subsequently spread laterally at a given angle. In addition, the size of polygons resulting from the cracking of a thin layer has been attributed to the strength and thickness of the layer (Goehring, 2013), leading to a prediction that the pattern wavelength is proportional to the crust thickness. Figure 1.3 shows observations of the crust thickness and wavelength of the surface pattern from sites at Badwater Basin and Owens Lake (Lasser et al., 2020). These observations show that, at these lakes, the crust thickness ranges from a few centimetres to tens of centimetres while the polygons express

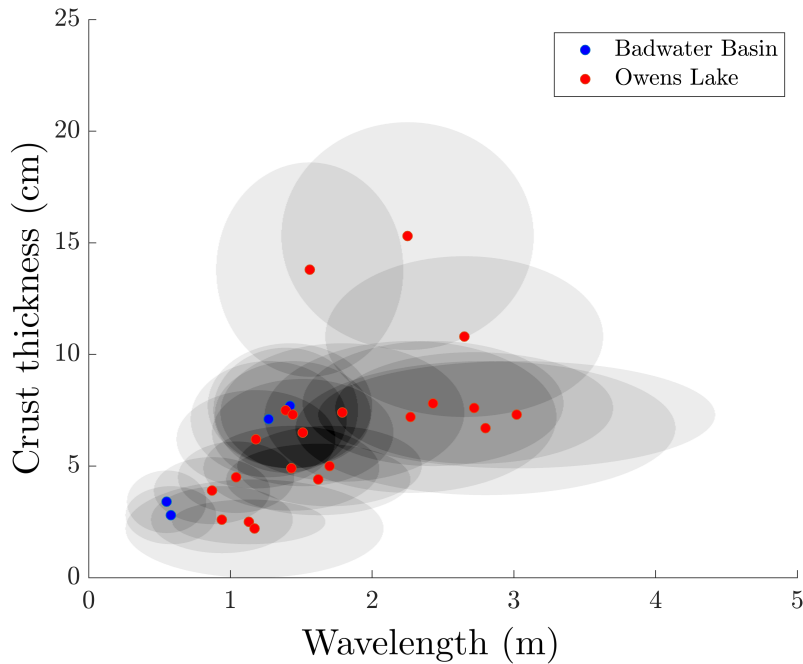


Figure 1.3: Crust thickness and polygon wavelength at various sites at Badwater Basin and Owens Lake (Lasser et al., 2020), showing the data concentrating around one to a few metres for the wavelength. Ellipses represent one standard deviation about each data point.

a wavelength of one to a few metres across. In addition, other observations (Kransley, 1970; Lowenstein & Hardie, 1985) have found crusts ranging from millimetres to several tens of centimetres in thickness. Thus, these theories fail to explain why the pattern size is consistent in dry lakes around the world.

## 1.2 Importance

Owens Lake, situated near Los Angeles, is among the deepest valleys in the United States and experiences minimal precipitation. Surrounded by mountains, clouds struggle to reach the valley resulting in very little rainfall and for approximately three-quarters of the years between 1934 and 1985, Lone Pine, a neighbouring town, recorded an annual rainfall of less than 100 mm (Hollett et al., 1991). Despite this, rainfall from the Sierra Nevada mountains can find its way into Owens Lake, carrying dissolved solids with it (Pretti & Stewart, 2002). This groundwater flow not only replenishes the lake but also offsets evaporative losses. However, since the construction of the Los Angeles Aqueduct in 1913, water has been redirected to the city and Owens Lake has suffered from a negative water balance. This led to its gradual desiccation, resulting in complete dryness by 1926. As the lake dried, the surface has become coated with a notable concentration of sodium, calcium, and silicon (Gill et al., 2002), along with toxic elements like lead and arsenic

(Gill et al., 2002; Ryu et al., 2002), as well as significant levels of sulphates (Ryu et al., 2004).

Winds sweeping across Owens Lake (Zhong et al., 2008) continuously erode the surface crust, transporting dust and minerals away from the valley. Consequently, Owens Lake became North America's primary source of atmospheric dust (Reynolds et al., 2007). The presence of sulphates and arsenic in the air due to this phenomenon poses a significant air pollution challenge (Gill, 1996), with numerous studies linking particulate air pollution to adverse health effects (Aghababaeian et al., 2021). Owens Lake serves as a prime example, illustrating how dry salt lakes substantially contribute to atmospheric dust and its environmental impact. Understanding these primary dust sources is important for improving current atmospheric dust models (Washington et al., 2003) and understanding their impact on global climate dynamics (Prospero et al., 2002). In addition, the formation of salt crusts on dry lake surfaces alters their erosive characteristics. The surface roughness increases when ridges are present, which may interact with prevailing winds (Nield et al., 2016; Raupach et al., 1993), increasing the rate of dust production from the surface. Consequently, there remains significant uncertainty surrounding the amount of dust emitted by dry salt lakes (Marticorena & Bergametti, 1995). The fine sand particles emitted from these lakes can ascend easily and act as aerosols, influencing cloud formation (Koehler et al., 2007) and potentially impacting global temperatures. Specifically, when the average radius of dust particles surpasses a critical threshold, their greenhouse effect outweighs the albedo effect, leading to global warming (Lacis et al., 1992). Conversely, events like volcanic eruptions release aerosols that can lower surface temperatures (Robock & Mao, 1995), demonstrating the uncertainty in the effect that aerosols have on the global climate. Moreover, dust originating from dry lakes facilitates mineral transport to the oceans (Fung et al., 2000; Prospero et al., 2002), further illustrating the importance of dry lakes in the Earth's systems.

In recent decades, the significance of dry lakes in shaping global climate dynamics has become more apparent. The presence of a crust on these lakes' surfaces can significantly impact evaporation rates, dependent on the characteristics of the underlying porous soil. Continuous salt crusts tend to decrease evaporation rates compared to fragmented ones (Eloukabi et al., 2013). Moreover, in certain instances, these salt crusts can detach and rise above the porous soil, further dampening evaporation (Li & Shi, 2021). Consequently, dry salt lakes are an important aspect in climate modelling, as their salt crusts influence evaporation, moisture, and heat fluxes into the atmosphere, motivating their inclusion in

global energy balance calculations (Bryant & Rainey, 2002; Nield et al., 2015; North et al., 1981; Pitman, 2003).

After the Los Angeles Aqueduct was built and Owens Lake dried up, the hazardous salt crust now has to be carefully managed to mitigate the effects of the dust emission that would be a severe health hazard for the population of Los Angeles. Owens Lake is subsequently subject to huge efforts to reduce the dust emission potential of the dry lake bed (David, 2005). Several methods to control the dust emission are used, including flooding (Groeneveld & Barz, 2013), where the lake is flooded with a shallow layer of fresh water. However, this is not efficient as the amount of freshwater needed to cover the dry lake and the surrounding areas exceeds  $10^8 \text{ m}^3$  per year (Groeneveld & Barz, 2013), but would achieve 99% dust control with a 75% coverage of flooding. Another method to control dust emission is to cover the lake with vegetation (Nicholas & Andy, 1997) as this increases the wind velocity needed to induce erosion. Dust emission is eliminated when the vegetation coverage is at least 15% (Nicholas & Andy, 1997) but, just like shallow flooding, large amounts of fresh water are needed to irrigate the land so that the vegetation can grow. Methods that use a large amount of freshwater need also to be minimised due to the scarcity of fresh water in California. Alternatively, gravel may be used to cover the ground (David, 2005), physically stopping dust from being caught by the wind and escaping into the atmosphere. Again, this strategy is expensive to implement due to the large amount of gravel needed to cover the lake and additionally, it needs to be regularly cleaned (Los Angeles Department of Water and Power, 2013). Flooding the lake with brine is another possible mitigation strategy, which forms an artificial floating crust that reduces the evaporation to less than the precipitation (Groeneveld et al., 2010). This method ensures that the ground surface is wet at all times and thus reduces the dust emission potential of the lake. This provides a method to reduce the dust emission from the surface of the lake without the need for large amounts of freshwater that other strategies need.

Salar de Uyuni stands out as a significant salt lake, primarily due to its distinction as one of the world's largest lithium reserves. The vast expanse of a dry surface crust holds considerable economic promise, particularly amidst the worldwide shift towards renewable energy sources. The soaring demand for lithium-ion batteries, driven notably by advancements like electric vehicles, highlights its pivotal role in modern technology. However, the prospect of harnessing its resources through large-scale mining operations raises questions regarding environmental impact and sustainability. Therefore, understanding the importance of Salar de Uyuni is crucial not only for the transition to green energy but also for

ensuring its adherence to principles of environmental stewardship and responsible resource management (Flood, 2024; Graham, 2023).

The Great Salt Lake in Utah has emerged as an important geological feature over the last few years, serving as a significant habitat for a wide range of bird species as it provides an essential breeding environment. The lake also supports industries like tourism, mineral extraction, and recreational activities, which helps support and generate revenue for the local communities. However, the decline in water levels at the lake has been attributed to human activities such as water diversion, contributing to the shrinking of the lake (Wurtsbaugh et al., 2017). Such a collapse would have serious consequences for the wildlife dependent on the lake and the communities dependent on its resources. This highlights the need for intervening conservation action to preserve the lake and to prevent ecological degradation for future generations (Safdie, 2023; Siegler, 2024; Singh, 2023).

### 1.3 Convection

Dry lakes consist of a porous soil, which acts as a medium for groundwater to flow. Even in semi-arid environments, where there are strong evaporation rates (Tyler et al., 1997), the water table is often found very close to the surface (Bryant, 2003; Reynolds et al., 2007), allowing the water to connect to the surface through capillary action. To a good approximation, this means that the soil beneath dry lakes can be considered as being fully saturated with water. As this water evaporates, a crust forms from the precipitating salts and a throughflow is present to balance the evaporative losses, fuelled by a background reservoir of fresher water, which is located deep below the surface of the dry lake (Wooding, Tyler, & White, 1997). The fluid in contact with the crust is fully saturated with salt, leading to a situation where heavier saltier water overlies the lighter fresher water deeper in the lake. These dissolved salts contribute to fluid density, which may then lead to buoyancy-driven flows, or convection, within the porous soil (Wooding, Tyler, & White, 1997; Wooding, Tyler, White, & Anderson, 1997). Field-based resistivity measurements made by Stevens et al. (2009) and Van Dam et al. (2009) show evidence of such salinity-driven convection in groundwater at coastal sabkhas or tidal flats. These studies independently confirmed the presence of unstable inverted density gradients in these environments and made clear observations of high salinity plumes interleaved with less dense, rising fluid. Salinity profiles have also been measured at various salt lakes (Badwater Basin, Owens Lake and Sua Pan) which have revealed the presence of high salinity plumes

underneath the surface crust (Lasser, 2019; Lasser et al., 2023).

Similar to Rayleigh–Bénard convection (Bénard, 1900; Rayleigh, 1916), early studies of convection driven by density changes due to temperature in porous media typically focused on the onset of instability. When there is no fluid flow, heat is transported by conduction only and the temperature profile is linear. When the density gradient of this state exceeds a critical value, convection may occur (Horton & Rogers, 1945; Lapwood, 1948) and heat is additionally transported by advection. This theory was later complemented by numerics (Wooding, 1957) and broadened to the case of solute-driven flows (Wooding, 1969). The stability of a density-stratified liquid rising through a porous medium was initially explored by Wooding (1960), in the thermally-driven case of a geyser. The stability of this flow was explained in terms of the Rayleigh number of the system, a parameter that measures the strength of buoyancy effects relative to the background flow. A steady, constant throughflow is only stable when this number is less than a critical value. Theoretical considerations by Homsy and Sherwood (1976), accounting for viscosity variations due to temperature, found a convective instability, provided that a similar Rayleigh number exceeded a critical value. Experimental and numerical studies of thermally-driven convection in a porous medium have also been performed in two dimensions by Elder (1967). In this case, steady-state convection cells were found for a variety of boundary conditions, including fluid discharge forced through patches on the upper or lower surface of the domain. In the context of salinity-driven flow, convective motion can be generated naturally under conditions representative of the aquifers present beneath salt lakes (Wooding, Tyler, & White, 1997). They demonstrated that surface evaporation can form a near-surface boundary layer of water that is enhanced in salt and determined a critical Rayleigh number for the onset of convection. The further evolution of salt plumes that develop from an unstable boundary layer was then explored both numerically and experimentally in Hele-Shaw cells with a narrow gap acting as the porous medium (Wooding, Tyler, White, & Anderson, 1997). A subsequent stability analysis carried out by Duijn et al. (2002) is in good agreement with these results, and was further verified through more detailed two-dimensional numerical computations. Wooding (2007) extended this analysis to higher values of the Rayleigh number, in contrast with the near-critical conditions explored previously. The typical modelling approaches for the most common setup of Rayleigh–Bénard convection have been extensively studied (Hewitt, 2020) and numerical simulations have been carried out both in two (Hewitt et al., 2012; Otero et al., 2004; Slim, 2014) and three dimensions (Hewitt et al., 2014). Additionally, the resulting patterns in the convective

structures exhibited by this system have been studied (De Paoli et al., 2022; Fu et al., 2013).

Buoyancy-driven convection serves as a crucial mechanism in the area of carbon sequestration, in which CO<sub>2</sub> may be stored in rock formations by dissolution. Many studies aim to contribute to the development of strategies for carbon storage, helping to reduce the impact of CO<sub>2</sub> in the atmosphere and hence mitigate the effects of anthropogenic climate change (Metz et al., 2005; Neufeld et al., 2010; Slim et al., 2013; Slim & Ramakrishnan, 2010). Much like how buoyancy forces drive fluid motion beneath the crust of dry salt lakes, similar phenomena occur beneath the surface of the Earth in carbon storage formations. In both scenarios, variations in density gradients induce a convective flow and thus parallels can be drawn between buoyancy-driven convection processes and the dynamics beneath dry salt lakes. Furthermore, the study of convection in CO<sub>2</sub> dissolution offers valuable insights into the behaviour of fluids in porous media. However, it is essential to recognise the distinctions between these systems. While the physics present in both situations are the same, the geological and environmental contexts differ significantly. Dry salt lakes, for instance, are subject to a background throughflow, differing from carbon storage reservoirs. Thus, while using similar methods from the study of CO<sub>2</sub> dissolution, care must be taken when directly comparing the results to those of dry salt lakes.

The connection between subsurface convection and the surface patterns at dry lakes has recently been explored in two dimensions (Lasser, 2019; Lasser et al., 2021) using a model of solutal convection in a porous medium. This allows the prediction of groundwater flows in domains that are much deeper than the dynamics present near the surface. When this process is modelled, the wavelength of the convective cells that develop is in good agreement with that of the patterns observed at dry lakes (Lasser, 2019; Lasser et al., 2021). The presence of convection introduces spatial variation to the transport of salt to the surface, which may aid the growth of a crust in some areas and hinder it in others (Lasser et al., 2023). Numerical simulations were used to investigate the dynamics occurring in the system on finite, but thick, domains. These simulations showed how small-amplitude perturbations grow and interact, eventually leading to chaotic dynamics. However, these models have so far been largely restricted to simulations of dry lakes on two-dimensional domains. Nevertheless, this model provides a possible explanation for the presence of polygonal patterns observed at dry salt lakes: crust patterns are a surface expression of the subsurface convective dynamics.

## 1.4 Overview

This thesis aims to expand the model of dry lakes presented by Lasser et al. (2021) to three dimensions, allowing the surface expression of the domain to be two-dimensional. The addition of this extra dimension has already aided in predicting the qualitative nature of the surface patterns observed at dry lakes and some of the simulations presented here have contributed to the work published by Lasser et al. (2023). This allows for an improved prediction of the pattern wavelengths that are observed in the field. In addition, the depth of dry lakes has not been fully explored. Dry lakes can be as deep 150 m (Güler & Thyne, 2004) and modelling them as infinitely deep provides insight through analytical calculations. However, imposing a finite depth adds the flexibility of studying different depth lakes via an extra parameter. Moreover, when dry lakes are simulated numerically, a bottom boundary condition must be imposed regardless and acknowledging the finite depth in the modelling reduces the inconsistencies between the theory and the numerics. Using this model, the convective instabilities that result from the natural steady-state of the system will be explored. The system will be simulated numerically, using key quantities such as the average salinity transport to the surface and the typical scales that arise in the surface flux to investigate whether the emerging patterns compare to what is observed in the field. Agreement between real-world data and numerical simulations may indicate that the subsurface dynamics is likely a main contributor to the surface crust patterns observed at dry salt lakes.

The system that shall be used to model the three-dimensional dry lakes is formulated in Chapter 2, followed by a description of the numerical methods in Chapter 3. In Chapter 4, the results are presented, including those from the linear stability analysis, the early-time nonlinear behaviour and the transition to a late-time regime. The effect of varying the Rayleigh number and lake depth are also discussed here as well as a comparison to data obtained from dry lakes such as Badwater Basin and Owens Lake. Finally, in Chapter 5, the work is concluded with a discussion and suggestions for future work.

## Chapter 2

# Theory

To model dry salt lakes, the relevant physics must be incorporated into the modelling assumptions, governing equations and boundary conditions. The ground that makes up dry salt lakes is a porous soil, allowing the domain to be modelled as a porous medium and a constant porosity is assumed. Since the water table is close to the surface (Bryant, 2003; Reynolds et al., 2007), the porous soil beneath a dry lake can be considered as being fully saturated with water. As fluid is transported from the terrain surrounding dry lakes, it may collect salts, causing the fluid to have a nonzero salt concentration. This fluid acts as a source of both water and salt, located in a background reservoir, deep below the surface. Fluid flow within the porous medium is driven by evaporation applied at the surface, resulting in an upward throughflow beneath. When water evaporates at the surface, salt is left behind, forming a crust, which grows above the surface. This causes the fluid at the surface of the dry lake to be fully saturated with salt and is thus subject to the buoyancy force caused by the increased density. The competing effects of the evaporation-driven throughflow and the buoyancy of the fluid give rise to an incompressible fluid flow. The equations governing fluid flow and the coupling to a solute will be discussed here and the system that will be used to model dry lakes will be constructed, the results of which will be discussed further in Chapter 4.

## 2.1 Establishing the Governing Equations

The fluid flow  $\hat{\mathbf{v}}$  of a Newtonian fluid with density  $\rho$  and dynamic viscosity  $\mu$ , subject to a body force  $\hat{\mathbf{f}}$ , is governed by the Navier–Stokes equations:

$$\rho \left( \frac{\partial \hat{\mathbf{v}}}{\partial \hat{t}} + \hat{\mathbf{v}} \cdot \hat{\nabla} \hat{\mathbf{v}} \right) = -\hat{\nabla} \hat{p} + \mu \hat{\nabla}^2 \hat{\mathbf{v}} + \rho \hat{\mathbf{f}}, \quad (2.1)$$

where  $\hat{p}$  is the pressure of the fluid and  $\hat{t}$  is time. This is a statement of momentum conservation arising from Newton’s second law. If the flow has a typical velocity scale  $V$ , length scale  $L$  and time scale  $T = L/V$ , the nondimensional variables may be defined as:

$$\mathbf{v} = \frac{\hat{\mathbf{v}}}{V}, \quad \mathbf{x} = \frac{\hat{\mathbf{x}}}{L}, \quad t = \frac{\hat{t}}{T}. \quad (2.2)$$

The nondimensional Navier–Stokes equations can then be written as:

$$Re \left( \frac{\partial \mathbf{v}}{\partial t} + \mathbf{v} \cdot \nabla \mathbf{v} \right) = -\nabla p + \nabla^2 \mathbf{v} + \mathbf{f}, \quad (2.3)$$

where  $Re = \rho V L / \mu$  is the Reynolds number. A typical length for the pore scale is  $L = O(10^{-5} \text{ m})$  (Lasser et al., 2023) and for fluid flow driven by evaporation, a characteristic velocity is  $V = O(10^{-8} \text{ m s}^{-1})$ . This gives a Reynolds number  $Re = O(10^{-7})$ , allowing the left-hand side of (2.3) to be neglected, resulting in the Stokes equation:

$$-\hat{\nabla} \hat{p} + \mu \hat{\nabla}^2 \hat{\mathbf{v}} + \rho \hat{\mathbf{f}} = 0. \quad (2.4)$$

Porous media are materials that contain a network of structures that allow fluids to move through. These spaces are typically called pores and the material separating them is referred to as the solid matrix. The presence of an interface between the fluid and the solid matrix introduces extra shear stresses that must be considered in the momentum balance of the fluid. The viscous stress on the fluid is approximated to be a linear function of the velocity (Hall, 1956) and thus the Stokes equation becomes:

$$-\hat{\nabla} \hat{p} - \phi \frac{\mu}{\kappa} \hat{\mathbf{v}} + \rho \hat{\mathbf{f}} = 0, \quad (2.5)$$

where  $\phi$  is the porosity of the porous medium, the fraction of the total volume that the fluid can occupy,  $\kappa$  is permeability of the porous medium, a measure of a fluid’s ability to flow through the pores and  $\hat{\mathbf{v}}$  is now the interstitial fluid velocity, the velocity of the fluid

accounting for it navigating the solid matrix. For a body force consisting of gravity only, oriented in the positive  $\hat{z}$  direction,  $\mathbf{f} = g\mathbf{e}_z$ , (2.5) becomes:

$$\hat{\mathbf{u}} = -\frac{\kappa}{\mu} \left( \hat{\nabla} \hat{p} - \rho g \mathbf{e}_z \right), \quad (2.6)$$

where  $\hat{\mathbf{u}} = \phi \hat{\mathbf{v}}$  is the Darcy velocity, the volume of fluid per unit area travelling through the porous medium, not necessarily equal to the velocity at which the fluid is travelling. Conservation of mass must hold in a porous medium: the mass of fluid in a volume  $V$  changes due to the Darcy flux across the boundary:

$$\frac{d}{d\hat{t}} \int_V \phi \rho dV = - \int_{\partial V} \rho \hat{\mathbf{u}} \cdot \mathbf{n} dS, \quad (2.7)$$

where  $\partial V$  is the boundary of the volume  $V$ ,  $\mathbf{n}$  is the outward pointing normal on  $\partial V$ ,  $dV$  is a volume element in  $V$  and  $dS$  is a surface element on  $\partial V$ . This results in the continuity equation:

$$\frac{\partial}{\partial \hat{t}} (\phi \rho) + \hat{\nabla} \cdot (\rho \hat{\mathbf{u}}) = 0, \quad (2.8)$$

which simplifies to:

$$\phi \frac{\partial \rho}{\partial \hat{t}} + \hat{\mathbf{u}} \cdot \hat{\nabla} \rho + \rho \hat{\nabla} \cdot \hat{\mathbf{u}} = 0, \quad (2.9)$$

in the case that the porosity is independent of time. When the density is constant, the Darcy velocity satisfies the incompressibility condition:

$$\hat{\nabla} \cdot \hat{\mathbf{u}} = 0. \quad (2.10)$$

To describe how a solute moves through a porous medium, the salt mass fraction  $C$  is introduced. This is the mass of dissolved salt compared to the total mass of the fluid containing the salt, written as:

$$C = \frac{\text{mass of salt}}{\text{mass of fluid}}. \quad (2.11)$$

Since the density increases with the amount of dissolved salt in the fluid, the fluid density and salt content are related by:

$$\rho = \rho_0 [1 + \beta (C - C_0)], \quad (2.12)$$

where  $\beta$  is a constant and  $\rho_0 = \rho(C_0)$  is some reference density. The volume fraction of salt in a volume  $V$  of the porous medium with porosity  $\phi$  is then:

$$\int_V \phi C \, dV. \quad (2.13)$$

This may change due to a salt flux  $\hat{\mathbf{q}}$  across the boundary of  $V$ :

$$\frac{d}{dt} \int_V \phi C \, dV = - \int_{\partial V} \hat{\mathbf{q}} \cdot \mathbf{n} \, dS, \quad (2.14)$$

where  $\mathbf{n}$  is the outward pointing normal on the boundary  $\partial V$ ,  $dV$  is a volume element in  $V$  and  $dS$  is a surface element on  $\partial V$ . Applying the divergence theorem to the right-hand side of (2.14), the continuity equation for the mass fraction  $C$  is obtained:

$$\phi \frac{\partial C}{\partial t} + \hat{\nabla} \cdot \hat{\mathbf{q}} = 0. \quad (2.15)$$

The salt flux  $\hat{\mathbf{q}}$  consists of an advective component,  $C\hat{\mathbf{u}}$ , and a diffusive component,  $-\phi D \hat{\nabla} C$ :

$$\hat{\mathbf{q}} = C\hat{\mathbf{u}} - \phi D \hat{\nabla} C, \quad (2.16)$$

where  $D$  is the diffusivity of the dissolved salt and  $\hat{\mathbf{u}}$  is the Darcy velocity. Thus, upon simplification and using (2.10), the continuity equation (2.15) becomes:

$$\phi \frac{\partial C}{\partial t} + \hat{\mathbf{u}} \cdot \hat{\nabla} C = \phi D \hat{\nabla}^2 C. \quad (2.17)$$

## 2.2 Dry Lake Equations

Buoyancy-driven convection of an incompressible fluid with variable salt concentration in a three-dimensional porous medium is modelled by a Cartesian domain, constructed so that the  $x$ - and  $y$ -axes span the horizontal directions and the  $z$ -axis is vertical. The porous medium has depth  $H$  and is assumed to have constant permeability  $\kappa$  and porosity  $\phi$ . In reality, dry lakes can be as deep as  $H \approx 150$  m (Güler & Thyne, 2004) and for the world's largest dry lake, Salar de Uyuni, the horizontal area is approximately 9,000 km<sup>2</sup> (Borsa et al., 2008). Fluid flow is governed by Darcy's law and the incompressibility condition:

$$\hat{\mathbf{u}} = -\frac{\kappa}{\mu} \left( \hat{\nabla} \hat{p} - \rho g \mathbf{e}_z \right), \quad (2.18)$$

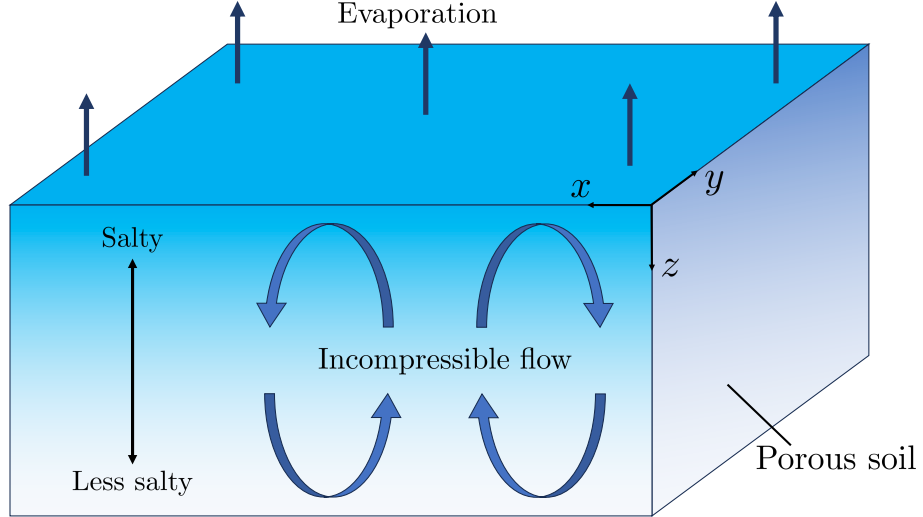


Figure 2.1: Sketch of a dry lake showing the porous soil located below the surface where evaporation drives an incompressible flow, in competition with buoyancy effects created by the salinity gradient. The crust (not shown here) is located above the porous soil and is responsible for the unstable salinity gradient.

$$\hat{\nabla} \cdot \hat{\mathbf{u}} = 0, \quad (2.19)$$

where hatted variables are dimensional,  $\hat{\mathbf{u}} = (\hat{u}, \hat{v}, \hat{w})$  is the Darcy velocity,  $\hat{p}$  the pressure and  $\hat{\nabla} = (\partial/\partial\hat{x}, \partial/\partial\hat{y}, \partial/\partial\hat{z})$ . Fluid is subject to a gravitational acceleration  $g\mathbf{e}_z$ , directed in the positive  $\hat{z}$  direction, given by the unit vector  $\mathbf{e}_z$ . The fluid viscosity  $\mu$  is constant and the density  $\rho$  depends on the amount of salt dissolved in the fluid. The system is sketched in Figure 2.1.

The relative salinity is defined by

$$S = \frac{\rho - \rho_0}{\rho_1 - \rho_0} = \frac{\rho - \rho_0}{\Delta\rho}, \quad (2.20)$$

where  $\rho_0$  is a reference density of fluid far from the surface of the dry lake,  $\Delta\rho = \rho_1 - \rho_0$  and  $\rho_1$  is the density of the fluid at the surface, which is in direct contact with the salt crust and assumed to be fully saturated with salt. The (relative) salinity can be related to the salt mass fraction using (2.12):

$$S = \frac{\rho_0\beta}{\Delta\rho} (C - C_0), \quad (2.21)$$

and since it is a linear function of the salt mass fraction  $C$ , it also obeys the advection-

diffusion equation:

$$\phi \frac{\partial S}{\partial t} + \hat{\mathbf{u}} \cdot \hat{\nabla} S = \phi D \hat{\nabla}^2 S, \quad (2.22)$$

where  $D$  is the diffusivity of salt, assumed to be constant. Equation (2.20) can be used to express the density in terms of the salinity:

$$\rho = \rho_0 + \Delta \rho S, \quad (2.23)$$

so that Darcy's law can be written as:

$$\hat{\mathbf{u}} = -\frac{\kappa}{\mu} \left[ \hat{\nabla} (\hat{p} - \rho_0 g \hat{z}) - \Delta \rho g S \mathbf{e}_z \right], \quad (2.24)$$

and the term  $\rho_0 g \hat{z}$  can then be absorbed into the pressure through the transformation:

$$\hat{p} \mapsto \hat{p} + \rho_0 g \hat{z}. \quad (2.25)$$

Thus, the dimensional system of equations governing the dynamics in dry salt lakes is:

$$\hat{\mathbf{u}} = -\frac{\kappa}{\mu} \left( \hat{\nabla} \hat{p} - \Delta \rho g S \mathbf{e}_z \right), \quad (2.26)$$

$$\hat{\nabla} \cdot \hat{\mathbf{u}} = 0, \quad (2.27)$$

$$\phi \frac{\partial S}{\partial t} + \hat{\mathbf{u}} \cdot \hat{\nabla} S = \phi D \hat{\nabla}^2 S. \quad (2.28)$$

Taking the divergence of (2.26) and using (2.27), a Poisson equation for the pressure is obtained:

$$\hat{\nabla}^2 \hat{p} = \Delta \rho g \frac{\partial S}{\partial \hat{z}}. \quad (2.29)$$

The thermal contributions to the density in these equations have been ignored as they are small compared to the solutal contributions (Lasser et al., 2021). In particular, if the diurnal temperature variation is assumed to be approximately 10°C, the density variation due to temperature is approximately  $\Delta \rho_T \approx 1 \text{ kg m}^{-3}$ . This, compared to the change in density due to salt, approximately  $\Delta \rho_S \approx 200 \text{ kg m}^{-3}$ , is a factor of 200 times smaller. Hence, the ratio of the magnitude of the thermally-driven flows to the solute-driven flows is:

$$\frac{\text{magnitude of thermally-driven flows}}{\text{magnitude of solute-driven flows}} = \frac{\Delta \rho_T}{\Delta \rho_S} \approx \frac{1}{200}, \quad (2.30)$$

and so double-diffusive effects can be ignored in the system.

The definition of relative salinity, (2.20), naturally imposes Dirichlet boundary conditions on the relative salinity,  $S$ . The evaporation rate driving the throughflow imposes a constant value for the vertical velocity at the surface. This is equivalent to imposing a constant value for the vertical pressure gradient as it is related to the vertical velocity via Darcy's law (2.26). Thus, equations (2.26)–(2.28) are accompanied with the boundary conditions:

$$S = 1, \quad \hat{w} = -E \quad \text{at } \hat{z} = 0, \quad (2.31)$$

$$S = 0 \quad \text{at } \hat{z} = H. \quad (2.32)$$

These boundary conditions are not mathematically sufficient: to determine  $\hat{p}$ , two conditions on  $\hat{w}$  (equivalently  $\partial\hat{p}/\partial\hat{z}$ ) must be provided. However, the model being used does not prescribe any other conditions on  $\hat{w}$  at  $\hat{z} = H$  and the system must be left underdetermined. Thus, an extra condition must be chosen to be imposed at the bottom of the domain. This is chosen to be:

$$\langle \hat{w} \rangle_{xy} = -E \quad \text{at } \hat{z} = H, \quad (2.33)$$

where  $\langle f \rangle_{xy}$  denotes the average of the function  $f(x, y, z, t)$  over the two horizontal directions. This is imposed in order to satisfy global mass conservation when the horizontal directions are assumed to be periodic (see Section 3.2). However, this boundary condition is not fully well-posed: it does not constrain the solutions enough to give a unique solution. This is discussed further in Section 3.2.

The system (2.26)–(2.28) along with the boundary conditions (2.31) and (2.32) admits a horizontally homogeneous steady state solution, given by:

$$S_b(\hat{z}) = \frac{\exp\left(-\frac{E\hat{z}}{\phi D}\right) - \exp\left(-\frac{EH}{\phi D}\right)}{1 - \exp\left(-\frac{EH}{\phi D}\right)}, \quad (2.34)$$

$$\hat{\mathbf{u}} = (0, 0, -E). \quad (2.35)$$

The length scale appearing in the exponential terms in  $S_b$ ,  $\phi D/E$ , is the length over which the upward advection (driven by evaporation) balances the downward diffusion of salt.

### 2.3 Scalings

Defining a characteristic velocity,  $V$ , and a characteristic length,  $L$ , and a characteristic time  $T = \phi L/V$ , the nondimensional variables may be defined as:

$$\mathbf{u} = \frac{\hat{\mathbf{u}}}{V}, \quad \mathbf{x} = \frac{\hat{\mathbf{x}}}{L}, \quad t = \frac{\hat{t}}{T}. \quad (2.36)$$

With these variables, Darcy's law becomes:

$$\begin{aligned} V\mathbf{u} &= -\frac{\kappa}{\mu} \left[ \hat{\nabla}(\hat{p} - \rho_0 g \hat{z}) - \Delta \rho S g \mathbf{e}_z \right] \\ \implies V\mathbf{u} &= -\frac{\kappa}{\mu L} \nabla(\hat{p} - \rho_0 g \hat{z}) + \mathcal{V}_B S \mathbf{e}_z, \end{aligned} \quad (2.37)$$

where  $\mathcal{V}_B = \kappa \Delta \rho g / \mu$  is the buoyancy velocity, the speed at which a fully saturated fluid parcel falls when surrounded by fresh fluid. The nondimensional modified pressure is defined as:

$$p = \frac{\kappa}{\mu L V} (\hat{p} - \rho_0 g \hat{z}). \quad (2.38)$$

This results in the nondimensional Darcy's law:

$$\mathbf{u} = -\nabla p + \frac{\mathcal{V}_B}{V} S \mathbf{e}_z. \quad (2.39)$$

The advection-diffusion equation for the relative salinity, (2.28), becomes:

$$\frac{\partial S}{\partial t} + \mathbf{u} \cdot \nabla S = \frac{\phi D}{LV} \nabla^2 S, \quad (2.40)$$

and the boundary conditions become:

$$S = 1 \quad w = -\frac{E}{V} \quad \text{at } z = 0, \quad (2.41)$$

$$S = 0 \quad \text{at } z = \frac{H}{L}. \quad (2.42)$$

The equations (2.39)–(2.42) contain four nondimensional groups:

$$\frac{\mathcal{V}_B}{V}, \quad \frac{\phi D}{LV}, \quad \frac{E}{V} \quad \text{and} \quad \frac{H}{L}, \quad (2.43)$$

The presence of the evaporation rate gives a natural characteristic velocity and so  $V = E$ , leaving the remaining three groups:

$$\frac{\mathcal{V}_B}{E}, \quad \frac{\phi D}{LE} \quad \text{and} \quad \frac{H}{L}. \quad (2.44)$$

The most appropriate length scale for the system is the length over which advection balances diffusion, rather than the lake depth,  $H$ , and so  $L = \phi D/E$ . This is the length scale appearing in the dimensional base state (2.34). This leaves two nondimensional groups,  $\mathcal{V}_B/E$  and  $H/L$ , which are denoted as the Rayleigh number,  $Ra$ , and the nondimensional lake depth,  $h$ :

$$Ra = \frac{\mathcal{V}_B}{E} = \frac{\kappa \Delta \rho g}{\mu E}, \quad (2.45)$$

$$h = \frac{H}{L} = \frac{HE}{\phi D}. \quad (2.46)$$

The Rayleigh number is the ratio of the buoyancy velocity to the evaporation rate, which controls the strength of the buoyancy forces compared to the background throughflow. The nondimensional lake depth is the location of the lower boundary of the domain. In their nondimensional form, the governing equations are:

$$\mathbf{u} = -\nabla p + Ra S \mathbf{e}_z, \quad (2.47)$$

$$\nabla \cdot \mathbf{u} = 0, \quad (2.48)$$

$$\frac{\partial S}{\partial t} + \mathbf{u} \cdot \nabla S = \nabla^2 S. \quad (2.49)$$

The Poisson equation for the pressure is:

$$\nabla^2 p = Ra \frac{\partial S}{\partial z}, \quad (2.50)$$

which will be used in the numerics, further described in Chapter 3. The equations are accompanied by the nondimensional boundary conditions:

$$S = 1, \quad w = -1, \quad \text{at } z = 0, \quad (2.51)$$

$$S = 0, \quad \langle w \rangle_{xy} = -1 \quad \text{at } z = h. \quad (2.52)$$

Imposing a Dirichlet condition on the vertical velocity corresponds to imposing a Neumann condition on the pressure since  $w$  and  $\partial p/\partial z$  are related through Darcy's law:

$$w = -\frac{\partial p}{\partial z} + Ra S. \quad (2.53)$$

This system has two parameters, the Rayleigh number,  $Ra$ , and the lake depth,  $h$ . Equations (2.5)–(2.50) along with boundary conditions (2.51) and (2.5) make up the dry lake system, which will be solved numerically. The numerical method will be described in Chapter 3 and the results will be discussed further in Chapter 4.

## 2.4 Parameter Values

Evaporation rates at dry salt lakes are typically of the order of  $1 \text{ mm day}^{-1}$  (Lasser et al., 2023), corresponding to a speed of approximately  $E \approx 10^{-8} \text{ m s}^{-1}$ . The diffusivity of salt is estimated to be approximately  $D \approx 10^{-9} \text{ m}^2 \text{ s}^{-1}$  which gives a characteristic length  $L = O(10 \text{ cm})$ . Data from Badwater Basin (Death Valley), Owens Lake (California) and Sua Pan (Botswana) (Lasser et al., 2023) shows values for the permeability in the range  $0.03 \times 10^{-11} \text{ m}^2 \leq \kappa \leq 27.42 \times 10^{-11} \text{ m}^2$  and observed Rayleigh numbers in the range  $48 \leq Ra \leq 310939$ . The corresponding pattern wavelengths were observed to be in the range  $0.41 \text{ m} \leq \lambda \leq 3.02 \text{ m}$ . This data is summarised in Table 2.1.

	$\min \kappa \text{ (m}^2\text{)}$	$\max \kappa \text{ (m}^2\text{)}$	$\min Ra$	$\max Ra$	$\min \lambda \text{ (m)}$	$\max \lambda \text{ (m)}$
Badwater Basin	$3.1 \times 10^{-11}$	$7.39 \times 10^{-11}$	5692	103415	0.55	1.42
Owens Lake	$0.03 \times 10^{-11}$	$27.42 \times 10^{-11}$	48	310939	0.87	3.02
Sua Pan	$0.13 \times 10^{-11}$	$0.2 \times 10^{-11}$	117	2456	0.41	0.95

Table 2.1: Minimum and maximum values for the data collected at Badwater Basin (Death Valley), Owens Lake (California) and Sua Pan (Botswana) (Lasser et al., 2023) for the permeability ( $\kappa$ ), Rayleigh number ( $Ra$ ) and the pattern wavelength ( $\lambda$ ).

## 2.5 Linear Stability

To investigate the fluid dynamics occurring in dry lakes, an initial condition must be chosen, from which an instability may grow. To observe an instability, heavier fluid must overlies lighter fluid, which is naturally enforced by the boundary conditions. The simplest case for an initial condition is zero salinity everywhere, except at the surface where the boundary condition  $S = 1$  is applied instantaneously at  $t = 0$ . This initial condition could describe a situation where there is a sudden change in the conditions at the surface of a dry lake, such as a flooding of brine (Lasser et al., 2021). For a horizontally homogeneous solution and early times, (2.49) can be approximated by pure diffusion:

$$\frac{\partial S}{\partial t} = \frac{\partial^2 S}{\partial z^2}, \quad (2.54)$$

since the magnitude of the diffusive term is much larger than that of the nonlinear term, due to the large vertical salinity gradient arising from the Dirac-like initial condition. Equation (2.54) can be solved via the use of the similarity variable  $\eta = zt^{-1/2}/2$  and when the bottom boundary is assumed to be at  $z = \infty$ , it has the solution (Slim et al., 2013):

$$S(z, t) = 1 - \operatorname{erf}\left(\frac{z}{2\sqrt{t}}\right), \quad (2.55)$$

where  $\operatorname{erf}(x)$  is the error function of  $x$ . On the infinite domain,  $[0, \infty)$ , and for moderate times,  $t \sim 1$ , there is a similar transient solution (Lasser et al., 2021; Wooding, Tyler, & White, 1997) when advection enters the dominant balance in (2.49):

$$S(z, t) = e^{-z/2} \left[ \frac{1}{2} e^{-z/2} \operatorname{erfc}\left(\frac{z-t}{2\sqrt{t}}\right) + \frac{1}{2} e^{z/2} \operatorname{erfc}\left(\frac{z+t}{2\sqrt{t}}\right) \right], \quad (2.56)$$

where  $\operatorname{erfc}(x) = 1 - \operatorname{erf}(x)$  is the complementary error function. A linear stability analysis of this transient state has been carried out by Lasser et al. (2021).

The horizontally homogeneous stationary solution to the system – is a more natural choice than (2.56) to investigate the development of any instability that may occur. This is referred to as the base state and in its nondimensional form, it is:

$$S_b(z) = \frac{e^{-z} - e^{-h}}{1 - e^{-h}}, \quad (2.57)$$

$$\mathbf{u}_b = (0, 0, -1), \quad (2.58)$$

$$p_b(z) = z + \frac{Ra}{1 - e^{-h}} \left(1 - e^{-z} - ze^{-h}\right), \quad (2.59)$$

where the constant of integration in the base state pressure has been chosen so that  $p_b(0) = 0$ . This state corresponds to the balance between the evaporation-driven throughflow and the downward diffusion of salt. To investigate the stability of the base state, (2.57)–(2.59), infinitesimally-small perturbations are added to the fields of the form:

$$S = S_b(z) + \epsilon S'(x, y, z, t), \quad (2.60)$$

$$\mathbf{u} = \mathbf{u}_b(z) + \epsilon \mathbf{u}'(x, y, z, t), \quad (2.61)$$

$$p = p_b(z) + \epsilon p'(x, y, z, t), \quad (2.62)$$

where  $\epsilon \ll 1$  and primed quantities are at most  $O(1)$ . Substituting (2.60) and (2.61) into (2.49), the equation for the salinity perturbation becomes:

$$\begin{aligned} & \epsilon \frac{\partial S'}{\partial t} + (\mathbf{u}_b + \epsilon \mathbf{u}') \cdot \nabla (S_b + \epsilon S') = \nabla^2 S_b + \epsilon \nabla^2 S' \\ \implies & \epsilon \frac{\partial S'}{\partial t} + \epsilon \mathbf{u}_b \cdot \nabla S' + \epsilon \mathbf{u}' \cdot \nabla S_b + \epsilon^2 \mathbf{u}' \cdot \nabla S' = \epsilon \nabla^2 S'. \end{aligned} \quad (2.63)$$

Neglecting the term which is of size  $O(\epsilon^2)$ , the first order balance is:

$$\frac{\partial S'}{\partial t} + \mathbf{u}_b \cdot \nabla S' + \mathbf{u}' \cdot \nabla S_b = \nabla^2 S'. \quad (2.64)$$

Similarly, substituting (2.60)–(2.62) into (2.5) and (2.50), the equation for the pressure and velocity perturbations are:

$$\nabla^2 p' = Ra \frac{\partial S'}{\partial z}, \quad (2.65)$$

$$\mathbf{u}' = -\nabla p' + Ra S' \mathbf{e}_z. \quad (2.66)$$

The base state variables can then be substituted into (2.64) as well as using (2.66) to eliminate the velocity in favour of the pressure to obtain:

$$\frac{\partial S'}{\partial t} - \frac{\partial S'}{\partial z} - \frac{e^{-z}}{1 - e^{-h}} \left( Ra S' - \frac{\partial p'}{\partial z} \right) = \nabla^2 S'. \quad (2.67)$$

It is assumed that  $S'$  and  $p'$  take the forms:

$$S'(x, y, z, t) = \hat{S}(z) \exp(i\mathbf{k} \cdot \mathbf{x}_H + \sigma t), \quad (2.68)$$

$$p'(x, y, z, t) = \hat{p}(z) \exp(i\mathbf{k} \cdot \mathbf{x}_H + \sigma t), \quad (2.69)$$

for functions  $\hat{S}$  and  $\hat{p}$ , wavevector  $\mathbf{k} = (k_x, k_y)$ , growth rate  $\sigma \in \mathbb{C}$ ,  $\mathbf{x}_H = (x, y)$  and  $i$  is the imaginary unit. Substituting (2.68) and (2.69) into (2.65) and (2.67), a system of coupled linear equations is obtained:

$$\frac{d^2 \hat{S}}{dz^2} - k^2 \hat{S} + \frac{d\hat{S}}{dz} + \frac{e^{-z}}{1 - e^{-h}} \left( Ra \hat{S} - \frac{d\hat{p}}{dz} \right) = \sigma \hat{S}, \quad (2.70)$$

$$\frac{d^2 \hat{p}}{dz^2} - k^2 \hat{p} = Ra \frac{d\hat{S}}{dz}, \quad (2.71)$$

where  $k = |\mathbf{k}| = \sqrt{k_x^2 + k_y^2}$  is the magnitude of the wavevector. Since the equations are isotropic, the dependence on  $\mathbf{k}$  only appears via the magnitude,  $k$ . It is thus sufficient to only consider two-dimensional perturbations with  $\mathbf{k} = (k, 0)$ . The boundary conditions for the salinity are  $S = 1$  at  $z = 0$  and  $S = 0$  at  $z = h$ . The salinity perturbation must then vanish at both boundaries and homogeneous Dirichlet boundary conditions are used:

$$\hat{S} = 0 \quad \text{at } z = 0, h. \quad (2.72)$$

The boundary condition on the vertical velocity at the surface is  $w = -1$  at  $z = 0$  but to complete the problem, a boundary condition on  $w$  must be specified at  $z = h$ . A uniform flow is also imposed at  $z = h$ , which is assumed to be far away from the unstable surface layer (Lasser et al., 2021). Dirichlet boundary conditions on the vertical velocity are equivalent to Neumann boundary conditions for the pressure, and so homogeneous Neumann boundary conditions for the pressure perturbation are used:

$$\frac{d\hat{p}}{dz} = 0 \quad \text{at } z = 0, h. \quad (2.73)$$

Equations (2.70) and (2.71) are solved numerically with boundary conditions (2.72) and (2.73), which is described in Chapter 3. The results from this will be described further in Chapter 4.

## 2.6 Other Convection Systems

In the absence of any external forcing, systems governing buoyancy-driven convection in porous media may be characterised as either two-sided or one-sided systems (Hewitt, 2020). In the former case, the lower and upper boundaries of the domain provide a positive and negative source of buoyancy respectively, but in the latter case, only one of the boundaries has a significant impact on the dynamics.

When both boundaries provide a source of buoyancy and the domain is of depth  $H$ , the boundary conditions impose a constant salinity at the upper boundary and a lower salinity at the bottom boundary:

$$S = 1 \quad \text{at } \hat{z} = 0, \quad (2.74)$$

$$S = 0 \quad \text{at } \hat{z} = H. \quad (2.75)$$

The dimensionless system of equations is obtained by using the domain depth  $H$  as the characteristic length, the buoyancy velocity for the characteristic velocity and the advective time scale. These equations are:

$$\mathbf{u} = -\nabla p + S\mathbf{e}_z, \quad (2.76)$$

$$\nabla \cdot \mathbf{u} = 0, \quad (2.77)$$

$$\frac{\partial S}{\partial t} + \mathbf{u} \cdot \nabla S = \frac{1}{Ra_{\text{TSC}}} \nabla^2 S, \quad (2.78)$$

complemented by no normal flow imposed at  $z = 0$  and  $z = 1$ . The Rayleigh number,  $Ra_{\text{TSC}} = HV_B(\phi D)^{-1}$ , is the only free parameter in this system which takes the form of an inverse diffusivity, controlling the relative magnitude of the diffusive term in the advection-diffusion equation. This system has been extensively studied (Nield & Bejan, 2017) and it has been shown that a horizontally homogeneous steady state exists, for which the salinity is a simple linear profile in depth (Lapwood, 1948). For Rayleigh numbers below a critical value, which can be shown to be  $Ra_{\text{TSC}} = 4\pi^2$  (Horton & Rogers, 1945), the conductive state is stable due to the large dissipative effects of diffusion and there is no fluid flow. For  $Ra_{\text{TSC}} > 4\pi^2$ , an instability may occur, consisting of convective rolls, enhancing the transport of solute via fluid flow.

When only one of the boundaries provides a source of buoyancy, and the upper boundary

is held at a constant concentration, the lower boundary is initially of little importance. It thus makes sense to use the length over which advection balances diffusion as the characteristic length,  $L = \phi D / \mathcal{V}_B$ . The dimensionless equations are then found to be:

$$\mathbf{u} = -\nabla p + S \mathbf{e}_z, \quad (2.79)$$

$$\nabla \cdot \mathbf{u} = 0, \quad (2.80)$$

$$\frac{\partial S}{\partial t} + \mathbf{u} \cdot \nabla S = \nabla^2 S, \quad (2.81)$$

complemented by the boundary conditions (Hewitt, 2020):

$$S = 1 \quad \text{at } z = 0, \quad (2.82)$$

$$\frac{\partial S}{\partial z} = 0 \quad \text{at } z = \frac{H}{L}. \quad (2.83)$$

In this case, there is no free parameter in the equations and instead, the Rayleigh number appears through the nondimensional location of the lower boundary:

$$z = Ra_{\text{OSC}} = \frac{H}{L} = \frac{H \mathcal{V}_B}{\phi D}. \quad (2.84)$$

This system is thus more applicable to physical situations such as CO<sub>2</sub> sequestration, as it more effectively models the convective dissolution of a dense solute from the upper boundary. Although this is the same Rayleigh number as in two-sided convection ( $Ra_{\text{OSC}} = Ra_{\text{TSC}}$ ), it now controls the relative distance that the bottom boundary is away from the surface,  $H$ , compared to the natural length scale,  $\phi D / \mathcal{V}_B$ . Thus, for one-sided convection, the flow regimes occur as the system evolves in time (Slim, 2014). This makes it clear that the dynamics will be mostly independent of the Rayleigh number until downwelling plumes feel the presence of the lower boundary. One-sided systems progress through various regimes, evolving toward a ‘shutdown’ regime where downwelling plumes reach the bottom of the domain and the system begins to transition toward a statistically steady end-state.

When a throughflow is present, driven by evaporation applied at the surface, another choice for the characteristic velocity is available through the magnitude of this flow, leading to a second free parameter. The throughflow also leads to a nonhomogeneous boundary

condition for the vertical velocity at the surface, as fluid leaves the domain. To relate the system used to model dry lakes with those described above, a transformation may be used to obtain a system with homogeneous boundary conditions on the vertical velocity. The original dry lake system in nondimensional variables is:

$$\mathbf{u} = -\nabla p + \frac{\mathcal{V}_B}{V} S \mathbf{e}_z, \quad (2.85)$$

$$\nabla \cdot \mathbf{u} = 0, \quad (2.86)$$

$$\frac{\partial S}{\partial t} + \mathbf{u} \cdot \nabla S = \frac{\phi D}{LV} \nabla^2 S, \quad (2.87)$$

where  $L$  is the characteristic length and  $V$  is the characteristic velocity. The boundary conditions are:

$$S = 1, \quad w = -\frac{E}{V} \quad \text{at } z = 0, \quad (2.88)$$

$$S = 0 \quad \text{at } z = \frac{H}{L}. \quad (2.89)$$

Instead of using the scalings described in Section 2.3, the same scalings as two-sided convection can be chosen: the characteristic velocity is taken to be the buoyancy velocity and the characteristic length is taken to be the domain depth:

$$V = \frac{\phi D}{\mathcal{V}_B}, \quad L = H, \quad T = \frac{\phi D}{V}. \quad (2.90)$$

This results in the system:

$$\mathbf{u} = -\nabla p + S \mathbf{e}_z, \quad (2.91)$$

$$\nabla \cdot \mathbf{u} = 0, \quad (2.92)$$

$$\frac{\partial S}{\partial t} + \mathbf{u} \cdot \nabla S = \frac{1}{Ra_{TSC}} \nabla^2 S, \quad (2.93)$$

with boundary conditions:

$$S = 1, \quad w = -\frac{1}{Ra} \quad \text{at } z = 0, \quad (2.94)$$

$$S = 0 \quad \text{at } z = 1. \quad (2.95)$$

Two parameters appear in this system. Firstly, the Rayleigh number of dry lakes,

$$Ra = \frac{\mathcal{V}_B}{E}, \quad (2.96)$$

appears in the vertical velocity boundary condition. Secondly, the two-sided Rayleigh number appears as an inverse diffusivity:

$$Ra_{\text{TSC}} = \frac{H\mathcal{V}_B}{\phi D}. \quad (2.97)$$

These two Rayleigh numbers are related through another parameter, defined to be the Péclet number:

$$Pe = \frac{HE}{\phi D}, \quad (2.98)$$

which controls the strength of the advective transport rate to the diffusive transport rate. This allows the Rayleigh number of two-sided convection to be written as:

$$Ra_{\text{TSC}} = \frac{H\mathcal{V}_B}{\phi D} = \frac{\mathcal{V}_B}{E} \frac{HE}{\phi D} = Ra Pe. \quad (2.99)$$

Finally, the transformation:

$$\mathbf{U} = \mathbf{u} - \left(0, 0, -\frac{1}{Ra}\right), \quad (2.100)$$

$$P = p - \frac{1}{Ra} z, \quad (2.101)$$

can be used to transform the equations so that the vertical velocity boundary condition at the surface is homogeneous:

$$\mathbf{U} = -\nabla P + S\mathbf{e}_z, \quad (2.102)$$

$$\nabla \cdot \mathbf{U} = 0, \quad (2.103)$$

$$\frac{\partial S}{\partial t} + \mathbf{U} \cdot \nabla S = \frac{1}{Ra Pe} \left( \nabla^2 S + Pe \frac{\partial S}{\partial z} \right), \quad (2.104)$$

$$S = 1, \quad W = 0 \quad \text{at } z = 0, \quad (2.105)$$

$$S = 0 \quad \text{at } z = 1. \quad (2.106)$$

This transformed system may now be compared to the two-sided case above but with an extra source term, proportional to the vertical salinity gradient. This system is discussed

further in Section 5.3.

## Chapter 3

# Numerics

In Chapter 2, the equations governing the nonlinear dynamics and those of the linear instability of the base state were derived. If the depth of the lake is assumed to be infinite, an analytical linear stability analysis can be produced via the use of hypergeometric functions (Lasser et al., 2021). When the depth of the lake is finite, the linear stability analysis must be carried out numerically, and a Chebyshev collocation method is used. This chapter will develop the numerical schemes that will be used to solve the equations discussed in the previous chapter, starting first with the linear stability analysis and then moving on to the full nonlinear dynamics. The numerical code for the latter was developed by C. Beaume (for further details, see Beaume (2024)). In each case, the numerical scheme will be validated.

### 3.1 Linear Stability

To analyse the linear stability of the base state, an eigenvalue problem must be solved for the growth rates and eigenfunctions described in Section 2.5. Given a Rayleigh number  $Ra$  and wavenumber  $k$ , the coupled linear equations that are to be solved for the eigenfunctions  $\hat{S}(z)$  and  $\hat{p}(z)$  are:

$$\left(\frac{d^2}{dz^2} - k^2 + \frac{d}{dz}\right)\hat{S} + \frac{e^{-z}}{1 - e^{-h}}\left(Ra\hat{S} - \frac{d\hat{p}}{dz}\right) = \sigma\hat{S}, \quad (3.1)$$

$$\left(\frac{d^2}{dz^2} - k^2\right)\hat{p} = Ra\frac{d\hat{S}}{dz}. \quad (3.2)$$

The boundary conditions to be used are:

$$\hat{S} = 0 \quad \text{at } z = 0, h, \quad (3.3)$$

$$\frac{d\hat{p}}{dz} = 0 \quad \text{at } z = 0, h. \quad (3.4)$$

The domain  $[0, h]$  is discretised using  $N + 1$  Chebyshev collocation points:

$$z_k = \frac{h}{2} \left( 1 - \cos \frac{k\pi}{N} \right), \quad k = 0, \dots, N, \quad (3.5)$$

and a differentiation matrix  $D$  with entries (Trefethen, 2000):

$$D_{00} = \frac{2}{h} \left( \frac{2N^2 + 1}{6} \right), \quad D_{NN} = -\frac{2}{h} \left( \frac{2N^2 + 1}{6} \right), \quad (3.6)$$

$$D_{jj} = \frac{2}{h} \left( \frac{-z_j}{2(1 - z_j^2)} \right), \quad j = 1, \dots, N - 1, \quad (3.7)$$

$$D_{ij} = \frac{2}{h} \left( \frac{c_i (-1)^{i+j}}{c_j (z_i - z_j)} \right), \quad i \neq j, \quad i, j = 0, \dots, N, \quad (3.8)$$

where

$$c_i = \begin{cases} 2 & i = 0 \text{ or } N \\ 1 & \text{otherwise} \end{cases}. \quad (3.9)$$

To solve (3.1) and (3.2) as a coupled system,  $\hat{p}$  is written in terms of  $\hat{S}$ :

$$\hat{p} = Ra \mathcal{M}^{-1} D \hat{S}, \quad (3.10)$$

where

$$\mathcal{M} = D^2 - k^2 I, \quad (3.11)$$

and  $I$  is the identity matrix. To invert the matrix  $\mathcal{M}$ , the pressure boundary conditions are used: the first and last rows of  $M$  are replaced with those of  $D$ . The right-hand side of (3.10) must also be modified to impose  $d\hat{p}/dz = 0$ , and so the matrix  $D$  has its first and last rows replaced with zeros. To denote these modifications, (3.10) is written as

$$\hat{p} = Ra \tilde{\mathcal{M}}^{-1} \tilde{D} \hat{S}, \quad (3.12)$$

and substituted into (3.1):

$$\left[ D^2 - k^2 I + D + \frac{Ra}{1 - e^{-h}} \mathcal{C} \left( I - D\tilde{\mathcal{M}}^{-1}\tilde{D} \right) \right] \hat{S} = \sigma \hat{S} \quad (3.13)$$

$$\implies \mathcal{L}\hat{S} = \sigma \hat{S}, \quad (3.14)$$

where  $\mathcal{C}$  is a diagonal matrix with entries  $\mathcal{C}_{ii} = \exp(-z_i)$ . This equation must account for the boundary conditions for the salinity. Since homogeneous Dirichlet boundary conditions are used, the matrix  $\mathcal{L}$  is stripped of its first and last rows and columns and the resulting reduced matrix is denoted by  $\tilde{\mathcal{L}}$ . The right-hand side has its first and last entries removed. The eigenvalues  $\sigma$  and eigenfunctions  $v_k$  of  $\tilde{\mathcal{L}}$  can then be computed, where

$$v_k = \hat{S}(z_k). \quad (3.15)$$

These eigenvalues are ordered based on the real part of their growth rate,  $\lambda = \text{Re}(\sigma)$ . Further analysis of this eigenvalue problem is left for Chapter 4.

### 3.1.1 Linear Stability Validation

To solve the eigenvalue problem numerically, the minimum number of collocation points must be determined to ensure the accuracy of the results is sufficient. The number of points to use must also depend on the lake depth: for larger values of  $h$ , more points must be used to maintain the desired accuracy. To determine this for  $h = 10$ , the eigenvalue problem is solved for  $N = 20, \dots, 150$  and the growth rates

$$\lambda_i = \text{Re}(\sigma_i), \quad i = 0, \dots, N \quad (3.16)$$

are computed. In particular, the largest growth rate,

$$\lambda^{(N)} = \max \lambda_i \quad (3.17)$$

is saved for each  $N$ . The superscript ( $N$ ) denotes the number of collocation points used in the computation of the associated growth rate. The relative error against the growth rate for the highest number of points,  $|\lambda^{(N)} - \lambda^{(150)}|/\lambda^{(150)}$ , is plotted in Figure 3.1(a). The relative error decreases exponentially with the number of collocation points until reaching a limit from where machine precision prevents any further decrease. This demonstrates

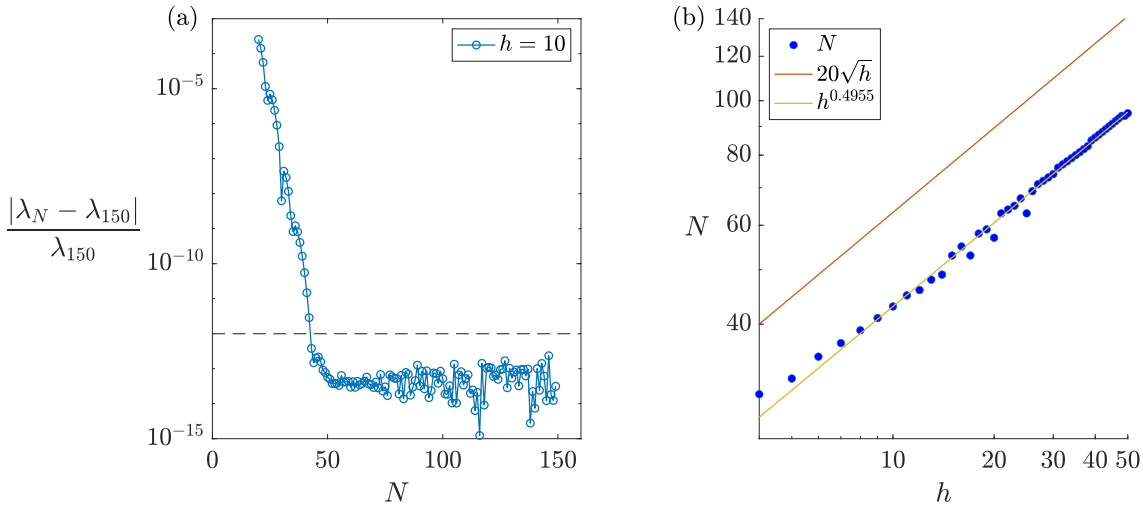


Figure 3.1: (a): Relative error of the growth rate,  $\lambda$  at  $Ra = 100$ , for  $k = 3$  and  $h = 10$ . The dashed line represents a relative error of  $10^{-12}$ . (b): Number of collocation points needed as a function of  $h$  to obtain a relative error of less than  $10^{-12}$ . A power law may be fitted to this data which is approximately  $N \sim h^{0.4955}$ . The rule used in practice is  $N = \lceil 20\sqrt{h} \rceil$ .

spectral convergence, hence validating the scheme used. Assuming that the growth rate computed with 150 collocation points is the exact value, the number of collocation points to be used is selected by determining the smallest  $N$  such that the relative error is less than  $10^{-12}$ :

$$\frac{|\lambda^{(N)} - \lambda^{(150)}|}{\lambda^{(150)}} \leq 10^{-12}. \quad (3.18)$$

This procedure is repeated for increasing values of  $h$ , thereby determining the number of collocation points needed as a function of  $h$ , which can be seen in Figure 3.1(b). A power law may be fitted,  $N \sim h^b$  for some constant  $b$ , resulting in an approximately square root law, where the multiplicative constant is increased to maintain a conservative rule for each  $h$ :

$$N = \lceil 20\sqrt{h} \rceil, \quad (3.19)$$

where  $\lceil x \rceil$  denotes the ceiling function, which rounds a real number  $x$  up to the nearest integer.

## 3.2 Fully Nonlinear Dynamics

The complete set of equations to model the fluid dynamics of dry lakes is:

$$\mathbf{u} = -\nabla p + Ra \mathbf{S} \mathbf{e}_z, \quad (3.20)$$

$$\nabla \cdot \mathbf{u} = 0, \quad (3.21)$$

$$\frac{\partial S}{\partial t} + \mathbf{u} \cdot \nabla S = \nabla^2 S, \quad (3.22)$$

where  $S$  is the salinity,  $\mathbf{u}$  is the velocity field,  $p$  is the pressure and  $t$  is time. The Rayleigh number,  $Ra$ , is a free parameter controlling the relative strength of the buoyancy forces to the evaporation rate. Since the velocity is given in terms of the other state variables explicitly, this is only a system for the salinity and the pressure. Equations (3.20) and (3.21) are written as

$$\nabla^2 p = Ra \frac{\partial S}{\partial z}, \quad (3.23)$$

which is a Poisson equation for the pressure and equations (3.20), (3.22) and (3.23) make up the system of equations that are solved numerically. The boundary conditions in the vertical direction are:

$$S = 1, \quad w = -1 \quad \text{at } z = 0, \quad (3.24)$$

$$S = 0 \quad \text{at } z = h. \quad (3.25)$$

Assuming the salinity is specified at the surface and at the bottom of the domain, Dirichlet boundary conditions on the vertical velocity correspond to Neumann boundary conditions for the pressure via Darcy's law. The horizontal extent of dry lakes is much larger than their depth and so when they are simulated, the horizontal domain sizes must be restricted to a smaller region, denoted by  $\Gamma_x$  and  $\Gamma_y$ . Periodic boundary conditions are then used for the two horizontal directions to model the large horizontal domain sizes. The dry lake system provides boundary conditions for the velocity at the surface only and so an extra condition is required, which is chosen so that global mass conservation is satisfied. Since the periodic boundary conditions in the horizontal direction imply that fluid leaving the domain via one horizontal boundary enters through the other, the boundary condition at the bottom of the domain is chosen so that the horizontally averaged vertical velocity at the bottom of the domain balances the throughflow at the surface. This results in the global mass conservation condition:

$$\langle w \rangle_{xy} = -1 \quad \text{at } z = h, \quad (3.26)$$

where  $\langle f \rangle_{xy}$  denotes the average of the function  $f(x, y, z, t)$  over the two horizontal directions. The vertical component of Darcy's law (3.20) is used to write the boundary

conditions for the pressure by using the known values of the salinity and the vertical velocity:

$$\frac{\partial p}{\partial z} = Ra S - w. \quad (3.27)$$

Thus at the surface, where  $S = 1$  and  $w = -1$ ,

$$\frac{\partial p}{\partial z} = Ra + 1 \quad \text{at } z = 0, \quad (3.28)$$

and at the bottom, where  $S = 0$  and  $\langle w \rangle_{xy} = -1$ ,

$$\left\langle \frac{\partial p}{\partial z} \right\rangle_{xy} = 1 \quad \text{at } z = h. \quad (3.29)$$

However, when the solution is expanded in a Fourier–Galerkin expansion (see Section 3.4), (3.29) only constrains the constant mode as the nonzero wavenumber modes average to zero. As a result of this, the boundary condition (3.29) is not fully well-posed.

To summarise, the equations and boundary conditions to be solved numerically are:

$$\frac{\partial S}{\partial t} + \mathbf{u} \cdot \nabla S = \nabla^2 S, \quad (3.30)$$

$$\nabla^2 p = Ra \frac{\partial S}{\partial z}, \quad (3.31)$$

$$\mathbf{u} = -\nabla p + Ra S \mathbf{e}_z, \quad (3.32)$$

$$S = 1, \quad \frac{\partial p}{\partial z} = Ra + 1 \quad \text{at } z = 0, \quad (3.33)$$

$$S = 0, \quad \left\langle \frac{\partial p}{\partial z} \right\rangle_{xy} = 1 \quad \text{at } z = h. \quad (3.34)$$

The process of solving these equations sequentially is described in Section 3.3.3. Simulations are initialised with a salinity profile of the form:

$$S = S_b(z) + B\theta(x, y, z)\mathcal{E}(z), \quad (3.35)$$

where  $B \ll 1$  (typically  $B = 10^{-4}$ ),  $\theta(x, y, z)$  is a random number drawn from a uniform distribution on  $[-1, 1]$  at each mesh point  $(x, y, z)$  and  $\mathcal{E}(z)$  is a function that ensures the perturbation to the base state decays faster than the base state itself. The exact form of the function  $\mathcal{E}(z)$  will be discussed further in Chapter 4. Using the perturbation

given by (3.35), there is a possibility that the salinity will take values greater than 1 at the surface and less than 0 at the bottom. Nothing is done to prevent this, as the perturbation amplitude is small and values greater than 1 or smaller than 0 will be corrected by the boundary conditions at the following time step.

### 3.3 Temporal discretisation

Time is discretised with a constant time step  $\Delta t$  and an index  $n \geq 0$ ,

$$t_n = n\Delta t. \quad (3.36)$$

The value of a function  $f$  at time  $t_n$  is denoted by

$$f(t_n) = f(n\Delta t) = f^n. \quad (3.37)$$

The aim is to compute the solution at the next time step, knowing the solution at the current and previous time steps. The advection-diffusion equation is written as:

$$\left(\frac{\partial S}{\partial t}\right)^{n+1} + (\mathbf{u} \cdot \nabla S)^{n+1} = (\nabla^2 S)^{n+1}, \quad (3.38)$$

and each term will need to be approximated as a linear sum of the fields at previous time steps, except for the Laplacian, which is kept implicit to aid with the stability of the numerical scheme. The extrapolation of the time derivative and the nonlinear term will be of the same order.

#### 3.3.1 Time Derivative

To approximate the time derivative in the advection-diffusion equation, the salinity at time step  $n - m$  is expressed in a Taylor expansion:

$$S^{n-m} = S^n + (-m)\Delta t \frac{\partial S^n}{\partial t} + \frac{(-m)^2 \Delta t^2}{2!} \frac{\partial^2 S^n}{\partial t^2} + \frac{(-m)^3 \Delta t^3}{3!} \frac{\partial^3 S^n}{\partial t^3} + O(\Delta t^4) \quad (3.39)$$

for  $m = 0, 1, \dots$ . The trivial expansion  $S^n = S^n$  is included here since it will become part of the linear operator when the salinity equation is solved. For a scheme of order  $s$ , the equations for  $i = 0, \dots, s$  are combined to solve for the first time derivative. This results

$s$	$\Delta t \alpha_0$	$\Delta t \alpha_1$	$\Delta t \alpha_2$	$\Delta t \alpha_3$
1	1	-1	0	0
2	3/2	-2	1/2	0
3	11/6	-3	3/2	-1/3

Table 3.1: Time derivative scheme coefficients multiplied by the time step for a scheme order  $s$ .

in the expansion:

$$\frac{\partial S^{n+1}}{\partial t} = \sum_{m=0}^s \alpha_m S^{n-m+1} + O(\Delta t^s), \quad (3.40)$$

where the constants  $\alpha_m$  can be determined by solving the system:

$$\sum_{m=0}^s \alpha_m = 0, \quad (3.41)$$

$$\sum_{m=0}^s m \alpha_m = -\frac{1}{\Delta t}, \quad (3.42)$$

$$\sum_{m=0}^s \frac{m^j}{j!} \alpha_m = 0, \quad j = 2, \dots, s. \quad (3.43)$$

The coefficients  $\alpha_m$  can be seen in Table 3.1 for  $s = 1, 2$  and  $3$ . For example, at order  $s = 1$ , the system to solve for is:

$$\alpha_0 + \alpha_1 = 0, \quad (3.44)$$

$$\alpha_1 = -\frac{1}{\Delta t}, \quad (3.45)$$

which has solution  $\alpha_0 = 1/\Delta t$ ,  $\alpha_1 = -1/\Delta t$ . Hence

$$\frac{\partial S^{n+1}}{\partial t} = \frac{S^{n+1} - S^n}{\Delta t} + O(\Delta t) \quad (3.46)$$

gives the scheme at first-order.

### 3.3.2 Nonlinear Term

Using (3.39), instead with the nonlinear term  $N = \mathbf{u} \cdot \nabla S$ , the equations for  $m = 1, \dots, s$  (this time excluding  $m = 0$  to keep the nonlinear term explicit) are combined:

$$N^{m+1} = \sum_{m=1}^s \beta_m N^{n-m+1} + O(\Delta t^s), \quad (3.47)$$

$s$	$\beta_1$	$\beta_2$	$\beta_3$
1	1	0	0
2	2	-1	0
3	3	-3	1

 Table 3.2: Nonlinear term scheme coefficients for the scheme order  $s$ .

where the coefficients  $\beta_m$  satisfy:

$$\sum_{m=1}^s \beta_m = 1, \quad (3.48)$$

$$\sum_{m=1}^s \frac{m^j}{j!} \beta_m = 0, \quad j = 1, \dots, s. \quad (3.49)$$

The coefficients  $\beta_m$  can be seen in Table 3.2 for  $s = 1, 2$  and  $3$ . Again, with  $s = 1$ , the expansion results in

$$(\mathbf{u} \cdot \nabla S)^{n+1} = (\mathbf{u} \cdot \nabla S)^n + O(\Delta t), \quad (3.50)$$

giving the first-order scheme.

### 3.3.3 Method of Solution

Utilising the approximations (3.40) and (3.47), the discretised system is then written as:

$$(\alpha_0 - \Delta t \nabla^2) S^{n+1} = - \sum_{m=1}^s \alpha_m S^{n-m+1} - \Delta t \sum_{m=1}^s \beta_m (\mathbf{u} \cdot \nabla S)^{n-m+1} \quad (3.51)$$

$$\nabla^2 p^{n+1} = Ra \frac{\partial S^{n+1}}{\partial z}, \quad (3.52)$$

$$\mathbf{u}^{n+1} = -\nabla p^{n+1} + Ra S^{n+1} \mathbf{e}_z, \quad (3.53)$$

and is solved in this order at each time step. Given the fields  $S^n, \dots, S^{n-s+1}, \mathbf{u}^n, \dots, \mathbf{u}^{n-s+1}$ :

1. The salinity  $S^{n+1}$  is computed by inverting the operator  $\alpha_0 - \Delta t \nabla^2$  in (3.51) with Dirichlet boundary conditions  $S^{n+1}(z=0) = 1$  and  $S^{n+1}(z=h) = 0$ .
2. The value for the pressure boundary condition is computed via  $b(x, y) = -w^n + c$  for a constant  $c$  such that  $\langle b \rangle_{xy} = 1$ . In theory,  $w^n$  should already satisfy  $\langle w^n \rangle_{xy} = -1$  so this step is redundant, but done anyway. This is a first-order extrapolation of the vertical velocity and is done rather than a second-order extrapolation to avoid a scheme instability.
3. The pressure  $p^{n+1}$  is computed by solving the Poisson equation (3.52) (inverting  $\nabla^2$ )

with Neumann boundary conditions  $\partial p/\partial z (z = 0) = Ra + 1$  and  $\partial p/\partial z (z = h) = b(x, y)$ . This boundary condition only constrains the zero wavenumber mode and the nonzero wavenumbers thus take the value they had at the previous time step.

4. The velocity  $\mathbf{u}^{n+1}$  is evaluated using  $S^{n+1}$  and  $p^{n+1}$  via (3.53).

### 3.4 Horizontal Discretisation

In the dry lake system described in Chapter 2, no horizontal boundaries are considered. For numerical means, the horizontal domain is restricted to be of size  $\Gamma_x \times \Gamma_y$  and periodic boundary conditions are used, allowing the solution to be discretised using a Fourier–Galerkin expansion. When the salinity and pressure are solved for, Fourier transforms are used to eliminate the two horizontal directions, leaving a one-dimensional problem for the vertical direction for each pair of horizontal wavenumbers. This is done by the use of the Fast Fourier Transform (FFT) (Frigo & Johnson, 2005), an algorithm that computes the Discrete Fourier Transform (DFT) in  $O(N \log N)$  operations (with  $N$  being the number of mesh points) as opposed to  $O(N^2)$  operations that would be used by simply applying the definition of the DFT.

#### 3.4.1 Fourier Discretisation in One Dimension

The domain  $[0, \Gamma]$  is discretised using  $M$  equidistributed points:

$$x_i = \frac{\Gamma i}{M}, \quad i = 0, \dots, M - 1, \quad (3.54)$$

where the last point has been omitted since  $f(\Gamma) = f(0)$  for a  $\Gamma$ -periodic function  $f(x)$ . An example mesh can be seen in Figure 3.2 for  $\Gamma = 4$  and  $M = 8$ . The Fourier transform  $\hat{f}(k)$  of a function  $f(x)$ ,  $x \in \mathbb{R}$ , is defined by:

$$\hat{f}(k) = \int_{-\infty}^{\infty} f(x) \exp(-ikx) dx, \quad (3.55)$$

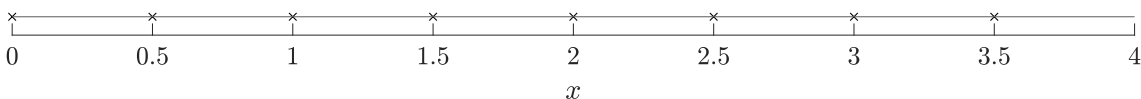


Figure 3.2: Fourier mesh for  $\Gamma = 4$  and  $M = 8$ . The mesh point at  $x = 4$  (for  $M = 8$ ) is omitted since any  $\Gamma$ -periodic function with period  $M = 8$  has  $f(x_8) = f(x_0)$ .

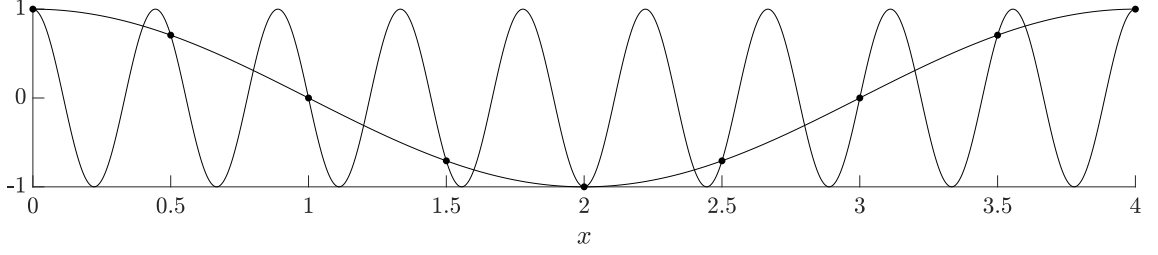


Figure 3.3: Functions  $\cos(2\pi x/\Gamma)$  and  $\cos(18\pi x/\Gamma)$  along with the values these functions take on the grid given by  $\Gamma = 4$ ,  $M = 8$ . The dots, representing the locations and values of the two functions coincide, indicating that if the continuous representation of the two functions were omitted, they would be indistinguishable from each other.

where  $\iota$  is the imaginary unit. The quantity  $\hat{f}(k)$  is the complex amplitude of the function  $f$  projected onto the wavenumber  $k$ . The inverse Fourier transform is given by:

$$f(x) = \frac{1}{2\pi} \int_{-\infty}^{\infty} \hat{f}(k) \exp(\iota kx) dk. \quad (3.56)$$

When the value of  $x$  is discretised, the wavenumber  $k$  will be restricted to lie in an interval of length  $2\pi M/\Gamma$ . This is due to *aliasing* and can be demonstrated by considering two complex exponentials:

$$f_1(x) = \exp(\iota k_1 x), \quad f_2(x) = \exp(\iota k_2 x). \quad (3.57)$$

These are unequal if  $k_1 \neq k_2$  but when evaluated on the discretised mesh:

$$f_1(x_i) = \exp(\iota k_1 x_i), \quad f_2(x_i) = \exp(\iota k_2 x_i), \quad (3.58)$$

they are equal whenever  $k_1$  and  $k_2$  differ by an integer multiple of  $2\pi M/\Gamma$ :

$$\begin{aligned} f_2(x_i) &= \exp \left[ \iota \left( k_1 + n \frac{2\pi M}{\Gamma} \right) x_i \right] \\ &= \exp(\iota k_1 x_i) \exp(2\pi n \iota) \\ &= \exp(\iota k_1 x_i), \end{aligned} \quad (3.59)$$

where  $n \in \mathbb{Z}$ . It is thus sufficient to only consider wavenumbers in an interval  $[-\pi M/\Gamma, \pi M/\Gamma]$ . Introducing the integer wavenumber  $m$  so that  $k = 2\pi m/\Gamma$ , it is equivalent to only consider modes in an interval  $[-M/2, M/2]$ . Figure 3.3 demonstrates the aliasing of the functions  $\cos(k_1 x)$  and  $\cos(k_2 x)$  ( $k_1 = 2\pi/\Gamma$ ,  $k_2 = 18\pi/\Gamma$ ) on the mesh given by  $\Gamma = 4$ ,  $M = 8$ .

The Fourier transform restricted to the mesh is given by the DFT:

$$\hat{f}_m = \frac{1}{M} \sum_{i=0}^{M-1} f(x_i) \exp\left(-i \frac{2\pi}{M} mi\right), \quad m = -M/2 + 1, \dots, M/2, \quad (3.60)$$

for which its inverse is given by:

$$f_i = f(x_i) = \sum_{m=-M/2+1}^{M/2} \hat{f}_m \exp\left(i \frac{2\pi}{M} mi\right), \quad i = 0, \dots, M-1. \quad (3.61)$$

Dividing by the normalisation factor of  $M$ , here written in (3.60), can be carried out in either the forward or the backward transform. Aliasing then implies that a mode  $n$  projects onto a mode  $m$  when  $n \equiv m \pmod{M}$ . This is the reason for the limited summation range of  $m$  in (3.61): all the information is contained in the band of integer wavenumbers  $[-M/2 + 1, M/2]$ .

A phenomenon called *frequency folding* is also present, where the energy from one mode is redistributed to another mode. For an integer  $l < M/2$ , the mode  $m = M/2 + l$  ‘folds’ onto the mode  $m = M/2 - l$ :

$$\exp\left[i \left(\frac{M}{2} + l\right) i \frac{2\pi}{M}\right] = (-1)^i \exp\left(-li \frac{2\pi}{M}\right)^* \quad (3.62)$$

$$= \exp\left[i \left(\frac{M}{2} - l\right) i \frac{2\pi}{M}\right]^*, \quad (3.63)$$

where the Fourier coefficient is complex conjugated. The mode  $M/2$  is called the Nyquist frequency and modes above this value are incorrectly represented. The solution to this is described in Section 3.4.2. Expanding (3.61) into two sums and writing the first and last terms explicitly:

$$\begin{aligned} f_i = \hat{f}_0 + & \sum_{m=-M/2+1}^{-1} \hat{f}_m \exp\left(i \frac{2\pi}{M} mi\right) \\ & + \sum_{m=1}^{M/2-1} \hat{f}_m \exp\left(i \frac{2\pi}{M} mi\right) \\ & + \hat{f}_{M/2} (-1)^i \end{aligned} \quad (3.64)$$

$$\begin{aligned} \Rightarrow f(x_i) = \hat{f}_0 + \sum_{m=1}^{M/2-1} & \left[ \hat{f}_m \exp\left(i\frac{2\pi}{M}mi\right) \right. \\ & \left. + \hat{f}_m^* \exp\left(-i\frac{2\pi}{M}mi\right) \right] \\ & + \hat{f}_{M/2} (-1)^i, \end{aligned} \quad (3.65)$$

where  $\hat{f}_{-m} = \hat{f}_m^*$  since  $f(x)$  is real-valued function: the Fourier coefficient for mode  $-m$  is the complex conjugate of the Fourier coefficient for mode  $m$ . This allows for the omission of the wavenumbers  $-M/2 + 1 \leq m \leq -1$ . The forward transform is then written as:

$$\hat{f}_m = \frac{1}{M} \sum_{i=0}^{M-1} f_i \exp\left(-i\frac{2\pi}{M}mi\right), \quad m = 0, \dots, \frac{M}{2}, \quad (3.66)$$

and the inverse transform is written as:

$$f_i = \hat{f}_0 + \sum_{m=1}^{M/2-1} \left[ \hat{f}_m \exp\left(i\frac{2\pi}{M}mi\right) + \hat{f}_m^* \exp\left(-i\frac{2\pi}{M}mi\right) \right] + \hat{f}_{M/2} (-1)^i, \quad (3.67)$$

for  $i = 0, \dots, M - 1$ , provided  $f(x)$  is a real-valued function.

### 3.4.2 De-aliasing

In addition to the mode  $m = M/2 + l$  ‘folding’ onto the mode  $m = M/2 - l$ , a further redistribution can occur when functions that are decomposed into complex exponentials are multiplied together. For example, for  $m, n \in \mathbb{Z}$ :

$$\exp\left(i\frac{2\pi}{\Gamma}mx\right) \exp\left(i\frac{2\pi}{\Gamma}nx\right) = \exp\left[i\frac{2\pi}{\Gamma}(m+n)x\right], \quad (3.68)$$

giving a complex exponential with a wavenumber that is the sum of the two individual wavenumbers. If a complex exponential with wavenumber  $k$  is multiplied by itself  $\eta \in \mathbb{Z}$  times, the result will be a complex exponential with wavenumber  $\eta k$ . Thus, a nonlinearity of order  $\eta$  redistributes the energy contained in the mode with wavenumber  $k$  to a mode with wavenumber  $\eta k$ . Furthermore, if the Fourier mesh does not contain enough mesh points, energy will be redistributed into modes with lower wavenumbers. To prevent this from happening, a Fourier filter can be used that zeros out wavenumbers above a threshold value. This threshold value is chosen such that when the nonlinearity redistributes the energy of the largest acceptable mode,  $k$ , to the higher mode  $\eta k$ , it folds around the mode  $M/2$  to the smallest value strictly greater than the threshold wavenumber  $k$ . Specifically,

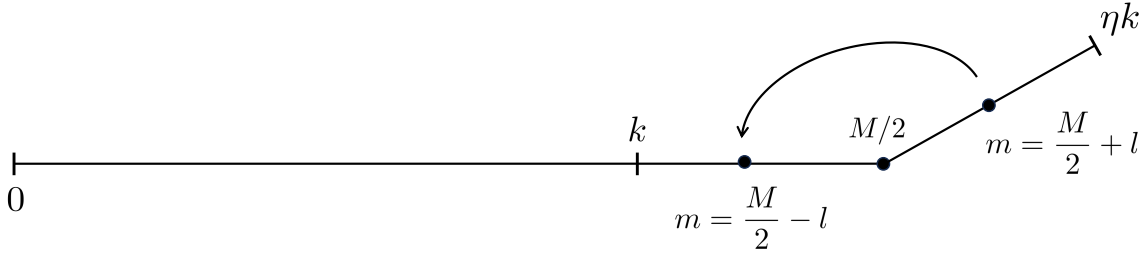


Figure 3.4: Modes project onto themselves up until  $m \leq M/2$  and from there on, a mode with  $m = M/2 + l$  ‘folds’ around  $M/2$  to a mode with  $m = M/2 - l$ . The threshold wavenumber  $k$  is chosen so that when the nonlinearity of order  $\eta$  redistributes the energy in the mode with wavenumber  $k$  to the mode with wavenumber  $\eta k$ , it folds around  $M/2$  to the smallest value  $m > k$ .

the wavenumber  $\eta k$ , which can be written as:

$$\eta k = \frac{M}{2} + l, \quad (3.69)$$

for some  $l$ , is folded over to the wavenumber

$$m = \frac{M}{2} - l. \quad (3.70)$$

This implies that:

$$m + \eta k = M, \quad (3.71)$$

and since it is desired that  $m > k$  must lie as close as possible to  $k$ , the wavenumber  $k$  must satisfy:

$$\begin{aligned} k &< M - \eta k \\ \implies k &< \frac{M}{\eta + 1}, \end{aligned} \quad (3.72)$$

which is illustrated in Figure 3.4. This implies that the Fourier filter should zero out the wavenumbers

$$k \geq \frac{M}{\eta + 1}, \quad (3.73)$$

which, in the case of a second-order nonlinearity, the largest wavenumber to remain unfiltered is:

$$k = \left\lfloor \frac{M}{3} \right\rfloor, \quad (3.74)$$

where  $\lfloor x \rfloor$  denotes the largest integer less than or equal to  $x \in \mathbb{R}$ .

### 3.4.3 Fourier Discretisation in Two Dimensions

For a horizontal domain of size  $\Gamma_x \times \Gamma_y$ , the Fourier mesh is defined as

$$x_i = \frac{\Gamma_x i}{M}, \quad i = 0, \dots, M-1, \quad (3.75)$$

$$y_j = \frac{\Gamma_y j}{N}, \quad j = 0, \dots, N-1, \quad (3.76)$$

where  $M$  and  $N$  are the number of points in the  $x$ -direction and  $y$ -direction respectively.

The Fourier transform of a two-dimensional real field  $f(x, y)$  is defined as:

$$\hat{f}_{mn} = \frac{1}{MN} \sum_{i=0}^{M-1} \sum_{j=0}^{N-1} f(x_i, y_j) \exp(-ik_m x_i) \exp(-il_n y_j), \quad (3.77)$$

where  $i$  is the imaginary unit and

$$k_m = \frac{2\pi}{\Gamma_x} m, \quad m = 0, \dots, \frac{M}{2}, \quad (3.78)$$

$$l_n = \frac{2\pi}{\Gamma_y} n, \quad n = -\frac{N}{2} + 1, \dots, \frac{N}{2}, \quad (3.79)$$

are the wavenumbers in the  $x$ - and  $y$ -directions respectively. When written as:

$$\hat{f}_{mn} = \sum_{j=0}^{N-1} \left\{ \sum_{i=0}^{M-1} f(x_i, y_j) \exp(-ik_m x_i) \right\} \exp(-il_n y_j), \quad (3.80)$$

the two-dimensional transform can be seen to be the Fourier transform of the field  $f(x, y)$  first in the  $x$ -direction, then in the  $y$ -direction. Consequently, only the summation over the wavenumbers in the  $x$ -direction may be reduced to the positive range. The inverse transform is then:

$$\begin{aligned} f_{ij} = f(x_i, y_j) = & \sum_{n=-N/2+1}^{N/2} \exp(il_n y_j) \left[ \hat{f}_{0n} \right. \\ & + \sum_{m=1}^{M/2-1} \left( \hat{f}_{mn} \exp(ik_m x_i) + \hat{f}_{mn}^* \exp(-ik_m x_i) \right) \\ & \left. + \hat{f}_{\frac{M}{2}n} (-1)^i \right] \end{aligned} \quad (3.81)$$

When solving the dry lake equations numerically, the operators (the left-hand sides of

(3.51) and (3.52)) that need to be inverted are both of the form

$$\phi_1 \nabla^2 + \phi_2, \quad (3.82)$$

for some constants  $\phi_1$  and  $\phi_2$ . For the salinity operator,  $\phi_1^S = -\Delta t$ ,  $\phi_2^S = \alpha_0$  and for the pressure operator,  $\phi_1^P = 1$ ,  $\phi_2^P = 0$ . To solve the equation

$$(\phi_1 \nabla^2 + \phi_2) u = f, \quad (3.83)$$

in two dimensions for a general field  $u(x, y)$  and forcing  $f(x, y)$ , Fourier transforms are first taken:

$$[-\phi_1 (k_m^2 + l_n^2) + \phi_2] \hat{u}_{mn} = \hat{f}_{mn} \quad (3.84)$$

$$\implies \left[ -4\pi^2 \phi_1 \left( \frac{m^2}{\Gamma_x^2} + \frac{n^2}{\Gamma_y^2} \right) + \phi_2 \right] \hat{u}_{mn} = \hat{f}_{mn}, \quad (3.85)$$

so that each mode  $(k_m, l_n) = (2\pi m/\Gamma_x, 2\pi n/\Gamma_y)$  has been decoupled from the others and solving for the Fourier coefficients  $\hat{u}_{mn}$  amounts to dividing by a constant for each pair  $(m, n)$ . The inverse transform is then taken to obtain the solution in physical space.

### 3.5 Vertical Discretisation

The vertical direction is bounded and Dirichlet boundary conditions are used for the salinity and Neumann boundary conditions are used for the pressure. The vertical domain  $[0, h]$  is divided into  $N_e$  equally spaced elements, each of size  $h/N_e$ . Each element then spans the subdomain  $[z_{\min}^l, z_{\max}^l]$ , where  $l = 1, \dots, N_e$  and  $z_{\min}^l$  and  $z_{\max}^l$  denote the endpoints for the  $l^{\text{th}}$  element:

$$z_{\min}^l = (l-1) \frac{h}{N_e}, \quad (3.86)$$

$$z_{\max}^l = l \frac{h}{N_e}. \quad (3.87)$$

Each element contains  $N_z + 1$  collocation nodes, which are determined via the use of the Legendre polynomials:

$$z_k^l = \begin{cases} z_{\min}^l & k = 0 \\ z_{\min}^l + \frac{z_{\max}^l - z_{\min}^l}{2} (1 + \zeta_k) & k = 1, \dots, N_z - 1 \\ z_{\max}^l & k = N_z \end{cases} \quad (3.88)$$

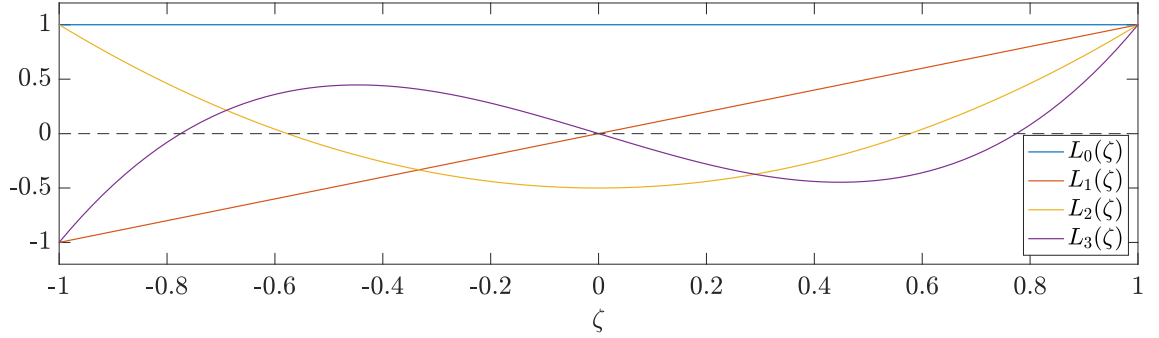


Figure 3.5: First four Legendre polynomials. At the endpoints, the polynomials satisfy  $L_N(1) = 1$  and  $L_N(-1) = (-1)^N$ .

The value  $\zeta_k$  is the  $k^{\text{th}}$  root of  $L'_{N_z}(\zeta)$  ( $\zeta \in [-1, 1]$ ), the first derivative of the Legendre polynomial of degree  $N_z$ . The Legendre polynomials can be determined via the recurrence relation:

$$L_0(\zeta) = 1, \quad (3.89)$$

$$L_1(\zeta) = \zeta, \quad (3.90)$$

$$L_{k+1}(\zeta) = \frac{2k+1}{k+1} \zeta L_k(\zeta) - \frac{k}{k+1} L_{k-1}(\zeta), \quad (3.91)$$

and the first four polynomials can be seen in Figure 3.5. The equations will be solved using a weak formulation and a Gaussian quadrature will be used to approximate the integrals:

$$\int_{z_{\min}^l}^{z_{\max}^l} f(z) dz \approx \sum_{k=0}^{N_z} \rho_k^l f(z_k^l), \quad (3.92)$$

where  $\rho_k^l$ ,  $k = 0, \dots, N_z$ ,  $l = 1, \dots, N_e$  are the weights. Using the weak formulation along with the quadrature (3.92) provides an advantage because it computes integrals with high accuracy and, in particular, (3.92) is exact when  $f(z)$  is a polynomial of degree  $2N_z - 1$ . The weights  $\rho_k^l$  are given by (Canuto et al., 1988):

$$\rho_k^l = \frac{z_{\max}^l - z_{\min}^l}{N_z (N_z + 1) L_{N_z}(\zeta_k)^2}, \quad (3.93)$$

where  $k = 0 \dots, N_z$ ,  $l = 1, \dots, N_e$ . Each element spans the same distance, meaning the weights are independent of the element index and so:

$$\rho_k = \frac{h}{N_e N_z (N_z + 1) L_{N_z}(\zeta_k)^2}. \quad (3.94)$$

Since the Legendre polynomials are used to determine the nodes and weights, this quadrature is referred to as the Gauss–Lobatto–Legendre quadrature.

The process of solving a Helmholtz problem on the vertical domain will first be described in the case of only one element and will be expanded to multiple elements afterwards (see Section 3.5.1). Similar to the horizontal directions, Helmholtz problems are of the form:

$$\left(\chi_1 \frac{d^2}{dz^2} + \chi_2\right) u(z) = f(z), \quad (3.95)$$

for  $z \in [z_{\min}, z_{\max}]$  and  $\chi_1$  and  $\chi_2$  constants. To solve (3.95), it is first multiplied by a set of test functions, chosen to be the Lagrange functions:

$$\psi_i(z) = \prod_{l \neq i} \frac{z - z_l}{z_i - z_l}, \quad i = 0, \dots, N_z, \quad (3.96)$$

and then integrated over the domain to yield  $N_z + 1$  equations:

$$\chi_1 \int_{z_{\min}}^{z_{\max}} \psi_i(z) \frac{d^2 u}{dz^2} dz + \chi_2 \int_{z_{\min}}^{z_{\max}} \psi_i(z) u dz = \int_{z_{\min}}^{z_{\max}} \psi_i(z) f(z) dz, \quad i = 0, \dots, N_z. \quad (3.97)$$

Integration by parts is used on the first term which yields a term that is only evaluated at the endpoints:

$$\chi_1 \left[ \psi_i(z) \frac{du}{dz} \right]_{z_{\min}}^{z_{\max}} - \chi_1 \int_{z_{\min}}^{z_{\max}} \frac{d\psi_i}{dz} \frac{du}{dz} dz + \chi_2 \int_{z_{\min}}^{z_{\max}} \psi_i(z) u dz = \int_{z_{\min}}^{z_{\max}} \psi_i(z) f(z) dz. \quad (3.98)$$

The solution,  $u(z)$ , and the right-hand side,  $f(z)$ , are written as a sum of the Lagrange functions  $\psi_i(z)$ :

$$u(z) = \sum_{k=0}^{N_z} u_k \psi_k(z), \quad (3.99)$$

$$f(z) = \sum_{k=0}^{N_z} f_k \psi_k(z), \quad (3.100)$$

and using the property that  $\psi_i(z_k) = \delta_{ik}$ , the coefficients  $u_k$  and  $f_k$  satisfy

$$u_k = u(z_k), \quad f_k = f(z_k). \quad (3.101)$$

Thus,

$$\begin{aligned} \chi_1 \left[ \psi_i(z) \frac{du}{dz} \right]_{z_{\min}}^{z_{\max}} - \chi_1 \int_{z_{\min}}^{z_{\max}} \frac{d\psi_i}{dz} \sum_{k=0}^{N_z} u_k \frac{d\psi_k}{dz} dz + \chi_2 \int_{z_{\min}}^{z_{\max}} \psi_i(z) \sum_{k=0}^{N_z} u_k \psi_k(z) dz \\ = \int_{z_{\min}}^{z_{\max}} \psi_i(z) \sum_{k=0}^{N_z} f_k \psi_k(z) dz. \end{aligned} \quad (3.102)$$

All integrals are then approximated using the quadrature (3.92),

$$\begin{aligned} \chi_1 \left[ \psi_i(z) \frac{du}{dz} \right]_{z_{\min}}^{z_{\max}} - \chi_1 \sum_{l=0}^{N_z} \rho_l \frac{d\psi_i}{dz} \sum_{k=0}^{N_z} u_k \frac{d\psi_k}{dz} + \chi_2 \sum_{l=0}^{N_z} \rho_l \psi_i(z_l) \sum_{k=0}^{N_z} u_k \psi_k(z_l) \\ = \sum_{l=0}^{N_z} \rho_l \psi_i(z_l) \sum_{k=0}^{N_z} f_k \psi_k(z_l), \end{aligned} \quad (3.103)$$

and terms are simplified using the property  $\psi_i(z_l) = \delta_{il}$ :

$$\begin{aligned} \chi_1 \left[ \psi_i(z) \frac{du}{dz} \right]_{z_{\min}}^{z_{\max}} - \chi_1 \sum_{l=0}^{N_z} \rho_l \frac{d\psi_i}{dz} \sum_{k=0}^{N_z} u_k \frac{d\psi_k}{dz} + \chi_2 \rho_i \sum_{k=0}^{N_z} u_k \psi_k(z_i) \\ = \rho_i \sum_{k=0}^{N_z} f_k \psi_k(z_i), \end{aligned} \quad (3.104)$$

and  $\psi_k(z_i) = \delta_{ki}$ :

$$\chi_1 \left[ \psi_i(z) \frac{du}{dz} \right]_{z_{\min}}^{z_{\max}} - \chi_1 \sum_{l=0}^{N_z} \rho_l \frac{d\psi_i}{dz} \sum_{k=0}^{N_z} u_k \frac{d\psi_k}{dz} + \chi_2 \rho_i u_i = \rho_i f_i. \quad (3.105)$$

Dividing by  $\rho_i$ , evaluating the boundary term and rearranging, this becomes

$$-\frac{\chi_1}{\rho_i} \sum_{l=0}^{N_z} \rho_l \frac{d\psi_i}{dz} \sum_{k=0}^{N_z} u_k \frac{d\psi_k}{dz} + \chi_2 u_i = f_i - \frac{\chi_1}{\rho_i} \left[ \frac{du}{dz}(z_{\max}) \delta_{iN_z} - \frac{du}{dz}(z_{\min}) \delta_{i0} \right]. \quad (3.106)$$

To evaluate the derivatives, the differentiation matrix associated with the Gauss–Lobatto–

Legendre quadrature is used:

$$dz_{kl} = \begin{cases} \frac{2L_{N_z}(z_k)}{(z_{\max} - z_{\min})(z_k - z_l)L_{N_z}(z_l)} & k \neq l \\ \frac{N_z(N_z + 1)}{2(z_{\max} - z_{\min})} & k = l = 0 \\ -\frac{N_z(N_z + 1)}{2(z_{\max} - z_{\min})} & k = l = N_z \\ 0 & \text{otherwise} \end{cases}. \quad (3.107)$$

This allows the derivatives to be written as

$$\frac{d\psi_i}{dz} = \sum_{j=0}^{N_z} dz_{lj} \psi_i(z_j) = dz_{li} \quad (3.108)$$

and

$$\frac{du}{dz} = \sum_{j=0}^{N_z} dz_{lj} u(z_j) = dz_{lj} u_j. \quad (3.109)$$

Thus,

$$-\frac{\chi_1}{\rho_i} \sum_{k=0}^{N_z} \sum_{l=0}^{N_z} \rho_l dz_{li} dz_{lk} u_k + \chi_2 u_i = f_i - \frac{\chi_1}{\rho_i} (dz_{N_z j} u_j \delta_{i N_z} - dz_{0j} u_j \delta_{i0}). \quad (3.110)$$

This is a linear system of equations, which can be written in matrix form:

$$\mathcal{M}u = f + \mathcal{B}, \quad (3.111)$$

where

$$\mathcal{M}_{ij} = \chi_1 A_{ij} + \chi_2 \delta_{ij}, \quad (3.112)$$

$$A_{ij} = -\frac{1}{\rho_i} \sum_{k=0}^{N_z} \rho_k dz_{ki} dz_{kj}, \quad (3.113)$$

and the boundary term  $\mathcal{B}$  is given by

$$\begin{aligned} \mathcal{B}_i &= -\frac{\chi_1}{\rho_i} \left[ \frac{du}{dz}(z_{\max}) \delta_{i N_z} - \frac{du}{dz}(z_{\min}) \delta_{i0} \right] \\ &= -\frac{\chi_1}{\rho_i} (dz_{N_z j} u_j \delta_{i N_z} - dz_{0j} u_j \delta_{i0}), \end{aligned} \quad (3.114)$$

which is only nonzero for the  $i = 0$  and  $i = N_z$  entries. If Neumann boundary conditions are used, the right-hand side can be simplified by substituting the value of the boundary condition directly. For example, if:

$$\frac{du}{dz}(z_{\min}) = a, \quad \frac{du}{dz}(z_{\max}) = b, \quad (3.115)$$

then

$$\mathcal{B}_i = -\frac{\chi_1}{\rho_i} (b\delta_{iN_z} - a\delta_{i0}). \quad (3.116)$$

If Dirichlet boundary conditions are to be used, the equations for  $i = 0$  and  $i = N_z$  are unnecessary and are removed. There is then no contribution from the boundary term  $\mathcal{B}_i$ . The known terms from the left-hand side are moved to the right-hand side and the reduced system is formed:

$$\mathcal{M}_{ij}u_j = f_i - \mathcal{M}_{i0}u_0 - \mathcal{M}_{iN_z}u_{N_z}, \quad (3.117)$$

where the summation is now over  $i, j = 1, \dots, N_z - 1$ . In either case, determining the solution is done by inverting the matrix  $\mathcal{M}$  which is most efficient if it is diagonalised. First, the linear system is written as:

$$\mathcal{M}u = \mathcal{F}, \quad (3.118)$$

where

$$\mathcal{F}_i = \begin{cases} f_i - \mathcal{M}_{i0}u_0 - \mathcal{M}_{iN_z}u_{N_z} & \text{for Dirichlet BCs,} \\ f_i + \mathcal{B}_i & \text{for Neumann BCs.} \end{cases} \quad (3.119)$$

The matrix  $\mathcal{A}$  is diagonalised:

$$\mathcal{A} = P\Lambda Q, \quad (3.120)$$

where  $\Lambda$  is diagonal, the entries of which are the eigenvalues of  $\mathcal{A}$ ,  $P$  is the transfer matrix, which has the eigenvectors of  $\mathcal{A}$  as its columns and  $Q = P^{-1}$ . Thus,

$$(\chi_1 P_{i\mu} \Lambda_{\mu\nu} Q_{\nu j} + \chi_2 \delta_{ij}) u_j = \mathcal{F}_i. \quad (3.121)$$

The Gauss–Lobatto–Legendre transform is then defined as

$$\hat{u} = Qu = P^{-1}u, \quad (3.122)$$

where  $\hat{u}$  is the spectral representation of  $u$ , where vectors are expressed in the basis of eigenvectors of the matrix  $\mathcal{A}$ . Multiplying by the forward transform,  $P^{-1}$ , (3.121) becomes

$$\chi_1 P_{ki}^{-1} P_{i\mu} \Lambda_{\mu\nu} Q_{\nu j} u_j + \chi_2 P_{ki}^{-1} u_i = P_{ki}^{-1} \mathcal{F}_i, \quad (3.123)$$

for which  $P_{ki}^{-1} P_{i\mu} = \delta_{k\mu}$ ,  $Q_{\nu j} u_j = \hat{u}_\nu$ ,  $P_{ki}^{-1} u_i = \hat{u}_k$  and  $P_{ki}^{-1} \mathcal{F}_i = \hat{\mathcal{F}}_k$ . This simplifies to

$$\chi_1 \Lambda_{k\nu} \hat{u}_\nu + \chi_2 \hat{u}_k = \hat{\mathcal{F}}_k \quad (3.124)$$

and hence

$$(\chi_1 \Lambda + \chi_2 I) \hat{u} = \hat{\mathcal{F}}. \quad (3.125)$$

Determining the solution  $\hat{u}$  amounts to dividing by the eigenvalues:

$$\hat{u}_i = \frac{\mathcal{F}_i}{\chi_1 \lambda_i + \chi_2}, \quad (3.126)$$

where  $\lambda_i = \Lambda_{ii}$  are the individual elements of the diagonal matrix  $\Lambda$ . Obtaining the solution back in physical space uses the inverse Gauss–Lobatto–Legendre transform:

$$u = P \hat{u}. \quad (3.127)$$

For a one-dimensional problem of the form (3.95), obtaining the solution involves transforming the right-hand side to spectral space, dividing by the eigenvalues and transforming back to physical space. Transforming to spectral space and back involves multiplication by the appropriate matrix.

### 3.5.1 Spectral Elements

The use of a single element to span the whole domain is suited to small domains in the vertical direction. The two length scales present in the system are the size of the solutal boundary layer and the overall domain depth. When these lengths are not comparable, the use of a single element is not ideal. As either the Rayleigh number or lake depth is increased, more mesh points are needed to either resolve the finer scale dynamics or to span in the increased size of the vertical domain. However, increasing the number of mesh points results in large differences between the density of mesh points at the boundaries and in the middle of the domain, leading to an unnecessarily large mesh density at the bottom of the domain, where the dynamics are mostly diffusive. In addition, when salinity plumes

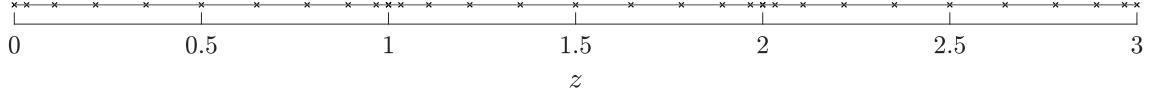


Figure 3.6: Example of the spectral element mesh using  $N_e = 3$ ,  $N_z = 10$  on a domain with depth  $h = 3$ .

descend into the middle of the domain, the large salinity gradients that are present at the plume tips still need to be accurately resolved. Increasing the number of mesh points to satisfy the accuracy in the middle of the domain contributes to an increased computational cost, as more mesh points are placed at the boundaries relative to where they are desired. To resolve this, multiple elements are used to span the vertical direction, allowing a better distribution of mesh points throughout the whole domain.

As previously stated, the domain  $[0, h]$  is divided into  $N_e$  equally spaced elements, each of size  $h/N_e$ , in which each element uses an identical Gauss–Lobatto–Legendre quadrature. An example domain with  $h = 3$ ,  $N_e = 3$  and  $N_z = 10$  is visualised in Figure 3.6. This distributes the mesh points more evenly although a higher density of mesh points occurs near the interfaces of neighbouring elements. Meshing the vertical domain in this way allows larger domains to be used and a better distribution of mesh points over the whole domain.

Each element is identical and so the same weights  $\rho_k$  and the same differentiation matrix  $dz$  are used for all elements. The same procedure for the Helmholtz problem is followed as before, but the equation is instead multiplied by a test function given by:

$$\psi_i^l(z) = \begin{cases} \prod_{j \neq i} \frac{z - z_j^l}{z_i^l - z_j^l} & \text{if } z \in [z_{\min}^l, z_{\max}^l] \\ 0 & \text{otherwise} \end{cases}, \quad (3.128)$$

where  $i = 0, \dots, N_z$  and  $l = 1, \dots, N_e$  and after integrating by parts, a similar equation is obtained:

$$\chi_1 \left[ \psi_i^l(z) \frac{du}{dz} \right]_0^h - \chi_1 \int_0^h \frac{d\psi_i^l}{dz} \frac{du}{dz} dz + \chi_2 \int_0^h \psi_i^l(z) u dz = \int_0^h \psi_i^l(z) f(z) dz. \quad (3.129)$$

The integrals can be split up into their contributions from each element:

$$\begin{aligned}
 -\chi_1 \sum_{l=1}^{N_e} \int_{z_{\min}^l}^{z_{\max}^l} \frac{d\psi_i^l}{dz} \frac{du}{dz} dz + \chi_2 \sum_{l=1}^{N_e} \int_{z_{\min}^l}^{z_{\max}^l} \psi_i^l(z) u dz &= \sum_{l=1}^{N_e} \int_{z_{\min}^l}^{z_{\max}^l} \psi_i^l(z) f(z) dz \\
 -\chi_1 \left[ \frac{du}{dz} (z_{N_z}^{N_e}) \delta_{iN_z} \delta_{lN_e} - \frac{du}{dz} (z_0^1) \delta_{i0} \delta_{l1} \right], & \quad (3.130)
 \end{aligned}$$

for  $i = 0, \dots, N_z$ . As  $\psi_i^l(z) \equiv 0$  when  $z \notin [z_{\min}^l, z_{\max}^l]$ , this can be decomposed further to obtain an equation on each element:

$$-\chi_1 \int_{z_{\min}^l}^{z_{\max}^l} \frac{d\psi_i^l}{dz} \frac{du}{dz} dz + \chi_2 \int_{z_{\min}^l}^{z_{\max}^l} \psi_i^l(z) u dz = \int_{z_{\min}^l}^{z_{\max}^l} \psi_i^l(z) f(z) dz \quad (3.131)$$

$$-\chi_1 \left[ \frac{du}{dz} (z_{N_z}^{N_e}) \delta_{iN_z} \delta_{lN_e} - \frac{du}{dz} (z_0^1) \delta_{i0} \delta_{l1} \right], \quad (3.132)$$

where  $i = 0, \dots, N_z$  and  $l = 1, \dots, N_e$  and the quadrature may be used again to approximate integrals:

$$-\chi_1 \sum_{k=0}^{N_z} \rho_k \frac{d\psi_i^l}{dz} (z_k^l) \frac{du}{dz} (z_k^l) + \chi_2 \sum_{k=0}^{N_z} \rho_k \psi_i^l (z_k^l) u_k^l = \sum_{k=0}^{N_z} \rho_k \psi_i^l (z_k^l) f_k^l \quad (3.133)$$

$$-\chi_1 \left[ \frac{du}{dz} (z_{N_z}^{N_e}) \delta_{iN_z} \delta_{lN_e} - \frac{du}{dz} (z_0^1) \delta_{i0} \delta_{l1} \right]. \quad (3.134)$$

The solution  $u(z)$  and right-hand side  $f(z)$  are again expanded in terms of the Lagrange functions:

$$u(z) = \sum_{k=0}^{N_z} \sum_{l=1}^{N_e} u_k^l \psi_k^l(z), \quad (3.135)$$

$$f(z) = \sum_{k=0}^{N_z} \sum_{l=1}^{N_e} f_k^l \psi_k^l(z), \quad (3.136)$$

giving:

$$-\frac{\chi_1}{\rho_i} \sum_{k=0}^{N_z} \rho_k dz_{ki} dz_{kj} u_j^l + \chi_2 \delta_{ij} u_j^l = f_i^l + \mathcal{B}_i^l. \quad (3.137)$$

This gives a linear problem on each element:

$$\mathcal{M}^l u^l = f^l + \mathcal{B}^l, \quad l = 1, \dots, N_e, \quad (3.138)$$

where

$$\mathcal{M}_{ij}^l = \chi_1 \mathcal{A}_{ij} + \chi_2 \delta_{ij}, \quad (3.139)$$

which is independent of the element  $l$  due to the Helmholtz problem being identical over

all elements. The boundary term is now

$$\mathcal{B}_i^l = -\frac{\chi_1}{\rho_i} \left[ \frac{du}{dz} (z_{N_z}^{N_e}) \delta_{iN_z} \delta_{lN_e} - \frac{du}{dz} (z_0^1) \delta_{i0} \delta_{l1} \right], \quad (3.140)$$

which is again only nonzero at the boundaries of the domain.

The linear problems (3.138) each have dimension  $N_z + 1$ . A larger linear problem of dimension  $N_e(N_z + 1)$  may be defined by joining each individual problem in (3.138) into a larger matrix. This yields a block-diagonal matrix:

$$\begin{pmatrix} \mathcal{M}^1 & 0 & \dots & 0 \\ 0 & \mathcal{M}^2 & & \vdots \\ \vdots & & \ddots & 0 \\ 0 & \dots & 0 & \mathcal{M}^{N_e} \end{pmatrix} \begin{pmatrix} u_{top}^1 \\ u_R^1 \\ u_{btm}^1 \\ u_{top}^2 \\ u_R^2 \\ u_{btm}^2 \\ \vdots \\ u_{top}^{N_e} \\ u_R^{N_e} \\ u_{btm}^{N_e} \end{pmatrix} = \begin{pmatrix} f_{top}^1 \\ f_R^1 \\ f_{btm}^1 \\ f_{top}^2 \\ f_R^2 \\ f_{btm}^2 \\ \vdots \\ f_{top}^{N_e} \\ f_R^{N_e} \\ f_{btm}^{N_e} \end{pmatrix} + \begin{pmatrix} \mathcal{B}_{top} \\ 0 \\ 0 \\ 0 \\ 0 \\ 0 \\ \vdots \\ 0 \\ 0 \\ \mathcal{B}_{btm} \end{pmatrix}. \quad (3.141)$$

Here, the solution  $u$  and the forcing  $f + \mathcal{B}$  have been separated into interface values and interior vectors. The interface values are denoted by  $u_{top}^l$  and  $u_{btm}^l$  and the interior vector is denoted by  $u_R^l$  with a similar notation used for  $f$ . The boundary term  $\mathcal{B}$  is only nonzero on the first and last elements, for which it is only nonzero for the first and last entries, taking values  $\mathcal{B}_{top} = \mathcal{B}_0^1$  and  $\mathcal{B}_{btm} = \mathcal{B}_{N_z}^{N_e}$  respectively. Since neighbouring elements share an interface mesh point, there are two equations for each element interface. Thus, (3.141) is modified by taking the average of these equations. The interface variables are defined as:

$$u_I^l = \frac{u_{btm}^l + u_{top}^{l+1}}{2}, \quad (3.142)$$

$$f_I^l = \frac{f_{btm}^l + f_{top}^{l+1}}{2}, \quad (3.143)$$

for  $l = 1, \dots, N_e - 1$ . The equation involving the last row of  $\mathcal{M}^l$ ,

$$\mathcal{M}_{N_z 0}^l u_{top}^l + \mathcal{M}_{N_z j}^l u_{R,j}^l + \mathcal{M}_{N_z N_z}^l u_{btm}^l = f_{btm}^l, \quad (3.144)$$



$N_e(N_z + 1)$  to  $(N_e N_z + 1) \times (N_e N_z + 1)$ , i.e.  $N_e - 1$  rows and columns are removed.

### 3.5.2 Schur Decomposition

Since neighbouring elements only couple to each other by their interface points, the entries can be reordered:

$$\begin{pmatrix} u_{top}^1 \\ u_R^1 \\ u_{btm}^1 \\ \hline u_{top}^2 \\ u_R^2 \\ u_{btm}^2 \\ \hline \vdots \\ \hline u_{top}^{N_e} \\ u_R^{N_e} \\ u_{btm}^{N_e} \end{pmatrix} \rightarrow \begin{pmatrix} u_R^1 \\ u_R^2 \\ \vdots \\ u_R^{N_e} \\ \hline u_{top} \\ u_I^1 \\ \vdots \\ u_I^{N_e-1} \\ u_{btm} \end{pmatrix}. \quad (3.150)$$

Once this is done, the system can be written as:

$$\begin{pmatrix} \mathcal{M}_{RR}^1 & 0 & \dots & 0 & \mathcal{M}_{RI}^1 \\ 0 & \mathcal{M}_{RR}^2 & & 0 & \mathcal{M}_{RI}^2 \\ \vdots & & \ddots & & \vdots \\ 0 & 0 & \dots & \mathcal{M}_{RR}^{N_e} & \mathcal{M}_{RI}^{N_e} \\ \mathcal{M}_{IR}^1 & \mathcal{M}_{IR}^2 & \dots & \mathcal{M}_{IR}^{N_e} & \mathcal{M}_{II} \end{pmatrix} \begin{pmatrix} u_R^1 \\ u_R^2 \\ \vdots \\ u_R^{N_e} \\ u_I \end{pmatrix} = \begin{pmatrix} f_R^1 \\ f_R^2 \\ \vdots \\ f_R^{N_e} \\ f_I \end{pmatrix} + \begin{pmatrix} 0 \\ 0 \\ \vdots \\ 0 \\ \mathcal{B}_I \end{pmatrix}, \quad (3.151)$$

where  $\mathcal{M}_{RR}^l$  are defined as in (3.148),  $\mathcal{M}_{RI}^l$  are matrices of size  $(N_z - 1) \times (N_e + 1)$  and have nonzero entries in their  $l^{\text{th}}$  and  $(l+1)^{\text{st}}$  columns which are  $\mathcal{M}_{\leftarrow}^l$  and  $\mathcal{M}_{\rightarrow}^l$  respectively. The matrices  $\mathcal{M}_{IR}^l$  are of size  $(N_e + 1) \times (N_z - 1)$  and have nonzero entries in their  $l^{\text{th}}$  and  $(l+1)^{\text{st}}$  rows which are  $\mathcal{M}_{\uparrow}^l/2$  and  $\mathcal{M}_{\downarrow}^l/2$  respectively. Finally, the matrix  $\mathcal{M}_{II}$  is

tridiagonal:

$$\mathcal{M}_{II} = \begin{pmatrix} \mathcal{M}_{\searrow}^1 & \mathcal{M}_{\nearrow}^1 & 0 & \dots & 0 & 0 \\ \frac{\mathcal{M}_{\searrow}^1}{2} & \frac{\mathcal{M}_{\searrow}^1 + \mathcal{M}_{\searrow}^2}{2} & \frac{\mathcal{M}_{\nearrow}^2}{2} & & & 0 \\ 0 & \frac{\mathcal{M}_{\searrow}^2}{2} & \frac{\mathcal{M}_{\searrow}^2 + \mathcal{M}_{\searrow}^3}{2} & \ddots & & \vdots \\ \vdots & & \ddots & \ddots & & 0 \\ 0 & 0 & & & \frac{\mathcal{M}_{\searrow}^{N_e-1} + \mathcal{M}_{\searrow}^{N_e}}{2} & \frac{\mathcal{M}_{\nearrow}^{N_e}}{2} \\ 0 & 0 & \dots & 0 & \mathcal{M}_{\searrow}^{N_e} & \mathcal{M}_{\searrow}^{N_e} \end{pmatrix}. \quad (3.152)$$

The vectors  $u_I$  and  $f_I$  are of size  $N_e + 1$  and consist of the boundary and interface values of  $u$  and  $f$  respectively. The vector  $\mathcal{B}_I$ , of size  $N_e + 1$ , also only contains the interface values of  $\mathcal{B}$ , which in this case are nonzero at the boundaries, with values  $\mathcal{B}_{top}$  and  $\mathcal{B}_{btm}$ . Equation (3.151) can then be written as a system of matrix equations:

$$\mathcal{M}_{RR}^l u_R^l + \mathcal{M}_{RI}^l u_I = f_R^l, \quad l = 1, \dots, N_e, \quad (3.153)$$

$$\sum_{l=1}^{N_e} \mathcal{M}_{IR}^l u_R^l + \mathcal{M}_{II} u_I = f_I + \mathcal{B}_I. \quad (3.154)$$

Once this rearrangement is done, the system must be adapted for Dirichlet or Neumann boundary conditions by modifying (3.154). If Neumann boundary conditions are used, nothing is changed since  $\mathcal{B}_I$  already contains the boundary conditions. If Dirichlet boundary conditions are used, the first and last rows of the right-hand side of (3.154) are replaced with the values of the boundary conditions. In addition, the first and last rows of the matrices on the left-hand side of (3.154) are modified accordingly: the first and last rows of  $\mathcal{M}_{IR}^l$  are replaced with zeros for  $l = 1, \dots, N_e$  and the first and last rows of  $\mathcal{M}_{II}$  are replaced with those of the identity matrix.

The interior solution values can be written in terms of solution values at the interfaces:

$$u_R^l = \left( \mathcal{M}_{RR}^l \right)^{-1} \left( f_R^l - \mathcal{M}_{RI}^l u_I \right). \quad (3.155)$$

Substituting this into (3.154), an equation for the interface values is obtained:

$$\left[ \mathcal{M}_{II} - \sum_{l=1}^{N_e} \mathcal{M}_{IR}^l \left( \mathcal{M}_{RR}^l \right)^{-1} \mathcal{M}_{RI}^l \right] u_I = f_I + \mathcal{B}_I - \sum_{l=1}^{N_e} \mathcal{M}_{IR}^l \left( \mathcal{M}_{RR}^l \right)^{-1} f_R^l, \quad (3.156)$$

which can be solved by inverting the matrix on the left-hand side. Defining the matrices:

$$\mathcal{S}_L = \mathcal{M}_{II} - \sum_{l=1}^{N_e} \mathcal{M}_{IR}^l \left( \mathcal{M}_{RR}^l \right)^{-1} \mathcal{M}_{RI}^l, \quad (3.157)$$

$$\mathcal{S}_R^l = \mathcal{M}_{IR}^l \left( \mathcal{M}_{RR}^l \right)^{-1}, \quad l = 1, \dots, N_e, \quad (3.158)$$

this becomes

$$\mathcal{S}_L u_I = f_I + \mathcal{B}_I - \sum_{l=1}^{N_e} \mathcal{S}_R^l f_R^l, \quad (3.159)$$

and then the interior values are determined by (3.155). The matrix  $\mathcal{S}_L$  is tridiagonal. This can be seen by writing each of the terms in the sum explicitly, using the fact that  $\mathcal{M}_{IR}^l$  is only nonzero in its  $l^{\text{th}}$  and  $(l+1)^{\text{st}}$  rows and  $\mathcal{M}_{RI}^l$  is only nonzero in its  $l^{\text{th}}$  and  $(l+1)^{\text{st}}$  columns:

$$\left( \mathcal{M}_{IR}^l \right)_{ij} = \delta_{il} a_j^l + \delta_{i(l+1)} b_j^l, \quad (3.160)$$

$$\left( \mathcal{M}_{RI}^l \right)_{ij} = c_i^l \delta_{jl} + d_i^l \delta_{j(l+1)}, \quad (3.161)$$

for some vectors  $a^l$ ,  $b^l$ ,  $c^l$  and  $d^l$ . Thus, when multiplied together, they yield four similarly structured matrices:

$$\left( \delta_{il} a_k^l + \delta_{i(l+1)} b_k^l \right) \left[ \left( \mathcal{M}_{RR}^l \right)^{-1} \right]_{km} \left( c_m^l \delta_{jl} + d_m^l \delta_{j(l+1)} \right) \quad (3.162)$$

$$= \delta_{il} \gamma_1^l \delta_{jl} + \delta_{il} \gamma_2^l \delta_{j(l+1)} + \delta_{i(l+1)} \gamma_3^l \delta_{jl} + \delta_{i(l+1)} \gamma_4^l \delta_{j(l+1)}, \quad (3.163)$$

where

$$\gamma_1^l = a_k^l \left[ \left( \mathcal{M}_{RR}^l \right)^{-1} \right]_{km} c_m^l, \quad (3.164)$$

$$\gamma_2^l = a_k^l \left[ \left( \mathcal{M}_{RR}^l \right)^{-1} \right]_{km} d_m^l, \quad (3.165)$$

$$\gamma_3^l = b_k^l \left[ \left( \mathcal{M}_{RR}^l \right)^{-1} \right]_{km} c_m^l, \quad (3.166)$$

$$\gamma_4^l = b_k^l \left[ \left( \mathcal{M}_{RR}^l \right)^{-1} \right]_{km} d_m^l, \quad (3.167)$$

are scalars for each  $l = 1, \dots, N_e$ . It can then be seen that each of the four matrices in (3.163) are only nonzero in exactly one entry for each  $l$ , where the row number and column number of the nonzero entry may differ by a maximum value of one. The addition of all these matrices then results in a tridiagonal matrix, and since  $\mathcal{M}_{II}$  is also tridiagonal, so

### 3. NUMERICS

Matrix	Rows	Columns	Saved?	Total saved	Name
$\mathcal{S}_L$	$N_e + 1$	$N_e + 1$	No		s_schur_lhs
$L$	$N_e + 1$	1	Yes	$N_e + 1$	s_schur_lhs_lower
$U$	$N_e + 1$	2	Yes	$2(N_e + 1)$	s_schur_lhs_upper
$\mathcal{S}_R^1$	$N_e + 1$	$N_z - 1$	Yes	$(N_e + 1)(N_z - 1)$	↑
⋮	⋮	⋮	⋮	⋮	s_schur_rhs_mat
$\mathcal{S}_R^{N_e}$	$N_e + 1$	$N_z - 1$	Yes	$(N_e + 1)(N_z - 1)$	↓
$\mathcal{M}_{RR}$	$N_z - 1$	$N_z - 1$	No		
$\lambda$	$N_z - 1$	1	Yes	$N_z - 1$	s_gllap_eig
$P$	$N_z - 1$	$N_z - 1$	Yes	$(N_z - 1)^2$	s_gllap_tr
$P^{-1}$	$N_z - 1$	$N_z - 1$	Yes	$(N_z - 1)^2$	s_gllap_tr_inv
$\mathcal{M}_{RI}^1$	$N_z - 1$	$N_e + 1$	Yes	$(N_z - 1)(N_e + 1)$	↑
⋮	⋮	⋮	⋮	⋮	s_gllap_ri
$\mathcal{M}_{RI}^{N_e}$	$N_z - 1$	$N_e + 1$	Yes	$(N_z - 1)(N_e + 1)$	↓

Table 3.3: Number of rows and columns for each matrix (associated with the vertical direction) computed at the start of any simulation and whether it needs to be saved. The final column denotes the total number of real (double precision) numbers needed to store each matrix. Since both the salinity and the pressure are needed to be solved for, there will be two of each matrix described here, one for each of the respective Helmholtz problems. (For the ‘Name’ column, the pressure matrices have the first letter ‘s’ replaced with ‘p’.)

is  $\mathcal{S}_L$ . At the start of a simulation, the matrices  $\mathcal{S}_R^l$ ,  $\mathcal{S}_L$ ,  $\mathcal{M}_{RR}^l$  and  $\mathcal{M}_{RI}^l$  are computed. The LU-factorisation of the matrix  $\mathcal{S}_L$  is computed:

$$\mathcal{S}_L = LU, \quad (3.168)$$

and since  $\mathcal{S}_L$  is tridiagonal, the lower matrix  $L$  can be saved with only  $N_e + 1$  entries and the upper matrix  $U$  can be saved with  $2(N_e + 1)$  entries. The matrices  $\mathcal{M}_{RR}^l$  are independent of the index  $l$ , since all the elements are identical, and so only one is needed to be saved, denoted by  $\mathcal{M}_{RR}$ . This matrix is then diagonalised and the eigenvalues,  $\lambda$ , are saved along with the transfer matrix,  $P$ , and its inverse,  $P^{-1}$ . Table 3.3 lists the size and number of each of these matrices that are required to be saved at the start of any simulation. The accuracy used to save these matrices is double precision, where each real number needs a total of 64 bits (8 bytes) of memory. Solving a vertical Helmholtz problem can be summarised as follows:

1. Compute the terms in the right-hand side of (3.159) by multiplying each  $f_R^l$  by  $S_R^l$ , involving  $O(N_z N_e^2)$  operations. Also compute  $f_I$  (size  $N_e + 1$ ) and  $\mathcal{B}_I$  (size  $N_e + 1$ , of which only two entries are nonzero).
2. Multiply the right-hand side of (3.159) by  $(\mathcal{S}_L)^{-1}$  to determine  $u_I$ . This uses an  $LU$  factorisation of a tridiagonal matrix and so only involves  $O(N_e)$  operations.
3. For each  $l$ , compute  $u_R^l$  using (3.155):
  - (a) Compute  $\mathcal{M}_{RI}^l u_I$ , involving  $O(N_z N_e)$  operations, and  $f_R^l$ .
  - (b) Transform to spectral space, involving  $O(N_z^2)$  operations.
  - (c) Invert  $\mathcal{M}_{RR}^l$  in spectral space by dividing by its eigenvalues, involving  $O(N_z)$  operations.
  - (d) Transform back to physical space, involving  $O(N_z^2)$  operations.

This step thus involves  $O(N_z N_e (N_z + N_e))$  operations.

Since a vertical Helmholtz problem must be solved for each wavenumber pair, the number of operations associated with vertical problems scales like  $N_x N_y N_z N_e (N_z + N_e)$ . In addition, to arrive at this, a forward Fourier transform has to be taken, the number of operations of which scales like  $N_x \log N_x N_y \log N_y N_z N_e$ . The total number of operations at each time step thus scales like:

$$N_{\text{operations}} \sim N_x N_y N_z N_e (\log N_x \log N_y + N_z + N_e). \quad (3.169)$$

(This can be verified by summing the size of the ‘for’ loops in the numerical code and taking the leading order contributions.)

## 3.6 Solving the Dry Lake Equations

The equations and boundary conditions that are solved when simulating dry lakes are:

$$\frac{\partial S}{\partial t} + \mathbf{u} \cdot \nabla S = \nabla^2 S, \quad (3.170)$$

$$\nabla^2 p = Ra \frac{\partial S}{\partial z}, \quad (3.171)$$

$$\mathbf{u} = -\nabla p + Ra S \mathbf{e}_z, \quad (3.172)$$

$$S = 1, \quad \frac{\partial p}{\partial z} = Ra + 1 \quad \text{at } z = 0, \quad (3.173)$$

$$S = 0, \quad \left\langle \frac{\partial p}{\partial z} \right\rangle = 1 \quad \text{at } z = h. \quad (3.174)$$

The domain is discretised using a Fourier mesh in each of the horizontal directions:

$$x_i = \frac{\Gamma_x i}{N_x}, \quad i = 0, \dots, N_x - 1, \quad (3.175)$$

$$y_j = \frac{\Gamma_y j}{N_y}, \quad j = 0, \dots, N_y - 1, \quad (3.176)$$

where  $N_x$  and  $N_y$  are the number of mesh points in the  $x$ - and  $y$ -direction respectively. The vertical direction is discretised using  $N_e$  uniform elements, each using a Gauss–Lobatto–Legendre discretisation with  $N_z + 1$  points per element:

$$z_k^l = \frac{(l-1)h}{N_e} + \tilde{z}_k, \quad k = 0, \dots, N_z, \quad l = 1, \dots, N_e, \quad (3.177)$$

where the points  $\tilde{z}_k$  are the nodes of the Gauss–Lobatto–Legendre discretisation on the first element,  $[0, h/N_e]$ :

$$\tilde{z}_k = \frac{h}{2N_e} (1 + \zeta_k), \quad (3.178)$$

where  $\zeta_k$  is the  $k^{\text{th}}$  root of  $L'_{N_z}(z)$ . This uses a total of  $N_e(N_z + 1)$  mesh points in the vertical direction. The salinity is discretised as:

$$\begin{aligned} S_{ijkl} = S(x_i, y_j, z_k^l) &= \sum_{q=0}^{N_z} \sum_{n=-N_y/2+1}^{N_y/2} \psi_q^l(z_k^l) \exp\left(i \frac{2\pi}{N_y} n j\right) \left\{ \tilde{S}_{0nql} \right. \\ &+ \sum_{m=1}^{N_x/2-1} \left[ \tilde{S}_{mnql} \exp\left(i \frac{2\pi}{N_x} m i\right) + \tilde{S}_{mnql}^* \exp\left(-i \frac{2\pi}{N_x} m i\right) \right] \\ &\left. + \tilde{S}_{\frac{N_x}{2}nql} (-1)^i \right\}, \end{aligned} \quad (3.179)$$

where  $i = 0, \dots, N_x - 1$ ,  $j = 0, \dots, N_y - 1$ ,  $k = 0, \dots, N_z$  and  $l = 1, \dots, N_e$ . The coefficients  $\tilde{S}_{mnql}$  are complex numbers and denote the solution in spectral space. The Lagrange polynomials are defined as

$$\psi_q^r(z) = \begin{cases} \prod_{s \neq q} \frac{z - z_s^r}{z_q^r - z_s^r} & \text{if } z \in [z_{\min}^r, z_{\max}^r] \\ 0 & \text{otherwise} \end{cases} \quad (3.180)$$

for  $q = 0, \dots, N_z$ ,  $r = 1, \dots, N_e$ . Fourier transforms are first taken, resulting in  $(N_x/2 + 1) \times N_y$  decoupled equations for the salinity and pressure:

$$\frac{\partial}{\partial t} \hat{S}_{mn} + \hat{N}_{mn} = \left[ \frac{\partial^2}{\partial z^2} - 4\pi^2 \left( \frac{m^2}{\Gamma_x^2} + \frac{n^2}{\Gamma_y^2} \right) \right] \hat{S}_{mn}, \quad (3.181)$$

$$\left[ \frac{\partial^2}{\partial z^2} - 4\pi^2 \left( \frac{m^2}{\Gamma_x^2} + \frac{n^2}{\Gamma_y^2} \right) \right] \hat{p}_{mn} = Ra \frac{\partial}{\partial z} \hat{S}_{mn}, \quad (3.182)$$

where  $\hat{N}$  is the Fourier transform of  $\mathbf{u} \cdot \nabla S$ . The Taylor expansions of Section 3.3 are applied to the time derivative and the nonlinear term:

$$\left\{ \alpha_0 - \Delta t \left[ \frac{\partial^2}{\partial z^2} - 4\pi^2 \left( \frac{m^2}{\Gamma_x^2} + \frac{n^2}{\Gamma_y^2} \right) \right] \right\} \hat{S}_{mn}^t = - \sum_{i=1}^s \alpha_i \hat{S}_{mn}^{t-i\Delta t} - \Delta t \sum_{i=1}^s \beta_i \hat{N}_{mn}^{t-i\Delta t}, \quad (3.183)$$

$$\left[ \frac{\partial^2}{\partial z^2} - 4\pi^2 \left( \frac{m^2}{\Gamma_x^2} + \frac{n^2}{\Gamma_y^2} \right) \right] \hat{p}_{mn}^t = Ra \frac{\partial}{\partial z} \hat{S}_{mn}^t, \quad (3.184)$$

where  $\Delta t$  is the time step,  $s$  is the order of the time stepping scheme,  $\alpha_i$ ,  $i = 0, \dots, s$  are the coefficients for the time derivative expansion (see Section 3.3.1) and  $\beta_i$ ,  $i = 1, \dots, s$  are the coefficients for the extrapolation of the nonlinear term (see Section 3.3.2). First, the salinity is solved for via:

$$\mathcal{H}_{mn}^S \hat{S}_{mn}^t = - \sum_{i=1}^s \alpha_i \hat{S}_{mn}^{t-i\Delta t} - \Delta t \sum_{i=1}^s \beta_i \hat{N}_{mn}^{t-i\Delta t}, \quad (3.185)$$

where

$$\mathcal{H}_{mn}^S = \alpha_0 - \Delta t \left[ \frac{\partial^2}{\partial z^2} - 4\pi^2 \left( \frac{m^2}{\Gamma_x^2} + \frac{n^2}{\Gamma_y^2} \right) \right] \quad (3.186)$$

is the Helmholtz operator for the salinity. The boundary conditions used are:

$$S^t = 1 \quad \text{at } z = 0, \quad (3.187)$$

$$S^t = 0 \quad \text{at } z = h. \quad (3.188)$$

Once  $S^t$  is known, the pressure is solved for via:

$$\mathcal{H}_{mn}^p \hat{p}_{mn}^t = Ra \frac{\partial}{\partial z} \hat{S}_{mn}^t, \quad (3.189)$$

where

$$\mathcal{H}_{mn}^p = \frac{\partial^2}{\partial z^2} - 4\pi^2 \left( \frac{m^2}{\Gamma_x^2} + \frac{n^2}{\Gamma_y^2} \right) \quad (3.190)$$

is the Helmholtz operator for the pressure. The boundary conditions for the pressure are:

$$\frac{\partial p^t}{\partial z} = Ra + 1 \quad \text{at } z = 0, \quad (3.191)$$

$$\frac{\partial p^t}{\partial z} = -w^{t-\Delta t} - \langle -w^{t-\Delta t} \rangle + 1 \quad \text{at } z = h. \quad (3.192)$$

The physical fields  $S^t$  and  $p^t$  are recovered via the inverse Fourier transform for which then the velocity field is directly evaluated since it is given explicitly in terms of the pressure and the salinity:

$$\mathbf{u}^t = -\nabla p^t + Ra S^t \mathbf{e}_z. \quad (3.193)$$

## 3.7 Validation

To simulate dry lakes, the Rayleigh number,  $Ra$ , lake depth,  $h$ , and horizontal domain sizes,  $\Gamma_x$  and  $\Gamma_y$ , must be set at the start of the simulation. Along with these physical parameters, the parameters governing the temporal and spatial discretisations must be chosen. That is, the time step,  $\Delta t$ , and the number of mesh points in each direction:  $N_x$ ,  $N_y$ ,  $N_z$  and  $N_e$ . These parameters must be chosen to ensure sufficient accuracy for the simulation, ensure numerical stability of the time stepping scheme and to be not too small or too large that simulations are overly costly to run on the hardware available. This highlights the need for certain rules to be used to help design individual simulations. The choices used in subsequent simulations will be discussed here and justified by means of numerical validations.

### 3.7.1 Horizontal Directions

As the Rayleigh number is increased, smaller scale dynamics need to be resolved by simulating higher wavenumbers. Since the maximum wavenumbers modelled in the numerical simulations are directly related to the number of mesh points in the horizontal directions, there is a need to increase  $N_x$  and  $N_y$  as  $Ra$  is increased (and as the horizontal domain sizes  $\Gamma_x$  and  $\Gamma_y$  are increased). The number of mesh points is determined by aiming to model all wavenumbers up to the point when they have a relative power below a certain

threshold. Thus, a relation between the mesh density, defined as

$$\rho_x = \frac{N_x}{\Gamma_x}, \quad \rho_y = \frac{N_y}{\Gamma_y}, \quad (3.194)$$

and the Rayleigh number is sought. To do this, a criterion is constructed that determines the maximum wavenumber to model as a function of the energy in each wavenumber. Firstly, the energy contained in the wavenumber pair  $(k, l)$  at depth  $z$  and time  $t$  is defined as:

$$E(k, l, z, t) = |\mathcal{F}\{S\}(k, l)|^2, \quad (3.195)$$

where  $\mathcal{F}$  denotes the Fourier transform over the two horizontal directions. A wavenumber pair  $(k, l)$  is chosen to be ignored at time  $t$  if:

$$\frac{E(k, l, z, t)}{E(0, 0, z, t)} \leq 10^{-M} \quad \forall z \in [0, h], \quad (3.196)$$

where  $M \geq 0$  is the threshold number. This states that a wavenumber pair  $(k, l)$  should be ignored if its energy is less than  $10^M$  times smaller than the energy of the constant mode at that particular time. The energy of the constant mode is used to provide a reference energy (at each depth  $z$  and time  $t$ ) to compare all higher modes to. From this definition, it is anticipated that, for higher values of  $M$ , more mesh points are needed in the horizontal directions to model the increasingly higher wavenumbers. The threshold energy at depth  $z$  and time  $t$  is then defined to be

$$E_M(z, t) = 10^{-M} E(0, 0, z, t). \quad (3.197)$$

To determine  $N_x$  and  $N_y$ , the energy  $E(k, l, z, t)$  is saved at specified times. At all depths  $z$  and time  $t$ , the condition  $E(k, l, z, t) \geq E_M(z, t)$  is evaluated, which can be seen in Figure 3.7. The minimum distance from  $(0, 0)$  is then computed for which all wavenumber pairs  $(k, l)$  beyond this distance have energy less than the threshold energy. This distance is denoted by  $d(z, t)$  and is visualised by the white arcs in Figure 3.7. The number of mesh points required is then

$$N_M(z, t) = 2 \left\lceil \frac{3d(z, t)}{2} \right\rceil, \quad (3.198)$$

where the factor of 3 comes from the Fourier filter threshold frequency (resulting from a second-order nonlinearity) and the ceiling function ensures  $N_M$  is even (as required by the

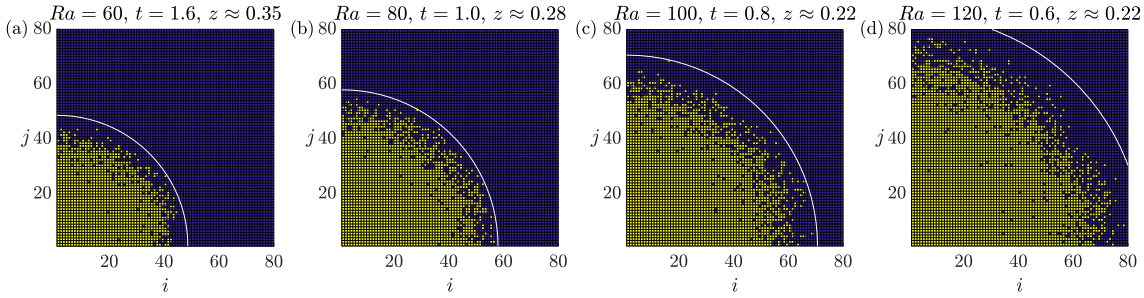


Figure 3.7: Example of the threshold criterion using  $M = 8$ . Yellow (resp. blue) pixels denote the integer wavenumber pairs  $(i, j)$  that have energy greater (resp. lower) than the threshold energy. The white arc shows the minimum distance  $d(z, t)$  for which all wavenumber pairs  $(k, l)$  outside this radius have energy less than the threshold energy.

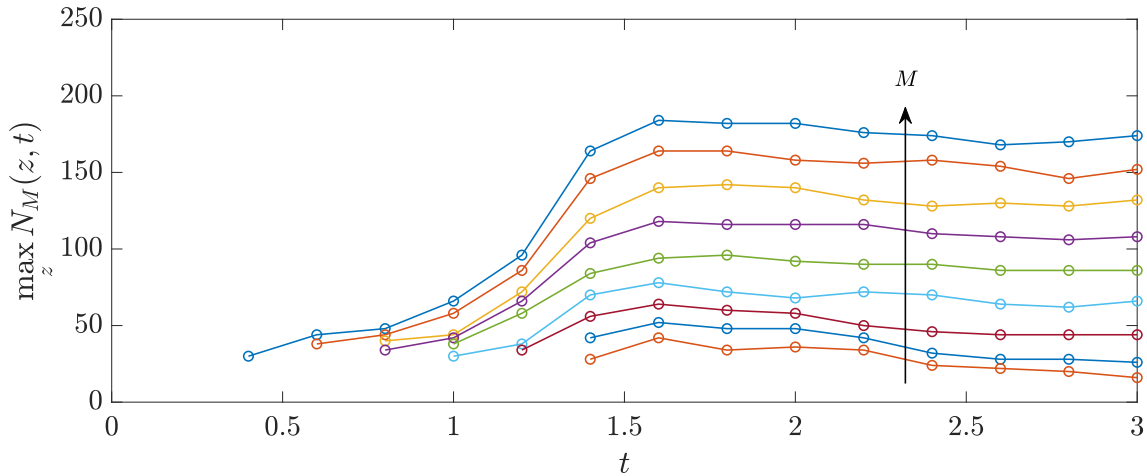


Figure 3.8: Maximum number of mesh points required as a function of time during a simulation with  $Ra = 60$  to ignore all wavenumbers of energy less than the threshold energy. Values of the threshold used are  $M = 2, \dots, 10$ .

Fourier mesh). The number of mesh points,  $N_M$ , is then maximised over  $z$  to determine the minimum number of mesh points needed at time  $t$  to satisfy the criterion (3.196). This can be seen in Figure 3.8 for various values of  $M$ . For example, it can be seen that the most demanding time at  $Ra = 60$  is at  $t = 1.6$ , needing  $N_x = N_y = 184$  mesh points in the horizontal directions to satisfy (3.196) with a threshold of  $M = 10$ . It can also be seen that for larger  $M$ , more mesh points are needed and simulations will have an increased accuracy. However, if more mesh points are used in simulations, the computational cost will be increased, so a balance between the accuracy of the solution and the time and resources used to obtain it needs to be found. Since the dynamics of the system are chaotic, it is difficult to reproduce a nonlinear solution using the same initial condition to a high accuracy. The value of  $M$  chosen is  $M = 6$ , which is conservative, but not overly so to not penalise speed. The final number of mesh points needed can be determined by finding the maximum needed over the times that have been plotted (see Figure 3.8). With

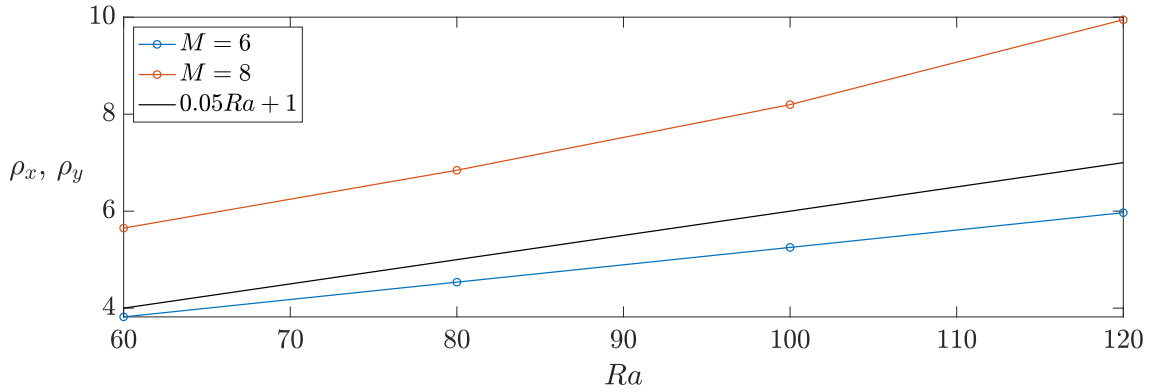


Figure 3.9: Required mesh density as a function of  $Ra$  using threshold values  $M = 6$  and  $M = 8$ . Linear fit (black line) to be used to determine mesh density in further simulations.

a threshold  $M = 6$ ,  $Ra = 60$  requires  $N_x = N_y = 96$  (at  $t = 1.8$ ) mesh points for a domain of size  $\Gamma_x = \Gamma_y = 8\pi$ , leading to a required mesh density of approximately  $\rho_x = \rho_y \approx 3.8$ . The most constraining value  $N_x = N_y = 96$  at  $t = 1.8$  was found to be close to the surface, at  $z \approx 0.35$ , which is due to the dynamics being driven by the surface boundary condition and any small-scale structures present near the boundary will diffuse as they descend downwards. Repeating this process over a range of Rayleigh numbers, a relation is obtained, which can be seen in Figure 3.9. For  $60 \leq Ra \leq 120$ , a linear fit is computed that ensures wavenumbers are kept that have energy above a threshold of  $M = 6$ . The mesh densities in the horizontal directions can then be computed as

$$\rho_x = \rho_y = 0.05Ra + 1. \quad (3.199)$$

### 3.7.2 Vertical Direction

The parameters for the vertical mesh must also be determined and two methods for doing this will be shown here. The first method matches the vertical mesh spacing to the horizontal mesh spacing. The second method uses a small nonlinear simulation that is converged to a steady-state and the error made compared to an over-resolved choice of mesh parameters is analysed.

As the horizontal mesh density has already been determined, the number of elements and the number of mesh points per element in the vertical direction could be chosen by matching the vertical mesh spacing to the horizontal mesh spacing. Since the Gauss–Lobatto–Legendre mesh has non-uniform mesh spacing, a choice must be made whether the horizontal mesh spacing is matched to the minimum, maximum or average mesh spacing in the vertical direction. Figure 3.10 shows how the maximum and minimum

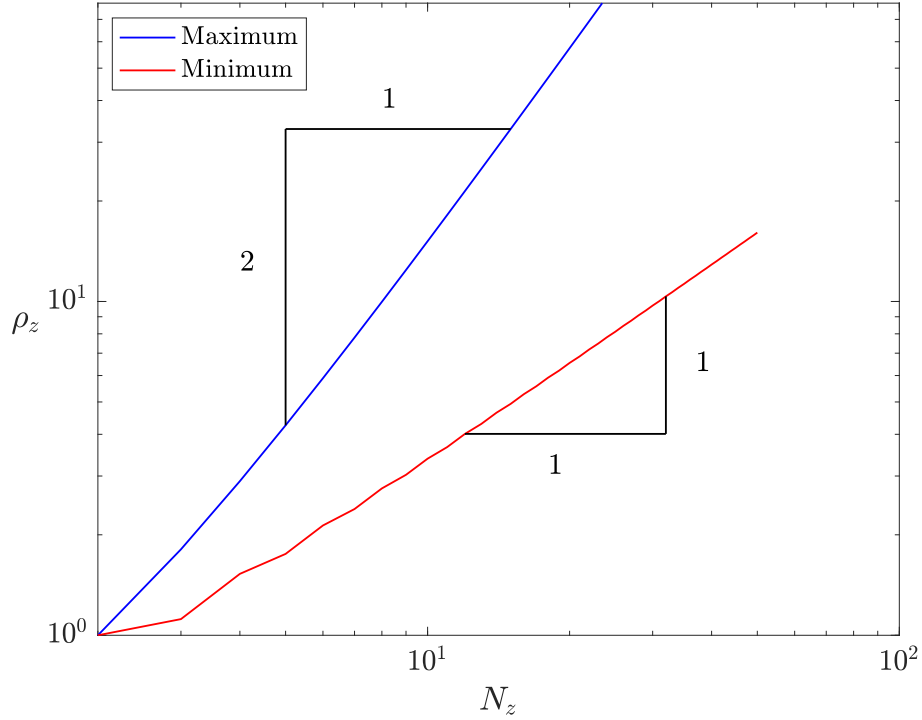


Figure 3.10: Maximum and minimum vertical mesh densities as a function of the number of mesh points in the vertical direction,  $N_z$ .

mesh densities scale with the number of points per element,  $N_z$ . On each element, the minimum mesh density occurs at the centre of each element where the mesh density scales linearly with the number of mesh points (see the red line in Figure 3.10):

$$\min \rho_z \sim \frac{N_e N_z}{h} \quad \text{as } N_z \rightarrow \infty. \quad (3.200)$$

The maximum mesh density occurs at the boundary of each element where the mesh density scales with the square of the number of points (see the blue line in Figure 3.10):

$$\max \rho_z \sim \frac{N_e N_z^2}{h} \quad \text{as } N_z \rightarrow \infty. \quad (3.201)$$

Finally, the average density is the total number of points used divided by the distance over which those points are distributed:

$$\langle \rho_z \rangle = \frac{N_e N_z}{h}, \quad (3.202)$$

which follows the same scaling as the minimum density. If the minimum vertical mesh density is matched to the horizontal mesh density,  $\min \rho_z \sim \rho_x$ , the number of mesh points

in the vertical direction would scale linearly with  $Ra$ :

$$N_z \sim Ra, \quad (3.203)$$

assuming the number of elements remains constant. This results in a large number of mesh points needed in the vertical direction, vastly increasing the computational cost. Instead, if the maximum mesh density is matched to the horizontal mesh density,  $\max \rho_z \sim \rho_x$ , the number of mesh points in the vertical direction will scale as

$$N_z \sim \sqrt{Ra}, \quad (3.204)$$

which is a weaker dependence on  $Ra$  than (3.203). Another consequence of matching the maximum mesh density in the vertical direction to the mesh density in the horizontal directions is that mesh cells will have an aspect ratio of one at the boundaries of the elements. Thus the vertical mesh spacing is equal to the horizontal mesh spacing at the surface, where it matters most, as the dynamics are driven by the surface boundary condition. The trade-off of sacrificing a higher mesh density in the centre of elements for decreased resource usage is acceptable due to the chaotic nature of the system. The mesh spacing  $\Delta z$  is then defined to be the minimum mesh spacing in the vertical direction:

$$\Delta z = \min_{k,l} \Delta z_{k,l} = \Delta z_{1,1}, \quad (3.205)$$

where  $\Delta z_{k,l} = |z_{k,l} - z_{k-1,l}|$  is the mesh spacing between the  $k^{th}$  and the  $(k-1)^{st}$  mesh point in the  $l^{th}$  element. Since the mesh spacing  $\Delta z$  is linear in  $h/N_e$  and is expected to scale with  $N_z^{-2}$  for large  $N_z$ , a scaling is sought:

$$\Delta z = a \frac{h}{N_e} N_z^b, \quad (3.206)$$

where  $a > 0$  and  $b$  are constants to be determined. It is expected that  $b$  will tend to 2 as  $N_z$  is increased, but is kept general here so it can be determined for the practical range of  $N_z$ . The constants  $a$  and  $b$  are determined numerically by calculating the minimum mesh spacing (3.205) for  $10 \leq N_z \leq 30$  and fitting a law of the form (3.206) using MATLAB's nonlinear least squares algorithm. Fitting this law gives  $a \approx 2.772$  and  $b \approx -1.923$ , but

are rounded to yield the approximation:

$$\Delta z \approx 3 \frac{h}{N_e} N_z^{-2}, \quad (3.207)$$

which approximately determines the minimum mesh spacing. If the horizontal mesh spacing is chosen to match the vertical, a relationship is obtained:

$$N_e N_z^2 = 3h(0.05Ra + 1), \quad (3.208)$$

which may be used to compute  $N_z$  and  $N_e$  for the given parameters  $Ra$  and  $h$ . For example, at  $Ra = 100$  and  $h = 10$ , if  $N_e = 5$  elements are used, each element would need  $N_z = 6$  to have the required mesh density.

The error made when using these parameters can be analysed by running two-dimensional simulations at  $Ra = 100$ ,  $h = 10$  for a fixed value of  $N_e$  and a range of  $N_z$ . These simulations are initialised with a perturbation that projects only onto the most unstable mode,  $k^*$ , of the base state using a domain size that exactly fits this mode:

$$S = S_b(z) + B \hat{S}(z) e^{ik^*x}, \quad (3.209)$$

where  $\hat{S}(z)$  is the eigenfunction of the most unstable wavenumber,  $B \ll 1$  and the horizontal domain size is  $\Gamma_x = 2\pi/k^*$ . This initial condition is simulated until a steady-state is reached, determined by

$$\left\langle \left[ \frac{1}{h} \int_0^h \left( \frac{\partial S}{\partial t} \right)^2 dz \right]^{1/2} \right\rangle_{xy} \leq 1 \times 10^{-6}. \quad (3.210)$$

Once this condition is met, the average salinity is computed:

$$\Sigma_{N_z} = \frac{1}{h} \left\langle \int_0^h S dz \right\rangle_{xy}, \quad (3.211)$$

where the subscript  $N_z$  denotes the number of mesh points per element used in the simulation. The relative error compared to the most resolved case,  $N_z = 30$ , is computed and shown for selected values of  $N_e$  in Figure 3.11(a). To obtain an error less than  $10^{-10}$ ,  $N_z = 19$  must be used for  $N_e = 5$ , a value larger than what was initially chosen by matching the vertical mesh spacing to the horizontal mesh spacing. Thus, determining the vertical mesh parameters will be done via this second method, as opposed to the first.

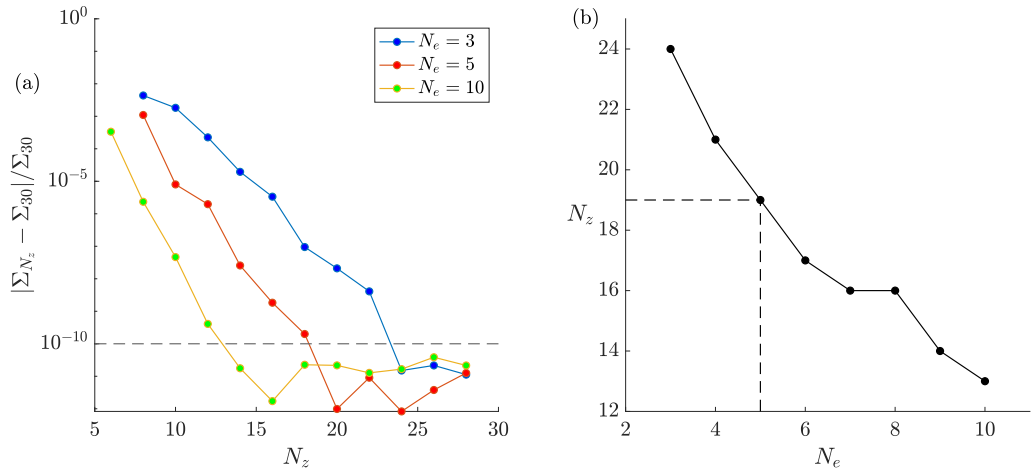


Figure 3.11: (a) Relative error in the average salinity against the most resolved case for  $N_e = 3, 5$  and  $10$  after the solution has converged to a steady-state (see (3.210)) for  $Ra = 100$  and  $h = 10$ . (b) The number of mesh points per element to be used is determined so that the relative error is less than  $10^{-10}$ .

Figure 3.11(b) shows the value of  $N_z$  as a function of  $N_e$ , determined to be the smallest value that obtains an error (shown in Figure 3.11(a)) of less than  $10^{-10}$  for the given value of  $N_e$ . Full nonlinear simulations (with a large number of time steps and fixed  $\Delta t$ ) are then run with these pairs to a given time and timed. The time that a simulation takes may depend on the architecture being used to run the simulation on since a machine with a larger number of computational cores will perform better in the routines that make use of parallelisation. Additionally, there will be fluctuations in the time each individual simulation takes due to the need to share memory across individual cores (which can behave differently depending on the total load over all the cores). Also, physical reasons such as temperature management of the cores being used may impact the time taken for a simulation. The quickest of these simulations then determines which pair is used and for the computational hardware used here (typically 8 or 16 cores),  $N_e = 5$  and  $N_z = 19$  is the fastest. Maintaining a scaling where  $N_z \sim \sqrt{Ra}$  (to keep the number of mesh points per element reasonably small for larger  $Ra$ ), the relationship is sought:

$$3 \frac{h}{N_e} N_z^{-2} = \frac{c}{Ra}, \quad (3.212)$$

where  $c = 2$  is determined by imposing the result that  $N_z = 19$ ,  $N_e = 5$  at  $Ra = 100$ ,  $h = 10$  is needed to obtain a satisfactory error. Using the condition (3.212) and choosing  $N_e = h/2$  so that  $N_e = 5$  for  $h = 10$ , the vertical mesh is determined for parameters  $Ra$  and  $h$  as follows:

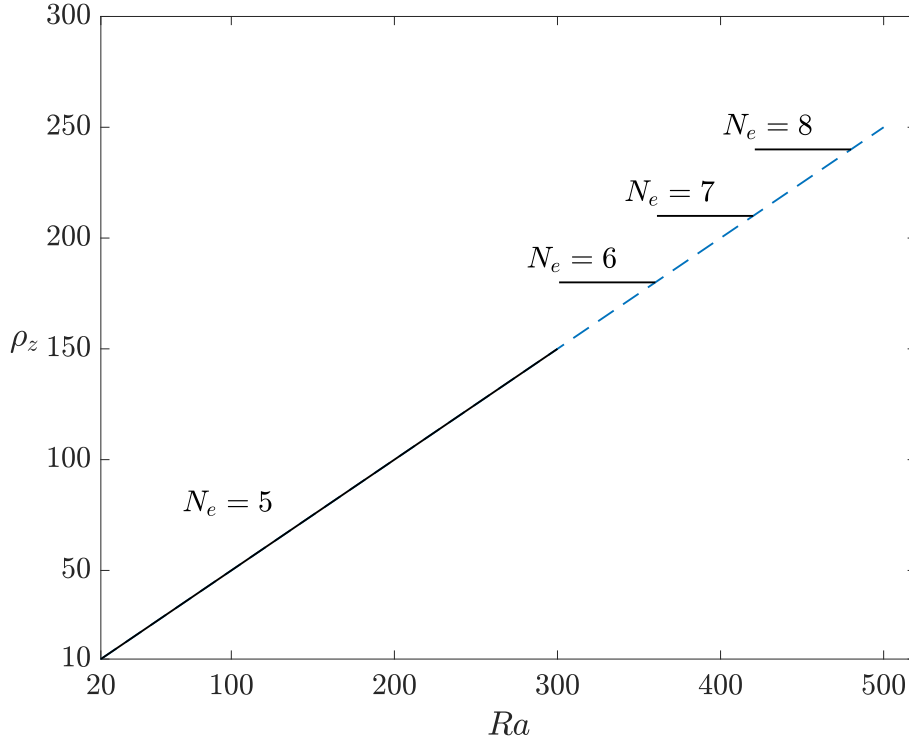


Figure 3.12: Vertical mesh density as a function of  $Ra$  for  $h = 10$ .

1. Compute

$$N_z = \lceil \sqrt{3Ra} \rceil. \quad (3.213)$$

2. If  $N_z > 30$ ,

$$N_z = 30, \quad N_e = \left\lceil \frac{3}{2} h Ra N_z^{-2} \right\rceil \quad (3.214)$$

Otherwise,

$$N_z = \lceil \sqrt{3Ra} \rceil, \quad N_e = \left\lceil \frac{h}{2} \right\rceil. \quad (3.215)$$

For  $20 \leq Ra \leq 500$ , the resulting mesh density from this algorithm is plotted in Figure 3.12, showing the discontinuity at  $Ra \approx 300$  when  $N_z$  exceeds 30 and more elements are preferable to more points per element. This is because if too many points per element are used, a similar problem to the one described previously is encountered, where large a difference in the mesh density at the boundaries and in the middle of the elements arises.

### 3.7.3 Time Step

To motivate the choice of the time step, the Courant–Friedrichs–Lewy condition (Courant et al., 1928) is used to provide an upper bound for the time step. The Courant number

in the  $i^{\text{th}}$  direction is defined as

$$C_i = \frac{U_i \Delta t}{\Delta x_i}, \quad (3.216)$$

where  $U_i = \max u_i$  is the maximum velocity in the  $i^{\text{th}}$  direction,  $\Delta t$  is the time step and  $\Delta x_i$  is the mesh spacing in the  $i^{\text{th}}$  direction. A choice must be made for the mesh spacing in the  $z$ -direction and the average spacing is used so that  $\Delta x_3 = h/N_z N_e$ . The total Courant number is then the sum:

$$C = \sum_{i=1}^3 C_i. \quad (3.217)$$

The Courant number in the vertical direction is used to determine an upper bound on the time step:

$$C_3 \leq \frac{1}{2}, \quad (3.218)$$

where the value of  $1/2$  is chosen so that  $C_3$  is certainly less than one, but is not too small that it imposes an unnecessarily small maximum allowed time step. Since the vertical velocity scales with  $Ra$ , the time step is chosen to satisfy

$$\Delta t \leq \frac{h}{2Ra N_z N_e}. \quad (3.219)$$

This choice aims to keep the time step small enough to avoid a scheme instability but large enough that simulations do not take an unreasonable amount of time. The  $1/Ra$  factor in (3.219) as well as the  $Ra$  dependence in both  $N_z$  and  $N_e$  mean that the time step has a strong dependence on  $Ra$ . This means that the range of  $Ra$  that can be simulated in a reasonable amount of time is smaller than what would be ideal. Nevertheless, using values such as  $Ra = 100$  produces interesting dynamics, which will further be discussed in Chapter 4.

The mesh studies presented in Section 3.7 were performed on an older version of the numerical code that is currently used. The changes that were made since the validations were performed focused on performance (Beaume, 2024) and should not affect the accuracy of the simulations that were used to determine the required mesh parameters and the time step. It is thus a reasonable assumption that the validations apply to the current version of the numerical code. However, the speed of the simulations will be significantly different, resulting in differing simulation times to those found in Section 3.7.2.



# Chapter 4

## Results

In this chapter, the dynamics of salt lakes will be discussed. Starting in Section 4.1, a brief overview of the dynamics will be presented, both in two and three dimensions. The two-dimensional dynamics (also see Lasser et al. (2021)) illustrate the formation of high-salinity plumes and are included to complement the description of the three-dimensional dynamics. In Section 4.2, the results from the linear stability analysis will be presented, which describe the initial growth of plumes from the high salinity boundary layer. This is done by considering one horizontal direction only, as it directly applies to the linear stability analysis for the full three-dimensional system. Then, in Section 4.3 and Section 4.4, the first nonlinear effects will be discussed as the linear instability saturates. The dynamics from three-dimensional simulations for  $Ra = 100$  and  $h = 10$  will be presented and the additional features that the extra dimension introduces will be discussed. Then, in Section 4.5, the dependence on the depth and Rayleigh number will be explored. Finally, in Section 4.6, these results will be compared to field observations taken from Badwater Basin, Owens Lake and Sua Pan.

### 4.1 Overview of Dynamics

Previous simulations of dry salt lakes have largely been restricted to two dimensions (Lasser, 2019; Lasser et al., 2021). These simulations capture the convective dynamics resulting from the unstable density gradient and can predict the wavelength of the surface pattern arising on the (one-dimensional) surface of the domain. However, the surface pattern observed at dry lakes is inherently two-dimensional, which can only be simulated if the domain is three-dimensional. Nevertheless, two-dimensional simulations provide a

strong starting point before the full three-dimensional simulations are analysed.

Starting from the base state, a random perturbation is added:

$$S = S_b(z) + B\theta(x, y, z)\mathcal{E}(z), \quad (4.1)$$

where  $S_b(z)$  is the base state salinity:

$$S_b(z) = \frac{\exp(-z) - \exp(-h)}{1 - \exp(-h)}, \quad (4.2)$$

$B \ll 1$  (typically  $B = 10^{-4}$ ),  $\theta(x, y, z)$  is a random number drawn from a uniform distribution on  $[-1, 1]$  and  $\mathcal{E}(z)$  is a vertical profile chosen so that the perturbation to the base state decays faster than the base state itself. For the following simulations presented in this chapter, the vertical profile is chosen to be:

$$\mathcal{E}(z) = \mathcal{E}_1(z) = \exp(-z^2), \quad (4.3)$$

but an alternate profile is discussed in Section 4.2.2.

To understand how the subsurface fluid dynamics of dry salt lakes influences the surface pattern, the salinity flux to the surface is tracked, defined by:

$$\begin{aligned} J &= -\mathbf{e}_z \cdot (S\mathbf{u} - \nabla S)|_{z=0} \\ &= 1 + \left. \frac{\partial S}{\partial z} \right|_{z=0}. \end{aligned} \quad (4.4)$$

The orientation of the surface flux is chosen so that positive values of  $J$  correspond to salinity transport upward and into the surface (hence driving the growth of a crust) and negative values denote salinity transport away from the surface. The advective component of the salinity flux is constant and positive due to the boundary condition, whereas its diffusive counterpart is always negative, as the salinity must decrease away from its surface value. Figure 4.1 and Figure 4.2 show snapshots of an illustrative two-dimensional simulation at  $Ra = 100$  and  $h = 10$ . The surface flux of salinity is plotted above each salinity field, displaying the horizontal variation in the salinity transport to the surface. Figure 4.1(a) displays the system at the end of the linear regime, where downwelling plumes start to become visible. The downwelling plumes continue to grow, seen in Figure 4.1(b) and begin to move laterally while falling and potentially merging with neighbouring

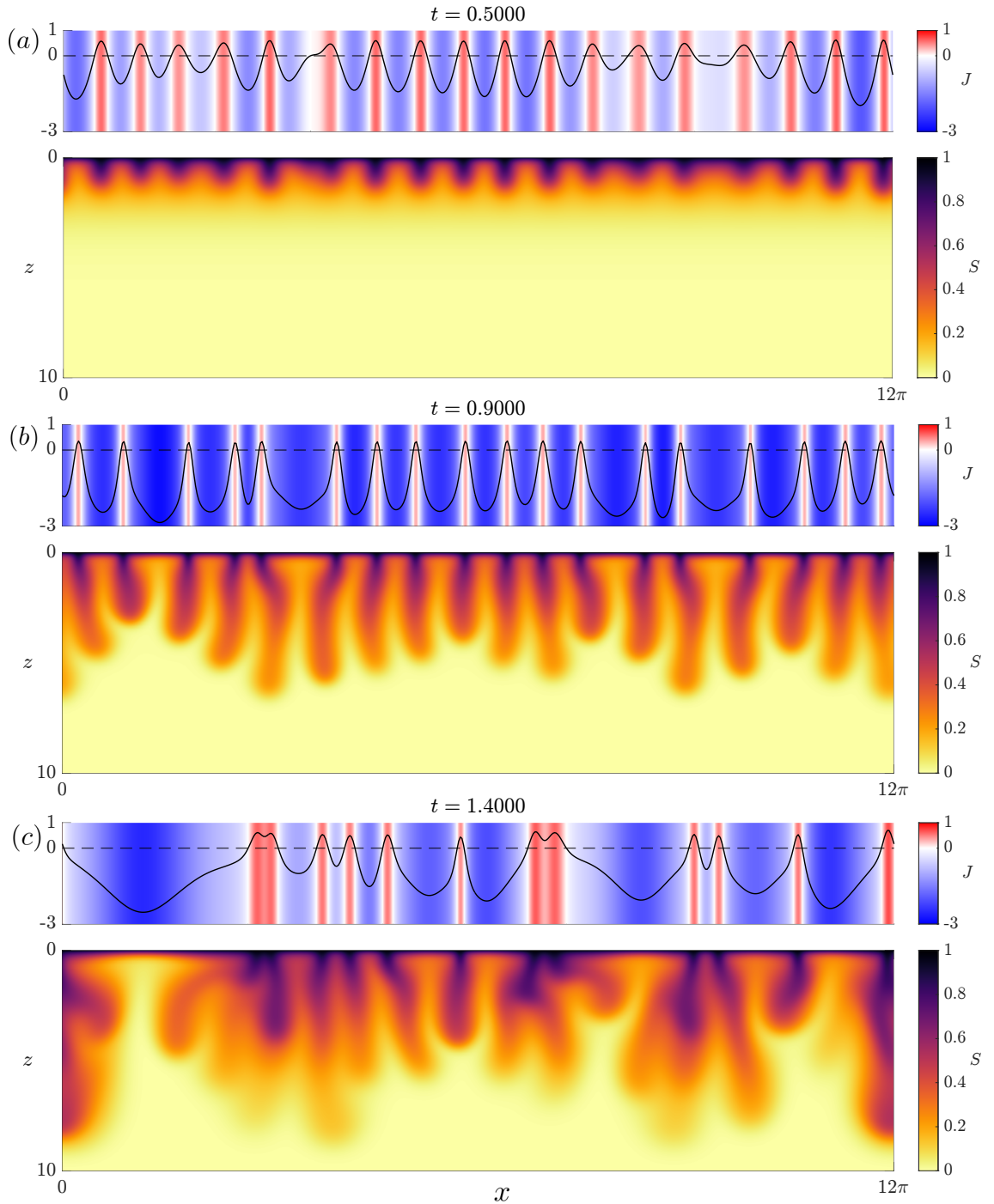


Figure 4.1: Snapshots at (a)  $t = 0.5$ , (b)  $t = 0.9$  and (c)  $t = 1.4$  of a two-dimensional dry lake simulation. The surface flux (positive flux to the surface in red, negative flux away from the surface in blue) is plotted above the salinity field to provide a visual representation of the magnitude of the flux. Local maxima of the surface flux correspond to regions of downwelling fluid while negative surface fluxes correspond to regions of upwelling fluid. Other parameters are  $Ra = 100$ ,  $h = 10$  and  $\Gamma_x = 12\pi$ .

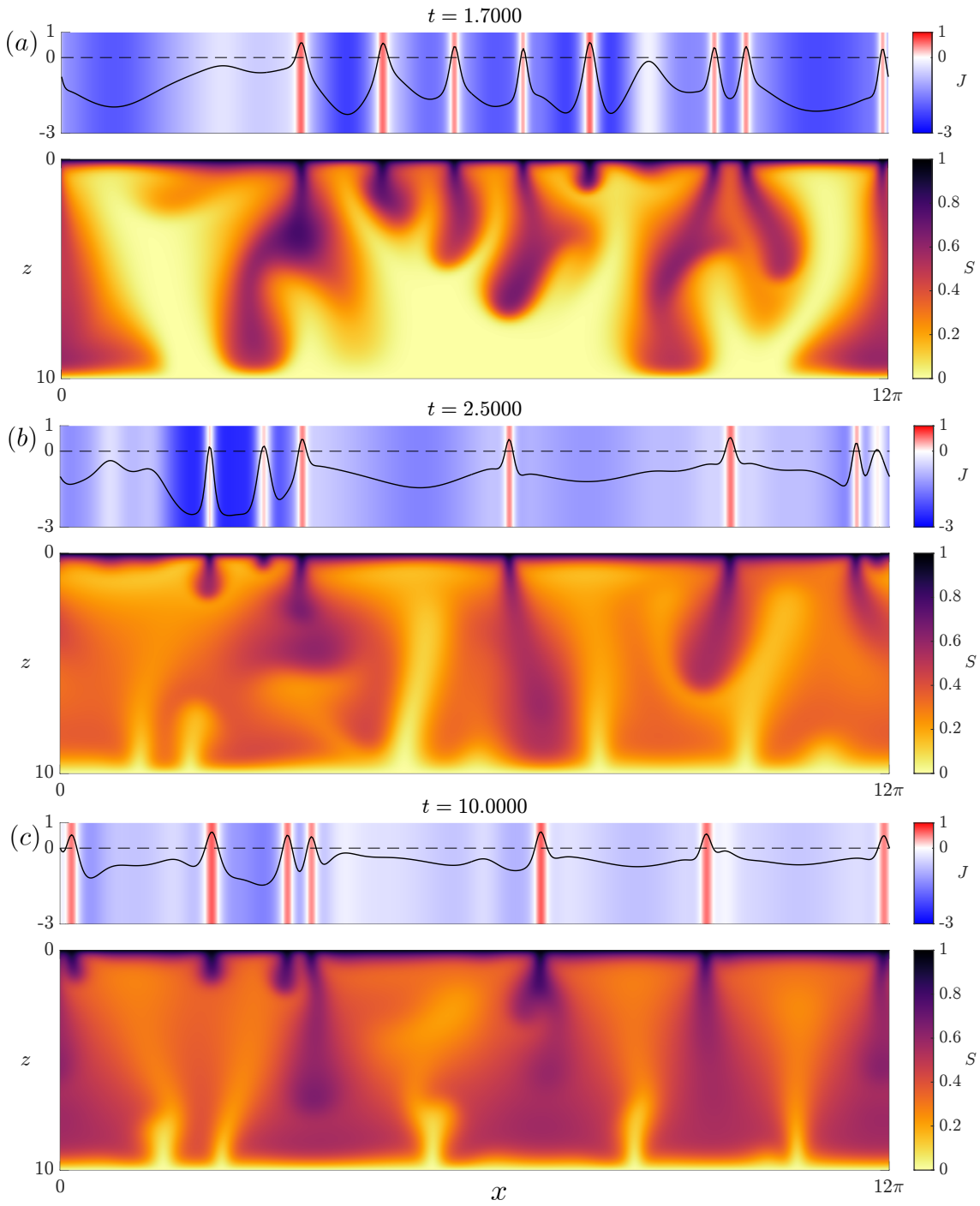


Figure 4.2: Continuation of Figure 4.1, with snapshots at (a)  $t = 1.7$ , (b)  $t = 2.5$  and (c)  $t = 10$ .

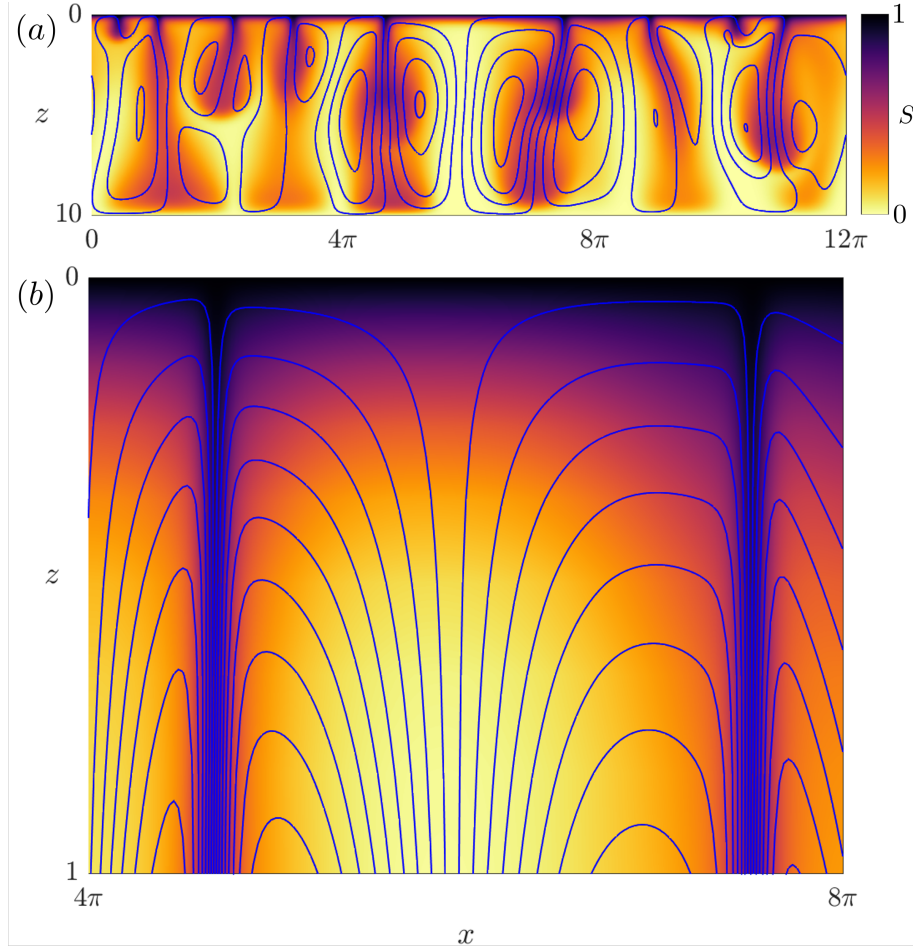


Figure 4.3: Streamlines at  $t = 1.5$  illustrating the two-dimensional flow over the whole domain (panel (a)) and the region  $4\pi \leq x \leq 8\pi$ ,  $0 \leq z \leq 1$  (panel (b)). Other parameters are  $Ra = 100$ ,  $h = 10$  and  $\Gamma_x = 12\pi$ .

plumes, as seen in Figure 4.1(c). When the plumes reach the bottom, as seen in Figure 4.2(a), fluid leaving the domain initiates upwelling plumes from the bottom boundary (to maintain  $\langle w \rangle_{xy} = -1$ ), which rise upwards, shown by Figure 4.2(b). From this point onwards, the system begins to transition to a statistically steady end-state, shown by Figure 4.2(c). In addition, Figure 4.3 displays streamlines indicating the direction of fluid flow for a two-dimensional simulation. Figure 4.3(a) displays the streamlines for the whole domain, illustrating the large-scale convective rolls of rising upwellings and descending downwellings. On the other hand, Figure 4.3(b) shows the streamlines in a region close to the boundary ( $z \leq 1$ ). This shows that the induced buoyancy velocities are far more prominent than those caused by evaporation: the streamlines within the salinity boundary layer are primarily horizontal, showing that the horizontal velocity driven by convection outweighs the upward flow induced by evaporation.

Simulating dry salt lakes in three dimensions results in the surface being two-dimensional,

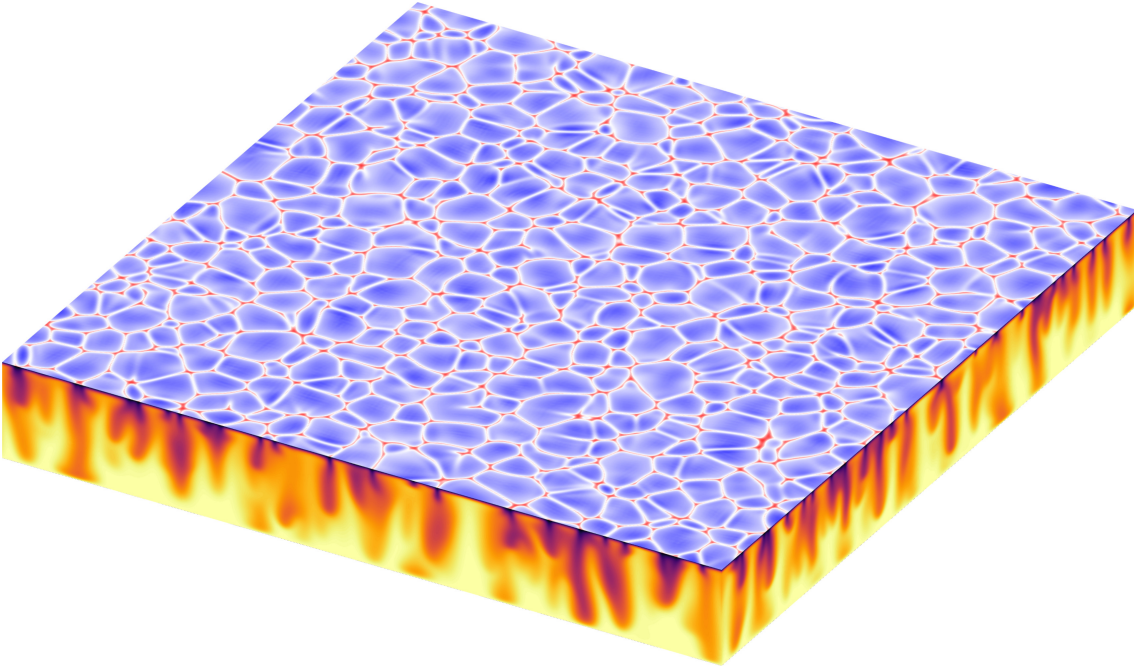


Figure 4.4: Snapshot of a three-dimensional dry lake simulation at  $t = 1.3$ . The top face displays the surface flux (positive flux in red, negative flux in blue) and the side faces display the salinity field (darker colours correspond to saltier fluid). Other parameters are  $Ra = 100$ ,  $h = 10$  and  $\Gamma_x = \Gamma_y = 24\pi$ .

allowing more complex patterns to develop in the surface flux of salinity. Figure 4.4 shows a snapshot of a three-dimensional dry lake simulation, displaying the surface flux on the top face and the salinity field on the side faces. Similar to the two-dimensional simulation, Figure 4.4 displays the surface flux taking positive values above downwelling regions of fluid and negative values above upwelling regions. Figure 4.5 shows the pattern in the surface flux at four representative times during a typical simulation with  $Ra = 100$ ,  $h = 10$  and  $\Gamma_x = \Gamma_y = 12\pi$ . The nature of the two-dimensional patterns occurring on the surface of three-dimensional dry lake simulations transitions through various stages. The linear instability gives rise to small regions of weakly positive and negative salinity flux into the surface (see Figure 4.5(a)). The surface flux initially takes values that are approximately distributed symmetrically around the base state but, as nonlinear terms enter the dominant balance, the growth of the small-wavelength pattern produced by the linear instability slows down and the surface flux pattern becomes biased: regions of negative salinity flux dominate over those of positive flux (see Figure 4.5(b)). As downwelling plumes merge, the pattern coarsens, seen by the increase in the size of the areas of negative flux in Figure 4.5(c) and Figure 4.5(d).

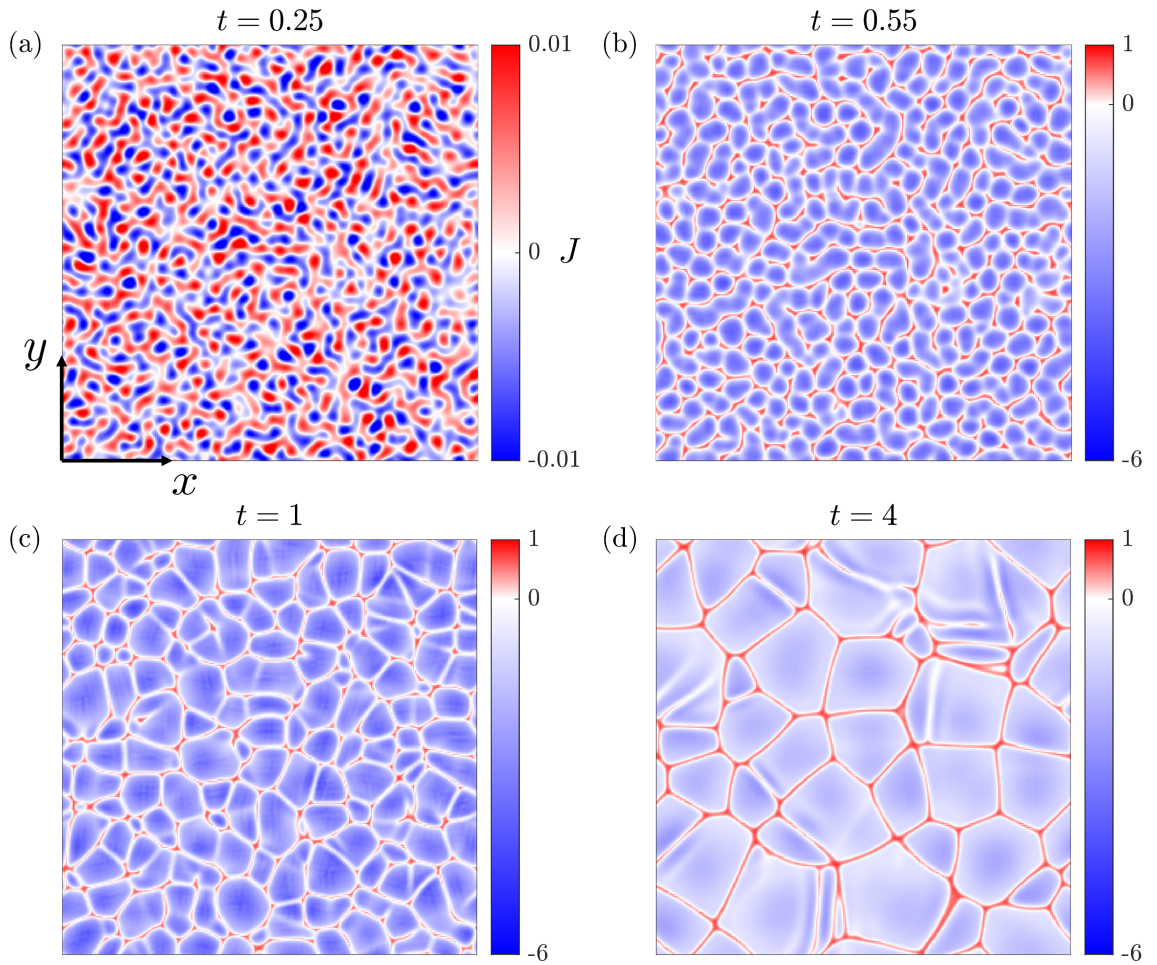


Figure 4.5: Snapshots of the surface salinity flux  $J$  at different times  $t$  for a representative simulation with  $Ra = 100$ , on a domain of depth  $h = 10$  and of horizontal size  $12\pi \times 12\pi$ .

## 4.2 Linear Stability

In Chapter 2, the coupled linear equations were obtained:

$$\frac{d^2 \hat{S}}{dz^2} - k^2 \hat{S} + \frac{d\hat{S}}{dz} + \frac{e^{-z}}{1 - e^{-h}} \left( Ra \hat{S} - \frac{d\hat{p}}{dz} \right) = \sigma \hat{S}, \quad (4.5)$$

$$\frac{d^2 \hat{p}}{dz^2} - k^2 \hat{p} = Ra \frac{d\hat{S}}{dz}. \quad (4.6)$$

These equations govern the eigenfunctions  $\hat{S}(z)$  and  $\hat{p}(z)$  along with their corresponding growth rate  $\sigma \in \mathbb{C}$  for a perturbation with wavenumber  $k$  and Rayleigh number  $Ra$ . When this system is solved numerically,  $N$  solutions are found, where  $N$  is the number of collocation points used in the Chebyshev discretisation. Amongst these solutions, the one of most interest is that which has the largest growth rate,  $\lambda = Re(\sigma)$ , (the real part of the eigenvalue  $\sigma$ ) since this mode dictates the dominant behaviour of the system and will trigger any instability first. The system is solved for each pair  $(k, Ra)$  and the growth rate is saved to generate a two-dimensional field  $\lambda(k, Ra)$ , which can be seen in Figure 4.6. For each wavenumber  $k$ , there is a value of the Rayleigh number,  $Ra_n$ , such that for  $Ra < Ra_n$ , the growth rate is negative and perturbations with this wavenumber decay. For  $Ra > Ra_n$ , the growth rate is positive and perturbations with this wavenumber grow. The boundary,  $Ra_n(k)$ , is the neutral stability curve where the growth rate is zero. The smallest value of  $Ra_n$  is denoted by  $Ra_c$ , the critical Rayleigh number, the minimum value of the Rayleigh number that an instability may occur. The value of the wavenumber that the critical Rayleigh number occurs at is denoted by  $k = k_c$ , the critical wavenumber. For  $h = 10$ , the critical values are  $k_c \approx 0.7590$  and  $Ra_c \approx 14.3518$ . For  $Ra < Ra_c$ , the system is stable and a linear instability is never observed. For  $Ra > Ra_c$ , there is a band of wavenumbers for which the growth rate is positive and the wavenumber at which the maximum growth rate is located at is the most unstable mode, denoted as  $k^*$ . Figure 4.7(a) shows the growth rates for the band of unstable wavenumbers at various choices of the Rayleigh number. As  $Ra$  is increased,  $k^*$  increases, leading to the emergence of finer structures during this instability. The growth rate associated with  $k^*$  also increases, resulting in faster dynamics for higher values of  $Ra$ . The eigenfunction corresponding to the most unstable wavenumber is shown in Figure 4.7(b). These eigenfunctions take their maximum value of 1 close to the surface and the location of the maximum becomes progressively closer to the surface as  $Ra$  is increased. The eigenfunctions also decay rapidly with depth, demonstrating that the instability is most prominent near the surface

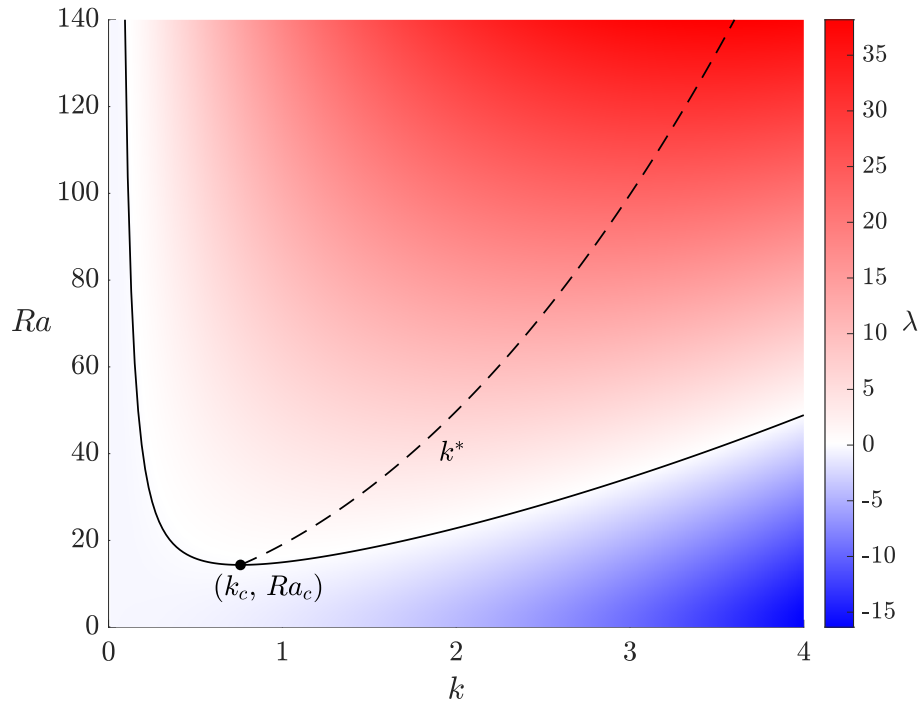


Figure 4.6: Growth rate  $\lambda$  at wavenumber  $k$  and Rayleigh number  $Ra$  for  $h = 10$ . The solid black line is the neutral stability curve,  $Ra_n(k)$ , denoting the modes that have a zero growth rate ( $\lambda = 0$ ). Stable modes ( $\lambda < 0$ ) lie beneath the neutral stability curve, shown in blue while unstable modes ( $\lambda > 0$ ) lie above the neutral stability curve, shown in red. The critical Rayleigh number,  $Ra_c \approx 14.3518$  denotes the minimum value of the Rayleigh number that an instability may be observed, occurring at the critical wavenumber,  $k_c \approx 0.7590$ . The black dashed denotes the most unstable mode,  $k^*$ , for each Rayleigh number above the critical point.

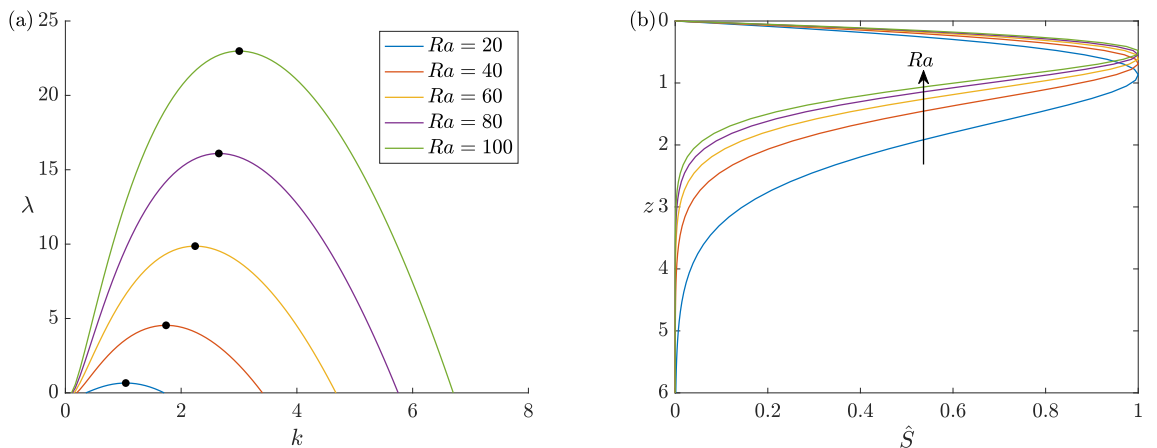


Figure 4.7: (a) Growth rates  $\lambda$  as a function of the wavenumber  $k$  for several values of  $Ra$  and  $h = 10$ . The black circles denote the most unstable wavenumber,  $k^*$ , occurring at the maximum of the curves. (b) Most unstable eigenfunctions for  $h = 10$ . Eigenfunctions take their maximum value close to the surface and decay rapidly with depth. As  $Ra$  is increased, the maximum value becomes closer to the surface.

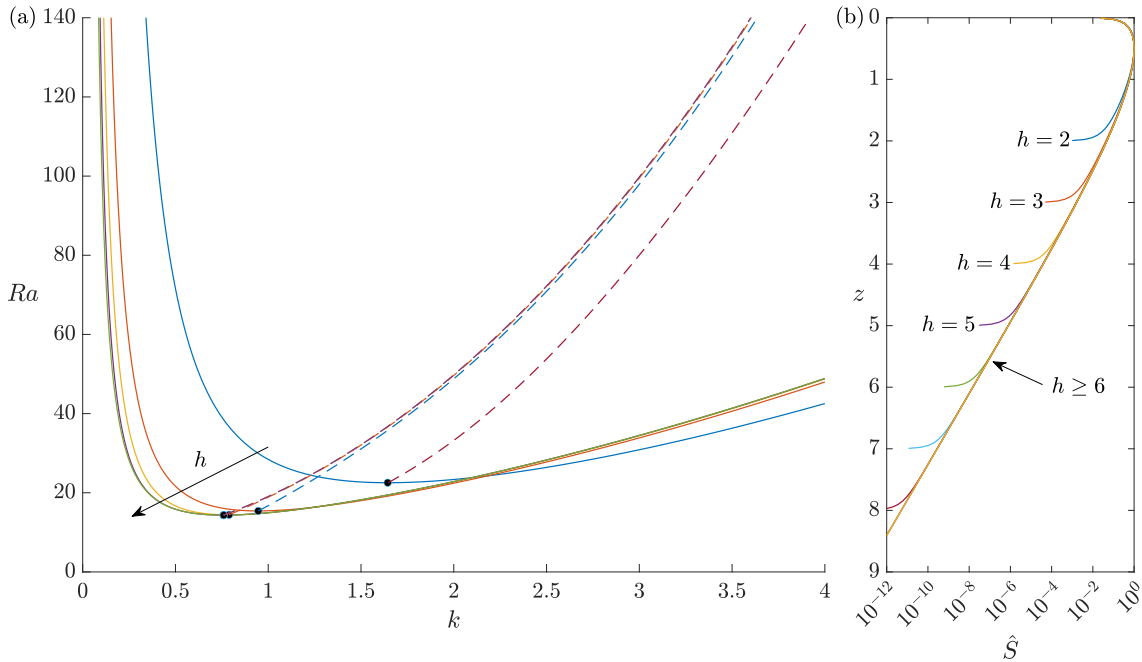


Figure 4.8: (a): Neutral stability curves (solid lines) and most destabilising eigenmode (dashed lines) for  $h = 2$ ,  $h = 4$ ,  $h = 6$ ,  $h = 10$  and  $h = 20$ . Stable eigenmodes lie below the neutral stability curves, and unstable modes lie above them. (b): Most unstable eigenmodes at  $Ra = 100$  for several values of  $h$ .

and instabilities will arise in the solutal boundary layer.

Lasser et al. (2021) and Wooding (1960) approached the linear stability analysis with an infinite lake depth and the latter study also focused on the special case of neutral stability ( $\lambda = 0$ ). In this limit, the eigenfunctions may be expanded in terms of four hypergeometric functions (Lasser et al., 2021). To investigate the effect of the finite depth, the eigenvalue problem is solved for various values of  $h$  and the neutral stability curves and the wavenumber of the most unstable modes are plotted in Figure 4.8(a). The critical Rayleigh number decreases as  $h$  is increased, resulting in a less stable system due to the reduced spatial constraint imposed by the bottom boundary. In addition, the critical wavenumber and the wavenumber of the most unstable mode (for a given  $Ra$ ) are smaller for these deeper lakes. The most destabilising eigenmodes for  $Ra = 100$  and a variety of domain depths  $h$  are represented in Figure 4.8(b). This shows that the most unstable eigenmodes decay nearly exponentially away from the surface and only differ from each other near the bottom of the domain where the eigenfunctions depart from their bulk behaviour to match the boundary condition. Figure 4.9 shows the relative error between the critical values and the infinite depth case, for which the critical values are  $k_c^\infty \approx 0.758867$ ,  $Ra_c^\infty \approx 14.35219121494$  (Lasser et al., 2021). The error for  $Ra_c$  levels off around  $10^{-12}$ , reflecting the precision with which the critical values for an infinitely

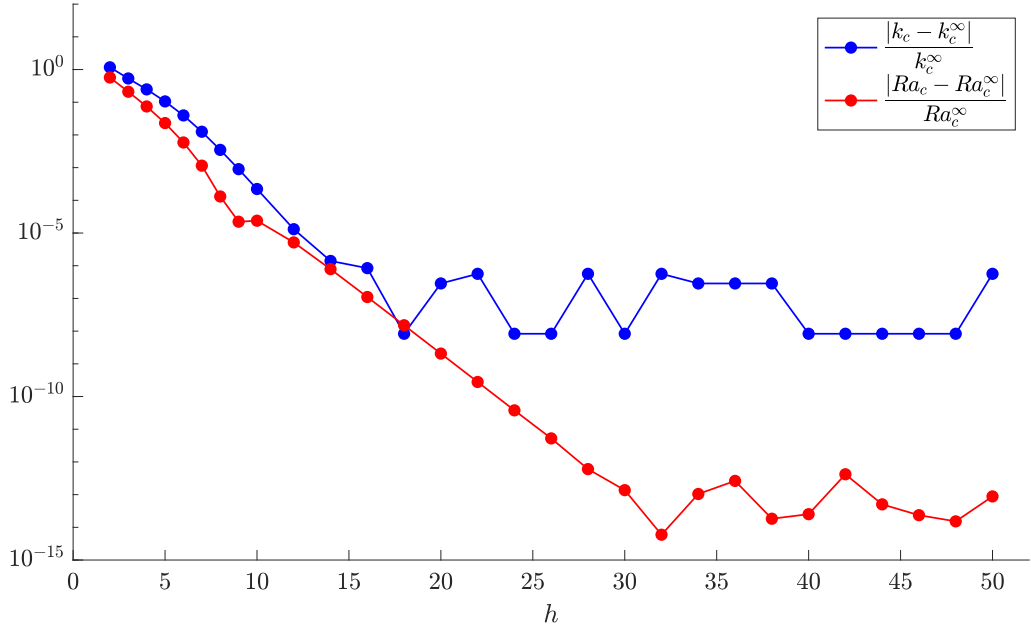


Figure 4.9: Relative error between the critical values and the infinite depth case as the domain thickness is increased. The infinite lake values were obtained from Lasser et al. (2021).

deep lake have been calculated (which is larger than machine precision). The error for  $k_c$  is larger, saturating at around  $10^{-6}$ , owing to the quadratic behaviour of the neutral stability curve in the vicinity of the critical point. Observing the same results as Lasser et al. (2021) and in particular, the convergence of these results to the infinite depth case, provides validation for the model used.

#### 4.2.1 Linear Regime

The random component in the initial condition (4.1) results in a numerical transient before the system exhibits the characteristic exponential growth associated with the linear instability. To illustrate the exponential growth away from the base state, the departure from the base state is computed, given by:

$$A = \frac{1}{\Gamma_x \Gamma_y h} \int_0^{\Gamma_x} \int_0^{\Gamma_y} \int_0^h |S - S_b| dx dy dz. \quad (4.7)$$

This quantity is plotted in Figure 4.10(a). Since a small perturbation is added to the base state,  $A$  is initially nonzero but small and the initial decrease in  $A$  is due to the stable modes from the random perturbation decaying at a faster rate than the unstable modes. Once the stable modes have decayed, the unstable modes have a stronger contribution to  $A$ , and the characteristic exponential growth can be seen, shown by the approximately linear relation  $\log A \sim t$  for times  $t \lesssim 0.4$  displayed in Figure 4.10(a). The gradient of

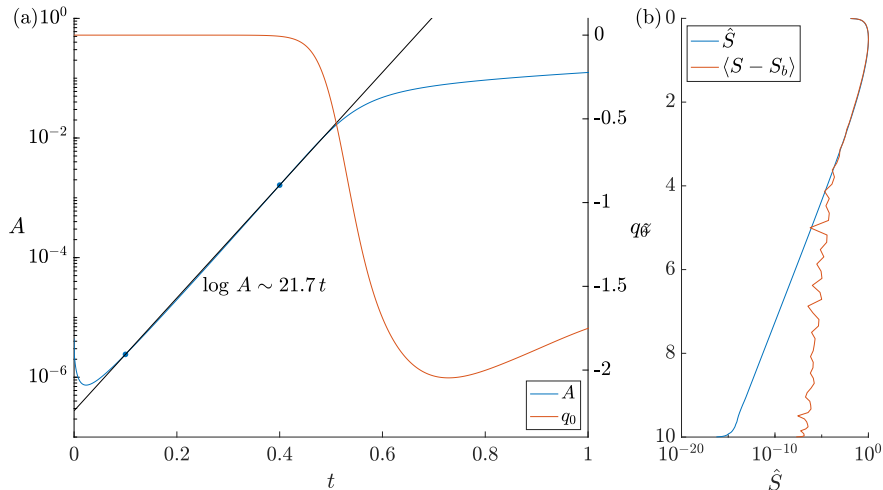


Figure 4.10: (a) Departure from the base state,  $A$  and the average flux of salinity to the surface,  $q_0$ , for  $Ra = 100$  and  $h = 10$ . The departure from the base state grows approximately linearly,  $\log A \sim 21.7t$ , for times  $0.1 \lesssim t \lesssim 0.4$ . This differs from the value predicted by the linear stability analysis by 5%. (b) Most unstable eigenfunction for  $Ra = 100$  and  $h = 10$  and the horizontal average of the salinity at  $t = 0.3$  with the base state subtracted.

this line is approximately 21.7173, which has a percentage error of 5% compared to value predicted by the linear instability of 22.9793. Figure 4.10(a) also shows the average salinity flux to the surface, defined by:

$$q_0 = \langle J \rangle_{xy}. \quad (4.8)$$

As the instability grows, small-amplitude patterns in the surface flux emerge (seen in Figure 4.5(a)). These do not have an impact on the average surface flux because the horizontal average of the perturbation is zero. Thus, the average surface flux remains unchanged:

$$q_0 = q_b \approx 0, \quad (4.9)$$

where

$$q_b = -\frac{e^{-h}}{1 - e^{-h}} \quad (4.10)$$

is the average salinity flux to the surface associated with the base state. Figure 4.10(b) shows the most unstable eigenfunction for  $Ra = 100$  and  $h = 10$  along with the horizontal average of the salinity at  $t = 0.3$  with the base state subtracted. This indicates that the departure of the salinity from the base state closely matches the most unstable eigenfunction at shallow depths.

Mode selection during the linear phase of the instability can be visualised via the nor-

malised power spectrum of the surface flux,  $P(k)$ , where  $k = (k_x^2 + k_y^2)^{1/2}$  is now generalised as the radial wavenumber. The power spectrum of the surface flux is computed first in terms of the two horizontal wavenumbers:

$$\hat{P}(k_x, k_y) = |\hat{J}(k_x, k_y)|^2, \quad (4.11)$$

where  $\hat{J}$  is the Fourier transform of the surface flux. This field is then radially averaged using a binning process, dividing the plane of wavenumber pairs into annuli of a given thickness and averaging the values of the power that fall into each annulus. The thickness of each annulus is defined to be

$$\delta k = \frac{k_{\max}}{m}, \quad (4.12)$$

where  $k_{\max}$  is the maximum value of  $k = (k_x^2 + k_y^2)^{1/2}$  over the horizontal mesh and  $m$  is the number of bins in the radial direction. This thickness is constant for each annulus and the radial discretisation is constructed so that:

$$k_l = l\delta k - \frac{\delta k}{2}, \quad l = 1, \dots, m. \quad (4.13)$$

The wavenumber pairs  $(k_{x;i}, k_{y;j})$  are divided into the  $m$  bins by assigning its bin index,  $M_{ij}$ , which is chosen to be index  $l$  of the closest wavenumber given by (4.13):

$$M_{ij} = \arg \min_l \left| k_l - \sqrt{k_{x;i}^2 + k_{y;j}^2} \right|. \quad (4.14)$$

The values of the power are then summed for each bin, and then divided by the area of the associated annulus, giving the radially averaged power spectrum:

$$P(k_l) = P_l = \frac{\frac{1}{2} \sum \hat{P}_{ij}}{\pi (r_{\max}^2 - r_{\min}^2)}, \quad l = 1, \dots, m, \quad (4.15)$$

where  $r_{\min}$  and  $r_{\max}$  are the minimum and maximum radius of the associated annulus and the sum is over the pairs  $(i, j)$  such that  $M_{ij} = l$ . The radially averaged power spectrum is shown in Figure 4.11 for the same simulation as in Figure 4.5. The random initial perturbation projects energy onto a large range of  $k$  but, as the linear stage of the instability progresses, the relative energy of the pattern is redistributed onto the wavenumbers associated with the most destabilising modes. This is evidenced in Figure 4.11 by the progressive focusing of the power spectrum towards the region  $2 \lesssim k \lesssim 4.5$ , until  $t \approx 0.4$ . The power spectrum can be further characterised by the wavenumber that

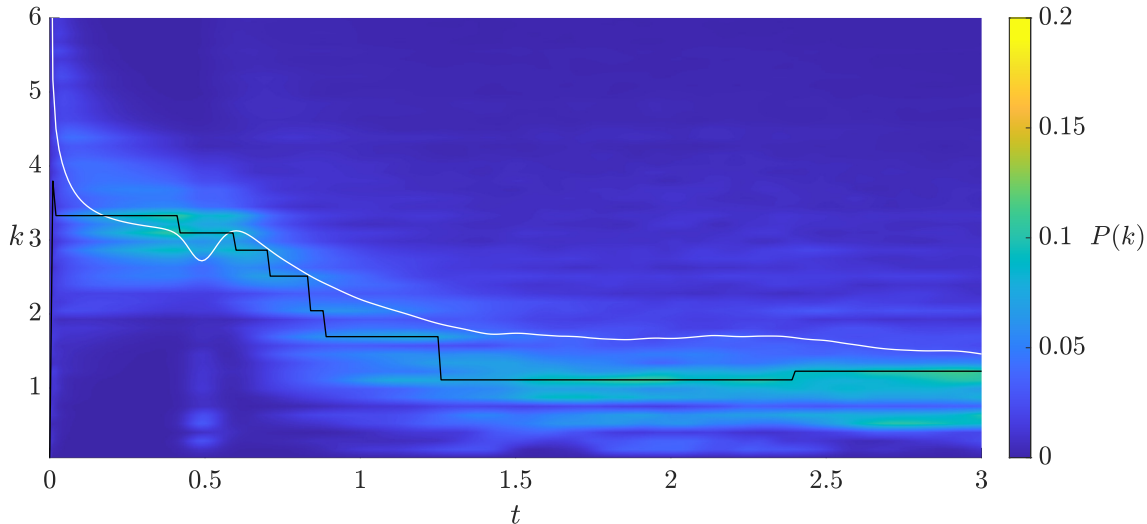


Figure 4.11: Wavelength selection for the simulation and patterns presented in Figure 4.5. The normalised radial power spectrum of the salinity flux to the surface  $P(k)$  is shown in colour as a function of wavenumber  $k$  and time  $t$ , along with the average wavenumber  $\bar{k}$  (white) and dominant wavenumber  $k_M$  (black). The value of the average wavenumber converges to  $\bar{k} \approx 3.1011$ , which differs by approximately 3% from the wavenumber of the most unstable mode predicted by the linear stability analysis. The dominant wavenumber,  $k_M \approx 3.3293$ , differs by approximately 11%.

contains the highest spectral power,  $k_M$ , and the average wavenumber (Hewitt et al., 2014):

$$\bar{k} = \frac{\int kP(k) dk}{\int P(k) dk}. \quad (4.16)$$

In the case shown in Figure 4.11, during the growth of the linear instability, the average wavenumber converges to  $\bar{k} \approx 3.1011$ . This value differs by approximately 3% from the wavenumber of the most unstable mode predicted by the linear stability analysis,  $k^* \approx 3.0043$ . On the other hand, the dominant wavenumber is  $k_M \approx 3.3293$  which differs by approximately 11%.

#### 4.2.2 Alternative Perturbation

Rather than perturbing the system using the vertical profile given by (4.3), the most unstable eigenfunction may be used to design the perturbation in such a way as to trigger the instability more naturally. As previously shown, the most unstable eigenfunction has a maximum value of 1 close to the surface and beyond this depth, the decay is approximately exponential:

$$\hat{S} \sim \exp(-mz). \quad (4.17)$$

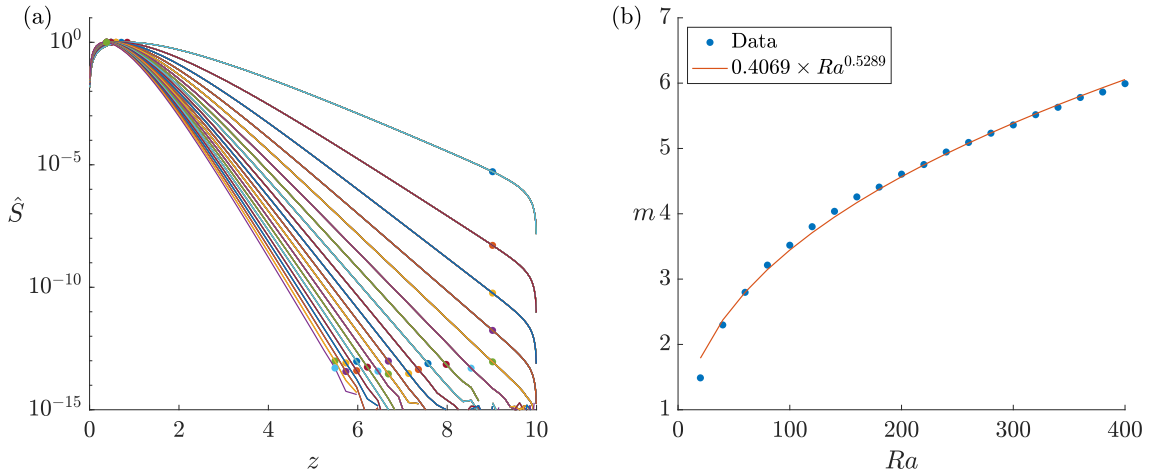


Figure 4.12: Linear fit to the most unstable eigenfunction. (a) Most unstable eigenfunctions for  $Ra = 20, 40, \dots, 400$ . Points marked on each eigenfunction indicate the location where a linear fit is computed. (b) Gradient of the straight line computed along with a power law fitted to the data.

Figure 4.12(a) shows the most unstable eigenfunctions for various values of  $Ra$  on a logarithmic scale, which shows the approximate exponential behaviour for depths  $z \gtrsim 2$ . The gradient of these curves may be approximated by a straight line drawn through the point of the maximum and the intersection of  $z = 9$ . For curves where the value of the eigenfunction at  $z = 9$  is less than  $10^{-13}$ , the intersection of  $\hat{S} = 10^{-13}$  is used instead. Figure 4.12(b) shows the computed gradient of the approximate linear profile at each value of  $Ra$  and a power law fit, showing that the gradient depends on the Rayleigh number in an approximately square root fashion. The vertical profile for the salinity perturbation may then be chosen as:

$$\mathcal{E}(z) = \mathcal{E}_2(z) = \exp\left(-0.4\sqrt{Ra} z\right). \quad (4.18)$$

To compare the differences when using these vertical profiles, a set of ten simulations are run, five using the vertical profile given by (4.3) and five using (4.18) and the departure from the base state and average salinity flux into the surface are plotted in Figure 4.13. For the simulations using  $\mathcal{E}_1$ , the quantities  $A$  and  $q_0$  depart from their base state values at an earlier time than the corresponding simulations for  $\mathcal{E}_2$ , signifying that the perturbation associated with  $\mathcal{E}_1$  has a larger projection onto the unstable manifold than the perturbation associated with  $\mathcal{E}_2$ . In particular,  $\mathcal{E}_2$  is smaller than  $\mathcal{E}_1$  for  $z < 0.4 Ra^{1/2}$  and larger than  $\mathcal{E}_1$  for  $z > 0.4 Ra^{1/2}$ , illustrating that the perturbation associated with  $\mathcal{E}_1$  injects more energy closer to the surface, where the instability is most prominent. However, once the linear instability saturates, the values for  $A$  and  $q_0$  from the two sets of simulations are indistinguishable, implying that the form of the perturbation is not as important at later

## 4. RESULTS

---

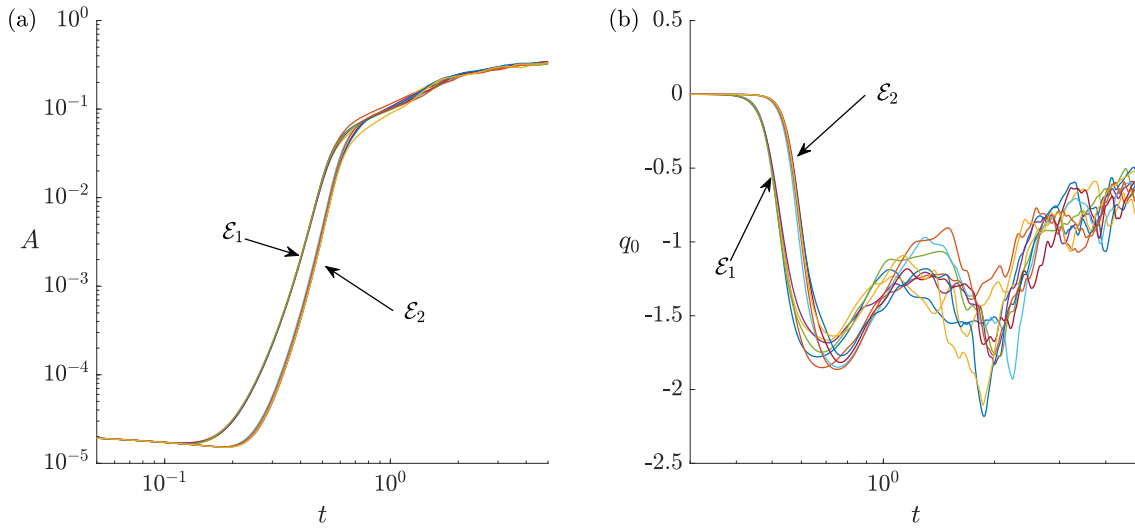


Figure 4.13: (a) Departure from the base state,  $A$  and (b) average salinity flux to the surface for ten simulations, five using the vertical profile  $\mathcal{E}_1$  and five using  $\mathcal{E}_2$ . The parameters used for these were  $Ra = 100$  and  $h = 10$ .

times in the simulation.

### 4.3 Emergence of Polygons

For  $Ra = 100$ ,  $t \approx 0.4$  marks the time for which the dynamics become noticeably nonlinear, and the salinity perturbations begin to develop asymmetrically. This is shown in Figure 4.14 for a two-dimensional simulation. Above the downwellings, the vertical gradient of salinity is small and the salinity flux into the surface is controlled by advection rather than diffusion and thus  $J$  takes positive values. On the other hand, upwelling flows are restricted by a solutal boundary layer, where the salinity gradients are large. In these regions, diffusion dominates the salinity flux into the surface leading to the injection of salinity into the domain. The additional salinity is entrained by the horizontal flow at the top of the convective cells and travels laterally before being redistributed into the lake by descending, high-salinity plumes. The salinity flux has a natural upper bound,  $J = 1$ , which is only approached near downwelling plumes, where the vertical salinity gradients are weak. Above upwelling currents, however, the boundary layer can accommodate larger gradients, and the flux reaches correspondingly larger magnitudes (although now negative, denoting salinity transport into the lake). Owing to this asymmetry, as the initial perturbations begin to saturate, a net flux of salinity from the surface into the lake is created:  $q_0 < 0$ . This bias can be seen in Figure 4.5(b) and is shown more explicitly in Figure 4.15.

At  $t \approx 0.5$ , the average wavenumber of the surface flux,  $\bar{k}$ , passes through a local minimum, shown in Figure 4.11. Figure 4.16 explores the instability that underlies this effect, which is due to the presence of short-lived, low-wavenumber modes. Before these modes grow, up to  $t = 0.4$ , the pattern of the salinity flux  $J$  resembles that of the linear regime (compare Figure 4.16(a) with Figure 4.5(a)). By  $t = 0.5$ , however, noticeable changes have already taken place, as seen in Figure 4.16(b), with narrow, well-connected regions of positive flux surrounding wide areas of negative flux. To identify the role of the low wavenumber modes in the emergence of this pattern, a low-pass filter ( $k \leq 1$ ) is applied to the salinity flux in Figure 4.16(b). The resulting long wavelength pattern is shown in Figure 4.16(c) and highlights two important dynamical changes: the average salinity flux to the surface is now negative (see also Figure 4.10) and the low wavenumber salinity flux pattern shows a correlation with the full salinity flux field before the instability (Figure 4.16(a)). Specifically, the regions exhibiting the greatest spatial variations in salinity flux before the instability are those characterised by the highest magnitude of low wavenumber contribution. The growth of the low wavenumber modes consequently mainly alters the regions where flux variations are initially strong by favouring the areas of negative flux

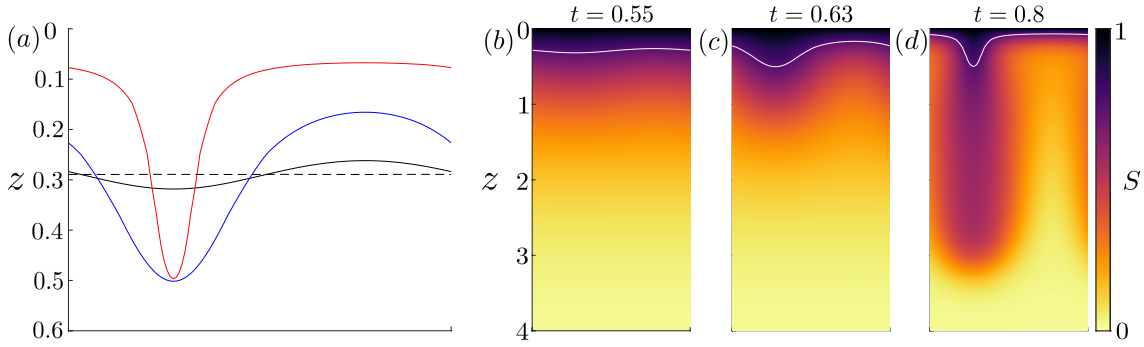


Figure 4.14: Two-dimensional simulation demonstrating how the asymmetry of the boundary layer leads to the formation of a salinity plume. The initial condition is the base state perturbed only by the most unstable mode,  $k^* \approx 3.0043$ , at  $Ra = 100$  and  $h = 10$  and horizontal domain  $\Gamma_x = 2\pi/k^*$ . Solid lines in (a) show the salinity contour  $S = 0.75$  at  $t = 0.55$ ,  $0.63$  and  $0.8$ , while the dashed line indicates the base state contour. Panels (b)–(d) display the corresponding salinity fields with the  $S = 0.75$  salinity contour overlaid in white.

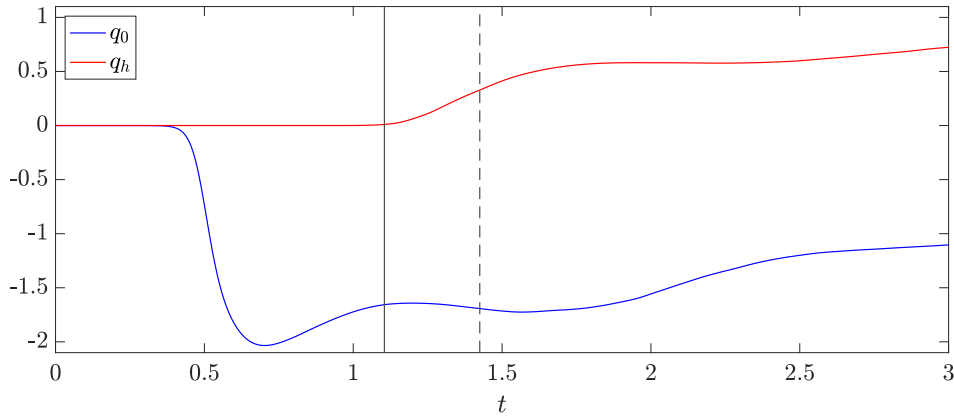


Figure 4.15: Time evolution of the average salinity flux into the surface,  $q_0$ , and out of the lake at  $z = h$ ,  $q_h$ , for the simulation presented in Figure 4.5. The solid black line at  $t \approx 1.1$  indicates the first time that  $q_h''(t)$  attains a local maximum and the dashed line indicates a time  $\approx 3h/Ra$  after the solid line (see Section 4.5.1).

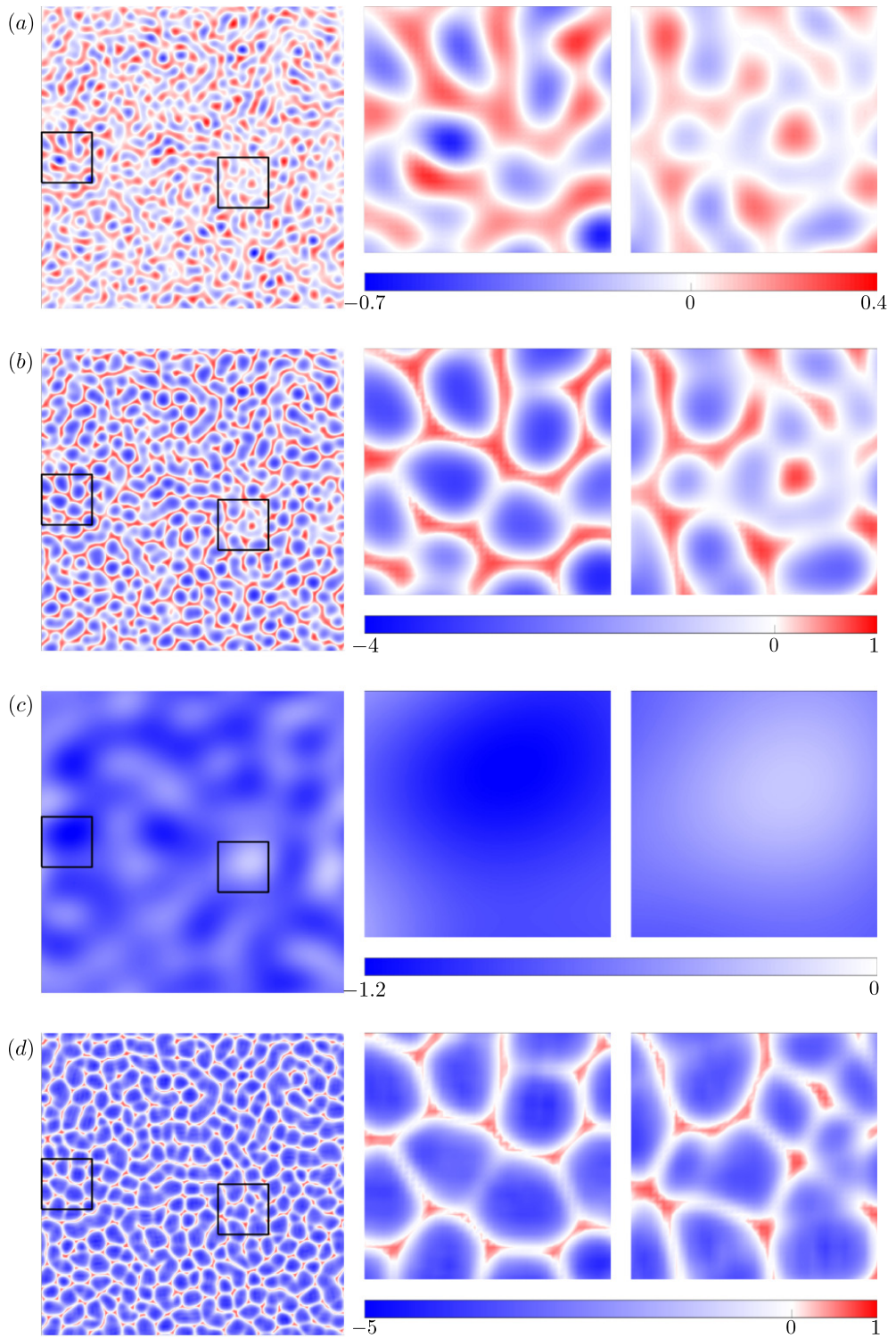


Figure 4.16: Salinity flux to the surface at  $t = 0.4$  (panel (a)),  $t = 0.5$  (panel (b)) and  $t = 0.6$  (panel (d)) for the simulation presented in Figure 4.5, with  $Ra = 100$ ,  $h = 10$  and  $\Gamma_x = \Gamma_y = 12\pi$ . The data of panel (b) was filtered to represent the contribution of the large-wavelength components ( $k \leq 1$ ) in panel (c). For each panel, the left plot represents the whole domain and the right panels correspond to enlargements of two square areas indicated by the black squares on the left plot.

which become broader and more intense. Between  $t = 0.5$  and  $t = 0.6$ , the energy contained in the low wavenumber modes decays as the average salinity flux continues to grow away from 0. These integral changes are accompanied by a modification of the surface flux pattern that is complementary to what is observed between  $t = 0.4$  and  $t = 0.5$ . The areas impacted by the first stage of this instability remain mostly unchanged but the areas displaying smaller variations in surface flux catch up here to look similar to them. The net result of the growth and decay of these low wavenumber modes, shown in the left panel of Figure 4.16(d), is the emergence of a polygonal pattern displaying narrow regions of salinity flux into the surface delimiting large areas where salinity is sent back into the lake.

#### 4.4 Late-Time Dynamics

Three-dimensional simulations reveal that the downwelling currents below a polygon vertex are qualitatively different from those located below a polygon edge. Figure 4.17 shows the flow structure at the surface, overlaid on top of the salinity flux. The upwellings drive an excess mass to the surface that is redistributed horizontally. Due to mass conservation, fluid accelerates as it gets further away from the centre of upwellings until it reaches the boundary of a convective cell. The horizontal flows generated by neighbouring upwellings meet at fairly straight boundaries, where the excess mass is evacuated by downwelling currents. The resulting currents are referred to as salinity sheets owing to their horizontal structure (white areas in Figure 4.17). Above them, a weak flow is driven along the polygon edge toward its vertices (red areas in Figure 4.17) in such a way that the excess mass at the vertices is greater than that at the top of salinity sheets. As a result, the downwelling flows below polygon vertices are stronger and form typical salinity plumes

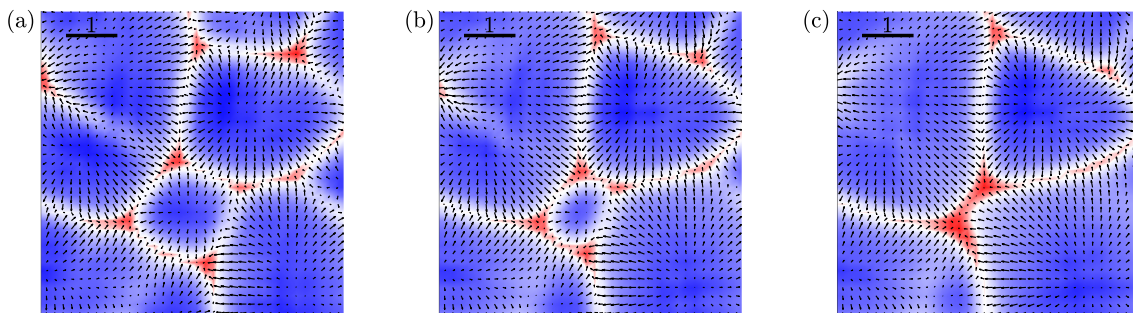


Figure 4.17: Regions of the surface flux of size  $6 \times 6$  at times (a)  $t = 0.7$ , (b)  $t = 0.8$  and (c)  $t = 0.9$ , taken from the simulation shown in Figure 4.5 ( $Ra = 100$ ,  $h = 10$  and  $\Gamma_x = \Gamma_y = 12\pi$ ). The horizontal velocity field is displayed by the vector field (black arrows).

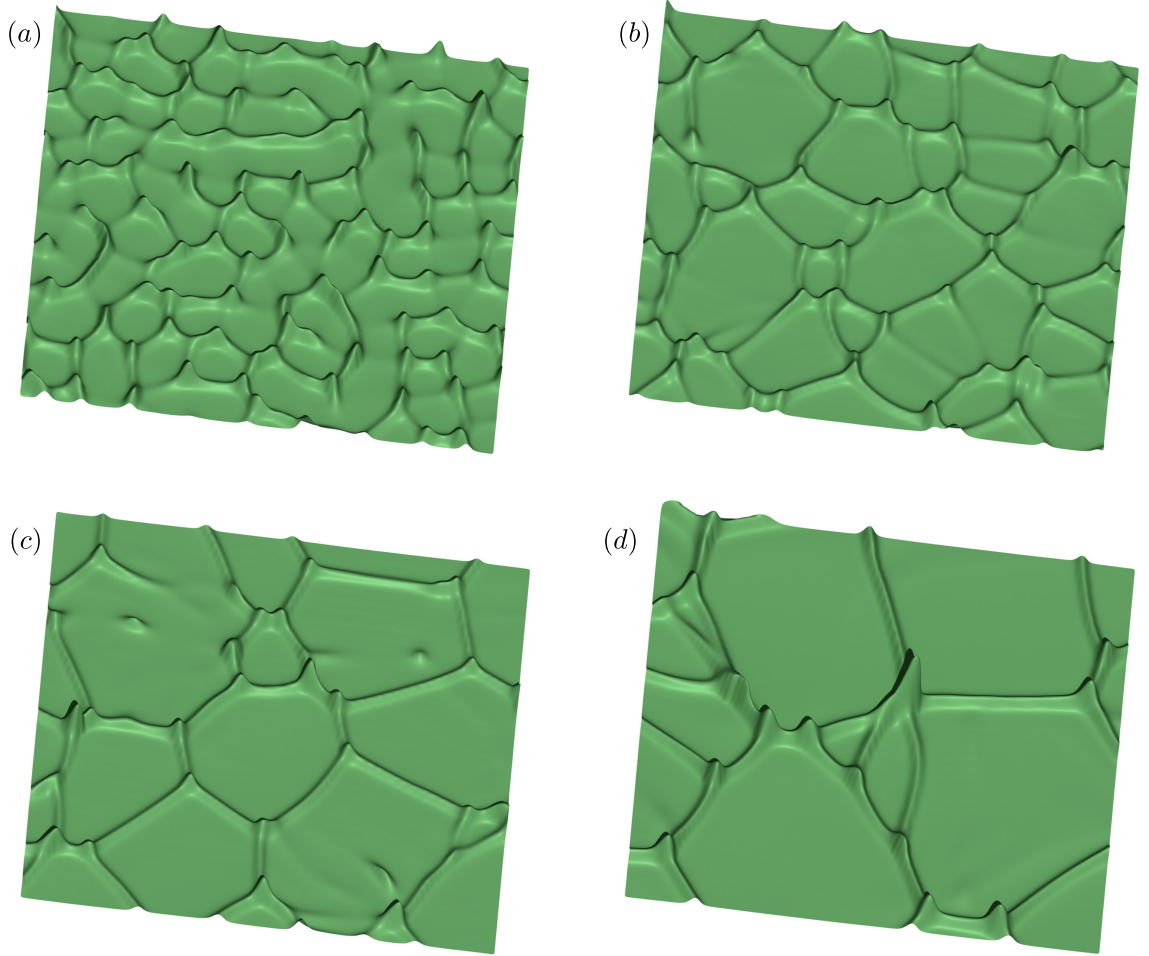


Figure 4.18: Representation of the depth of penetration of the salinity contour  $S = 0.75$  for a region of size  $6\pi \times 6\pi$  for  $Ra = 100$ ,  $h = 10$  and  $\Gamma_x = \Gamma_y = 12\pi$ . Times shown are (a)  $t = 0.6$ , (b)  $t = 1$ , (c)  $t = 2$  and (d)  $t = 7$ .

that reach greater depths than the salinity sheets connecting them. The structure of the resulting salinity currents is shown in Figure 4.18 at a variety of times. At  $t = 0.6$ , which approximately marks the end of the instability described in Section 4.3, the depth of penetration between the salinity plumes beneath polygon vertices and edges can be seen (Figure 4.18(a)). When the plumes or sheets are sufficiently large, they generate a horizontal velocity field near the surface that has the potential to entrain other convective structures. An example of such dynamics is shown in Figure 4.17, where the flow induced along the edges of polygons end up pushing the four vertices located near the centre of the represented region to merge. This process is evident from the plume and sheet profiles shown in Figure 4.18(a) and Figure 4.18(b). Merging events take place on a large-scale, leading to the decrease of the average and dominant wavenumber of the surface pattern (see Figure 4.11) and an overall increase in the pattern scale, illustrated by the difference in the size of the polygons in Figure 4.18(a) and Figure 4.18(b). From  $t \approx 1$ , the rate

at which the average wavenumber decreases slows down, seen by the relatively similar pattern size in Figure 4.18(b) and Figure 4.18(c), and the smaller rate of change of the average wavenumber in Figure 4.11.

As the surface pattern coarsens, the regions of upwelling fluid between the network of downwelling fluid increase in size. The thickness of the boundary layer is controlled by the competition between the throughflow and the buoyancy of the fluid, the relative strength of these forces being controlled by  $Ra$ . When the boundary layer is too thin, it grows due to diffusion (Slim et al., 2013), but when the boundary layer is too thick for the throughflow to support it, it becomes unstable to small-scale plumes, shedding material and allowing the boundary layer to decrease in thickness. These miniature plumes are named *protoplumes* (Hewitt et al., 2012) which differ significantly in size from the developed *megaplumes* that constitute the interior flow. When the excess mass from the boundary layer leaves via a protoplume, it is subject to the background velocity field, forcing it to be swept toward the nearest neighbouring downwelling. If the time taken for fluid to be advected horizontally within the boundary layer is longer than the time taken for the perturbation to grow to a macroscopic size, the protoplume may develop and grow to a comparable size to a megaplume (Slim et al., 2013). This results in a merging process: protoplumes form in between pre-existing plumes and subsequently merge with a neighbouring megaplume. When protoplumes form, they may be isolated from the surrounding network (see Figure 4.18(c)) or they may connect two edges of the polygon that they form in, visible through the ‘ribs’ that form in the interior of polygons (see Figure 4.5(d) and Figure 4.18(d)), which are swept toward the nearest edge or vertex in the network, corresponding to the nearest megaplume.

Figure 4.19(a) shows the average wavenumber of the salinity as a function of depth. For example, at  $t = 10$ , this wavenumber is largest close to the surface and the bottom, where it captures the small-scale dynamics of the protoplumes initiating from the boundaries, and smallest around the midplane,  $z = h/2$ , where the convection mainly consists of megaplumes. Figure 4.19(b) shows the evolution of the average wavenumber of the salinity field at the midplane of the domain,  $z = h/2$ . The average wavenumber of the salinity at the midplane remains smaller than the average wavenumber of the surface flux at all times with smaller variations. This suggests that the large-scale convection imposes a larger pattern size, since the surface is a footprint of the interior dynamics, and that the average wavenumber of the midplane salinity may be more suitable to use as a metric for the pattern scale.

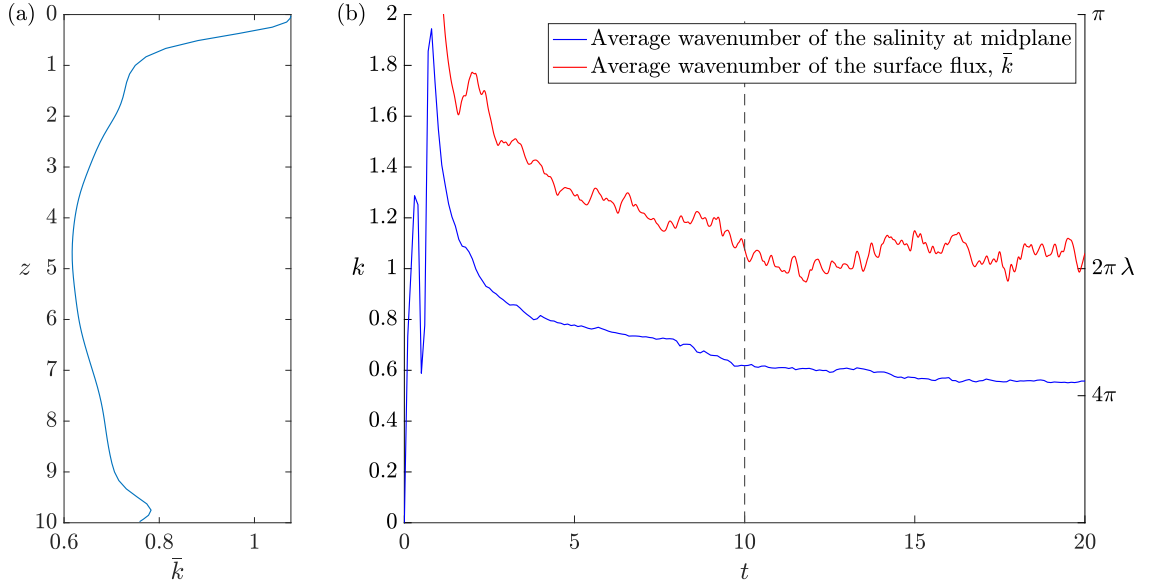


Figure 4.19: (a) Average wavenumber of the salinity as a function of the depth at time  $t = 10$ . (b) Average wavenumber of the salinity at the midplane as a function of time. The dashed line indicates the time that the profile in panel (a) is taken at.

When plumes reach the bottom, the average salinity flux leaving the domain through  $z = h$ , defined by:

$$q_h = - \left\langle \frac{\partial S}{\partial z} \Big|_{z=h} \right\rangle_{xy}, \quad (4.19)$$

departs from 0 due to the sharp salinity gradients that are needed to satisfy the bottom boundary condition. This departure is shown in Figure 4.15 through the solid line, marking the first time,  $t = t_1$ , at which  $q_h''(t)$  reaches a local maximum ( $t_1$  is the smallest value of  $t$  such that  $q_h'''(t = t_1) = 0$ ), indicating the time at which the rate of growth of  $q_h(t)$  is growing the fastest. After this time, the dynamics on the whole domain no longer represent that of an infinitely deep lake, but the surface pattern remains undisturbed. The disturbance from the bottom boundary then travels back to the surface and the pattern in the surface flux of salinity no longer represents that of an infinitely deep lake. The dashed line in Figure 4.15 denotes the approximate time that the surface feels the presence of the bottom boundary, and the determination of this time is discussed further in Section 4.5. The presence of plumes at the bottom boundary increases the rate at which fluid leaves the domain in these regions which is opposed by an increase in fluid entering the domain (since  $\langle w \rangle_{xy} = -1$ ) via regions of upwelling fluid. Upwelling plumes initiate from the bottom boundary which rise upwards and the system begins to approach a statistically steady end-state.

Quantities such as the average fluxes,  $q_0$ ,  $q_h$ , and the average wavenumber,  $\bar{k}$ , eventually fluctuate around an end-state value. Figure 4.20 shows plots of the salinity versus its time derivative at four randomly selected reference points near the surface of the lake for  $105 \leq t \leq 135$ . Panels (a)–(d) in Figure 4.20 are in increasing order of depth. At  $z \approx 0.02$ , the salinity takes values very close to 1, meaning the trajectory of Figure 4.20(a) remains close to  $(1, 0)$ . As the depth of the reference point increases, the salinity decreases from 1 and the time derivative increases in magnitude, resulting in a wider range of values obtained by  $\partial S/\partial t$ , displaying the dynamic nature of the boundary layer. By  $z \approx 0.5$ , the salinity displays values over a much wider range but has smaller values of the time derivative, suggesting that the slower behaviour of the megaplumes is being sampled here, compared to that of the protoplumes at the shallower reference points. Figure 4.20(e) shows the average surface flux and average wavenumber for the same simulation as panels (a)–(d). Beyond  $t \gtrsim 20$ , the average wavenumber fluctuates around its smallest value where the polygons in the surface pattern are at their largest. The values for  $q_0$  and  $\bar{k}$  are proceeding toward their end-state values, but have not yet fully converged. However, in this statistically steady end-state, the salinity entering the domain via the surface balances the salinity leaving through the bottom and so it is expected that  $q_0 \approx -q_h$ . The late-time values of these quantities in relation to  $h$  and  $Ra$  are discussed further in Section 4.5.

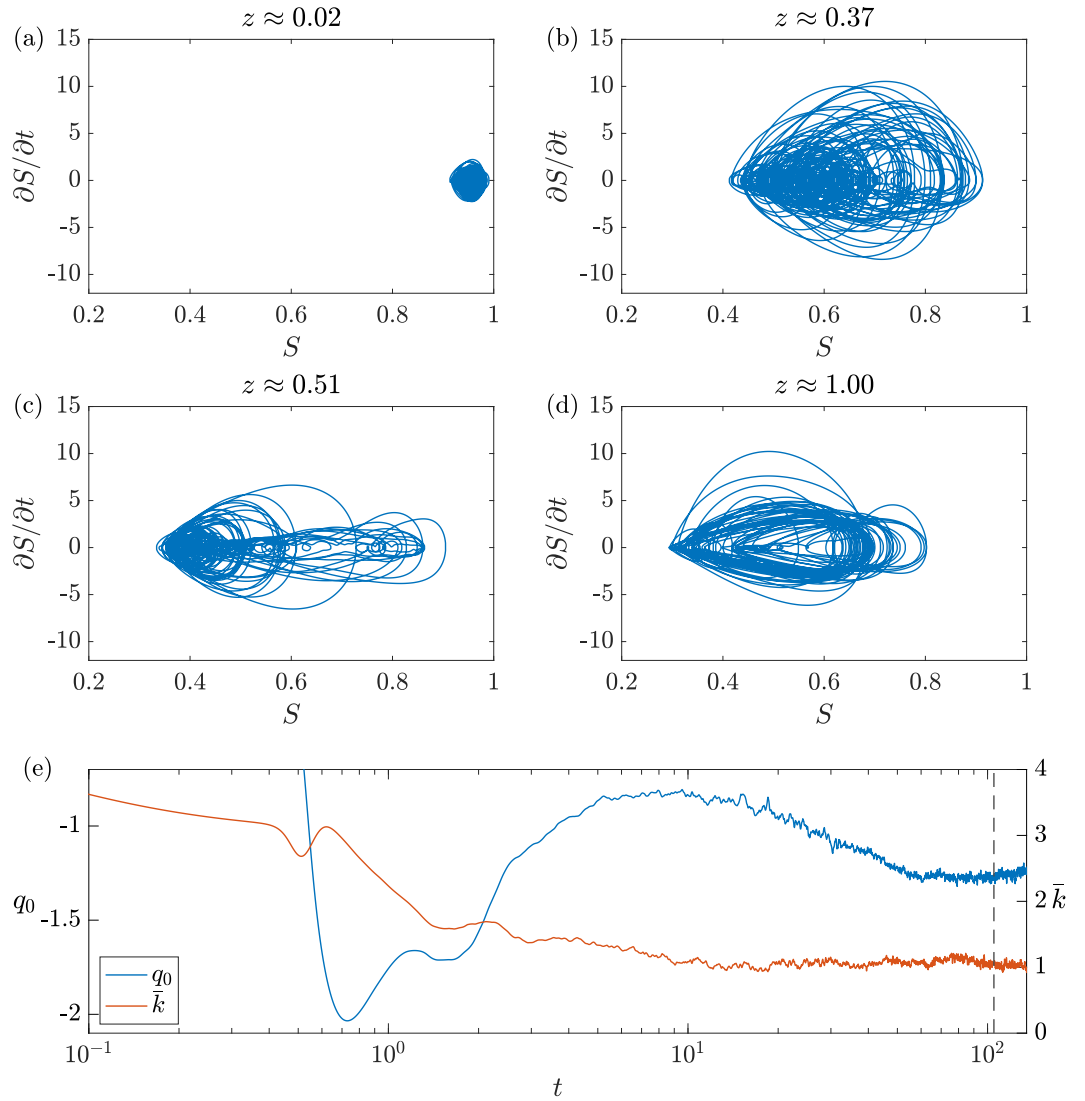


Figure 4.20: Transition towards a statistically steady end-state. (a)–(d): Salinity as a function of its time derivative at four randomly selected points near the surface of the lake. Trajectories have been plotted for  $105 \leq t \leq 135$ . (e): Average surface flux and average wavenumber for the whole simulation. The dashed line denotes the initial time of the phase space portraits ( $t = 105$ ).

## 4.5 Parametric Study

In Section 4.3 and Section 4.4, the dynamics at  $Ra = 100$  and  $h = 10$  have been studied. In Section 4.5.1 and Section 4.5.2, the effect of varying  $h$  and  $Ra$  will be explored and the influence this has on the pattern wavenumber and the transport of salinity.

### 4.5.1 Dependence on the Lake Depth

During the linear regime, the lake depth has little effect on the dynamics due to the fast convergence (as  $h$  is increased) of the results of the linear stability analysis. The eigenfunctions for different  $h$  differ close to the bottom of the lake, where the exponential tail must transition to zero (see Figure 4.8(b)). After this stage, the effect of the location of the bottom boundary is not felt until plumes have reached the bottom and when plumes have descended deep enough to feel the effect of the bottom boundary condition, simulations no longer resemble an infinitely deep lake. Figure 4.21 shows the average salinity flux into the surface (panel (a)), the average flux out through the bottom of the domain (panel (c)) and the average salinity leaving the domain (panel (e)) from simulations with various values of  $h$  and a fixed Rayleigh number,  $Ra = 100$ . Initially,  $q_0$  reaches a local minimum shortly after the saturation of the linear regime and a pattern in the surface flux has emerged (see Section 4.3). From this minimum value,  $q_0$  increases, encounters a local maximum and transitions toward chaotic behaviour at later times. When descending plumes reach the bottom of the domain, the average salinity flux,  $q_h$ , departs from zero, as seen in Figure 4.21(c). This time is denoted as  $t = t_1$  (see Section 4.4) and is a reasonable approximation to when downwelling plumes encounter the bottom boundary and it is thus expected that this time will increase for lakes with larger  $h$ . The surface flux curves then depart from those with larger  $h$  when the presence of the bottom boundary is felt by the surface. This is shown in Figure 4.21(a) by the sequential and relatively sudden increase in  $q_0$  from the bulk behaviour of the curves with larger values of  $h$ . This gives a second important time during a simulation: the time at which the average surface flux departs from the simulations with larger  $h$ , denoted as  $t = t_2$ , and marks the time that the surface pattern no longer represents that of an infinitely deep lake. Figure 4.21(e) also shows this behaviour through the total salinity leaving the domain,  $q_0 + q_h$ . In particular, these curves illustrate the early-time behaviour of  $q_0$  (since  $q_h \approx 0$ ), which subsequently transition to a statistically steady end-state, where  $q_0 + q_h \approx 0$ . The time over which this happens increases with  $h$  and can be seen through the approximate gradients of the transition from the surface flux departure time to the time at which  $q_0 + q_h \approx 0$ .

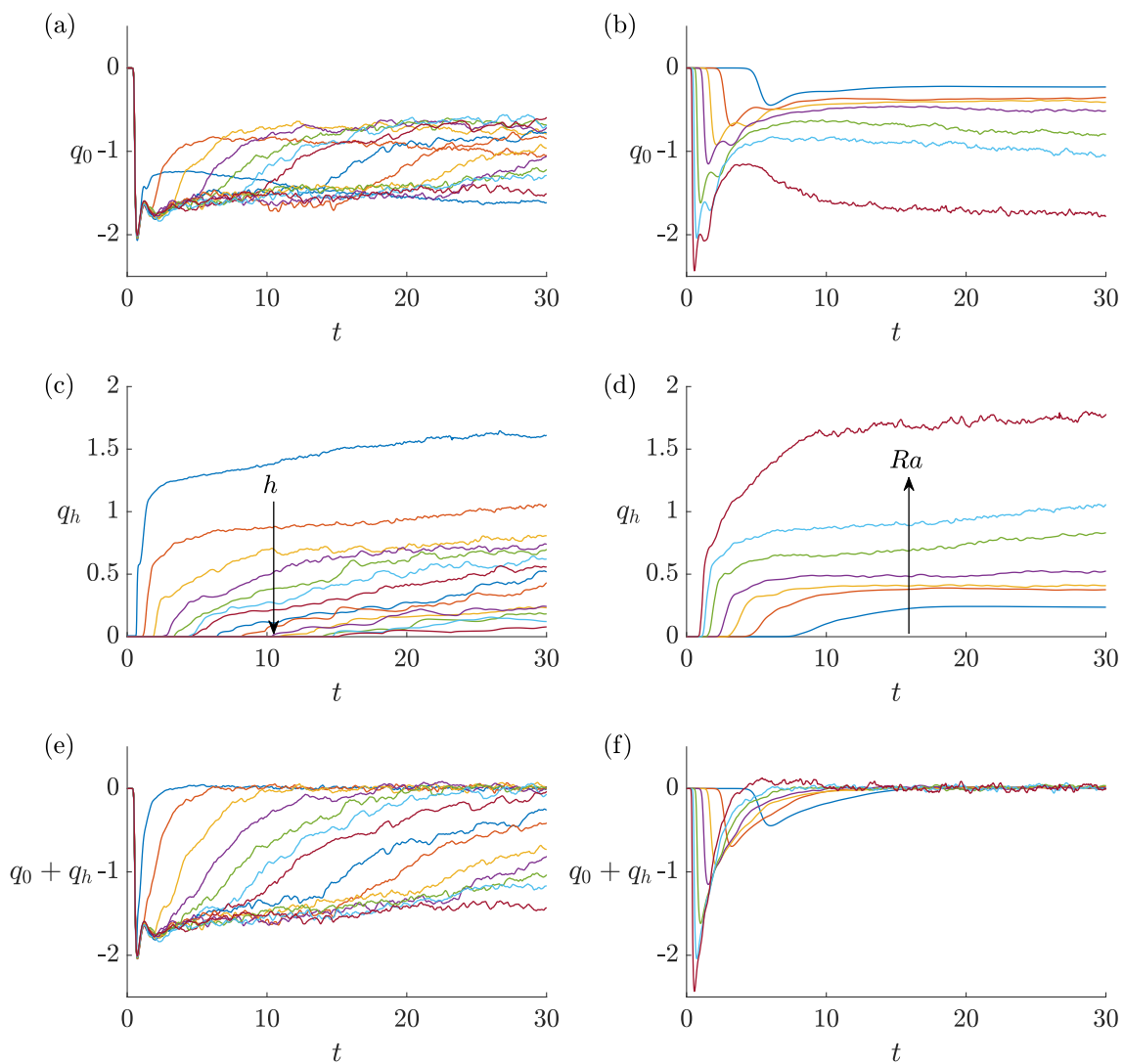


Figure 4.21: (a) Average surface flux, (c) average bottom flux and (e) average total flux ( $q_0 + q_h$ ) for times  $0 \leq t \leq 30$  and depths  $h = 5, 10, 20, 30, 40, 50, 60, 80, 100, 120, 140, 160, 180$  and  $200$  at  $Ra = 100$ . (b) Average surface flux, (d) average bottom flux and (f) average total flux for times  $0 \leq t \leq 30$  and Rayleigh numbers  $Ra = 30, 40, 50, 60, 80, 100$  and  $120$  at  $h = 10$ . The domain size is  $\Gamma_x = \Gamma_y = 12\pi$ .

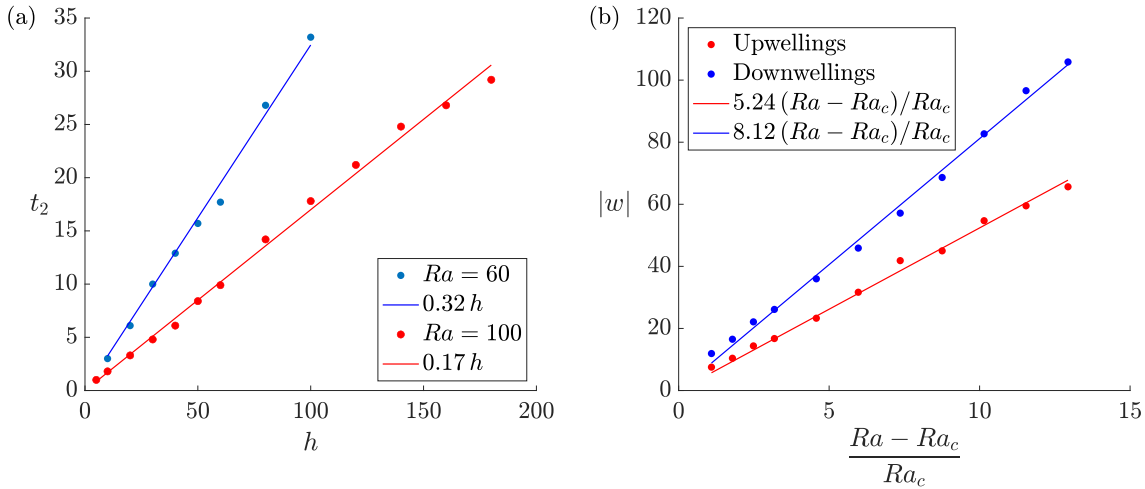


Figure 4.22: (a) Time at which surface flux curves depart from those for higher  $h$ ,  $t \approx t_2$ , (see Figure 4.21(a) for  $Ra = 100$ ). (b) Maximum upwelling and downwelling speeds as a function of  $(Ra - Ra_c)/Ra_c$  (Lasser et al., 2021) ( $h = 10$ ), determined by taking the minimum and maximum vertical velocities over the period  $0 \leq t \lesssim T(Ra)$ . The value of  $T(Ra)$  is explained in the text.

The time at which the surface feels the effect of the bottom boundary,  $t \approx t_2$ , (taken from Figure 4.21(a)) is plotted in Figure 4.22(a) for  $Ra = 60$  and  $Ra = 100$ . The computation of these times has not accounted for the initial phase of the instability caused by the initial condition. However, this contributes very little to the overall time and the value obtained here is a good approximation to when the surface pattern is impacted by the bottom boundary. The time at which the surface flux curves peel away from those for higher  $h$  appears to depend on  $h$  in an approximately linear fashion (within this range of  $h$ ).

Figure 4.23(a) shows the average surface flux at  $t = t_1$  and  $t \approx t_2$ . The behaviour of  $q_0(t = t_1)$  for  $h < 40$  captures the early-time dynamic behaviour of  $q_0$  for  $t \lesssim 5$  (see Figure 4.21(a)). As  $h$  is increased there is an increase in the average surface flux at both  $t = t_1$  and  $t \approx t_2$ . In addition, the average surface flux at  $t \approx t_2$  is greater than at  $t = t_1$  (when  $t \approx t_2$  occurs after the early-time behaviour for  $h \geq 20$ ). Also seen in Figure 4.23(a) is a late-time time averaged value of  $q_0$  and  $-q_h$ . These values were obtained by averaging the fluxes over 40 time units from the statistically steady end-state of a single simulation. For deeper lakes, plumes have diffused more by the time they have reached the bottom, resulting in a smaller vertical salinity gradient and hence a lower net flux out through the bottom. Since the average surface flux approximately balances the flux of salinity leaving the domain in the statistically steady end-state, there is a good agreement in the late-time values of  $q_0$  and  $-q_h$  for each  $h$ .

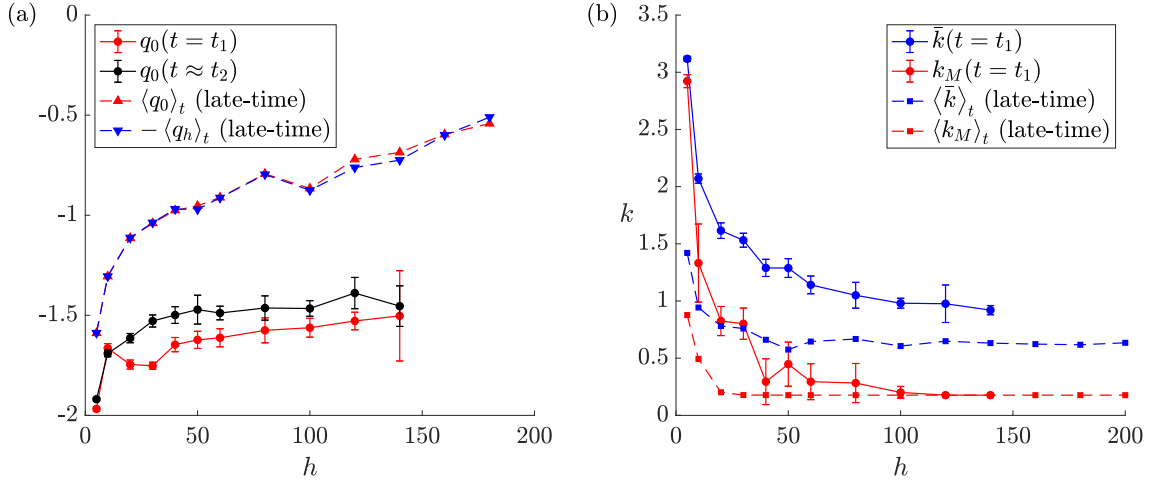


Figure 4.23: (a) Average surface flux,  $q_0$ , at the time plumes hit the bottom of the domain ( $t = t_1$ ), average surface flux at the time it departs from those with larger  $h$  ( $t \approx t_2$ ) and a late-time time averaged value much later in the simulation. Error bars on  $q_0$  at  $t = t_1$  and  $t = t_2$  represent one standard deviation. (b) Average wavenumber,  $\bar{k}$ , (solid blue line) and the most dominant wavenumber,  $k_M$ , (solid red line) at the same instant at  $t = t_1$ . Error bars on the quantities at  $t = t_1$  and  $t \approx t_2$  represent one standard deviation. Ten simulations were used for the averages for  $h = 5, \dots, 80$ , five for  $h = 100, 120$  and two for  $h = 140, \dots, 200$ . The blue and red dashed lines also show a late-time time averaged value for the average and dominant wavenumbers respectively.

Figure 4.23(b) shows the values of  $\bar{k}$  and  $k_M$  at the instant the plumes reach the bottom of the domain ( $t = t_1$ ) and a late-time time-averaged value. As  $h$  is increased, both the average and dominant wavenumbers at  $t = t_1$  decrease, tending towards their late-time values. The late-time average wavenumber also consistently lies above the dominant wavenumber. This can be seen in Figure 4.24 which displays the pattern of the salinity flux to the surface at four different times during the statistically steady end-state. The surface flux displays a large number of small-scale features, which contribute to the larger value of the average wavenumber compared to the dominant wavenumber. For very small lake depths, both the average and dominant wavenumbers take larger values. This corresponds to smaller wavelengths which arise due to the increased spatial restriction of shallower lakes and a tendency for them to avoid high aspect ratio convective rolls.

#### 4.5.2 Dependence on the Rayleigh Number

As  $Ra$  is increased, convection becomes more vigorous, and plumes descend faster, reaching the bottom in a shorter time. Lasser et al. (2021) introduced the quantity  $\varepsilon = (Ra - Ra_c) / Ra_c$  to describe the distance that the system is from the critical point. A new time may be defined as  $\tau = \varepsilon t$ , which can be useful to compare the dynamics at different  $Ra$ . Figure 4.25 shows the average surface flux and average flux through the bottom of

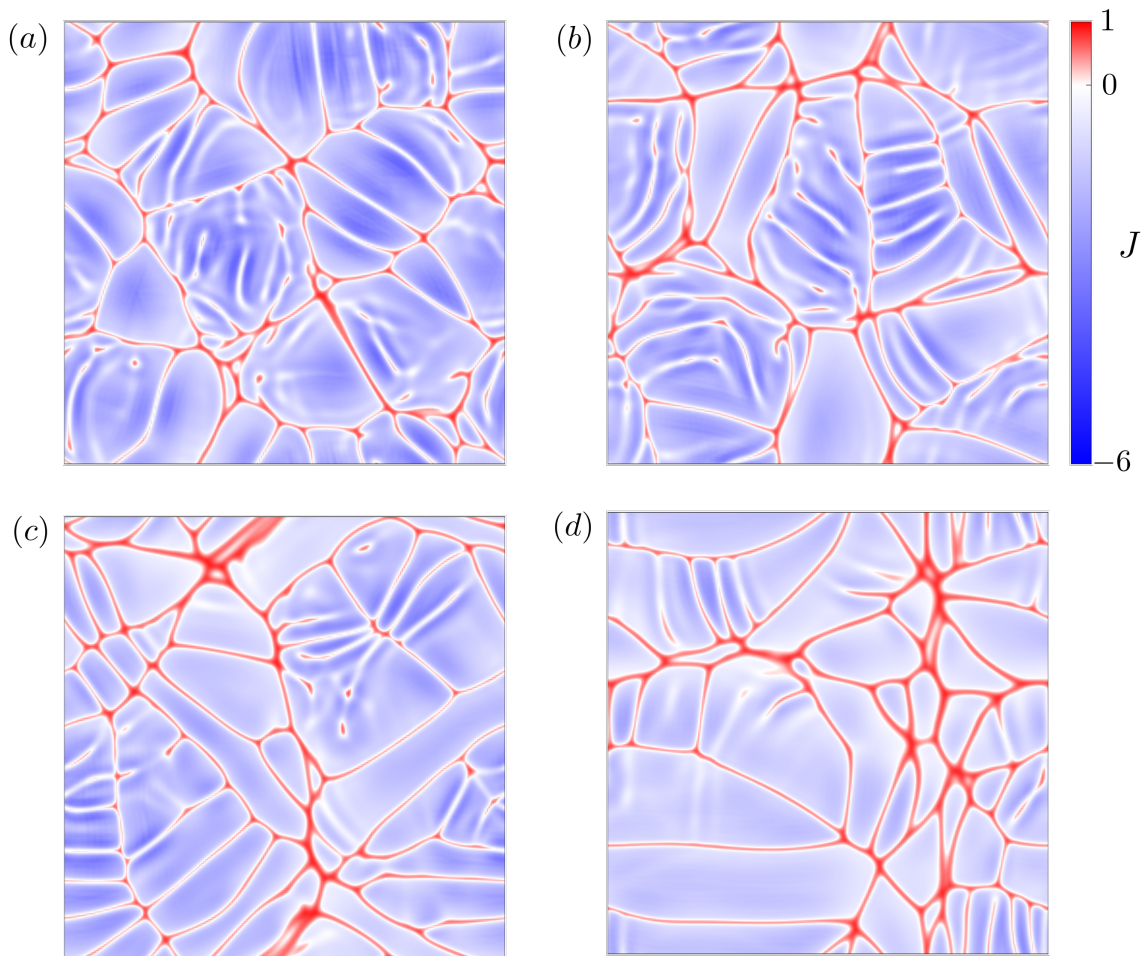


Figure 4.24: Surface flux at  $t = 150$  for (a)  $h = 10$ , (b)  $h = 20$ , (c)  $h = 50$ , (d)  $h = 100$  for  $Ra = 100$  and  $\Gamma_x = \Gamma_y = 12\pi$ .

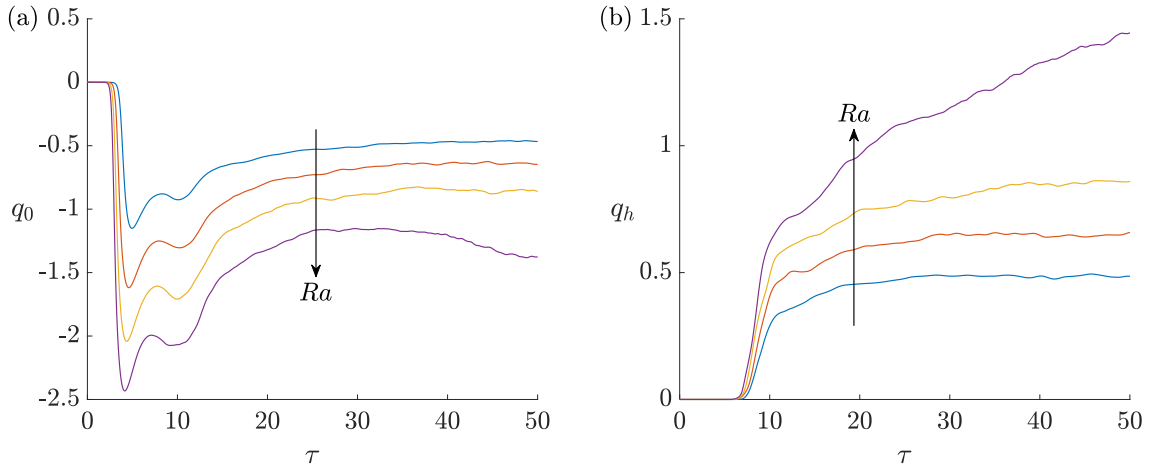


Figure 4.25: (a) Average surface flux,  $q_0$ , and (b) average flux through the bottom,  $q_h$ , as a function of the rescaled time,  $\tau = \varepsilon t$ , for  $Ra = 60, 80, 100$  and  $120$ .

the domain against this rescaled time for selected values of  $Ra$ . Plotting the values of the salinity fluxes against  $\tau$  demonstrates the effect of the rescaling:  $q_0$  is seen to depart from zero at roughly the same value of  $\tau$  for the different  $Ra$ . In addition, the local minimum of  $q_0$  occurs at approximately the same rescaled time, as well as the time at which  $q_h$  departs from zero. This allows comparisons between simulations with differing  $Ra$  to be made, provided they are made at the same rescaled time.

Figure 4.21 shows the average surface flux (panel (b)), the average bottom flux (panel (d)) and the average salinity leaving the domain (panel (f)) for simulations with varying  $Ra$  at a fixed  $h = 10$ . As  $Ra$  is increased and the dynamics speed up, the minimum in the average surface flux is reached sooner, where it also occurs at a larger absolute value. In addition, as  $Ra$  is increased, the time at which the  $q_h$  curves depart from zero occurs earlier, demonstrating that the downwelling plumes travel faster for higher values of  $Ra$ . Figure 4.22(b) shows the maximum upwelling and downwelling speeds as a function of  $(Ra - Ra_c)/Ra_c$  (Lasser et al., 2021). These values were obtained by computing the minimum and maximum vertical velocities over the period  $0 \leq t \leq T(Ra)$ , where

$$T \approx 0.17 h \frac{100 - Ra_c}{Ra - Ra_c}. \quad (4.20)$$

The values were computed over this range to avoid potentially smaller (and larger) values of the minimum (and maximum) vertical velocity that could have arisen once the upwelling plumes had reached the surface. From this, it can be seen that the downwellings travel faster ( $|w| \approx Ra/2$ ) than the upwellings ( $|w| \approx Ra/3$ ). The surface flux departure time

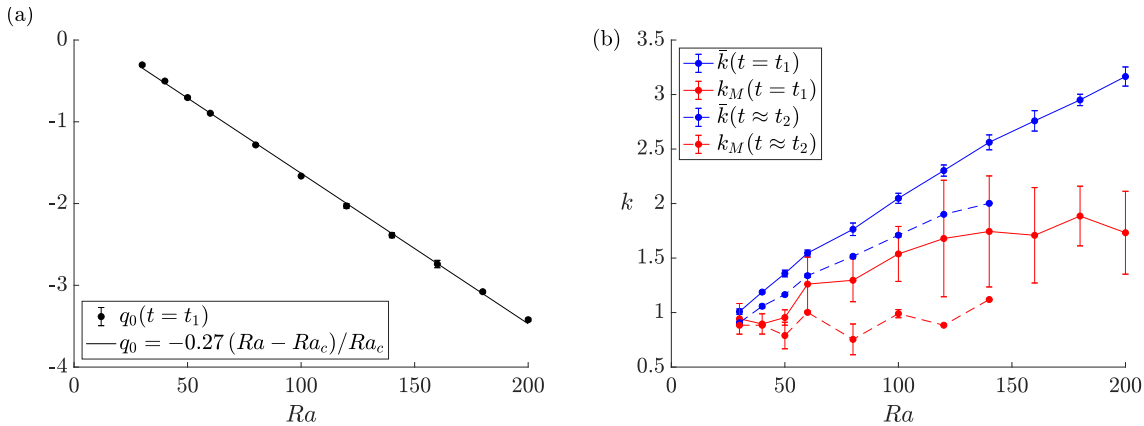


Figure 4.26: (a) Average surface flux,  $q_0$ , at when the plumes have reached the bottom of the domain ( $t = t_1$ ). (b) Average and dominant wavenumbers at the instant plumes hit the bottom of the domain ( $t = t_1$ ) and the approximate time that the disturbance has propagated back to the surface ( $t \approx t_2$ ). Error bars represent one standard deviation. For the data at  $t = t_1$ , twenty simulations were used for the averages for  $Ra = 30, \dots, 100$ , twelve for  $Ra = 120$  and ten for  $Ra = 140, \dots, 200$ . For  $t \approx t_2$ , ten simulations were used for  $Ra = 30, \dots, 100$  and two for  $Ra = 120, \dots, 200$ .

may then be approximated as:

$$t_2 \approx t_1 + \frac{h Ra_c}{5.24(Ra - Ra_c)}, \quad (4.21)$$

which is the time it takes an upwelling to travel a distance  $h$  from  $t = t_1$  (when plumes have reached the bottom).

Figure 4.26(a) shows the mean value of  $q_0$  at  $t = t_1$ . The average surface flux at  $t = t_1$  appears to decrease linearly for this range of  $Ra$ . While the throughflow transports salinity to the surface at a fixed rate (the surface flux always has a constant advective component of 1), the diffusive flux downward from the surface is determined by the vertical gradient of the salinity at the surface (see (4.4)). This means that the diffusive flux is roughly determined by the boundary layer thickness. In simulations presented by Lasser et al. (2021), the thickness of the boundary layer appears to scale with  $1/Ra$  and hence the diffusive flux in the upwelling regions of fluid should scale with  $Ra$ . The proportion of the surface that has a positive flux, denoted by  $\alpha$ , will also contribute to the value of  $q_0$  observed. The fraction of positive surface flux is shown in Figure 4.27(a) for various values of  $Ra$ . From the random initial condition, there is a decrease in  $\alpha$  which saturates at  $\alpha \approx 0.5$ , illustrating the approximately symmetrical state during the linear regime of the instability. Subsequently, a further decrease in  $\alpha$  displays the net result of the growth and decay of the low wavenumber modes described in Section 4.3 which resulted

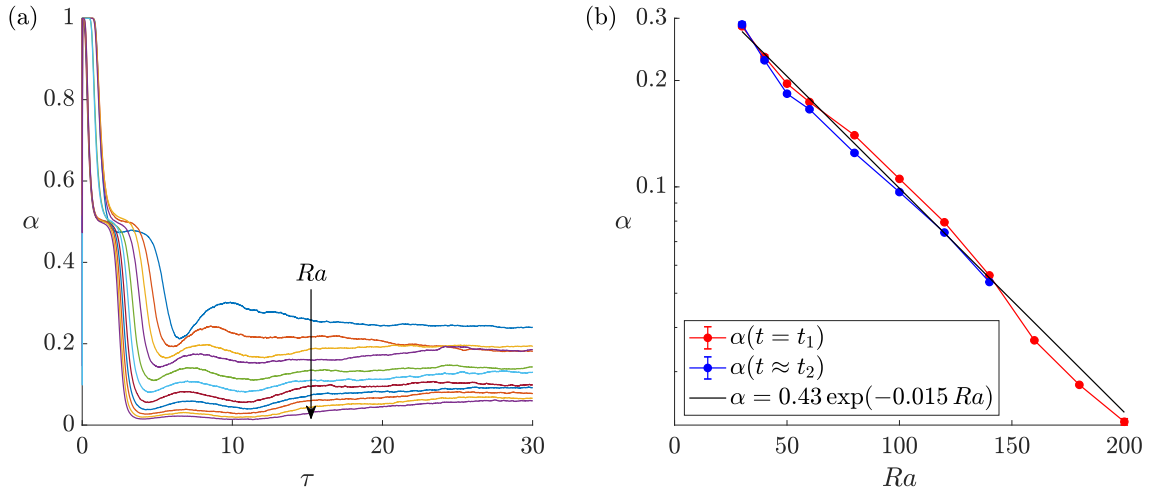


Figure 4.27: (a) Flux fraction,  $\alpha$ , as a function of the rescaled time,  $\tau$ . (b) Ensemble average of the flux fraction at  $t = t_1$  and  $t \approx t_2$ . Error bars represent one standard deviation. For the data at  $t = t_1$ , ten simulations were used for the averages for  $Ra = 30, \dots, 100$  and two for  $Ra = 120, \dots, 200$ . For  $t \approx t_2$ , ten simulations were used for  $Ra = 30, \dots, 100$  and two for  $Ra = 120, 140$ .

in a polygonal pattern of narrow region of positive flux delimiting larger areas of negative salinity flux. As  $Ra$  is increased, the positive regions make up a smaller proportion of the surface and the average salinity flux to the surface is dominated by the upwelling regions of fluid. Figure 4.27(b) shows the average value of  $\alpha$  at  $t = t_1$  and  $t \approx t_2$ , in addition to the approximate exponential fit, displaying the decrease in the fraction of the positive flux as  $Ra$  is increased. Thus, as  $Ra$  is increased, the magnitude of the diffusive flux away from the surface dominates the advective flux into the surface and additionally, there is an increase in area of negative flux regions. This results in the overall decrease in the average surface flux shown by Figure 4.26(a).

Figure 4.26(b) shows the average and dominant wavenumbers at both the instant the plumes reach the bottom of the domain ( $t = t_1$ ) and when the disturbance from the bottom boundary has reached the surface ( $t \approx t_2$ ). The average wavenumber at  $t = t_1$  and  $t \approx t_2$  increases with  $Ra$ , illustrating the appearance of smaller scale structures as the convection becomes more vigorous. The dominant wavenumber, which is consistently smaller than the average wavenumber, displays a weaker increase with  $Ra$  with a larger standard deviation in the measurements taken. However, the dominant wavenumber at  $t \approx t_2$  does not show a strong dependence on  $Ra$  for the range of  $Ra$  simulated here, suggesting that the large-scale structure around  $t \approx t_2$  remains approximately the same as  $Ra$  is increased. Figure 4.28 displays patterns of the surface flux at various values of  $Ra$  and  $\tau \approx 225$ , much later in the simulations than  $t \approx t_2$ . As  $Ra$  is increased, finer

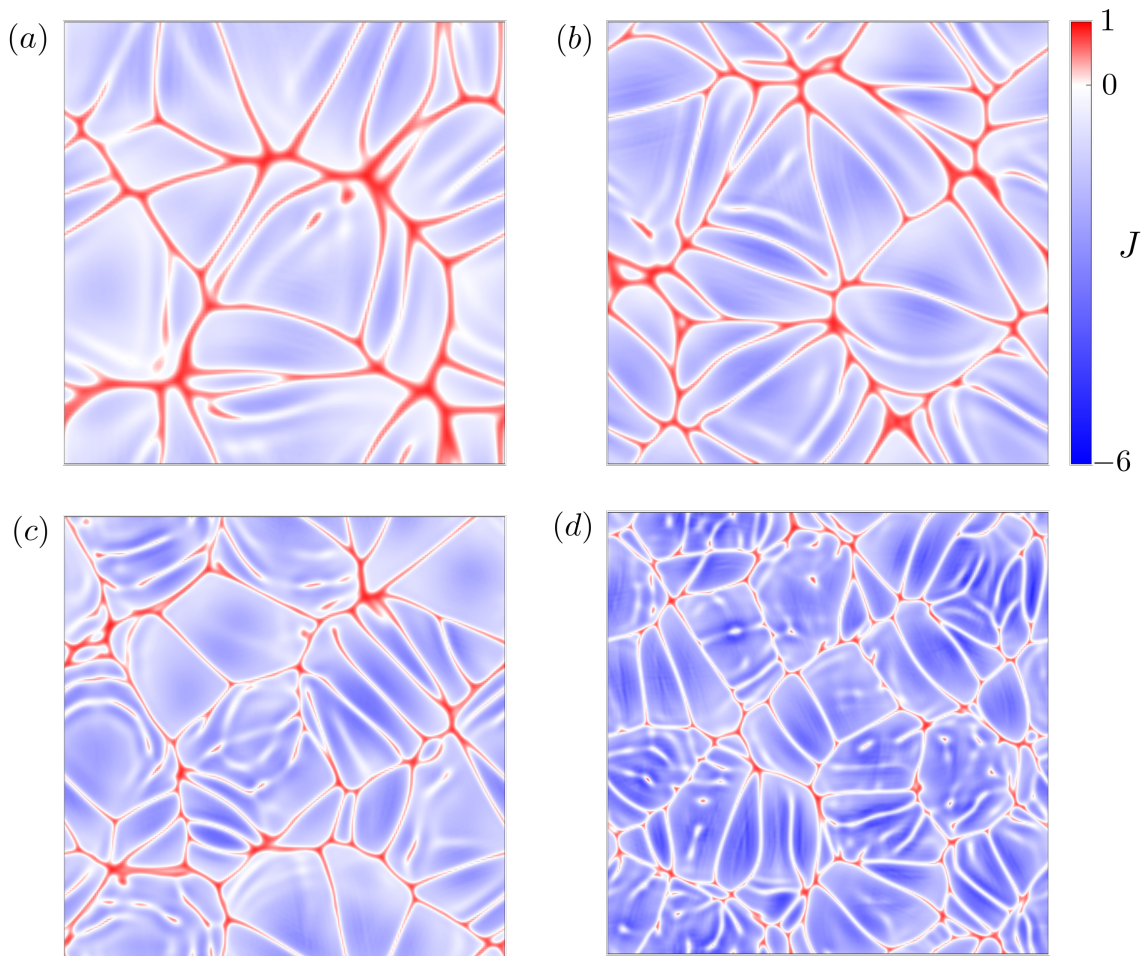


Figure 4.28: Surface flux at  $\tau \approx 225$  for (a)  $Ra = 60$ , (b)  $Ra = 80$ , (c)  $Ra = 100$ , (d)  $Ra = 120$  for  $h = 10$  and  $\Gamma_x = \Gamma_y = 12\pi$ .

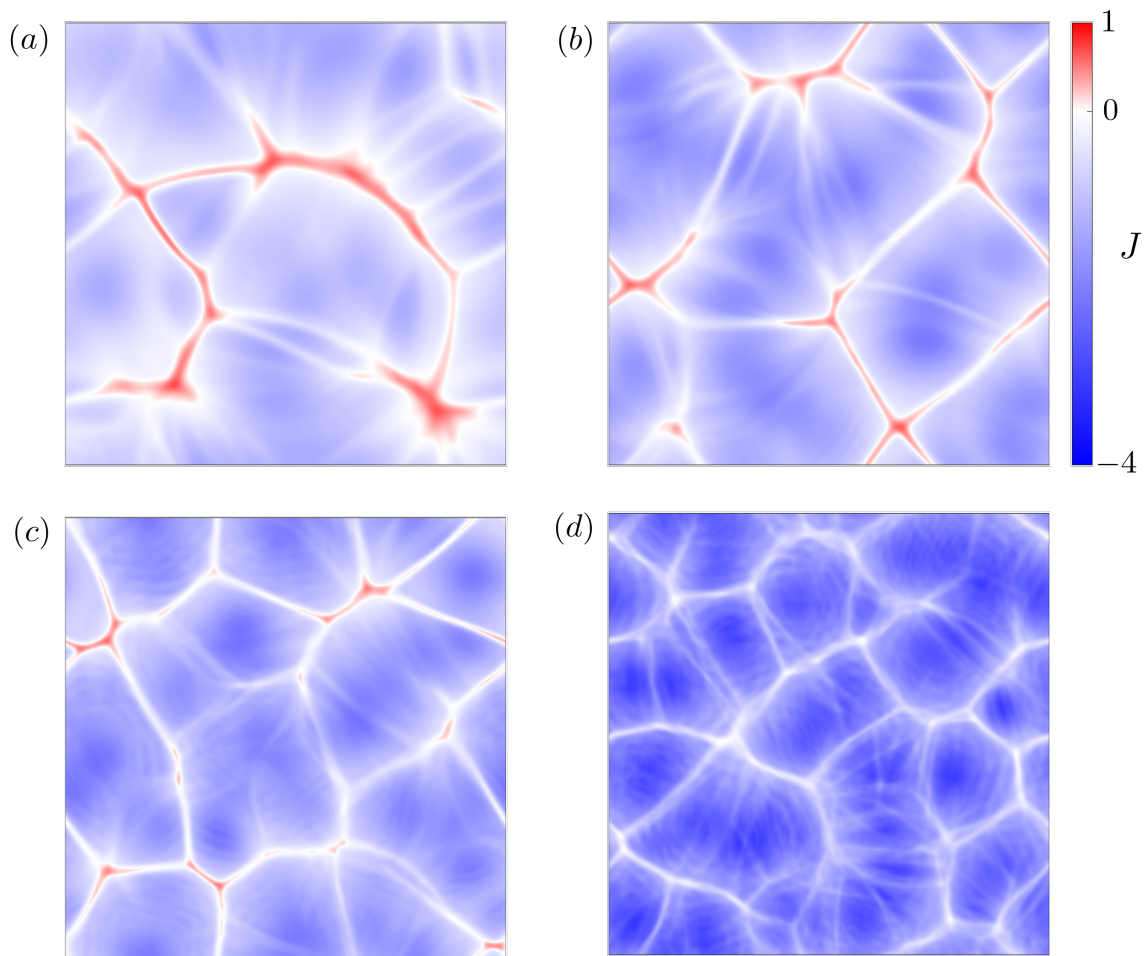


Figure 4.29: Time-averaged surface flux over  $200 \lesssim \tau \lesssim 250$  for (a)  $Ra = 60$  (157 frames), (b)  $Ra = 80$  (109 frames), (c)  $Ra = 100$  (83 frames) and (d)  $Ra = 120$  (68 frames) for  $h = 10$  and  $\Gamma_x = \Gamma_y = 12\pi$ .

structures can be seen in the surface flux, suggesting that the average wavenumber at these later times also increases with  $Ra$ . On the other hand, the increase in the dominant wavenumber can only vaguely be observed. Instead, a time average can be taken, centred at the time shown in Figure 4.28, and covering approximately  $50 \tau$  units. These fields can be seen in Figure 4.29. The fast-moving features that are seen in Figure 4.28 have been removed in the time-averaging, allowing the decrease in the pattern size to be observed as  $Ra$  is increased.

The simulations that were carried out here tended to diverge before the average salinity fluxes and wavenumbers had fully converged to their end-state values. This was also more evident for simulations with a higher Rayleigh number and the possible cause of this will be discussed further in Chapter 5.

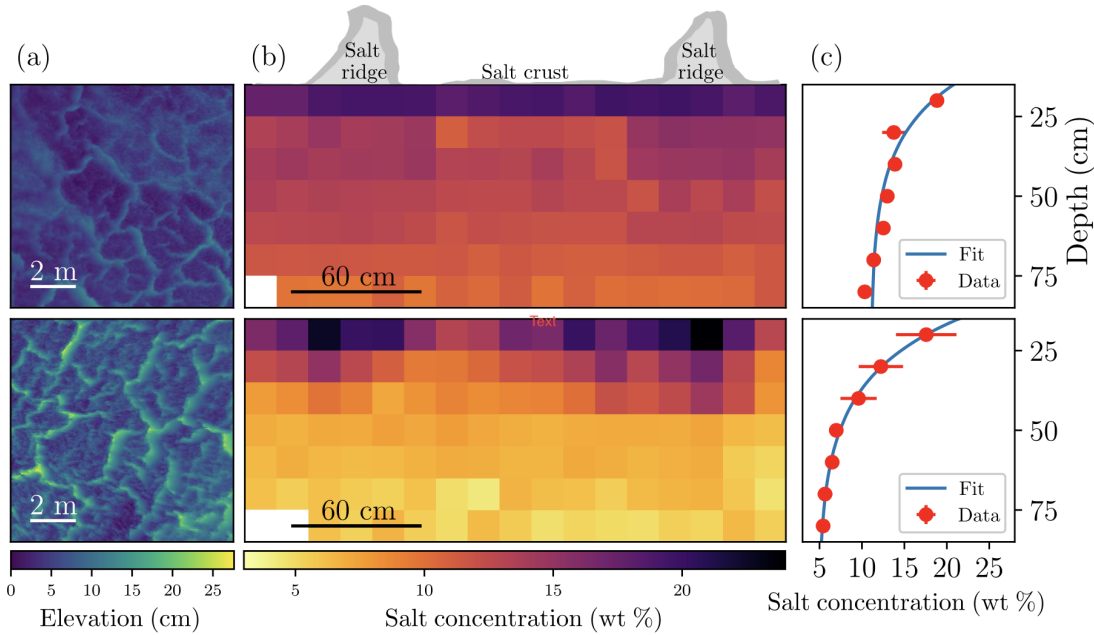


Figure 4.30: (a): Surface height maps provide data on the elevation of the crust ridges. (b): Salinity profiles from a cross section of a polygon, intersecting two bounding edges. (c): Exponential fits (see Lasser et al. (2023)) from horizontally-averaging the data in (b). Figure taken from Lasser et al. (2023).

## 4.6 Comparison to Field Observations

The patterns seen in the three-dimensional simulations (for example, in Figure 4.29(d)) are qualitatively similar to what is seen in the field. Moreover, the simulations produce a consistent pattern scale to the measured values, suggesting that the convective dynamics are an important driving force in the formation of the crust patterns. In the field, Rayleigh numbers can span an extensive range from  $O(10)$  to  $O(10^5)$  (Lasser et al., 2023). Dry lakes can also extend to over 150m in depth (Güler & Thyne, 2004), corresponding to a nondimensional depth of  $h \approx 1000$  (using an approximate value of  $L \approx 15\text{cm}$  for the characteristic length (Lasser et al., 2023)). Thus, the simulations presented previously have a similar Rayleigh number to the lower end of the field observations but are significantly shallower. This must be considered when predictions are made about the salinity fluxes and the pattern scales.

Figure 4.30 shows the field observations from two sites at Owens Lake, consisting of surface height maps and subsurface salinity profiles. Figure 4.30(a) shows two examples of the surface height maps obtained from Owens Lake, displaying a pattern scale of approximately a couple of metres. In addition, Figure 4.30(b) shows the salt concentration of the pore fluid as it varies with depth and position relative to the ridges. This shows the depth of

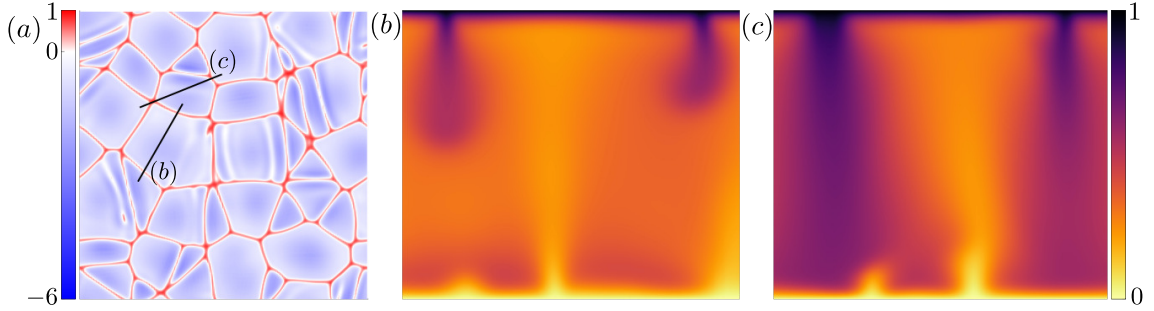


Figure 4.31: (a) Surface salinity flux for  $Ra = 100$  and  $h = 10$  at  $t = 5$ . Lines drawn on the surface indicate the locations of the cross sections in (b) and (c) which show the salinity profile beneath.

penetration of the salinity plumes, which descend to approximately  $\hat{z} \approx 50$  cm, equivalent to a nondimensional depth of approximately  $z \approx 3.3$  (using  $L \approx 15$  cm as the characteristic length, obtained using field data from Owens Lake (Lasser et al., 2023)). This may have been deeper if the pore samples were taken along a line intersecting two vertices of the crust pattern since the depth of penetration of the plumes beneath two intersecting edges was found to be larger (see Figure 4.18). Figure 4.30(c) shows exponential fits to the horizontal average of the field data from Figure 4.30(b) (for more details see Lasser et al. (2023)). Cross sections of the salinity field that lie directly beneath two vertices of the surface pattern can be computed and compared to the salinity field that lies directly beneath two opposite edges. Figure 4.31 shows the surface flux and the salinity profiles at selected cross-sections below two convective cells. When the cross-section intersects two edges, like the field data shown in Figure 4.30(b), plumes do not penetrate as deep as when the cross-section intersects two vertices, shown by Figure 4.31(c). Furthermore, the plumes shown in Figure 4.31(b) descend approximately halfway into the domain, which is the same order of magnitude as the distance the plumes in the field data have descended in Figure 4.30(b). This is a key feature of three-dimensional dry lakes that is absent from two-dimensional simulations.

The data obtained by Lasser et al. (2023) also provides the means to determine the length scales of the polygons appearing at multiple locations at each dry lake, for which the Rayleigh number was also computed. Figure 4.32 shows the linear stability diagram for  $h = 10$  from Section 4.2 with the field data overlaid. This is a reasonable approximation since the results from the linear stability analysis converge quickly as  $h$  is increased and the depth of the dry lakes is unknown but acknowledged to be as large as  $H \approx 150$  m (Güler & Thyne, 2004). The triangles show the field data collected from Owens Lake, Badwater Basin and Sua Pan, all of which lie above  $Ra_c$ , indicating that the linear stability analysis

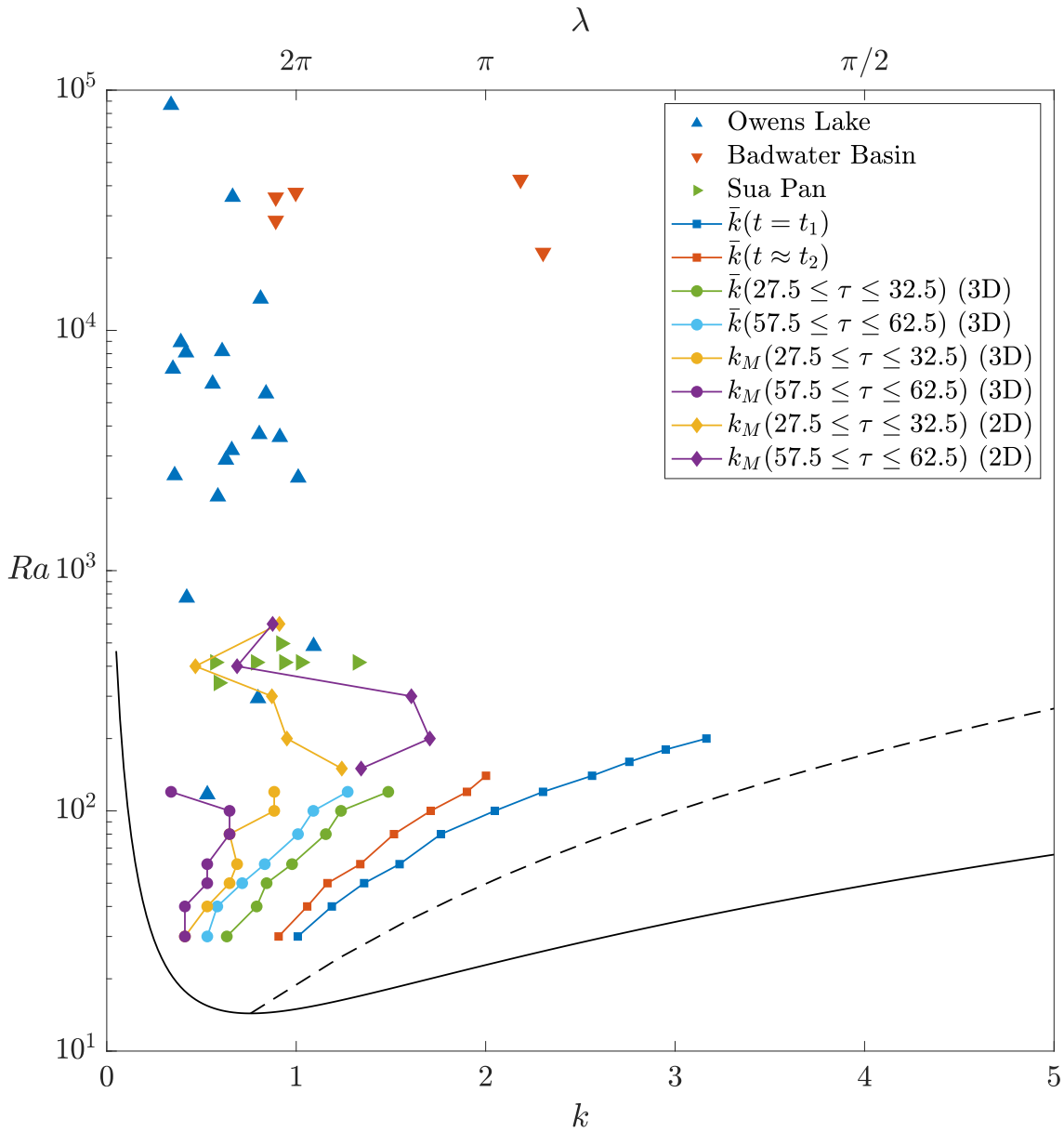


Figure 4.32: Field data from Owens Lake, Badwater Basin and Sua Pan displaying the observed wavenumbers at multiple sites at each dry lake along with values measured for the average and dominant wavenumber from simulations with varying  $Ra$ .

predicts an instability for these field conditions. In addition, the pattern wavenumbers observed at the field sites are smaller than the most unstable wavenumber for each  $Ra$ . The average wavenumber at  $t = t_1$  and  $t \approx t_2$  for  $h = 10$  (see Figure 4.26(b)) are shown by the squares in Figure 4.32. The average and dominant wavenumbers have also been time-averaged over 5  $\tau$  units, centred at both  $\tau \approx 30$  and  $\tau \approx 60$  for  $30 \leq Ra \leq 120$ , shown by the circles in Figure 4.32. This data shows that the average wavenumber has decreased from  $t \approx t_2$ , with the value at  $\tau \approx 60$  being smaller than the value at  $\tau \approx 30$ , indicating the decrease in the average wavenumber as the simulations progress. The dominant wavenumber has decreased further still, displaying the larger pattern scale that the computation of the dominant wavenumber identifies. However, at  $\tau \approx 30$  and  $\tau \approx 60$ , the dominant wavenumber does not display a clear dependence on  $Ra$  as the average wavenumber does, suggesting that later in the simulations, the Rayleigh number has a weaker effect on the dominant wavenumber than at earlier times. To obtain data for higher  $Ra$ , two-dimensional simulations are used to compute the time averaged dominant wavenumber centred at  $\tau \approx 30$  and  $\tau \approx 60$  for  $150 \leq Ra \leq 600$ , shown by the diamonds in Figure 4.32. This data does not show any particular trend as  $Ra$  is increased, which might be due to the poor performance of this metric on two-dimensional simulations. This limitation is discussed further in Section 5.2.2. Again, the depth used for the simulations was  $h = 10$ , which is recognised as not accurately reflecting the actual depth of dry lakes in nature.

The corresponding pattern scale,  $\lambda = 2\pi/k$ , has also been computed and is shown on the upper horizontal axis of Figure 4.32. From the field data (Lasser et al., 2023), the pattern scales observed at Badwater Basin were in the range  $0.55 \text{ m} \leq \lambda \leq 1.42 \text{ m}$ , at Owens Lake they were in the range  $0.87 \text{ m} \leq \lambda \leq 3.02 \text{ m}$  and at Sua Pan they were in the range  $0.41 \text{ m} \leq \lambda \leq 0.95 \text{ m}$  (see Table 2.1). For the dominant wavenumbers from the 3D simulations, the corresponding pattern wavelengths all lie in the interval  $1.1 \text{ m} \leq \lambda \leq 2.8 \text{ m}$  (using a characteristic length of 15 cm (Lasser et al., 2023)). In addition, the dominant wavenumber of the time averaged flux for  $Ra = 120$  (see Figure 4.29(d)) is  $k_M \approx 0.64$ , corresponding to a pattern scale of approximately 1.5 m.



# Chapter 5

## Discussion

### 5.1 Overview

The system presented in Section 2.2 models the competing effects of the evaporation-driven throughflow and the buoyancy of the fluid due to the varying salt content. These physical phenomena alone are enough to predict the emergence of dynamics that are suggestive of the surface crust pattern observed at dry lakes worldwide. In Chapter 2, a three-dimensional model for salt lakes was described, a natural extension to the two-dimensional model presented by Lasser et al. (2021) with the addition of a finite depth. This results in the system being controlled by two free parameters, the Rayleigh number and the nondimensional lake depth. A steady-state solution exists, a balance of upward advection driven by evaporation at the surface and the downward diffusion of salt. In Section 4.2, the linear stability of the base state was analysed and for Rayleigh numbers above a critical value, which was found to be  $Ra_c \approx 14.35$  for  $h = 10$ , this state is linearly unstable. This instability resulted in small-amplitude patterns in the surface flux of salinity. The values of the critical Rayleigh number and the critical wavelength computed in Section 4.2 were in good agreement with previous analyses (Homsy & Sherwood, 1976) and converge to the critical values of the infinitely deep lake (Duijn et al., 2002; Lasser et al., 2021; Wooding, 1960) as the lake depth increases. The saturation phase of the linear instability leads to a secondary instability, characterised by the development of plumes and chaotic dynamics. Subsequently, the pattern in the surface flux increases in amplitude and polygons begin to emerge (see Section 4.3). The three-dimensional simulations display complex dynamics as plumes descend and interact with each other. Simultaneously, protoplumes are created within the macroscopic network of downwelling currents

and are attracted toward the larger megaplumes, resulting in a dynamic pattern in the surface flux. Once the downwelling plumes reach the bottom of the domain, the system transitions towards a statistically steady end-state and the values of the salinity flux and wavenumbers fluctuate around a particular value. In Section 4.5.1, two important times were identified. The first is the time at which downwelling plumes reach the bottom of the domain, indicated by the growth of the average salinity flux out through the bottom of the domain. This is the time at which the whole simulation no longer resembles an infinitely deep lake. The second key time is when the disturbance from the bottom boundary reaches the surface. This was computed from analysing several curves of the surface flux: when the average surface flux curve of a particular  $h$  departs from the bulk behaviour of the curves for larger values of  $h$ , the surface flux has been influenced by the bottom boundary. The particular values of the average salinity fluxes and the wavenumbers were analysed at these two times and their dependence on the lake depth was explored. In Section 4.5.2, the effect of varying the Rayleigh number was investigated. The speed at which upwelling and downwelling plumes travel was found to increase approximately linearly with  $Ra$ , demonstrating how the dynamics occur on smaller time scales for larger  $Ra$ . In addition, as  $Ra$  is increased, the wavenumbers of the surface pattern increase, resulting in a smaller pattern scale. Finally, in Section 4.6, the results from numerical simulations were compared to the data obtained in the field. The pattern scales of the surface flux of salinity exhibited by the three-dimensional simulations were in excellent agreement with the scale of the crust pattern observed at dry lakes such as Owens Lake, Badwater Basin and Sua Pan.

### 5.1.1 Comparisons

Although the system simulated in this thesis differs from the two-sided convection system, the dynamics displayed here are qualitatively similar to other three-dimensional simulations (De Paoli et al., 2022; Fu et al., 2013; Hewitt et al., 2014). However, the main difference between the dry lake system and other systems that model convection in porous media is the applied throughflow which takes into account the evaporation of water at the surface. This gives rise to a Rayleigh number, the ratio of the buoyancy velocity to the applied evaporation rate, which is not the same as the Rayleigh number appearing in the two-sided convection system. To this extent, comparing how, for example, the average wavenumber depends on the Rayleigh number in both systems gives different results. Another key quantity that two-sided convection studies utilise is the Nusselt number,  $Nu$ , the ratio of the total solute (or heat) transfer compared to the conductive transfer. This

measure is useful for systems without throughflow, where the base state consists of transport via conduction only ( $Nu = 1$ ) and the onset of convection causes the Nusselt number to increase as the transport of solute is enhanced by fluid flow. For dry lakes, the solute transport is best measured by the salinity transport to the surface, as this has physical relevance to the salt available for crust growth. On the other hand, an important quantity in one-sided convection is the dissolution flux (Slim, 2014), measuring the rate at which solute is transported into the domain. This is relevant in the case of  $\text{CO}_2$  sequestration since it directly measures the rate of  $\text{CO}_2$  dissolution and the impact the porous medium is having at storing the greenhouse gas. This quantity is more comparable to the surface flux of salinity in dry lakes as it measures the same phenomenon: the transport of the dissolved quantity through the surface. In this context, the dry lake system is more similar to the one-sided convection system. However, in contrast with one-sided systems, the dry lake Rayleigh number measures how vigorous the convection is, and the Rayleigh number appearing in one-sided convection is more comparable to the nondimensional lake depth,  $h$ , since this is the parameter that measures how far the bottom boundary is from the surface.

## 5.2 Limitations

### 5.2.1 Bottom Boundary Condition

In the results presented in Chapter 4, the bottom boundary condition used was the most natural one:

$$\langle w \rangle_{xy} = -1, \quad (5.1)$$

imposing only global mass conservation. This is the least constraining boundary condition for the vertical velocity (equivalently the vertical pressure gradient) at the bottom of the domain. However, this boundary condition can lead to problems when downwelling plumes reach the bottom of the domain. Since the mean upward flow through the bottom of the domain must balance the evaporation through the surface, downwelling flows that reach the bottom of the domain induce upwelling plumes initiating from the bottom boundary, enhancing the local upflow. The strength of these flows scales with the Rayleigh number, which, along with the Dirichlet boundary condition  $S = 0$  at the bottom of the domain, leads to large vertical gradients in the salinity, especially as the Rayleigh number is increased. Figure 5.1(a) illustrates the large gradients that emerge when the boundary condition (5.1) is used at  $Ra = 500$  and  $h = 10$ . The close proximity of the upwelling

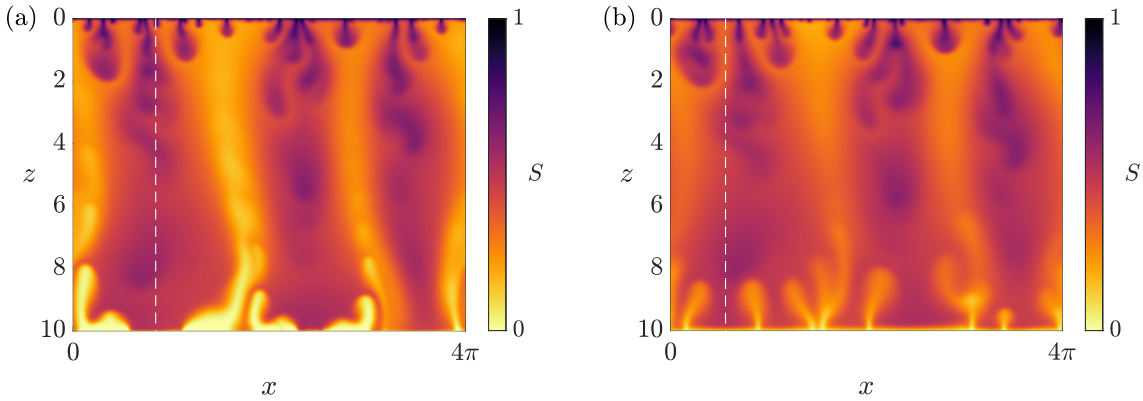


Figure 5.1: Salinity field of two 2D simulations at  $t \approx 10.1$  for  $Ra = 500$ ,  $h = 10$  and  $\Gamma_x = 4\pi$ . The bottom boundary conditions are (a)  $\langle w \rangle_x = -1$  at  $z = h$  and (b)  $w = -1$  at  $z = h$ . The white dashed lines represent the positions of the vertical salinity profiles shown in Figure 5.2.

regions of fluid with the downwelling regions of fluid also contributes to large horizontal gradients. These large gradients demand a more refined mesh close to the bottom boundary than what has already been constructed and therefore simulations have a tendency to diverge. Alternatively, the bottom boundary condition can be changed to a uniform upflow:

$$w = -1 \quad \text{at } z = h. \quad (5.2)$$

Figure 5.1(b) illustrates the same situation displayed in Figure 5.1(a) with the uniform boundary condition (5.2). Visually, this boundary condition appears to prevent the large-magnitude flows that are located at  $z = h$ , observed in Figure 5.1(a). In this case, the salinity field is drastically different, appearing more symmetrical than before. As the vertical velocity at  $z = h$  is now the same as the vertical velocity at  $z = 0$ , the symmetry of the system is only broken by the presence of the throughflow. However, since the strength of the throughflow is  $O(1)$ , the convective flows, the strengths of which are  $O(Ra)$ , are dominant leading to an apparent symmetry for large  $Ra$ . Also, the vertical salinity gradients in Figure 5.1(b) do not appear to be as large as those in Figure 5.1(a). The boundary layer profiles of the salinity near  $z = h$  are plotted in Figure 5.2 for both boundary conditions, showing the sharper boundary layer profile obtained for the natural boundary condition. However, further enquiry is needed to determine the behaviour of the salinity close to the boundary through the use of more mesh points.

In addition to the large velocities at the bottom boundary, the Dirichlet boundary condition  $S = 0$  further reinforces the sharp boundary layer seen in Figure 5.1(a), as the salinity must transition to zero where downwelling plumes touch the bottom of the domain. Modi-

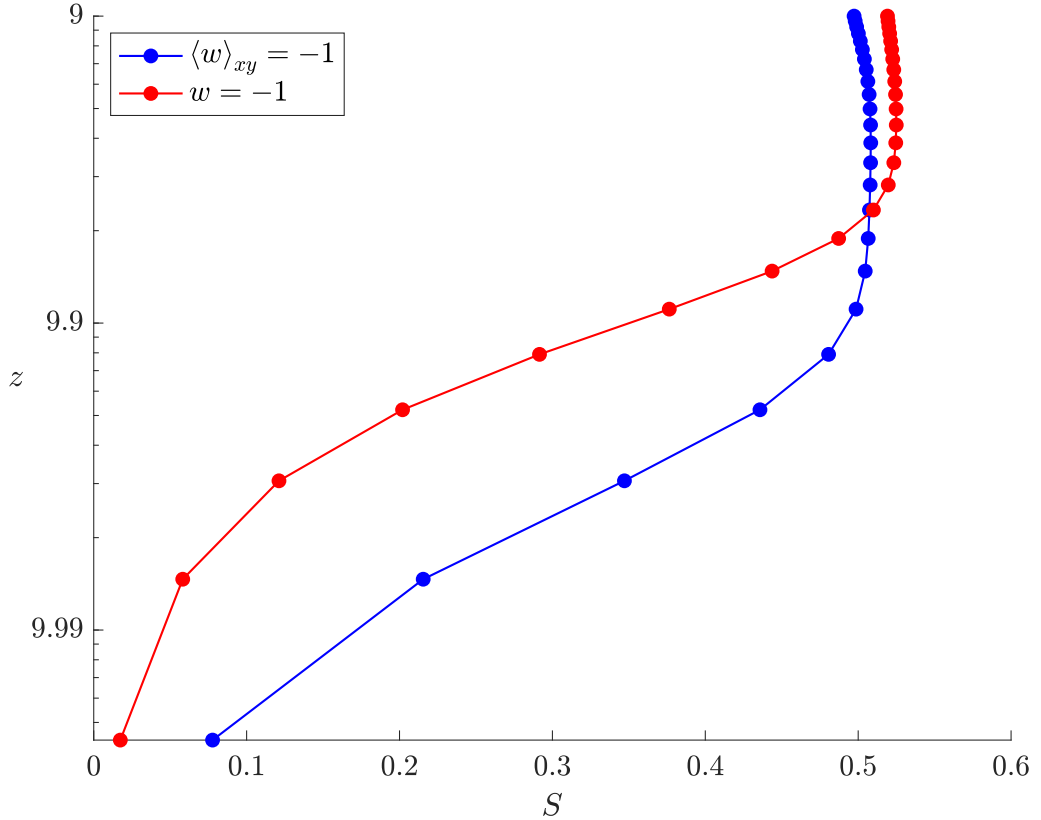


Figure 5.2: Vertical salinity profiles for  $Ra = 500$ ,  $h = 10$  and  $\Gamma_x = 4\pi$  at the bottom of the domain for both boundary conditions, located at the white dashed lines in Figure 5.1.

ifying this boundary condition may lead to more manageable salinity gradients, preventing simulations from diverging. Adopting the boundary conditions:

$$\frac{\partial S}{\partial z} = 0 \quad \text{at } z = h, \quad (5.3)$$

$$u = 0, \quad v = 0 \quad \text{at } z = h, \quad (5.4)$$

may be the least invasive option, constraining the vertical gradient of the salinity and imposing no horizontal flow but allowing the vertical velocity to be free. A piecewise condition may also be imposed, enforcing the salinity to vanish where the vertical velocity is negative and the vertical gradient of the salinity to vanish where the vertical velocity is positive:

$$\begin{cases} S = 0 & w \leq 0 \\ \frac{\partial S}{\partial z} = 0 & w > 0 \end{cases} \quad \text{at } z = h. \quad (5.5)$$

However, this is difficult to implement with the current numerical method since the boundary condition is spatially dependent on the sign of the vertical velocity.

	$\langle w \rangle_{xy}(z = h) = -1$	$w(z = h) = -1$
$\Delta t = 1 \times 10^{-5}$	Diverged	✓
$\Delta t = 5 \times 10^{-6}$	✓	✓

Table 5.1: Two-dimensional simulations at  $Ra = 500$ ,  $h = 10$  and  $\Gamma_x = 4\pi$  run with different time steps and bottom boundary conditions to test whether they diverge or not. Simulations labelled with a checkmark remained bounded.

The simulation shown in Figure 5.1(a) can be continued from a previously saved time, just before it diverged. This can be done for two different time steps and both boundary conditions and Table 5.1 shows which of these simulations diverge. These observations show that decreasing the time step with the natural boundary condition (5.1) can prevent the simulation from diverging. On the other hand, using the uniform boundary condition (5.2) avoids divergence for both values of the time step. This suggests that the natural boundary condition has more demanding numerical requirements for the time step than the uniform boundary condition does. Additionally, it would be of interest to investigate whether the mesh spacing in both the horizontal and vertical directions can be increased to avoid divergence.

Furthermore, in three dimensions, the salinity flux out through the bottom of the domain, defined by:

$$J_h = - \left. \frac{\partial S}{\partial z} \right|_{z=h}, \quad (5.6)$$

is plotted for a late-time in Figure 5.3 for two simulations with the two different boundary conditions. The natural boundary condition, shown in Figure 5.3(a),  $J_h$  displays larger values than in Figure 5.3(b), which shows  $J_h$  for the uniform boundary condition. This illustrates the larger vertical gradients in salinity displayed in the two-dimensional simulations shown in Figure 5.1(a). The more physically constraining boundary condition (5.2) may help to avoid simulations diverging when downwellings reach the bottom of the domain. The uniform boundary condition (Figure 5.3(b)) also mirrors what is seen at the surface: polygons denoting the locations of now upwelling fluid delimiting regions of heavier fluid impacting the bottom boundary. The upwelling fluid originating from the edges of the polygons has zero salinity at  $z = h$ , and so the vertical gradients of the salinity are weak, contributing to a small value of the flux. On the other hand, the heavier fluid

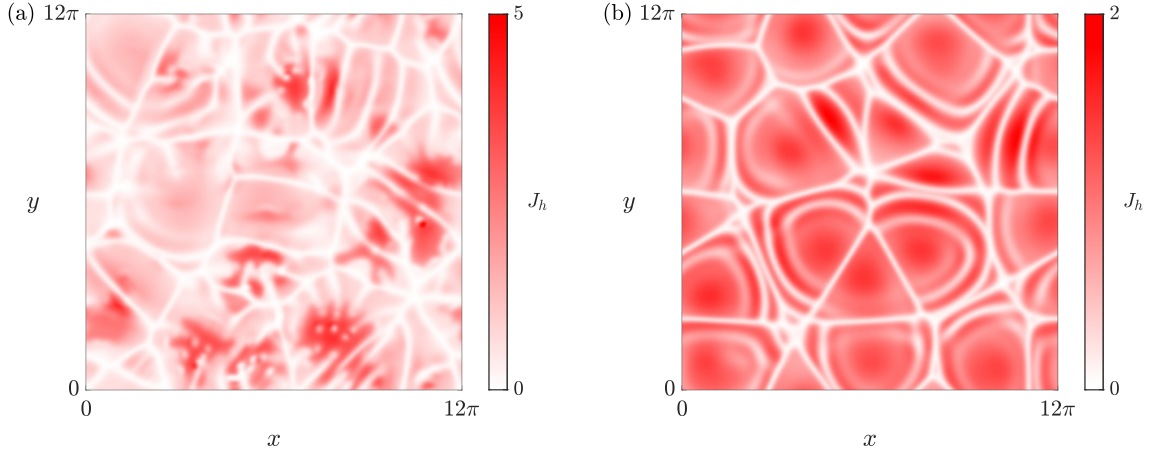


Figure 5.3: Salinity flux out through the bottom of the domain,  $J_h = -\partial S/\partial z$ , at  $t = 20$  for  $Ra = 100$  and  $h = 10$ . The natural boundary condition,  $\langle w \rangle_{xy} = -1$  at  $z = h$ , is shown in panel (a) and the uniform boundary condition,  $w = -1$  at  $z = h$ , is shown in panel (b).

impacting the bottom boundary contributes to larger salinity gradients and therefore a positive flux through the bottom boundary. The similarity of this pattern to the surface flux patterns owes itself to the approximate symmetry of the system when the uniform boundary condition is used.

An alternative way to avoid this problem is to simulate dry lakes with a depth large enough that downwelling flows will have diffused before they reach the bottom of the domain. The distance between plumes deep in the lake is approximately  $\lambda \approx 2\pi/k_M$ , using the most dominant wavenumber from the surface flux, which need a time  $t \sim \lambda^2$  to merge via diffusion. As plumes descend at a speed proportional to  $Ra$ , the depth at which this happens is  $z \sim Ra/k_M^2$ . This motivates a domain depth that scales approximately linearly with  $Ra$ , which gives rise to an increased computational requirement to avoid the problems described above. As described in Section 2.6, the two-sided Rayleigh number is equivalent to the dry lake Rayleigh number multiplied by the Péclet number:

$$Ra_{\text{TSC}} = Ra Pe = Ra \frac{EH}{\phi D} = Ra \frac{H}{L} = Ra h. \quad (5.7)$$

Requiring that  $h \sim Ra$  then results in the two-sided Rayleigh number scaling like  $Ra_{\text{TSC}} \sim Ra^2$ , illustrating that simulating  $Ra = 100$  for a dry lake is like simulating  $Ra_{\text{TSC}} = 10^4$  for the two-sided system. This highlights the significant computational demands of large  $Ra$  simulations.

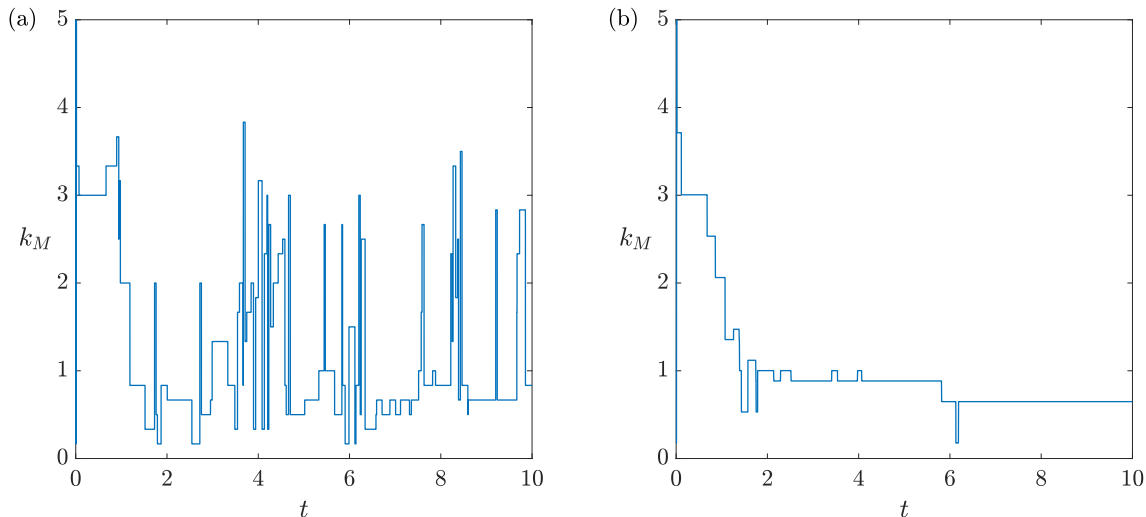


Figure 5.4: Dominant wavenumber for (a) a two-dimensional simulation and (b) a three-dimensional simulation with  $Ra = 100$ ,  $h = 10$  and  $\Gamma_x = \Gamma_y = 12\pi$ .

### 5.2.2 Dominant Wavenumber

Since the dominant wavenumber is determined to be that which has the highest spectral power, the allowed values are discretised. For two-dimensional simulations, the dominant wavenumber is computed from the surface flux directly, since no radial average is needed. This means that the dominant wavenumber is selected from  $k_i = 2\pi i/\Gamma_x$ , for  $i = 0, \dots, N_x/2$ . On the other hand, for three-dimensional simulations, the dominant wavenumber is determined from  $P(k)$  and so is discretised to the values determined by (4.13). Figure 5.4 shows the dominant wavenumber varying over time during a two- and three-dimensional simulation. As a result, the dominant wavenumber does not smoothly vary during a simulation and jumps from the allowed values. In particular, the range of values for the two-dimensional simulation is much larger than the three-dimensional simulation and the minimum value taken by  $k_M$  corresponds to a wavelength that spans the whole domain:  $k_M = 2\pi/L = 1/6$ . This highlights issues with the dominant wavenumber when it is used as an indicator for the overall pattern scale.

From the two-dimensional simulation shown in Figure 5.4(a), the surface flux at  $t \approx 6$  is plotted in Figure 5.5(a). This shows the structure of the upwelling and downwelling flows through the salinity transport to the surface: peaks in the flux correspond to downwellings and negative regions correspond to upwellings. In addition, the positive flux regions are much thinner than the negative flux regions. Figure 5.5(b) shows the power spectrum of the surface flux at this time as a function of the integer wavenumber. The solid red marker indicates the integer wavenumber that has the largest power (ignoring the constant mode).

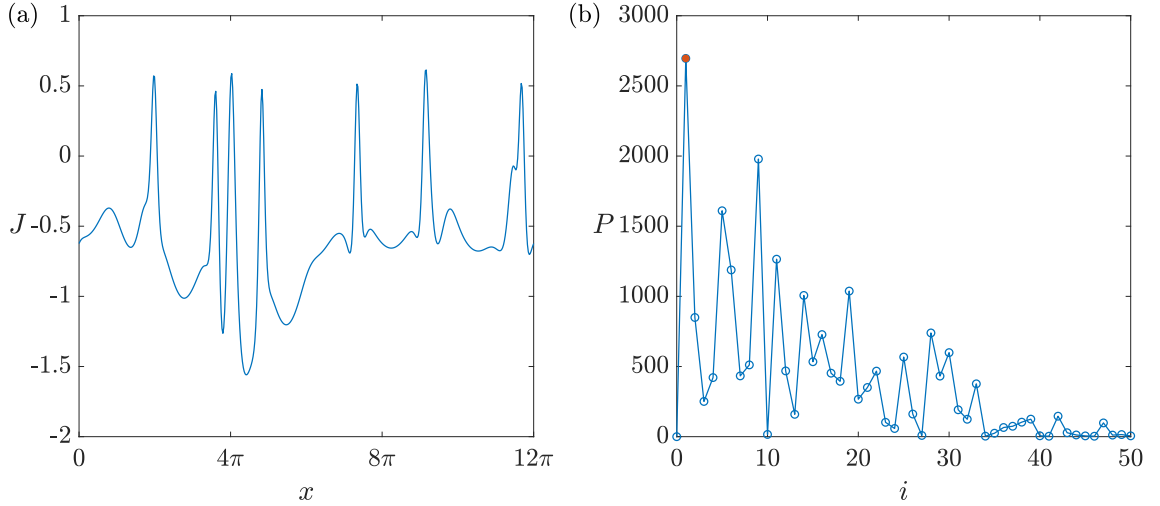


Figure 5.5: (a) Surface flux,  $J(x)$ , from a two-dimensional simulation ( $Ra = 100$ ,  $h = 10$  and  $\Gamma_x = 12\pi$ ). (b) Power spectrum of the surface flux against the integer wavenumber.

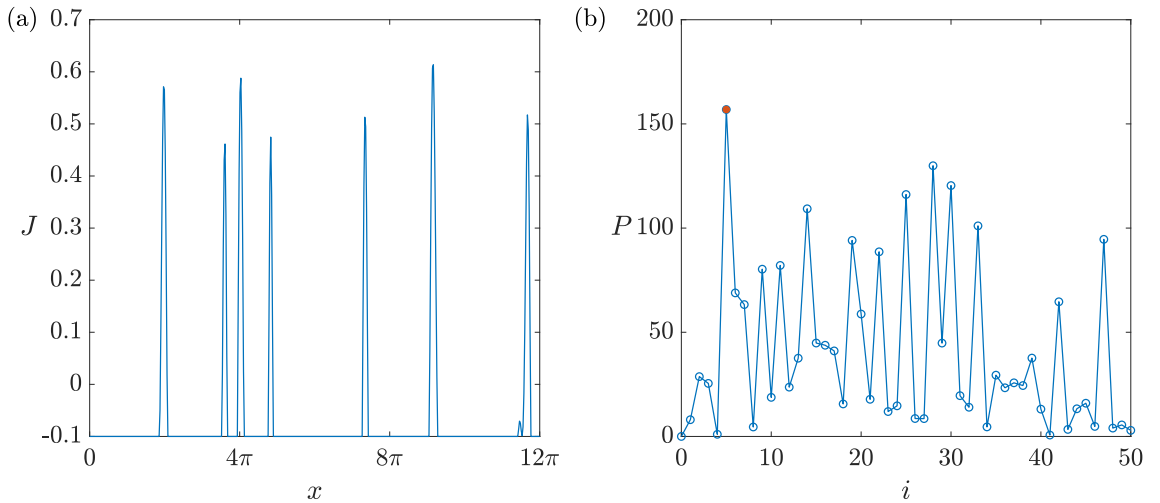


Figure 5.6: (a) Surface flux,  $J(x)$ , from a two-dimensional simulation ( $Ra = 100$ ,  $h = 10$  and  $\Gamma_x = 12\pi$ ) that has had a threshold applied to it: values with  $J < -0.1$  have been set to  $J = -0.1$ . (b) Power spectrum of the surface flux against the integer wavenumber.

The power spectrum indicates that the  $i = 1$  mode contains the most power, leading to a dominant wavenumber of  $k \approx 0.17$ . The surface flux shown in Figure 5.5(a) has a large contribution from the upwelling regions of fluid which introduces bias to the dominant wavenumber as it takes into account the structure of the upwelling flows. However, the pattern scale is determined by the spacing of the positive flux regions. So, to provide a better metric for the overall pattern scale, the surface flux may be post-treated by imposing a threshold on the negative values. For example, Figure 5.6(a) shows the surface flux when values that are smaller than  $-0.1$  are set to be equal to  $-0.1$ , eliminating the contribution from the structure of the upwellings in the computation of the dominant wavenumber. Again, the spectrum is shown in Figure 5.6(b), indicating that now the

dominant wavenumber corresponds to the  $i = 5$  mode, giving a value of  $k \approx 0.83$ . This post-treatment may provide not only more consistent results, avoiding the sporadic behavior of the dominant wavenumber seen in Figure 5.4, but also more accurate measurements of the overall pattern scale in the surface flux of salinity.

### 5.2.3 Crust Feedback

The modelling of dry lakes in this thesis has ignored the presence of a surface crust above the porous soil. However, coupling between the convective dynamics and the growth of the salt crust may contribute to a complex interplay between the presence of a crust and the subsurface fluid dynamics. Studies have shown that salt precipitation reduces the evaporation rate, acting as a barrier preventing moisture escaping from the surface (Nachshon et al., 2018). In the three-dimensional simulations, the surface pattern displays a tendency to slowly drift horizontally. This slow drift is expected to be due to the translational symmetry in the system since the equations and boundary conditions are invariant under the transformation:

$$x \mapsto x + x_0, \quad y \mapsto y + y_0, \quad (5.8)$$

where  $x_0$  and  $y_0$  are constants. Introducing a crust-evaporation feedback would break this symmetry, fixing the patterns in place and preventing the slow drift. This could be done by introducing a quantity to model the presence of a crust and allowing the evaporation rate at the surface to depend on this additional quantity. The effects of varying the evaporation rate over the surface of the domain have been explored in two dimensions (Lasser et al., 2021), but only by modulating the evaporation rate using a fixed wavenumber. The growth of a crust above a one-dimensional dry lake is explored further in Appendix A.

## 5.3 Perspectives

### 5.3.1 Evaporation Rate

The equations and boundary conditions that were solved in this thesis were:

$$\mathbf{u} = -\nabla p + Ra S \mathbf{e}_z, \quad (5.9)$$

$$\nabla \cdot \mathbf{u} = 0, \quad (5.10)$$

$$\frac{\partial S}{\partial t} + \mathbf{u} \cdot \nabla S = \nabla^2 S, \quad (5.11)$$

$$S = 1, \quad w = -1 \quad \text{at } z = 0, \quad (5.12)$$

$$S = 0 \quad \text{at } z = h. \quad (5.13)$$

The advantage of this system is the explicit appearance of the lake depth,  $h$ . This approach enabled a direct investigation of the lake depth by adjusting the position of the bottom boundary. However, the evaporation rate is present in both the Rayleigh number and the characteristic length ( $\phi D/E$ ), and thus investigating how the evaporation rate impacts the dynamics would modify both  $Ra$  and  $h$ . The limit  $E \rightarrow 0$  would imply both  $Ra \rightarrow \infty$  and  $h \rightarrow 0$ , preventing any comparisons to two-sided convection. Alternatively, the transformed system (see Section 2.6) may be used to study dry lakes instead. The equations and boundary conditions for this system are:

$$\mathbf{U} = -\nabla P + S\mathbf{e}_z, \quad (5.14)$$

$$\nabla \cdot \mathbf{U} = 0, \quad (5.15)$$

$$\frac{\partial S}{\partial t} + \mathbf{U} \cdot \nabla S = \frac{1}{Ra Pe} \left( \nabla^2 S + Pe \frac{\partial S}{\partial z} \right), \quad (5.16)$$

$$S = 1, \quad W = 0 \quad \text{at } z = 0, \quad (5.17)$$

$$S = 0 \quad \text{at } z = 1. \quad (5.18)$$

This introduces some flexibility that the original dry lake system does not have since the strength of throughflow can be modified by changing the value of  $Pe$ . Setting  $Pe = 0$  is allowed in this system because the product  $Ra Pe$  is equivalent to the Rayleigh number of two-sided convection,  $Ra_{\text{TSC}} = HV_B(\phi D)^{-1}$ , which is independent of the evaporation rate, and by doing this, the system given by (5.14)–(5.18) becomes the two-sided system described in Chapter 2. This would allow the effect of the evaporation rate to be studied by only changing the contribution of the extra source term on the right-hand side of (5.16) without modifying the location of the lower boundary. This not only provides the means to control the effect of the evaporation rate but also allows more direct comparisons to be made with the two-sided convection system. Additionally, the dependence of the pattern scale on the evaporation rate may be explored in more detail using this formulation and

any further studies of dry lakes may want to adopt this system instead.

### 5.3.2 Patterns

In Section 4.4, the creation and dynamics of protoplumes were discussed. However, the process of how the protoplumes form was not fully explored. These smaller features have a large contribution to the surface pattern and cause it to change over a small timescale. Protoplumes initiate from the surface and can form either isolated from the macroscopic pattern or connecting two different edges of a cell. Once protoplumes have developed, they merge with neighbouring macroscopic plumes and so they are only present near the surface of the domain. Protoplumes contribute to the surface pattern, as they enhance the local salinity flux to the surface, resulting in the surface pattern inheriting the complex dynamics that the protoplumes display. The formation and dynamics of protoplumes would be of interest for further work on dry lakes.

Throughout this study, patterns have been described qualitatively, but no further investigation has been done to characterise the quantitative nature of the polygons that emerge in the surface salinity flux. For example, what proportion of the surface pattern are hexagons? What about squares? In the case of two-sided convection with no throughflow, De Paoli et al. (2022) measured the areas of polygons observed close to the boundaries, finding similar distributions of the areas of the polygons as the Rayleigh number is increased. In addition, when the distribution of polygons is measured in terms of their circularity parameter,  $\mathcal{C} = 4\pi A\Pi^{-2}$ , ( $A$  is the area of the polygon and  $\Pi$  is the perimeter), the most common value was found to be  $\mathcal{C} \approx 0.8$ , corresponding to nearly square cells. Further to this, Domokos and Regős (2024) have constructed an evolution model for fracture networks that involves discrete events where cells are split into two via the introduction of a new edge in the network, followed by a rearrangement of the edges and nodes (Goehring, 2013). Dry lake simulations share some features of this dynamical system due to the nature of the protoplumes dividing convective cells. However, they have extra dynamics due to the merging events of the protoplumes and megaplumes, removing cells in the network that the evolution model does not include. Characterising the distribution of polygons in the simulated surface pattern and how the proportions of each type of shape evolve over time would be interesting to investigate further, as well as obtaining the equivalent data from dry lakes worldwide. This would allow further quantitative comparisons to be made between simulations and field observations.

### 5.3.3 Heterogeneous Porous Media

For a heterogeneous porous medium, where the porosity and the permeability may depend on space, Darcy's law is generalised to:

$$\hat{\mathbf{u}} = -\frac{\boldsymbol{\kappa}}{\mu} \cdot (\hat{\nabla}\hat{p} - \rho\hat{\mathbf{f}}), \quad (5.19)$$

where the permeability is now a second-rank tensor. The equation for the conservation of mass,

$$\frac{\partial}{\partial \hat{t}}(\phi\rho) + \hat{\nabla} \cdot (\rho\hat{\mathbf{u}}) = 0, \quad (5.20)$$

is unchanged and incompressibility still holds (provided the porosity is independent of time):

$$\hat{\nabla} \cdot \hat{\mathbf{u}} = 0. \quad (5.21)$$

However, the conservation of salt must be modified to:

$$\phi \frac{\partial C}{\partial \hat{t}} + \hat{\mathbf{u}} \cdot \hat{\nabla} C = D \hat{\nabla} \cdot (\phi \hat{\nabla} C), \quad (5.22)$$

assuming the diffusivity of salt remains constant. For homogeneous anisotropic porous media, where the solid matrix has a different permeability in the vertical direction than the two horizontal directions, the permeability tensor can be written as:

$$\boldsymbol{\kappa} = \begin{pmatrix} \kappa_h & 0 & 0 \\ 0 & \kappa_h & 0 \\ 0 & 0 & \kappa_v \end{pmatrix} = \kappa_v \begin{pmatrix} \gamma^{-1} & 0 & 0 \\ 0 & \gamma^{-1} & 0 \\ 0 & 0 & 1 \end{pmatrix}, \quad (5.23)$$

where  $\kappa_h$  and  $\kappa_v$  are the permeabilities in the horizontal and vertical direction respectively and  $\gamma = \kappa_v/\kappa_h$ . In this case, Darcy's law becomes:

$$\hat{u} = -\frac{\kappa_h}{\mu} \frac{\partial \hat{p}}{\partial \hat{x}} \quad (5.24)$$

$$\hat{v} = -\frac{\kappa_h}{\mu} \frac{\partial \hat{p}}{\partial \hat{y}} \quad (5.25)$$

$$\hat{w} = -\frac{\kappa_v}{\mu} \left( \frac{\partial \hat{p}}{\partial \hat{z}} - \rho g \right). \quad (5.26)$$

This is useful in a situation where the porous medium has less resistance to flow in the horizontal directions than the vertical direction ( $\gamma \leq 1$ ). De Paoli et al. (2016) showed that, in a two-sided system, the solute transport was enhanced when  $\gamma < 1$  compared

to the isotropic case ( $\gamma = 1$ ). Flows in sedimentary rock typically exhibit anisotropic permeability (Poulet et al., 2023), due to processes such as compaction that provide more resistance to flow vertically than horizontally. Thus, with further field data, generalising the dry lake system to an anisotropic porous medium may result in a more realistic model if differing permeabilities are observed in the porous soil.

# Appendix A

## One-Dimensional Crust Growth

### A.1 Introduction

In the work presented in this thesis, the presence of the surface crust has been ignored. To eventually arrive at a model that incorporates the crust, the growth of one must be understood. In this chapter, the growth of a one-dimensional crust will be investigated, ignoring the horizontal directions and therefore any convection that may be occurring in the porous soil beneath the surface. A model will be proposed where a crust may grow above the surface of the porous soil and the subsequent growth rate of the crust will be investigated. This work was undertaken as part of a David Crighton Fellowship at the Department of Applied Mathematics and Theoretical Physics, University of Cambridge under the supervision of Grae Worster.

### A.2 Model

The dry lake (porosity  $\phi$ ) will now assumed to be infinitely deep, occupying the region  $0 \leq z < \infty$ . A salt crust is allowed to develop above the dry lake ( $z < 0$ ) surface and grows as a porous structure itself, with solid fraction  $\xi$  (porosity  $1 - \xi$ ) and grows due to the precipitation of salt resulting from the evaporation of water at a rate  $E$ . This induces a throughflow within the porous soil and the crust, denoted by  $V$ . The salt crust, which has thickness  $\eta$ , is assumed to be fully saturated in brine since the water table lies close to the surface (Bryant, 2003; Reynolds et al., 2007). The brine has a salt concentration equal to the saturation concentration,  $C_s$ , and it is assumed that far away from the surface, the concentration is the background salt concentration,  $C_0$ . This set-up is sketched in Figure

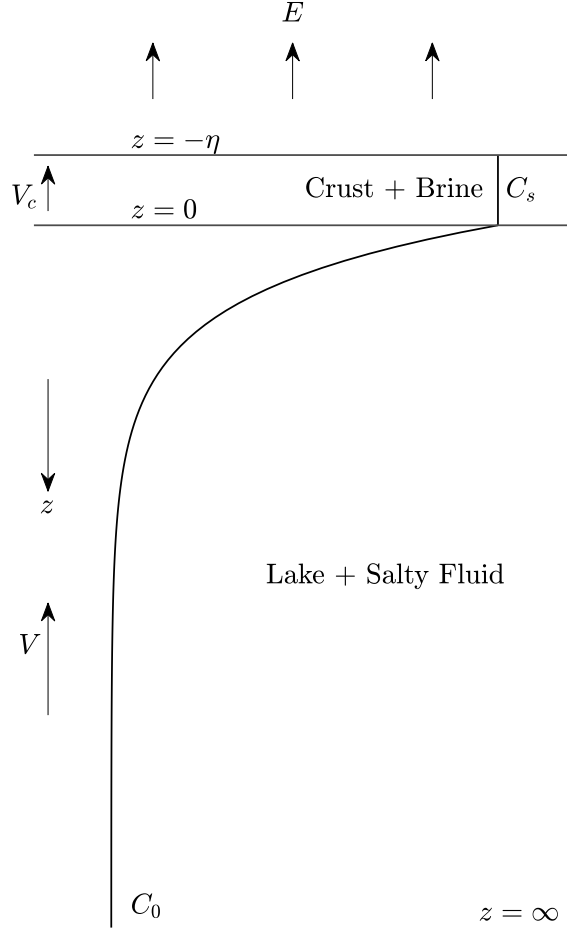


Figure A.1: Sketch of the initial 1D model. The lake occupies  $0 \leq z \leq \infty$  and the overlying crust has a thickness  $\eta$ . An evaporation rate of magnitude  $E$  is applied at the surface which results in a throughflow both in the porous soil ( $0 \leq z \leq \infty$ ) and the crust ( $-\eta \leq z \leq 0$ ).

**A.1.** The salt profile in the lake is governed by the one-dimensional advection-diffusion equation:

$$\phi \frac{\partial C}{\partial t} - V \frac{\partial C}{\partial z} = \phi D \frac{\partial^2 C}{\partial z^2}, \quad 0 \leq z < \infty, \quad (\text{A.1})$$

where  $C$  is the concentration of salt,  $D$  is the diffusivity and  $V$  is the Darcy velocity of the throughflow induced by the evaporation. The far-field boundary condition is:

$$C \rightarrow C_0 \quad \text{as } z \rightarrow \infty. \quad (\text{A.2})$$

In the crust, the salt concentration is constant:

$$C = C_s, \quad -\eta \leq z \leq 0. \quad (\text{A.3})$$

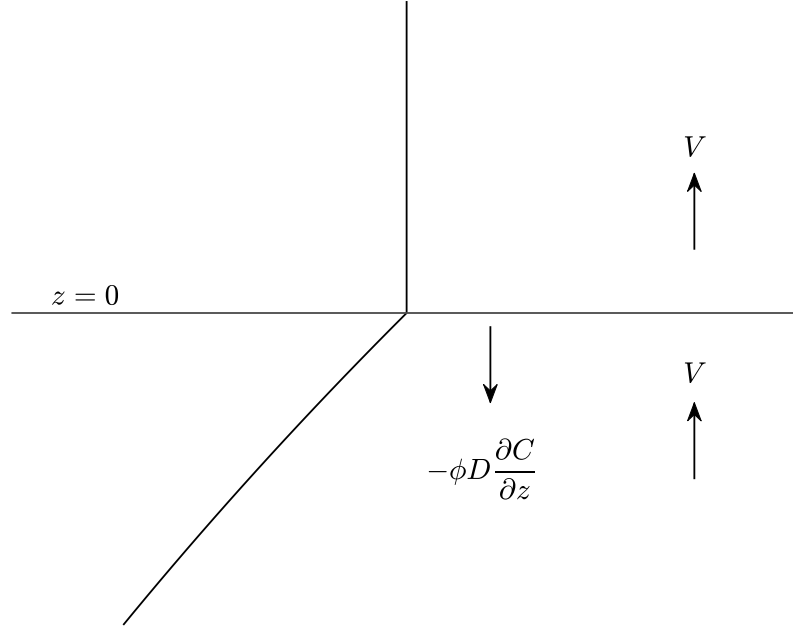


Figure A.2: Sketch of the initial lake–crust interface illustrating an inconsistent salt flux across  $z = 0$ .

The salt profiles must be continuous at the lake–crust interface ( $z = 0$ ) and so:

$$C = C_s \quad \text{at } z = 0. \quad (\text{A.4})$$

However, by considering the fluxes of salt at the lake–crust interface, it is clear that there is an inconsistency in the model. This is sketched in Figure A.2, The advective fluxes balance, since the salt is continuous at the interface and the throughflow is identical in the lake and the crust, but there is an additional diffusive flux arising from the gradient of the salt profile in the lake. The increase in the downward transport of salt in the lake must be balanced by the crust dissolving. Thus, an additional region of pure brine must be considered in this set-up, which is assumed to lie above the porous soil, and the crust is assumed to float above the brine. This is sketched in Figure A.3. The brine layer has thickness  $b$  and occupies  $-b \leq z \leq 0$  and the crust has thickness  $\eta$  and occupies  $-b - \eta \leq z \leq -b$ . In Section A.4, the weight of the crust will be taken into account and the effect of the crust sinking into the brine layer will be considered to develop the model further. In addition to the advection and diffusion of salt in the porous soil of the lake given by (A.1), the governing equation for the advection and diffusion of salt in the brine layer is:

$$\frac{\partial C}{\partial t} - V \frac{\partial C}{\partial z} = D \frac{\partial^2 C}{\partial z^2}, \quad -b \leq z \leq 0. \quad (\text{A.5})$$

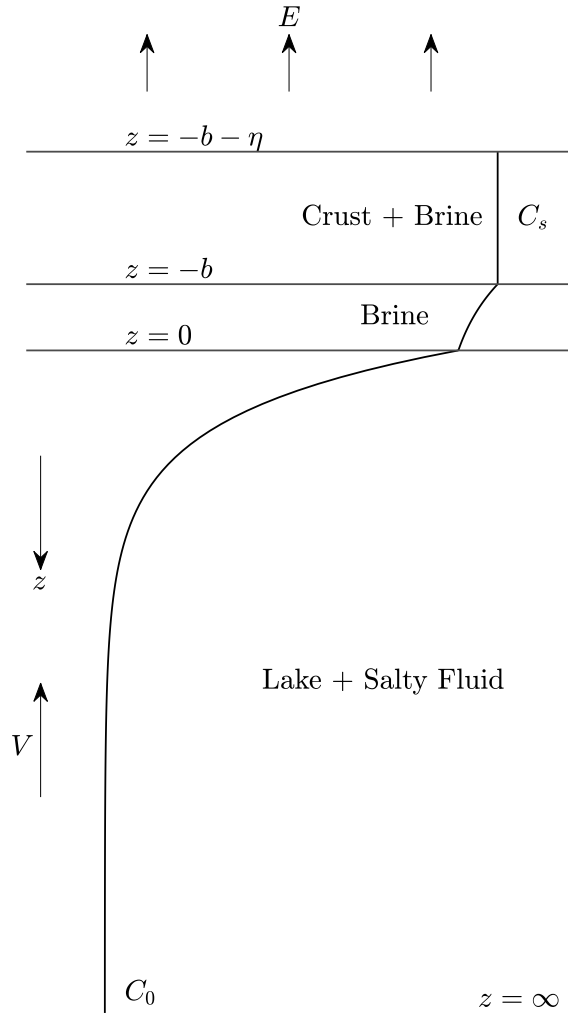


Figure A.3: Sketch of the 1D model. The lake occupies  $0 \leq z < \infty$ , the brine layer has thickness  $b$  and the overlying crust has thickness  $\eta$ .

The boundary and interfacial conditions that accompany these equations are:

$$C \rightarrow C_0 \quad \text{as } z \rightarrow \infty, \quad (\text{A.6})$$

$$C = C_s \quad \text{at } z = -b. \quad (\text{A.7})$$

$$C \text{ continuous} \quad \text{at } z = 0, \quad (\text{A.8})$$

$$\text{Salt flux continuous} \quad \text{at } z = 0, \quad (\text{A.9})$$

$$\text{Conservation of water} \quad \text{at } z = -b - \eta, \quad (\text{A.10})$$

$$\text{Conservation of salt} \quad \text{at } z = -b. \quad (\text{A.11})$$

### A.2.1 Steady State Solution

The system (A.1)–(A.8) can be solved for a steady state, denoting  $C_i = C(z = 0)$ . The following profiles for the salt concentration are obtained:

$$C = C_0 + (C_i - C_0) \exp\left(-\frac{z}{\phi L}\right), \quad (\text{A.12})$$

$$C = C_i + \frac{C_s - C_i}{\exp(b/L) - 1} \left[ \exp\left(\frac{-z}{L}\right) - 1 \right], \quad (\text{A.13})$$

where  $L = D/V$ . The value of  $C_i$  can be determined by imposing (A.9), the continuity of salt flux at  $z = 0$ :

$$-\phi D \left. \frac{\partial C}{\partial z} \right|_{z=0^+} = -D \left. \frac{\partial C}{\partial z} \right|_{z=0^-}, \quad (\text{A.14})$$

$$\implies C_i = \frac{C_s + C_0 [\exp(b/L) - 1]}{\exp(b/L)}. \quad (\text{A.15})$$

Equation (A.15) can be rearranged into:

$$(C_s - C_i) \exp\left(\frac{b}{L}\right) = (C_s - C_0) \left[ \exp\left(\frac{b}{L}\right) - 1 \right], \quad (\text{A.16})$$

allowing the salt profile in the brine layer to be written as:

$$C = C_i + \frac{C_s - C_0}{\exp(b/L)} \left[ \exp\left(-\frac{z}{L}\right) - 1 \right]. \quad (\text{A.17})$$

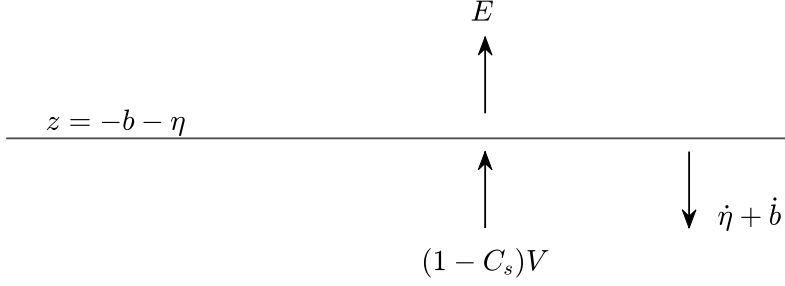


Figure A.4: In the frame of reference of the crust–air interface, fluid descends at speed  $\dot{\eta} + \dot{b}$  in the crust, with mass  $(1 - \xi)(1 - C_s)$ . Additionally, the throughflow transports a mass of water  $(1 - C_s)$  at speed  $V$  and water leaves by evaporation at rate  $E$ .

### A.2.2 Conservation Equations

In addition to the governing equations and boundary conditions, the total amount of salt and water must be conserved. Global salt conservation implies that salt entering the bottom of the lake must be accommodated in the lake, the brine layer or the crust:

$$C_0 V = \frac{d}{dt} \int_0^\infty \phi C \, dz + \frac{d}{dt} \int_{-b}^0 C \, dz + \bar{C} \dot{\eta} \quad (\text{A.18})$$

where  $\bar{C} = \xi + (1 - \xi)C_s$  denotes the average salt concentration in the crust (solid fraction and fluid fraction) and the dot over a variable indicates the full time derivative of that variable:  $\dot{\eta} = d\eta/dt$ . Using (A.1)–(A.7), this condition becomes

$$C_0 V = \int_0^\infty \frac{\partial}{\partial z} \left( CV + \phi D \frac{\partial C}{\partial z} \right) dz + C_s \dot{b} + \int_{-b}^0 \frac{\partial}{\partial z} \left( CV + D \frac{\partial C}{\partial z} \right) dz + \bar{C} \dot{\eta}, \quad (\text{A.19})$$

$$\implies C_0 V = C_s \dot{b} + \bar{C} \dot{\eta}. \quad (\text{A.20})$$

Global water conservation is equivalent to local water conservation at the surface of the crust. At the crust–air interface, any difference in the flux of water across  $z = -b - \eta$  must be accommodated in the growth of the crust. This situation is sketched in Figure A.4. Thus, at the crust–air interface:

$$(1 - C_s) V - E = (1 - \xi)(1 - C_s) (\dot{\eta} + \dot{b}). \quad (\text{A.21})$$

Finally, at the crust–brine interface, any imbalance in the salt flux must be accounted for in the movement of the interface:

$$(\bar{C} - C_s) \dot{b} = -D \left. \frac{\partial C}{\partial z} \right|_{z=-b}, \quad (\text{A.22})$$

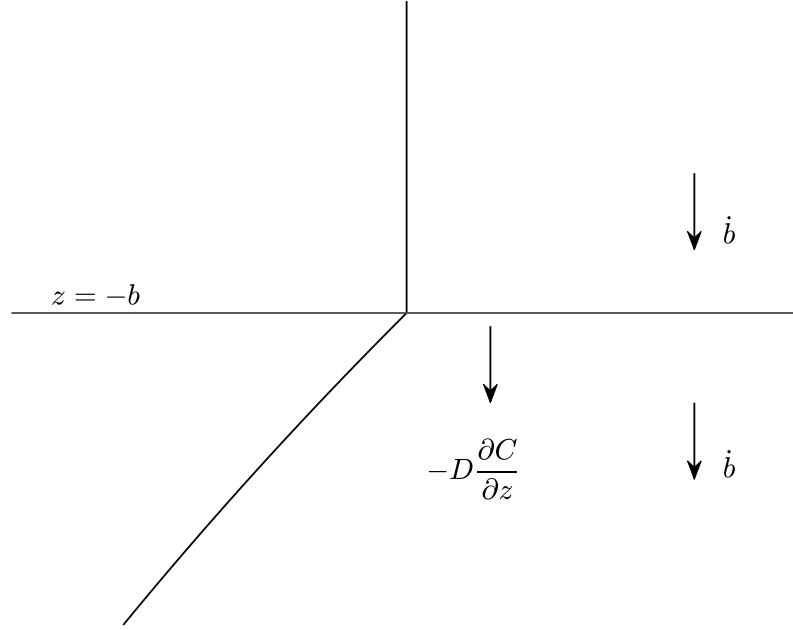


Figure A.5: In the frame of reference of the crust–brine interface, crust approaches at speed  $\dot{b}$  with average concentration  $\bar{C}$  and brine moves away at speed  $\dot{b}$  with a concentration profile given by (A.13).

$$\implies \xi(1 - C_s)\dot{b} = (C_s - C_0)V, \quad (\text{A.23})$$

and is sketched in Figure A.5.

### A.2.3 Solution

A solution to the following system of equations is sought:

$$C_0V = C_s\dot{b} + \bar{C}\dot{\eta}, \quad (\text{A.24})$$

$$(1 - C_s)V - E = (1 - \xi)(1 - C_s)(\dot{\eta} + \dot{b}), \quad (\text{A.25})$$

$$\xi(1 - C_s)\dot{b} = (C_s - C_0)V. \quad (\text{A.26})$$

This system consists of three equations for the unknown variables  $V$ ,  $\dot{\eta}$  and  $\dot{b}$  (assuming  $E$  is known). Upon eliminating  $\dot{b}$ , two equations for  $\dot{\eta}$  in terms of  $V$  are obtained:

$$\bar{C}\dot{\eta} = \frac{C_0\bar{C} - C_s^2}{\xi(1 - C_s)}V, \quad (\text{A.27})$$

$$\dot{\eta} = \frac{\xi(1 - C_0) - (C_s - C_0)}{\xi(1 - \xi)}V - \frac{E}{(1 - \xi)(1 - C_s)}. \quad (\text{A.28})$$

Equations (A.27) and (A.28) represent two straight lines in the  $(V, \dot{\eta})$ -plane. For there to be a solution with  $\dot{\eta} > 0$ , the gradient of both lines must be positive:

$$C_0 > \frac{C_s^2}{\bar{C}}, \quad (\text{A.29})$$

$$\xi + (1 - \xi) C_0 > C_s. \quad (\text{A.30})$$

Additionally, as the  $\dot{\eta}$ -intercept is negative, the gradient of (A.28) must exceed the gradient of (A.27):

$$\frac{\xi(1 - C_0) - (C_s - C_0)}{\xi(1 - \xi)} > \frac{C_0\bar{C} - C_s^2}{\xi(1 - C_s)\bar{C}}. \quad (\text{A.31})$$

### A.3 Initial Value Problem

To explore how a crust grows from The natural starting point to explore how a crust grows is zero crust ( $\eta = b = 0$ ) and a uniform salt concentration in the lake ( $C = C_0$ ). This initial value problem is described by the equations:

$$\phi \frac{\partial C}{\partial t} - V \frac{\partial C}{\partial z} = \phi D \frac{\partial^2 C}{\partial z^2}, \quad (\text{A.32})$$

$$C \rightarrow C_0 \quad \text{as } z \rightarrow \infty, \quad (\text{A.33})$$

$$C = C_0 \quad \text{at } t = 0, \quad (\text{A.34})$$

$$\eta = b = 0 \quad \text{at } t = 0. \quad (\text{A.35})$$

The conservation of water gives a condition relating  $V$  to  $E$  and in the absence of a crust and brine layer, this is

$$(1 - C_0)V - E = \frac{d}{dt} \int_0^\infty \phi(1 - C) dz, \quad (\text{A.36})$$

and the conservation of salt implies

$$C_0V = \frac{d}{dt} \int_0^\infty \phi C dz. \quad (\text{A.37})$$

Upon simplification, and using (A.1) to evaluate the integral, these conditions yield

$$V = E, \tag{A.38}$$

$$CV + \phi D \frac{\partial C}{\partial z} = 0 \quad \text{at } z = 0. \tag{A.39}$$

Scaling lengths with  $L = D/E$ , time with  $T = L/E = D/E^2$ , the non-dimensional equation is

$$\phi \frac{\partial C}{\partial t} - v \frac{\partial C}{\partial z} = \phi \frac{\partial^2 C}{\partial z^2}, \quad z \in [0, \infty), \tag{A.40}$$

where  $v = V/E$  and with boundary conditions

$$C \rightarrow C_0 \quad \text{as } z \rightarrow \infty, \tag{A.41}$$

$$Cv + \phi \frac{\partial C}{\partial z} = 0 \quad \text{at } z = 0. \tag{A.42}$$

Once  $C(z = 0) = C_s$ , the growth of a crust and brine layer is permitted. Since the salt concentration in the lake is not in a steady state, the analysis carried out in Section A.2 requires modification. The local conservation of salt at the surface of the crust still implies that

$$(1 - C_s)v - 1 = (1 - \xi)(1 - C_s)(\dot{\eta} + \dot{b}), \tag{A.43}$$

and the crust–brine interfacial condition must be kept at

$$(\bar{C} - C_s)\dot{b} = - \left. \frac{\partial C}{\partial z} \right|_{-b}, \tag{A.44}$$

$$\implies \xi(1 - C_s)\dot{b} = - \left. \frac{\partial C}{\partial z} \right|_{-b}. \tag{A.45}$$

Finally, the global salt conservation equation is:

$$C_0v = \frac{d}{dt} \int_0^\infty \phi C \, dz + \frac{d}{dt} \int_{-b}^0 C \, dz + \bar{C}\dot{\eta}, \tag{A.46}$$

$$\implies C_s v = - \left. \frac{\partial C}{\partial z} \right|_{-b} + C_s \dot{b} + \bar{C} \dot{\eta}. \tag{A.47}$$

Thus, the whole system can be written as:

$$\phi \frac{\partial C}{\partial t} - v \frac{\partial C}{\partial z} = \phi \frac{\partial^2 C}{\partial z^2}, \quad z \in [0, \infty), \quad (\text{A.48})$$

$$\frac{\partial C}{\partial t} - v \frac{\partial C}{\partial z} = \frac{\partial^2 C}{\partial z^2}, \quad z \in [-b, 0], \quad (\text{A.49})$$

$$C \rightarrow C_0 \quad \text{as } z \rightarrow \infty, \quad (\text{A.50})$$

$$C = C_s \quad \text{at } z = -b, \quad (\text{A.51})$$

$$C \text{ continuous} \quad \text{at } z = 0, \quad (\text{A.52})$$

$$-\phi \left. \frac{\partial C}{\partial z} \right|_{0+} = - \left. \frac{\partial C}{\partial z} \right|_{0-}, \quad (\text{A.53})$$

$$(1 - C_s) v - 1 = (1 - \xi) (1 - C_s) (\dot{\eta} + \dot{b}), \quad (\text{A.54})$$

$$\xi (1 - C_s) \dot{b} = - \left. \frac{\partial C}{\partial z} \right|_{-b}, \quad (\text{A.55})$$

$$C_s v = - \left. \frac{\partial C}{\partial z} \right|_{-b} + C_s \dot{b} + \bar{C} \dot{\eta}. \quad (\text{A.56})$$

### A.3.1 Method of Solution

To solve this numerically on an infinite domain and a moving interface  $z = -b(t)$ , two transformations are used. The first is:

$$x = 1 - \exp(-z), \quad \frac{dx}{dz} = \exp(-z) = 1 - x, \quad (\text{A.57})$$

which maps  $[0, \infty)$  onto  $[0, 1]$ . The second is

$$x = \frac{z}{b}, \quad \frac{\partial x}{\partial z} = \frac{1}{b}, \quad (\text{A.58})$$

which maps  $[-b, 0]$  onto  $[-1, 0]$ . The equation for the salt profile in the lake becomes:

$$\phi \frac{\partial C}{\partial t} + (\phi - v) (1 - x) \frac{\partial C}{\partial x} = \phi (1 - x)^2 \frac{\partial^2 C}{\partial x^2}, \quad x \in [0, 1], \quad (\text{A.59})$$

and the equation for the salt profile in the brine layer becomes:

$$\frac{\partial C}{\partial t} - \frac{1}{b} (x\dot{b} + v) \frac{\partial C}{\partial x} = \frac{1}{b^2} \frac{\partial^2 C}{\partial x^2}, \quad x \in [-1, 0]. \quad (\text{A.60})$$

Starting from a uniform salt concentration  $C_0$  in  $[0, 1]$  and no crust or brine layer, the first stage is to solve for the salt concentration in  $[0, 1]$  with the zero salt flux condition:

$$Cv + \phi \frac{\partial C}{\partial x} = 0 \quad \text{at } x = 0. \quad (\text{A.61})$$

At  $t = t_s$ , the time at which  $C(z = 0) = C_s$ , the crust and brine layer can begin to grow. For a small brine layer thickness,  $b \ll 1$ , the salt profile satisfies

$$b^2 \frac{\partial C}{\partial t} - b (x\dot{b} + v) \frac{\partial C}{\partial x} = \frac{\partial^2 C}{\partial x^2}, \quad (\text{A.62})$$

$$\implies \frac{\partial^2 C}{\partial x^2} = 0, \quad (\text{A.63})$$

to leading order. The boundary conditions are:

$$-\phi \frac{\partial C}{\partial z} \Big|_{0^+} = - \frac{\partial C}{\partial z} \Big|_{0^-}, \quad (\text{A.64})$$

$$C = C_s \quad \text{at } x = -1, \quad (\text{A.65})$$

and has solution:

$$C = \phi \frac{\partial C}{\partial z} \Big|_{0^+} (z + b) + C_s = \phi b \frac{\partial C}{\partial x} \Big|_{0^+} (x + 1) + C_s. \quad (\text{A.66})$$

Thus, for small  $b$ ,

$$v = 1 + \frac{C_s}{\xi(1 - C_s)}, \quad (\text{A.67})$$

$$\dot{\eta} = \frac{1}{\xi(1 - C_s)} \left( C_s + \phi \frac{\partial C}{\partial x} \Big|_{0^+} \right) = 0, \quad (\text{A.68})$$

$$\dot{b} = \frac{-\phi}{\xi(1 - C_s)} \frac{\partial C}{\partial x} \Big|_{0^+}. \quad (\text{A.69})$$

For  $b \neq 0$ , the conservation equations can be solved for  $v$ ,  $\dot{\eta}$  and  $\dot{b}$  analytically (in terms of the gradient at  $x = -1$ ):

$$v = 1 + \frac{C_s}{\xi(1 - C_s)}, \quad (\text{A.70})$$

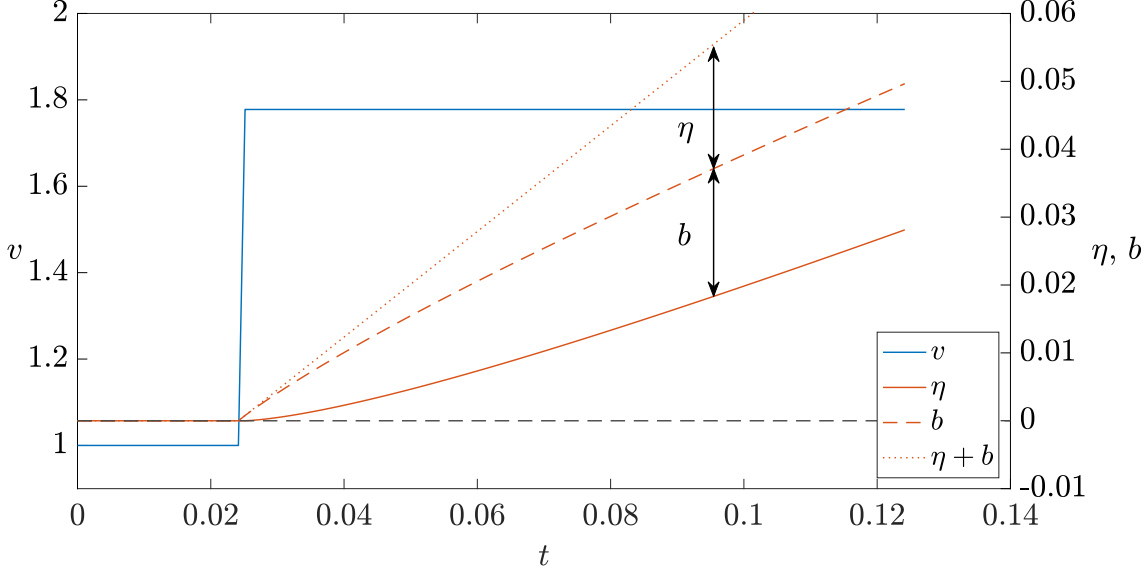


Figure A.6: Throughflow,  $v$ , crust thickness,  $\eta$ , brine thickness,  $b$ , and total thickness,  $\eta + b$ , as functions of time,  $t$ . The jump in  $v$  occurs at  $t = t_s \approx 0.024$  at which  $b$  grows linearly from zero and  $\eta$  begins to grow, initially with  $\dot{\eta} = 0$ .

$$\dot{\eta} = \frac{1}{\xi(1 - C_s)} \left( C_s + \left. \frac{\partial C}{\partial x} \right|_{-1} \right), \quad (\text{A.71})$$

$$\dot{b} = \frac{-1}{\xi(1 - C_s)} \left. \frac{\partial C}{\partial x} \right|_{-1}. \quad (\text{A.72})$$

In the numerical simulations, a single time step ( $\Delta t = 10^{-3}$ ) provided enough time for the brine layer thickness to grow to  $b \sim 10^{-4}$ , from which (A.60) is solved instead of (A.63).

### A.3.2 Results

Figure A.6 displays the (non-dimensional) throughflow velocity,  $v$  and the thicknesses  $\eta$ ,  $b$  and  $\eta + b$  which denote the size of the crust layer, the brine layer and the total thickness of the brine and crust respectively. Once a brine and crust layer is present, the value of the throughflow jumps instantaneously to account for the extra fluid that is required to be accommodated in the growing crust and brine layers. However, this is unphysical, and highlights one problem with the model as it currently stands. The initial growth of the brine layer is linear ( $\dot{b} \neq 0$ ) but the growth slows as the lake settles to a steady state. On the other hand, the initial growth of the crust is slower to respond:  $\dot{\eta} = 0$  at  $t = t_s$ . Since  $v$  and  $\eta$  are determined algebraically (once the diffusive flux is known numerically), the values of the growth rates  $\dot{\eta}$  and  $\dot{b}$  converge as the salt concentration in the lake approaches the steady state. This results in linear growth of  $\eta$  and  $b$  at later times.

## A.4 A Sinking Crust

Since the crust is more dense than the brine layer, it will sink and displace fluid until it is in contact with the underlying porous soil in the lake. To obtain an estimate for the speed that the crust sinks, an infinitely deep layer of fluid may be considered with a crust suspended in it. The crust will descend at a speed  $W_\infty$  and in a frame of reference where the crust is stationary, a fluid flow is present within the pore spaces of the crust. Using Darcy's law:

$$-W_\infty = -\frac{\kappa}{\mu} \left( \frac{\partial p}{\partial z} - \rho_l g \right), \quad (\text{A.73})$$

where  $\kappa$  is the permeability of the crust,  $\mu$  is the viscosity of water,  $\rho_l$  is the density of the liquid and  $g$  is the acceleration due to gravity. The pressure  $p$  is due to the mass of the crust and liquid lying above it:

$$\frac{\partial p}{\partial z} = [\xi \rho_s + (1 - \xi) \rho_l] g. \quad (\text{A.74})$$

Thus,

$$W_\infty = \frac{\kappa g}{\mu} \xi (\rho_s - \rho_l) \approx 10^{-3} \text{ m s}^{-1}, \quad (\text{A.75})$$

using  $\kappa \approx \delta^2/100$ ,  $\delta \approx 10^{-4} \text{ m}$ ,  $g \approx 10 \text{ m s}^{-2}$ ,  $\mu \approx 10^{-3} \text{ Pa s}$ ,  $\rho_s \approx 2 \text{ g cm}^{-3}$  and  $\rho_l \approx 10^3 \text{ kg m}^{-3}$ . Comparing this with the typical evaporation rates at salt lakes,  $E \approx 10^{-8} \text{ m s}^{-1}$ , it is clear that the descent rate of the crust should be almost instantaneous compared to the evaporation velocities. The descent rate of the crust will then be controlled by the dissolution of salt from the interface in contact with the lake below.

The crust of the salt lake will now be allowed to sink at speed  $W$  into the lake below. The advection-diffusion of salt still holds within the lake but the dissolution of the crust at  $z = 0$  induces a sink rate in the crust. The equations and boundary conditions governing this system are:

$$\phi \frac{\partial C}{\partial t} - V \frac{\partial C}{\partial z} = \phi D \frac{\partial^2 C}{\partial z^2}, \quad z \in [0, \infty), \quad (\text{A.76})$$

$$C = C_s \quad \text{at } z = 0, \quad (\text{A.77})$$

$$C \rightarrow C_0 \quad \text{as } z \rightarrow \infty, \quad (\text{A.78})$$

$$\text{Conservation of salt} \quad \text{at } z = 0, \quad (\text{A.79})$$

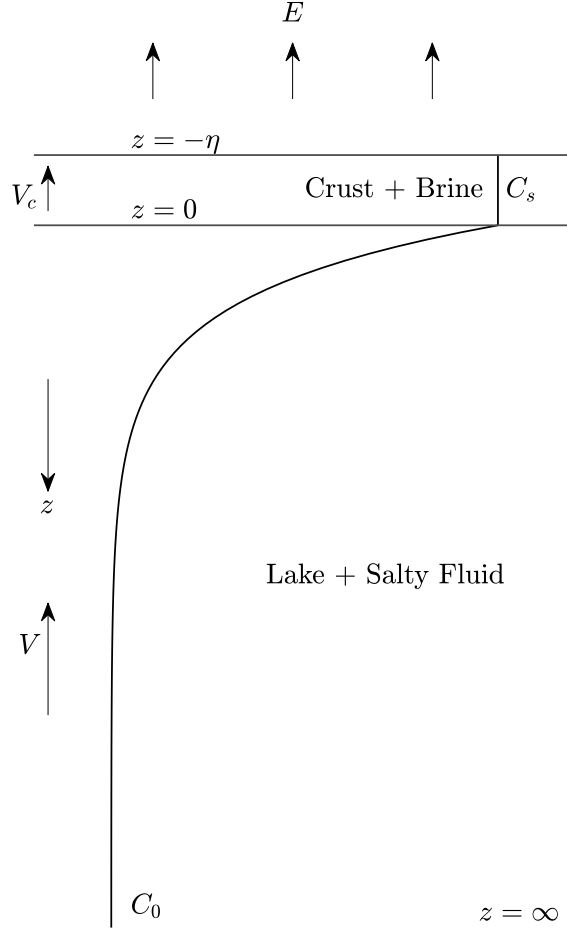


Figure A.7: Sketch of the 1D model for a sinking crust. The lake occupies  $0 \leq z < \infty$  and the overlying crust is of thickness  $\eta$ .

$$\text{Conservation of water at } z = -\eta. \quad (\text{A.80})$$

A sketch of this system is shown in Figure A.7, which is indistinguishable from the sketch in Figure A.1, except for the new throughflow in the crust layer. Since the crust is descending, the volume flux of fluid must increase in the crust. The volume flux of solid moving downwards is  $\xi W$ , giving the Darcy velocity in the crust to be:

$$V_c = V + \xi W. \quad (\text{A.81})$$

Salt must be conserved over the whole domain. This gives:

$$C_0 V = \frac{d}{dt} \int_0^\infty \phi C \, dz + \frac{d}{dt} \int_{-\eta}^0 \bar{C} \, dz, \quad (\text{A.82})$$

$$\implies C_s V + \phi D \left. \frac{\partial C}{\partial z} \right|_{0^+} = \bar{C} \dot{\eta}. \quad (\text{A.83})$$

At the lake–crust interface, salt must be conserved. Balancing salt fluxes, including the advective flux in the fluid and the transport of salt due to the movement of the crust, gives:

$$C_s V + \phi D \left. \frac{\partial C}{\partial z} \right|_{0+} = C_s (V + \xi W) - \xi W, \quad (\text{A.84})$$

$$\implies \xi (1 - C_s) W = -\phi D \left. \frac{\partial C}{\partial z} \right|_{0+}. \quad (\text{A.85})$$

At the crust–air interface, the mass of water must be conserved:

$$(1 - C_s) (V + \xi W) - E = (1 - \xi) (1 - C_s) \dot{\eta}. \quad (\text{A.86})$$

Thus, a solution to the following system of equations is sought:

$$C_s V + \phi D \left. \frac{\partial C}{\partial z} \right|_{0+} = \bar{C} \dot{\eta}, \quad (\text{A.87})$$

$$\xi (1 - C_s) W = -\phi D \left. \frac{\partial C}{\partial z} \right|_{0+}, \quad (\text{A.88})$$

$$(1 - C_s) (V + \xi W) - E = (1 - \xi) (1 - C_s) \dot{\eta}. \quad (\text{A.89})$$

The solution (in terms of the salt gradient at  $z = 0$ ) is:

$$W = -\frac{\phi D}{\xi (1 - C_s)} \left. \frac{\partial C}{\partial z} \right|_{0+}, \quad (\text{A.90})$$

$$V = E + \frac{1}{\xi (1 - C_s)} \left( C_s E + \phi D \left. \frac{\partial C}{\partial z} \right|_{0+} \right), \quad (\text{A.91})$$

$$\dot{\eta} = \frac{1}{\xi (1 - C_s)} \left( C_s E + \phi D \left. \frac{\partial C}{\partial z} \right|_{0+} \right). \quad (\text{A.92})$$

#### A.4.1 Results

Figure A.8 shows the results for the modified model (with velocities scaled with  $E$ , and lengths with  $L = D/E$ ), including the sink rate of the crust. There is a similar growth in  $\eta$  as before, initially with  $\dot{\eta} = 0$  which then grows linearly at later times. The throughflow is enhanced, similar to the case with the brine layer, but varies continuously rather than jumping instantaneously. The values for the throughflow converges to its steady state value as the salt profile in the lake converges to the steady state. A similar convergence

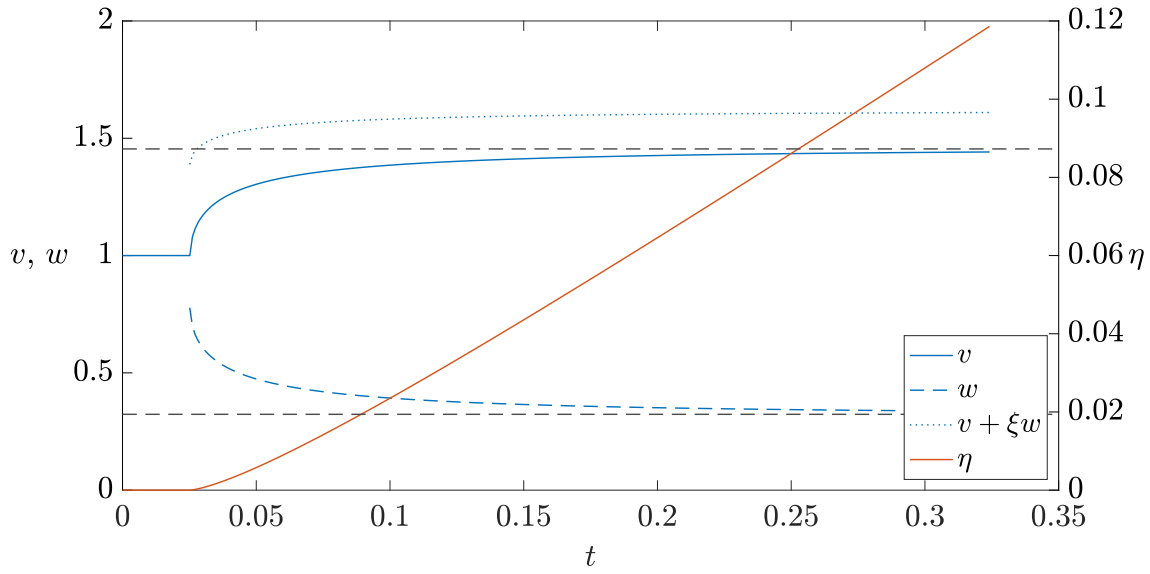


Figure A.8: Throughflow,  $v$ , sink rate,  $w$  and crust thickness,  $\eta$  as functions of time,  $t$ . The jump in  $v$  occurs at  $t = t_s \approx 0.025$  at which  $\eta$  begins to grow, initially with  $\dot{\eta} = 0$ .

is observed for the sink rate,  $w$ , but decreases from its initial maximum value at  $t = t_s$ .

## A.5 Discussion

In this chapter, a one-dimensional model for crust growth has been developed. The model demonstrates that to maintain consistent salt fluxes across the lake-crust interface, a brine layer forms between the lake and the crust. Initially, the salt crust was assumed to float on the brine layer, but it was later allowed to sink and come into contact with the lake surface, as the crust is denser than the brine. This change resulted in enhanced throughflow within the crust. Additionally, simulations were conducted to assess the lake dynamics and the growth rate of the crust's thickness. The results indicate that, over time, the crust's thickness increases linearly as the salt concentration profile in the lake approaches a steady state.

It may be of interest to couple this model with the convective dynamics previously explored. Solving the additional equations for the crust's growth rate within the full non-linear simulations presented in Chapter 4 is relatively straightforward. However, this approach predicts indefinite crust growth. Therefore, modifications will be necessary to limit crust growth when the thickness becomes large enough to hinder evaporation (e.g., when the crust becomes too thick for capillary action to connect groundwater to the crust surface).



# References

- Aghababaeian, H., Ostadtaghizadeh, A., Ardalan, A., Asgary, A., Akbary, M., Yekaninejad, M. S., & Stephens, C. (2021). Global Health Impacts of Dust Storms: A Systematic Review. *Environmental Health Insights*, 15. <https://doi.org/10.1177/11786302211018390>
- Beaume, C. (2024). DryLa Manual. [http://cbeaume.com/download/DryLa\\_manual.pdf](http://cbeaume.com/download/DryLa_manual.pdf)
- Bénard, H. (1900). Les tourbillons cellulaires dans une nappe liquide. *Revue Générale Sciences Pures et Appliquées*, 11, 1261–1271.
- Borsa, A. A., Bills, B. G., & Minster, J.-B. (2008). Modeling the topography of the Salar de Uyuni, Bolivia, as an equipotential surface of Earth's gravity field. *Journal of Geophysical Research: Solid Earth*, 113(B10). <https://doi.org/https://doi.org/10.1029/2007JB005445>
- Briere, P. R. (2000). Playa, playa lake, sabkha: Proposed definitions for old terms. *Journal of Arid Environments*, 45(1), 1–7. <https://doi.org/https://doi.org/10.1006/jare.2000.0633>
- Bryant, R. G. (2003). Monitoring Hydrological Controls on Dust Emissions: Preliminary Observations from Etosha Pan, Namibia. *The Geographical Journal*, 169(2), 131–141. <http://www.jstor.org/stable/3451394>
- Bryant, R. G., & Rainey, M. P. (2002). Investigation of flood inundation on playas within the Zone of Chotts, using a time-series of AVHRR. *Remote Sensing of Environment*, 82(2), 360–375. [https://doi.org/https://doi.org/10.1016/S0034-4257\(02\)00053-6](https://doi.org/https://doi.org/10.1016/S0034-4257(02)00053-6)
- Canuto, C., Hussaini, M. Y., Quarteroni, A., & Zang, T. A. (1988). *Spectral Methods in Fluid Dynamics*. Springer-Verlag Berlin Heidelberg New York.
- Christiansen, F. W. (1963). Polygonal Fracture and Fold Systems in the Salt Crust, Great Salt Lake Desert, Utah. *Science*, 139(3555), 607–609. <https://doi.org/10.1126/science.139.3555.607>

- Courant, R., Friedrichs, K., & Lewy, H. (1928). Über die partiellen Differenzgleichungen der mathematischen Physik. *Mathematische Annalen*, *100*, 32–74. <https://doi.org/10.1007/BF01448839/METRICS>
- Dang, Y., Xiao, L., Xu, Y., Zhang, F., Huang, J., Wang, J., Zhao, J., Komatsu, G., & Yue, Z. (2018). The Polygonal Surface Structures in the Dalangtan Playa, Qaidam Basin, NW China: Controlling Factors for Their Formation and Implications for Analogous Martian Landforms. *Journal of Geophysical Research: Planets*, *123*(10), 1910.
- David, M. (2005). The Owens Lake Project. *Niemand Reports*, *59*(1), 17–19. <https://davidmaisel.com/works/the-lake-project/>
- De Paoli, M., Pirozzoli, S., Zonta, F., & Soldati, A. (2022). Strong Rayleigh–Darcy convection regime in three-dimensional porous media. *Journal of Fluid Mechanics*, *943*, A51. <https://doi.org/10.1017/jfm.2022.461>
- De Paoli, M., Zonta, F., & Soldati, A. (2016). Influence of anisotropic permeability on convection in porous media: Implications for geological CO<sub>2</sub> sequestration. *Physics of Fluids*, *28*(5), 056601. <https://doi.org/10.1063/1.4947425>
- Dellwig, L. F. (1968). Significant Features of Deposition in the Hutchinson Salt, Kansas, and Their Interpretation. *Geological Society of America Special Papers*, 421–428. <https://doi.org/10.1130/spe88-p421>
- Domokos, G., & Regös, K. (2024). A discrete time evolution model for fracture networks. *Central European Journal of Operations Research*, *32*, 83–94. <https://doi.org/10.1007/S10100-022-00838-W/FIGURES/5>
- Duijn, C., Pieters, G.-J., Wooding, R., & Ploeg, A. (2002). Stability Criteria for the Vertical Boundary Layer Formed by Through-flow Near the Surface of a Porous Medium. *Geophysical Monograph Series*, 155–169. <https://doi.org/10.1029/129GM15>
- Eckardt, F. D., Bryant, R. G., McCulloch, G., Spiro, B., & Wood, W. W. (2008). The Hydrochemistry of a Semi-Arid Pan Basin Case Study: Sua Pan, Makgadikgadi, Botswana. *Applied Geochemistry : Journal of the International Association of Geochemistry and Cosmochemistry*, *23*, 1563.
- Elder, J. W. (1967). Steady free convection in a porous medium heated from below. *Journal of Fluid Mechanics*, *27*(1), 29–48. <https://doi.org/10.1017/S0022112067000023>
- Eloukabi, H., Sghaier, N., Nasrallah, S. B., & Prat, M. (2013). Experimental study of the effect of sodium chloride on drying of porous media: The crusty–patchy efflores-

- cence transition. *Heat and Mass Transfer*, 56, 80–93. <https://doi.org/10.1016/J.IJHEATMASSTRANSFER.2012.09.045>
- Eugster, H. P., & Hardie, L. A. (1978). Saline lakes. *Lakes*, 237–293. [https://doi.org/10.1007/978-1-4757-1152-3\\_8](https://doi.org/10.1007/978-1-4757-1152-3_8)
- Flood, A. (2024). Lithium mining looks set to reshape Bolivia’s Salar de Uyuni salt flat [Accessed: 2024-04-22]. <https://www.newscientist.com/article/mg26134750-200-lithium-mining-looks-set-to-reshape-bolivias-salar-de-uyuni-salt-flat/>
- Frigo, M., & Johnson, S. G. (2005). The Design and Implementation of FFTW3. *Proceedings of the IEEE*, 93(2), 216–231.
- Fu, X., Cueto-Felgueroso, L., & Juanes, R. (2013). Pattern formation and coarsening dynamics in three-dimensional convective mixing in porous media. *Philosophical Transactions of the Royal Society A*, 371(2004), 20120355. <https://doi.org/10.1098/rsta.2012.0355>
- Fung, I. Y., et al. (2000). Iron supply and demand in the upper ocean. *Global Biogeochemical Cycles*, 14(1), 281–295. <https://doi.org/10.1029/1999gb900059>
- Gill, T. E. (1996). Eolian sediments generated by anthropogenic disturbance of playas: human impacts on the geomorphic system and geomorphic impacts on the human system [Response of Aeolian Processes to Global Change]. *Geomorphology*, 17(1), 207–228. [https://doi.org/https://doi.org/10.1016/0169-555X\(95\)00104-D](https://doi.org/https://doi.org/10.1016/0169-555X(95)00104-D)
- Gill, T. E., et al. (2002). Elemental geochemistry of wind-erodible playa sediments, Owens Lake, California. *Nuclear Instruments and Methods in Physics*, 189(1), 209–213. [https://doi.org/10.1016/S0168-583X\(01\)01044-8](https://doi.org/10.1016/S0168-583X(01)01044-8)
- Goehring, L. (2013). Evolving fracture patterns: columnar joints, mud cracks and polygonal terrain. *Philosophical Transactions of the Royal Society A*, 371(2004), 20120353. <https://doi.org/10.1098/rsta.2012.0353>
- Graham, T. (2023). Bolivia’s dream of a lithium future plays out on high-altitude salt flats [Accessed: 2024-04-22]. <https://www.theguardian.com/world/2023/jan/25/bolivia-lithium-mining-salt-flats>
- Groeneveld, D., Huntington, J., & Barz, D. (2010). Floating brine crusts, reduction of evaporation and possible replacement of fresh water to control dust from Owens Lake bed, California. *Journal of Hydrology*, 392, 211–218. <https://doi.org/10.1016/j.jhydrol.2010.08.010>

- Groeneveld, D. P., & Barz, D. D. (2013). Remote Monitoring of Surfaces Wetted for Dust Control on the Dry Owens Lakebed, California. *Open Journal of Modern Hydrology*, 03(04), 241–252. <https://doi.org/10.4236/ojmh.2013.34028>
- Güler, C., & Thyne, G. (2004). Hydrologic and geologic factors controlling surface and groundwater chemistry in Indian Wells-Owens Valley area, southeastern California, USA. *Journal of Hydrology*, 285, 177–198. <https://doi.org/10.1016/j.jhydrol.2003.08.019>
- Hall, W. (1956). An analytical derivation of the Darcy equation. *Eos, Transactions American Geophysical Union*, 37(2), 185–188. <https://doi.org/https://doi.org/10.1029/TR037i002p00185>
- Hewitt, D. R. (2020). Vigorous convection in porous media. *Proceedings of the Royal Society A*, 476(2239), 20200111. <https://doi.org/10.1098/rspa.2020.0111>
- Hewitt, D. R., Neufeld, J. A., & Lister, J. R. (2012). Ultimate Regime of High Rayleigh Number Convection in a Porous Medium. *Physical Review Letters*, 108, 224503. <https://doi.org/10.1103/PhysRevLett.108.224503>
- Hewitt, D. R., Neufeld, J. A., & Lister, J. R. (2014). High Rayleigh number convection in a three-dimensional porous medium. *Journal of Fluid Mechanics*, 748, 879–895. <https://doi.org/10.1017/jfm.2014.216>
- Hollett, K. J., Danskin, W. R., McCaffrey, W. F., & Walti, C. L. (1991). Geology and water resources of Owens Valley, California. *Water Supply Paper*. <https://doi.org/10.3133/WSP2370B>
- Homsy, G. M., & Sherwood, A. E. (1976). Convective instabilities in porous media with through flow. *AIChE Journal*, 22(1), 168–174.
- Horton, C. W., & Rogers, F. T. (1945). Convection Currents in a Porous Medium. *Journal of Applied Physics*, 16, 367–370. <https://doi.org/10.1063/1.1707601>
- Koehler, K. A., et al. (2007). Potential impact of Owens (dry) Lake dust on warm and cold cloud formation. *Journal of Geophysical Research*, 112(D12). <https://doi.org/10.1029/2007jd008413>
- Krinsley, D. (1970). A geomorphological and paleoclimatological study of the playas of Iran. Part 1. *U.S. Geological Survey, CP 70-800*.
- Lacis, A., Hansen, J., & Sato, M. (1992). Climate forcing by stratospheric aerosols. *Geophysical Research Letters*, 19(15), 1607–1610. <https://doi.org/10.1029/92gl01620>

- Lapwood, E. R. (1948). Convection of a fluid in a porous medium. *Mathematical Proceedings of the Cambridge Philosophical Society*, 44(4), 508–521. <https://doi.org/10.1017/S030500410002452X>
- Lasser, J. (2019). *Geophysical Pattern Formation of Salt Playa* (Doctoral dissertation). Georg-August-Universität Göttingen.
- Lasser, J., Ernst, M., & Goehring, L. (2021). Stability and dynamics of convection in dry salt lakes. *Journal of Fluid Mechanics*, 917, A14. <https://doi.org/10.1017/jfm.2021.225>
- Lasser, J., Nield, J. M., Ernst, M., Karius, V., Wiggs, G. F. S., Threadgold, M. R., Beaume, C., & Goehring, L. (2023). Salt Polygons and Porous Media Convection. *Physical Review X*, 13, 011025. <https://doi.org/10.1103/PhysRevX.13.011025>
- Lasser, J., Nield, J. M., & Goehring, L. (2020). Surface and subsurface characterisation of salt pans expressing polygonal patterns. *Earth System Science Data*, 12(4), 2881–2898. <https://doi.org/10.5194/essd-12-2881-2020>
- Li, X., & Shi, F. (2021). Effects of evolving salt precipitation on the evaporation and temperature of sandy soil with a fixed groundwater table. *Vadose Zone Journal*, 20(3), e20122. <https://doi.org/https://doi.org/10.1002/vzj2.20122>
- Lokier, S. (2012). Development and evolution of subaerial halite crust morphologies in a coastal sabkha setting. *Journal of Arid Environments*, 79, 32–47. <https://doi.org/10.1016/j.jaridenv.2011.11.031>
- Los Angeles Department of Water and Power. (2013). Los Angeles Aqueduct. <https://www.ladwp.com/who-we-are/water-system/los-angeles-aqueduct>
- Lowenstein, T. K., & Hardie, L. A. (1985). Criteria for the recognition of salt-pan evaporites. *Sedimentology*, 32(5), 627–644. <https://doi.org/https://doi.org/10.1111/j.1365-3091.1985.tb00478.x>
- Marticorena, B., & Bergametti, G. (1995). Modeling the atmospheric dust cycle: 1. Design of a soil-derived dust emission scheme. *Journal of Geophysical Research*, 100(D8), 16415–16430. <https://doi.org/10.1029/95jd00690>
- Metz, B., Davidson, O., De Coninck, H. C., Loos, M., & Meyer, L. (2005). *IPCC special report on carbon dioxide capture and storage*. Cambridge: Cambridge University Press.
- Nachshon, U., Weisbrod, N., Katzir, R., & Nasser, A. (2018). NaCl Crust Architecture and Its Impact on Evaporation: Three-Dimensional Insights. *Geophysical Research Letters*, 45(12), 6100–6108. <https://doi.org/https://doi.org/10.1029/2018GL078363>

- Neufeld, J. A., Hesse, M. A., Riaz, A., Hallworth, M. A., Tchelepi, H. A., & Huppert, H. E. (2010). Convective dissolution of carbon dioxide in saline aquifers. *Geophysical Research Letters*, *37*(22). <https://doi.org/10.1029/2010GL044728>
- Nicholas, L., & Andy, B. (1997). Influence of vegetation cover on sand transport by wind: field studies at Owens Lake, California. *Earth Surface Processes and Landforms*, *23*(1), 69–82. [https://doi.org/10.1002/\(SICI\)1096-9837\(199801\)23:1<69::AID-ESP823>3.0.CO;2-G](https://doi.org/10.1002/(SICI)1096-9837(199801)23:1<69::AID-ESP823>3.0.CO;2-G)
- Nield, D. A., & Bejan, A. (2017). *Convection in Porous Media*. Springer International Publishing.
- Nield, J. M., et al. (2016). Evaporative sodium salt crust development and its wind tunnel derived transport dynamics under variable climatic conditions. *Aeolian Research*, *23*, 51–62. <https://doi.org/10.1016/j.aeolia.2016.09.003>
- Nield, J. M., Bryant, R. G., Wiggs, G. F., King, J., Thomas, D. S., Eckardt, F. D., & Washington, R. (2015). The dynamism of salt crust patterns on playas. *Geology*, *43*(1), 31–34. <https://doi.org/10.1130/G36175.1>
- North, G. R., Cahalan, R. F., & Coakley, J. A. (1981). Energy balance climate models. *Reviews of Geophysics*, *19*(1), 91. <https://doi.org/10.1029/rg019i001p00091>
- Otero, J., Dontcheva, L. A., Johnston, H., Worthing, R. A., Kurganov, A., Petrova, G., & Doering, C. R. (2004). High-Rayleigh-number convection in a fluid-saturated porous layer. *Journal of Fluid Mechanics*, *500*, 263–281. <https://doi.org/10.1017/S0022112003007298>
- Pitman, A. J. (2003). The evolution of, and revolution in, land surface schemes designed for climate models. *International Journal of Climatology*, *23*(5), 479–510. <https://doi.org/10.1002/joc.893>
- Poulet, T., Sheldon, H. A., Kelka, U., & Behnoudfar, P. (2023). Impact of permeability anisotropy misalignment on flow rates predicted by hydrogeological models. *Hydrogeology Journal*, *31*, 2129–2137. <https://doi.org/10.1007/S10040-023-02708-4/TABLES/1>
- Pretti, V. A., & Stewart, B. W. (2002). Solute sources and chemical weathering in the Owens Lake watershed, eastern California. *Water Resources Research*, *38*(8). <https://doi.org/10.1029/2001WR000370>
- Prospero, J. M., Ginoux, P., Torres, O., Nicholson, S. E., & Gill, T. E. (2002). Environmental characterization of global sources of atmospheric soil dust identified with the Nimbus 7 total ozone mapping spectrometer (TOMS) absorbing aerosol prod-

- uct. *Review of Geophysics*, 40(1), 2-1-2–31. <https://doi.org/https://doi.org/10.1029/2000RG000095>
- Raupach, M. R., Gillette, D. A., & Leys, J. F. (1993). The effect of roughness elements on wind erosion threshold. *Journal of Geophysical Research: Atmospheres*, 98(D2), 3023–3029. <https://doi.org/10.1029/92jd01922>
- Rayleigh, L. (1916). LIX. On convection currents in a horizontal layer of fluid, when the higher temperature is on the under side. *The London, Edinburgh, and Dublin Philosophical Magazine and Journal of Science*, 32(192), 529–546.
- Reynolds, R. L., Yount, J. C., Reheis, M., Goldstein, H., Chavez Jr., P., Fulton, R., Whitney, J., Fuller, C., & Forester, R. M. (2007). Dust emission from wet and dry playas in the Mojave Desert, USA. *Earth Surface Processes and Landforms*, 32(12), 1811–1827. <https://doi.org/https://doi.org/10.1002/esp.1515>
- Robock, A., & Mao, J. (1995). The Volcanic Signal in Surface Temperature Observations. *Journal of Climate*, 8(5), 1086–1103. [https://doi.org/10.1175/1520-0442\(1995\)008<1086:tvstis>2.0.co;2](https://doi.org/10.1175/1520-0442(1995)008<1086:tvstis>2.0.co;2)
- Ryu, J., et al. (2002). Arsenic distribution, speciation and solubility in shallow groundwater of Owens Dry Lake, California. *Geochimica et Cosmochimica Acta*, 66(17), 2981–2994. [https://doi.org/10.1016/S0016-7037\(02\)00897-9](https://doi.org/10.1016/S0016-7037(02)00897-9)
- Ryu, J., et al. (2004). Characterization of Redox Processes in Shallow Groundwater of Owens Dry Lake, California. *Environmental Science & Technology*, 38(22), 5950–5957. <https://doi.org/10.1021/es0306112>
- Safdie, S. (2023). What is the Problem With the Great Salt Lake Drying up? [Accessed: 2024-04-22]. <https://greenly.earth/en-gb/blog/ecology-news/what-is-the-problem-with-the-great-salt-lake-drying-up>
- Sanchez-Lopez, M. D. (2021). Territory and lithium extraction: The Great Land of the Uyuni Salt Flat in Bolivia. *Political Geography*, 90. <https://doi.org/https://doi.org/10.1016/j.polgeo.2021.102456>
- Sanford, W. E., & Wood, W. W. (2001). Hydrology of the Coastal Sabkhas of Abu Dhabi, United Arab Emirates. *Hydrogeology Journal*, 9(4), 358.
- Siegler, K. (2024). What biologists see from the shores of the drying Great Salt Lake [Accessed: 2024-04-22]. <https://www.npr.org/2024/04/13/1244169234/scientists-worry-about-ecological-collapse-at-great-salt-lake>

- Singh, M. (2023). 'Last nail in the coffin': Utah's Great Salt Lake on verge of collapse [Accessed: 2024-04-22]. <https://www.theguardian.com/environment/2023/jan/10/utah-great-salt-lake-collapse-imminent>
- Slim, A. C. (2014). Solutal-convection regimes in a two-dimensional porous medium. *Journal of Fluid Mechanics*, 741, 461–491. <https://doi.org/10.1017/jfm.2013.673>
- Slim, A. C., Bandi, M. M., Miller, J. C., & Mahadevan, L. (2013). Dissolution-driven convection in a Hele–Shaw cell. *Physics of Fluids*, 25(2), 024101. <https://doi.org/10.1063/1.4790511>
- Slim, A. C., & Ramakrishnan, T. S. (2010). Onset and cessation of time-dependent, dissolution-driven convection in porous media. *Physics of Fluids*, 22(12), 124103. <https://doi.org/10.1063/1.3528009>
- Star Wars: The Last Jedi. (2017). [Film]. Johnson, R. dir. USA: Lucasfilm Ltd.
- Stevens, J. D., Sharp, J. M., Simmons, C. T., & Fenstermaker, T. (2009). Evidence of free convection in groundwater: Field-based measurements beneath wind-tidal flats. *Journal of Hydrology*, 375(3), 394–409. <https://doi.org/https://doi.org/10.1016/j.jhydrol.2009.06.035>
- Talbot, C. J., et al. (1996). Epitaxial salt reefs and mushrooms in the southern Dead Sea. *Sedimentology*, 43(6), 1025–1047. <https://doi.org/10.1111/j.1365-3091.1996.tb01517.x>
- Trefethen, L. N. (2000). *Spectral Methods in MATLAB*. Society for Industrial & Applied Mathematics.
- Tucker, R. M. (1981). Giant polygons in the Triassic salt of Cheshire, England; a thermal contraction model for their origin. *Journal of Sedimentary Research*, 51(3), 779–786. <https://doi.org/10.1306/212F7DA6-2B24-11D7-8648000102C1865D>
- Tyler, S., Kranz, S., Parlange, M., Albertson, J., Katul, G., Cochran, G., Lyles, B., & Holder, G. (1997). Estimation of groundwater evaporation and salt flux from Owens Lake, California, USA. *Journal of Hydrology*, 200(1), 110–135. [https://doi.org/https://doi.org/10.1016/S0022-1694\(97\)00007-3](https://doi.org/https://doi.org/10.1016/S0022-1694(97)00007-3)
- Van Dam, R. L., Simmons, C. T., Hyndman, D. W., & Wood, W. W. (2009). Natural free convection in porous media: First field documentation in groundwater. *Geophysical Research Letters*, 36(11). <https://doi.org/https://doi.org/10.1029/2008GL036906>
- Wadge, G., Archer, D., & Millington, A. (1994). Monitoring Playa Sedimentation Using Sequential Radar Images. *Terra Nova*, 6, 391.

- Washington, R., Todd, M., Middleton, N. J., & Goudie, A. S. (2003). Dust-Storm Source Areas Determined by the Total Ozone Monitoring Spectrometer and Surface Observations. *Annals of the Association of American Geographers*, *93*(2), 297–313. <https://doi.org/https://doi.org/10.1111/1467-8306.9302003>
- Wooding, R. A. (1957). Steady state free thermal convection of liquid in a saturated permeable medium. *Journal of Fluid Mechanics*, *2*(3), 273–285. <https://doi.org/10.1017/S0022112057000129>
- Wooding, R. A. (1960). Rayleigh instability of a thermal boundary layer in flow through a porous medium. *Journal of Fluid Mechanics*, *9*(2), 183–192. <https://doi.org/10.1017/S0022112060001031>
- Wooding, R. A. (1969). Growth of fingers at an unstable diffusing interface in a porous medium or Hele-Shaw cell. *Journal of Fluid Mechanics*, *39*(3), 477–495. <https://doi.org/10.1017/S002211206900228X>
- Wooding, R. A. (2007). Variable-density saturated flow with modified Darcy's law: The salt lake problem and circulation. *Water Resource Research*, *43*(2).
- Wooding, R. A., Tyler, S. W., & White, I. (1997). Convection in groundwater below an evaporating Salt Lake: 1. Onset of instability. *Water Resource Research*, *33*(6), 1199–1217. <https://doi.org/https://doi.org/10.1029/96WR03533>
- Wooding, R. A., Tyler, S. W., White, I., & Anderson, P. A. (1997). Convection in groundwater below an evaporating Salt Lake: 2. Evolution of fingers or plumes. *Water Resource Research*, *33*(6), 1219–1228. <https://doi.org/https://doi.org/10.1029/96WR03534>
- Wurtsbaugh, W. A., Miller, C., Null, S. E., DeRose, R. J., Wilcock, P., Hahnenberger, M., Howe, F., & J., M. (2017). Decline of the world's saline lakes. *Nature Geoscience*, *10*, 816–821.
- Yechieli, Y., & Wood, W. W. (2002). Hydrogeologic processes in saline systems: playas, sabkhas, and saline lakes. *Earth-Science Reviews*, *58*, 343–365. [https://doi.org/10.1016/S0012-8252\(02\)00067-3](https://doi.org/10.1016/S0012-8252(02)00067-3)
- Zhong, S., Li, J., Whiteman, C. D., Bian, X., & Yao, W. (2008). Climatology of High Wind Events in the Owens Valley, California. *Monthly Weather Review*, *136*(9), 3536–3552. <https://doi.org/10.1175/2008MWR2348.1>